BEILSTEIN JOURNAL OF NANOTECHNOLOGY

Nanomanipulation and environmental nanotechnology

Edited by Enrico Gnecco

Imprint

Beilstein Journal of Nanotechnology
www.bjnano.org
ISSN 2190-4286
Email: journals-support@beilstein-institut.de

The *Beilstein Journal of Nanotechnology* is published by the Beilstein-Institut zur Förderung der Chemischen Wissenschaften.

Beilstein-Institut zur Förderung der Chemischen Wissenschaften
Trakehner Straße 7–9
60487 Frankfurt am Main
Germany
www.beilstein-institut.de

BEILSTEIN JOURNAL OF NANOTECHNOLOGY

Nanomanipulation and environmental nanotechnology

Enrico Gnecco*[1], Andre Schirmeisen[2], Carlos M. Pina[3] and Udo Becker[4]

Editorial

Open Access

Address:
[1]Instituto Madrileño de Estudios Avanzados en Nanociencia (IMDEA Nanociencia), Campus Universitario de Cantoblanco, Calle Faraday 9, 28049 Madrid, Spain, [2]Institute of Applied Physics, Justus-Liebig Universität Giessen, Heinrich-Buff-Ring 16, 35392 Giessen, Germany, [3]Department of Crystallography and Mineralogy, Complutense University of Madrid, 28040 Madrid, Spain and [4]Department of Earth and Environmental Sciences, University of Michigan, Ann Arbor, Michigan 48109-1005, USA

Email:
Enrico Gnecco* - enrico.gnecco@imdea.org

* Corresponding author

Beilstein J. Nanotechnol. **2014,** *5,* 2079–2080.
doi:10.3762/bjnano.5.216

Received: 01 September 2014
Accepted: 15 October 2014
Published: 11 November 2014

This article is part of the Thematic Series "Nanomanipulation and environmental nanotechnology".

Editor-in-Chief: T. Schimmel

The leitmotif of this Thematic Series is the application of nanotechnology to environmental issues. Since the subject is broad and rapidly evolving it is clearly not possible to completely cover it in the limited space at our disposal. We have rather caught different “flavors” of emerging technologies and presented them as described by the scientists who are actively contributing to their development.

Nanotechnology enters the characterization of processes of environmental interest in a multidisciplinary way. The techniques include atomic force microscopy (AFM), scanning electron microscopy (SEM), transmission electron microscopy (TEM), diffraction methods and advanced chemical analysis. Furthermore, one has often to deal with tiny particles, whose study frequently requires their nanomanipulation. One advantage of scanning probe techniques is that they allow interacting directly with the particles and displacing them in a controlled way on different substrates. In this way, adhesion and friction can be precisely quantified in different environments. Although very few experiments of this kind have been reported so far, the potential of these techniques is enormous.

This Thematic Series is a compilation of papers which provide a wide variety of examples in which nanotechnologies are used to study or potentially solve environmental problems. For example, organic pollutants can be successfully removed from wastewater using the unique catalytic properties of pyrite nanoparticles. Adhesion of marine bacteria can be prevented by new coating materials based on polyethylene oxide. The surface reactivity of minerals in contact with aqueous solutions can be investigated by laser confocal microscopy, as shown on the example of dissolution of the mineral biotite in solutions with acid and basic pH. Recent nanofiltration techniques are reviewed with emphasis on their applicability, costs and up-scaling. A novel gas sensor based on ZnO nanoparticles doped with palladium is presented.

An invaluable support comes from theory, which in combination with experimental techniques can decisively contribute to a better understanding of important nanoscale processes. For example, the photocatalytic degradation of pollutants can be interpreted using density functional theory. On a different scale, AFM measurements in liquid environments can be supported by

advanced contact mechanics models including the squeeze-out of wetting fluids.

Adhesion of fluorite nanoparticles on enamel is important in dental applications, as shown by AFM nanomanipulation experiments. The motion of nanoparticles on a surface can be also driven by quartz tuning forks coupled to scanning electron microscopy. As mentioned above, these techniques hold great potential for a better understanding of friction and adhesive forces on the nanoscale.

Last but not least, we would like to mention that this Thematic Series was partially inspired by the "Advanced Materials Science Networking (AMASING)" workshop organized by Prof. Gianaurelio Cuniberti in Da Nang, Vietnam, in March 2013. This was one of the rare occasions to gather together scientists with different background and geographical distribution who are working in the field.

In conclusion, we would like to thank all the researchers who submitted their contributions to the Thematic Series, the reviewers who carefully checked the accuracy of the manuscripts, and the Beilstein Journal of Nanotechnology for providing an open access platform where the scientists involved in such an important subject have found a direct way to disseminate their results at no additional cost.

Enrico Gnecco, Andre Schirmeisen, Carlos M. Pina and Udo Becker

September 2014

Beilstein Journal of Nanotechnology

New hybrid materials based on poly(ethyleneoxide)-grafted polysilazane by hydrosilylation and their anti-fouling activities

Thi Dieu Hang Nguyen*[1,2], François-Xavier Perrin[2] and Dinh Lam Nguyen[1]

Full Research Paper

Open Access

Address:
[1]Danang University of Science and Technology, University of Danang, 54 Nguyen Luong Bang, Danang, Vietnam and [2]Institut des Sciences de l'Ingénieur de Toulon - Var (ISITV), Université du Sud Toulon - Var, Av. G. Pompidou, BP 56, 83162 La Valette Cedex, France

Email:
Thi Dieu Hang Nguyen* - ntdhang@dut.udn.vn

* Corresponding author

Keywords:
antibacterial; hybrid materials; hydrosilylation; poly(ethyleneoxide); polysilazane

Beilstein J. Nanotechnol. **2013,** *4,* 671–677.
doi:10.3762/bjnano.4.75

Received: 21 May 2013
Accepted: 01 October 2013
Published: 21 October 2013

This article is part of the Thematic Series "Nanomanipulation and environmental nanotechnology".

Guest Editor: E. Gnecco

Abstract

The objective of this work was to develop new coating materials based on poly(ethyleneoxide) (PEO), which was grafted onto polysilazane (PSZ) by hydrosilylation. Three types of PEO with different molecular weights (350, 750, 2000 g/mol) were studied. The kinetics and yields of this reaction have been surveyed by ^{1}H and ^{13}C NMR spectroscopy. The PEO grafting-density onto PSZ by hydrosilylation increases with a reduction of the S–H/allyl ratio and a decrease of the PEO chain-length. The PEO-*graft*-PSZ (PSZ-PEO) hybrid coatings, which can be used to prevent the adhesion of marine bacteria on surfaces, were applied by moisture curing at room temperature. The anti-adhesion performance, and thus the anti-fouling activity, of the coatings against three marine bacteria species, *Clostridium sp.* SR1, *Neisseria sp.* LC1 and *Neisseria sp.* SC1, was examined. The anti-fouling activity of the coatings depends on the grafting density and the chain length of PEO. The shortest PEO(350 g/mol)-*graft*-PSZ with the highest graft density was found to have the best anti-fouling activity. As the density of grafted PEO(750 g/mol) and PEO(2000 g/mol) chains onto the PSZ surface is approximately equal, the relative effectiveness of these two types of PEO is controlled by the length of the PEO chain. The PEO(2000 g/mol)-*graft*-PSZ coatings are more efficient than the PEO(750 g/mol)-*graft*-PSZ coatings for the bacterial anti-adhesion.

Introduction

To date, polysilazanes with the general formula $-(SiR^1R^2-NR^3)_n-$, have been mainly used as ceramic precursors Si/C/N for high-temperature applications [1-3]. The Clariant Company has developed formulations based on polysilazanes that could crosslinked by humid air through hydrolysis and condensation reactions [4,5]. This method was used to prepare coatings of thicknesses from 0.3 to 50 micrometers that have an excellent resistance against corrosion and abrasion

because of their exceptional adhesion to a variety of substrates (glass, polycarbonate, aluminium, steel, etc.) combined with a high brightness, a non-stick surface, and the resistance to heat, fire and UV irradiation.

Poly(ethylene oxide) or poly(oxyethylene) (PEO) is a non-toxic polymer, which is used as a surface-modification agent, because it is effective in reducing bio-adhesion, i.e., protein adsorption, or the adhesion of bacteria and cells. The environmentally friendly coatings obtained by the grafting of PEO onto PSZ are a promising way to prevent the deposition of marine fouling materials onto the hulls of ships [6]. Several factors have been hypothesized to explain the anti-fouling property of these surfaces. These include the hydrophilicity [7], the mobility, the large exclusion volume in water and the effect of steric repulsion [8-11]. The effect of the molecular weight and the grafting density of PEO on the anti-fouling capacity has been widely studied [12-14].

Several methods to modify surfaces with PEO chains were investigated. These include the covalent grafting [15,16], the chemical adsorption [17], the formation of self-assembled monolayers [18,19], plasma treatment [12,20] or the use of supercritical CO_2 [21,22]. Kingshott et al. have demonstrated that the grafting of PEO onto the substrates by covalent bonding is necessary for an anti-fouling activity [23]. Herein, we propose a new synthetic strategy to prepare hybrid materials based on polysilazane (PSZ), which have an enhanced resistance against bacteria adhesion, through the incorporation of allyl PEO monomethyl ether by covalent grafting.

Experimental

Materials. Monomethoxy poly(ethylene oxide) glycol (MPEG) with average molecular weights of 350 g/mol, 750 g/mol and 2000 g/mol and Karstedt's catalyst were purchased from Sigma-Aldrich. All three types of MPEG were dried under vacuum before usage. The polysilazane precursor, polylmethyhydrosilazane containing triethoxysilanes, was provided by the Clariant Company. The molecular structure of the polysilazane precursor is described on Figure 1. PSZ was used as received without any further purification. Allyl bromide (allyl-Br) purchased from Acros was distilled under a nitrogen atmosphere in the dark and subsequently kept in darkness before usage. Allyl-Br is sensitive to light and may polymerize on exposure to light.

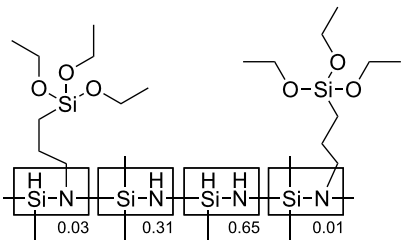

Figure 1: Molecular structure and distribution of the functional groups of the polysilazane precursor provided by the Clariant Company.

NMR. ^1H and ^{13}C NMR spectra were obtained on a Bruker FT-NMR 400 MHz spectrometer.

Protocol of the marine bacterial adhesion. Three marine bacteria species, bacillus *Clostridium sp.* SR1, micrococcus *Neisseria sp.* LC1 and micrococcus *Neisseria sp.* SC1, were used for the adhesion studies. The culture media was Vätäänen nine-salt solution (VNSS). The PSZ and PSZ-PEO coatings, which were moisture-cured at ambient conditions, were previously sterilized in methanol, immersed in VNSS that contained the bacteria and were finally incubated at 30 °C for 24 h. Then coatings were rinsed in sterilized phosphate buffered saline to remove the non-adhered bacteria. The adhered bacteria were removed from the surfaces using an ultrasonic cleaner for 5 min with sterilized synthetic sea water. The number of adhered bacteria (CFU/cm^2) was determined by using a Colony Counter BZG30.

Synthesis of allyl-PEO. Allyl-terminated monomethyl poly(ethylene oxide) (allyl-PEO) ethers were synthesized via the reaction of MPEG with an excess amount of allyl-Br [24]. The equation of this synthesis reaction is described in Scheme 1.

Synthesis of PSZ-PEO. Grafting of allyl-PEO molecules onto the polysilazane (PSZ) chain was performed by using a hydrosilylation reaction between the Si–H group of PSZ and the terminal C=C bond of the allyl-PEO with an excess amount of PSZ in presence of Karstedt's catalyst (Scheme 2). We define that **a**, **b**, **c** are the different protons and carbon atoms on the allyl branch of the PEO molecule, whereas **a′**, **b′**, **c′** are the different protons and carbon atoms of the same branch *after* being grafted onto the PZS chain.

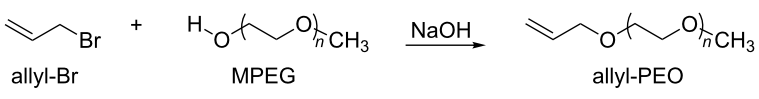

Scheme 1: Equation of the allyl-PEO synthesis reaction.

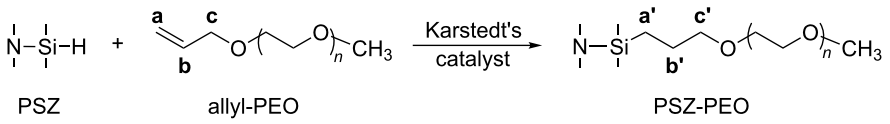

Scheme 2: Principle of hydrosilylation between the Si–H group of PSZ and the C=C bond of the allyl-PEO.

The most favorable conditions for the grafting of allyl-PEO chains on PSZ are the following: a temperature of 80 °C and a molar ratio of Pt/allyl of 3×10^{-3} under argon atmosphere. Different Si–H/allyl molar ratios of 10, 16.5 and 26.5, respectively, were investigated for all three types of allyl-PEO. The grafted products are symbolized as PSZ-PEO**X**-**Y** with **X** being the molecular weight of MPEG and **Y** being the Si–H/allyl molar ratio.

Results and Discussion

Grafting of allyl-PEO molecules onto the PSZ chain

The kinetics and yields of the grafting reactions have been surveyed by ^{1}H and ^{13}C NMR spectroscopy. Figure 2 shows the ^{1}H NMR and ^{13}C NMR spectra of the mixture of the reactants and of the grafting products. In Figure 1 and in Scheme 2, it is found that the structure of the grafted group ≡Si–CH_2–CH_2–CH_2–O– of PSZ-PEO is very close to that of the group ≡Si–CH_2–CH_2–CH_2–N– of the PSZ precursor. In the ^{1}H NMR spectra, the resonance peaks of the protons $\boldsymbol{H_{a'}}$ and $\boldsymbol{H_{b'}}$ of PSZ-PEO therefore appear at chemical shifts very similar to those of the protons ≡Si–C$\boldsymbol{H_2}$–CH_2– (0.62 ppm) and ≡Si–CH_2–C$\boldsymbol{H_2}$– (1.5 ppm) of PSZ, respectively. Likewise, the chemical shift of the proton $\boldsymbol{H_{c'}}$ of PSZ-PEO is very close to that of protons –O–C$\boldsymbol{H_3}$ and –O–C$\boldsymbol{H_2}$–C$\boldsymbol{H_2}$–O– of PEO, situated at around 3.4 ppm (Figure 2A). The same difficulties in identifying the grafted PEO are encountered during the analysis of the ^{13}C NMR spectra. This is because the ^{13}C NMR chemical shifts of the carbon atoms at positions $\boldsymbol{C_{a'}}$ and ≡Si–$\boldsymbol{C}H_2$–CH_2–, $\boldsymbol{C_{b'}}$ and ≡Si–CH_2–$\boldsymbol{C}H_2$–, $\boldsymbol{C_{c'}}$ and –O–$\boldsymbol{C}H_2$–$\boldsymbol{C}H_2$–O– of PEO are very close, as shown in Figure 2B. In order to circumvent theses complications, the kinetic investigation of the hydrosilylation reaction was carried out by following the decrease of the intensity of the allyl-proton resonances in the ^{1}H NMR spectra.

The evolution of the ^{1}H NMR spectra of the reactant mixture over the reaction time is shown in Figure 3. These results verify that the intensities of the ^{1}H MNR peaks attributed to the allyl group (–C$\boldsymbol{H}$ = at 5.87ppm, C$\boldsymbol{H_2}$ = at 5.22ppm and –$\boldsymbol{CH_2}$– at 3.99ppm) [24] decrease continuously. This diminution can be used to confirm the participation of the allyl group in the hydrosilylation during the grafting of allyl-PEO onto the PSZ chain.

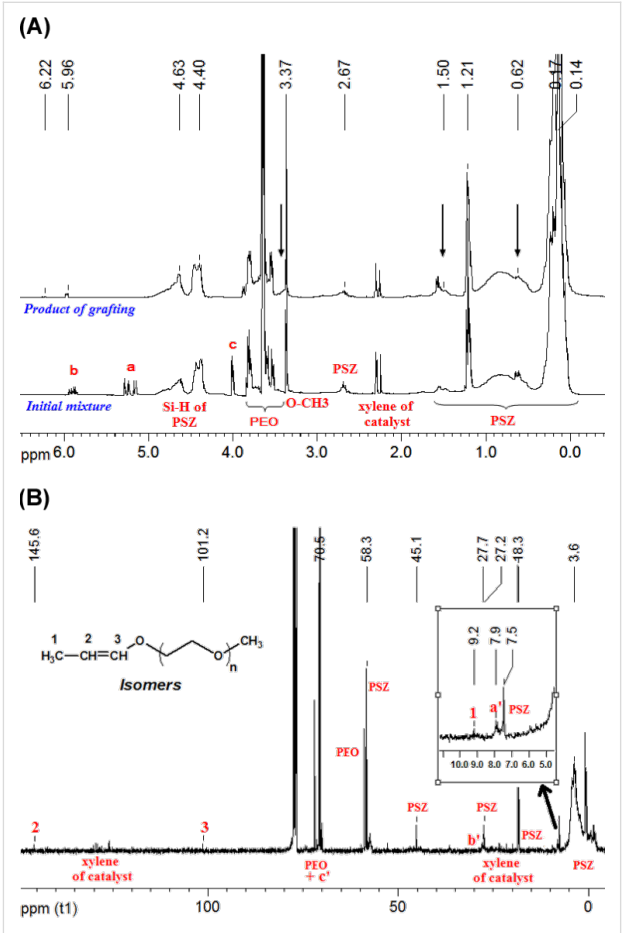

Figure 2: Identification of the grafting of PEO350 molecules onto PSZ chain. (A) Comparison of ^{1}H NMR spectra of initial mixture and grafting product. (B) ^{13}C NMR spectrum of grafting product.

After few hours of the grafting reaction, we recognized the appearance of two new ^{1}H NMR peaks at chemical shifts of 5.9 and 6.2 ppm. The intensities of two new peaks increase with reaction time. These two peaks have been verified to match the =C$\boldsymbol{H}$– protons of the *cis*- and *trans*-isomers, respectively, of the propenyl ether group, which results from the isomerization of allyl-PEO [25] (Figure 4). In the ^{13}C NMR spectrum (Figure 2), the position of the propenyl ether group has been recognized in

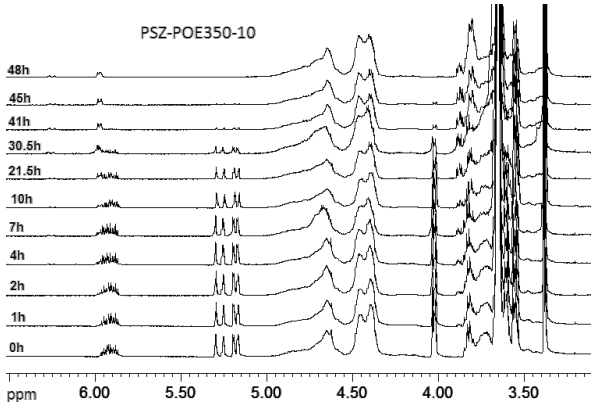

Figure 3: Investigation of grafting allyl-PEO350 onto the PSZ chain by ^{1}H NMR (SiH/allyl = 10).

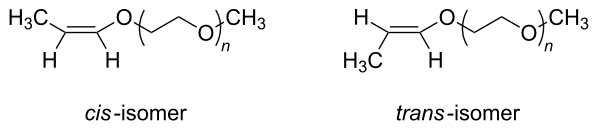

Figure 4: Chemical structure of *cis*- and *trans*-isomers of allyl-PEO.

the region of low fields (***C***H_3− at 9.2ppm, −***C***H= at 145.6ppm and =***C***H−O at 101.2ppm). The isomerization of the allyl-PEO was therefore considered as a secondary reaction that takes place simultaneously to the hydrosilylation. The optimum conditions for the grafting of PEO were defined to reach a high selectivity toward the hydrosilylation in comparison to the isomerisation.

It was observed that the conversion of allyl-PEO350-10 was 100% after 48 h. In contrast, allyl-PEO750 and allyl-PEO2000 were not converted completely in any ratio of SiH/allyl after 55 h of grafting (Figure 5 and below in Table 1). The amount of non-reacted allyl-PEO2000 can be seen very clearly in the ^{1}H NMR spectra. This means, the longer the molecule the more difficult is its grafting. Therefore, the products of the grafting of allyl-PEO750 and allyl-PEO2000 are mixtures of PSZ-PEO, PSZ surplus, propenyl ether isomers and unreacted allyl-PEO.

The decrease in the ^{1}H NMR signal of C***H*****$_2$**= was also used to evaluate the conversion of allyl-PEO during grafting. The total conversion of allyl-PEO (%$C_{AP,total}$), the conversion of Allyl-PEO associated with isomerization (%$C_{AP,iso}$) and the conversion of allyl-PEO associated with hydrosilylation (%$C_{AP,hydro}$) were calculated according to the following equations:

$$\%C_{AP,total} = \frac{I_{CH_2^=(0)} - I_{CH_2^=(t)}}{I_{CH_2^=(0)}} \times 100\,, \qquad (1)$$

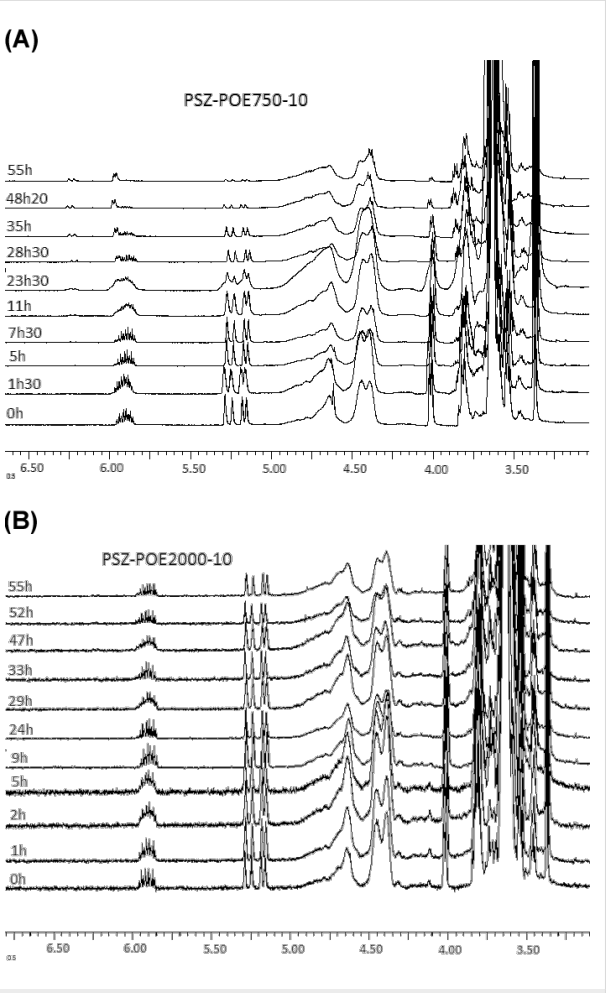

Figure 5: Investigation of grafting allyl-PEO750 (A) and allyl-PEO2000 (B) onto the PSZ chain by ^{1}H NMR (SiH/allyl = 10).

$$\%C_{AP,iso} = \frac{2\times\left(I_{CH,cis} + I_{CH,trans}\right)_{(t)}}{I_{CH_2^=(0)}} \times 100\,, \qquad (2)$$

$$\%C_{AP,hydro} = \%C_{AP,total} - \%C_{AP,iso}\,, \qquad (3)$$

in which $I_{CH2=(0)}$ is the integral of the C***H*****$_2$**= resonance in the ^{1}H-NMR spectrum of the initial mixture and $I_{CH2=(t)}$, $I_{CH,cis(t)}$ and $I_{CH,trans(t)}$ are the integrals of the C***H*****$_2$**=, *cis*-C***H***=, and *trans*-C***H***= resonances at time *t*, respectively.

The density (δ) of grafted PEO molecules onto the PSZ chain expressed by the amount of PEO attaching to 10 equiv of initial S−H has been calculated according to

$$\delta = \frac{10}{Y} \times \left(1 - \frac{\%C_{AP,iso}}{100}\right). \qquad (4)$$

The conversions of all three types of allyl-PEO in the different reactions during grafting as well as the density of grafted allyl-PEO molecules onto the PSZ chain are listed in Table 1. It should be noted that the degree of hydrosilylation increases when increasing the Si–H/allyl ratio and decreasing the molecular weight of PEO. Contrary to this, the degree of isomerization reduces significantly when increasing the Si–H/allyl ratio. In particular, when Si–H/allyl = 26.5, the *trans*-isomer could not be identified for both allyl-PEO750 and allyl-PEO2000 in their ^{1}H NMR spectra.

Table 1 clearly shows that the density of the grafted PEO onto PSZ chain increases when the initial S–H/allyl ratio and the PEO molecular weight decrease. To increase the Si–H/allyl ratio means that the concentration of allyl-PEO molecules will become low. So in this case, the density of grafted PEO was reduced despite increasing the degree of hydrosilylation.

Marine bacterial adhesion on modified surfaces

Figure 6 shows the influence of the length of the grafted PEO and of the Si–H/allyl ratio on the bacterial adhesion in VNSS media. Compared to the unmodified PSZ coating, all PSZ-PEO surfaces exhibit lower levels of bacteria adhesion. The inhibition efficiency varies inversely with the ratio of Si–H/allyl. It is remarkable that the PSZ-PEO350-10 surface shows the best inhibitory properties and leads to a reduction in the amount of adhered bacteria of approximately 70% for all three types of bacteria when compared to the pure PSZ coating. The anti-fouling activities of PSZ-PEO showed an increase in the sequence PEO750 < PEO2000 < PEO350. This result may seem to disagree with several previous studies showing that a PEO2000 chain is most effective against bacterial adhesion [12,26,27]. However, all PSZ-PEO350 coatings have a PEO grafting density that is higher than that of PSZ-PEO750 and PSZ-PEO2000 at the same Si–H/allyl ratio (see Table 1). The higher PEO grafting density of PSZ-PEO350 could explain its higher anti-fouling activity. These results are also in accordance with the works of Jeon et al. [9,10]. Based on a surface–protein interaction model these authors demonstrated that the surface density of the PEO chains have a greater effect than the length of the PEO chains in inhibiting bacterial adhesion. As the grafting density of PEO750 and PEO2000 onto PSZ is approximately equivalent, the effectiveness of these two

Table 1: Conversion of allyl-PEO and density of the grafted PEO chains onto PSZ calculated from ^{1}H NMR spectra.

X = $M_{allyl\text{-}PEO}$ (g/mol)	Y = SiH/allyl	*t* (h)	$\%C_{AP,total}$	$\%C_{AP,hydro}$	$\%C_{AP,iso}$	δ (mol PEO grafted/10 mol of Si–H)
350	10	48	100	71.78	28.22	0.72
	16.5	40	100	83.63	16.37	0.51
	26.5	30	100	91.84	8.16	0.35
750	10	55	96.72	62.84	33.88	0.63
	16.5	55	91.60	68.02	23.59	0.41
	26.5	55	97.35	88.86	8.49	0.34
2000	10	55	80.15	59.95	20.20	0.60
	16.5	55	72.65	61.96	10.69	0.38
	26.5	55	86.61	78.07	8.54	0.29

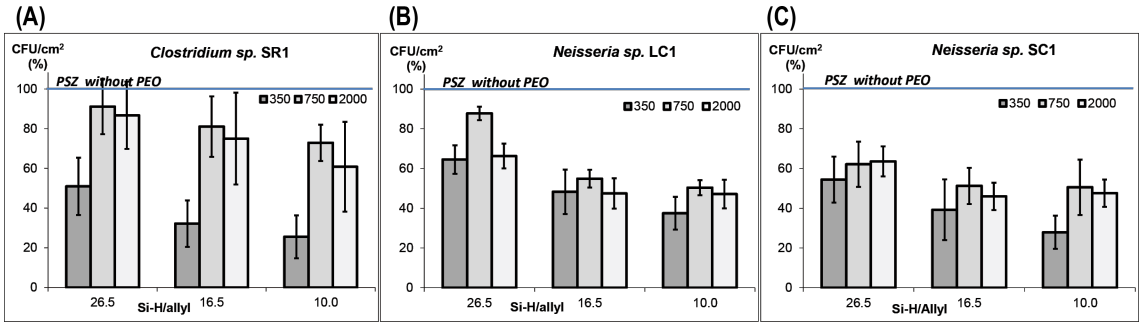

Figure 6: Marine bacteria adhesion on PSZ-PEO surfaces (mean ± SD, 100% corresponds to 13 × 10^2 CFU/cm^2 for *Clostridium sp.* SR1 (A); 8 × 10^3CFU/cm^2 for *Neisseria sp.* LC1 (B) and 11 × 10^3CFU/cm^2 for *Neisseria sp.* SC1 (C)).

types of hybrid materials is controlled by the chain length of PEO. Consequently, the PSZ-PEO2000 surfaces are more efficient than the PSZ-PEO750 surfaces in regarding to the anti-fouling activity.

Conclusion

The grafting of allyl-PEO molecules onto a PSZ chain in presence of Karstedt's catalyst has been successfully realized by hydrosilylation. The structure of the grafted products have been identified by ^{1}H NMR and ^{13}C NMR. After a few hours of the grafting reaction, there are the appearances of *trans*- and *cis*-isomers of allyl-PEO molecules. Apparently, isomerization occurs simultaneously to the hydrosilylation. The grafting density of PEO onto the PSZ chain increases with a reduction of the S–H/allyl ratio and a decrease of the chain length of PEO. At a molar ratio of Si–H/allyl = 10 for grafting allyl-PEO350 molecules, there is 0.72 chains of allyl-per ten Si–H groups of the PSZ chain. While at a molar ratio of Si–H/allyl = 26.5 for grafting allyl-PEO2000 molecules, there is 0.29 chains of allyl-PEO per ten Si–H groups of the PSZ chain.

The bacterial adhesion inhibition depends on the grafting density and the chain length of PEO. The role of the grafting density is more important than that of the chain length. The PSZ-PEO350 coatings prepared at a ratio SiH/allyl = 10 with the highest grafting density show the best anti-fouling activity for all three studied marine bacteria. While the densities of PEO750 and PEO2000 chains on the PSZ surface are practically equal, the PSZ-PEO2000 coatings are more efficient in anti-fouling than those with PSZ-PEO750. It is indispensable to find the optimal conditions for grafting allyl-PEO2000 on the PSZ chain in order to improve the degree of hydrosilylation and to increase the density of grafted allyl-PEO2000 molecules in PSZ-PEO anti-fouling surfaces.

Acknowledgements

The authors would like to thank the Clariant Company for its kind supply of the polysilazane. The contribution of Dinh Hung Lan Tran, Ngoc Tuan Nguyen, Thi Trang Nguyen, University of Danang - University of Science and Technology, with their experimental work on the marine bacterial adhesion is also very much acknowledged.

References

1. Choong Kwet Yive, N. S.; Corriu, R. J. P.; Leclercq, D.; Mutind, P. H.; Vioux, A. *Chem. Mater.* **1992,** *4,* 141–146. doi:10.1021/cm00019a029
2. Ya-Li, L.; Kroke, E.; Riedel, R.; Fasel, C.; Gervais, C.; Babonneau, F. *Appl. Organomet. Chem.* **2001,** *15,* 820–832. doi:10.1002/aoc.236
3. Seitz, J.; Bill, J.; Egger, N.; Aldinger, F. *J. Eur. Ceram. Soc.* **1996,** *16,* 885–891. doi:10.1016/0955-2219(96)00007-6
4. Lukacs, A., III; Knasiak, G. J. Thermally stable, moisture curable polysilazanes and polysiloxazanes. US Pat. 0083453A1, May 1, 2003.
5. Bauer, F.; Decker, U.; Dierdorf, A.; Ernst, H.; Heller, R.; Liebe, H.; Mehnert, R. *Prog. Org. Coat.* **2005,** *53,* 183–190. doi:10.1016/j.porgcoat.2005.02.006
6. Glinel, K.; Jonas, A. M.; Jouenne, T.; Leprince, J.; Galas, L.; Huck, W. T. S. *Bioconjugate Chem.* **2009,** *20,* 71–77. doi:10.1021/bc800280u
7. Herrwerth, S.; Eck, W.; Reinhardt, S.; Grunze, M. *J. Am. Chem. Soc.* **2003,** *125,* 9359–9366. doi:10.1021/ja034820y
8. Knoll, D.; Hermans, J. *J. Biol. Chem.* **1983,** *258,* 5710–5715.
9. Jeon, S. I.; Lee, J. H.; Andrade, J. D.; De Gennes, P. G. *J. Colloid Interface Sci.* **1991,** *142,* 149–158. doi:10.1016/0021-9797(91)90043-8
10. Jeon, S. I.; Andrade, J. D. *J. Colloid Interface Sci.* **1991,** *142,* 159–166. doi:10.1016/0021-9797(91)90044-9
11. Knerr, R.; Weiser, B.; Drotleff, S.; Steinem, C.; Gopferich, A. *Macromol. Biosci.* **2006,** *6,* 827–838. doi:10.1002/mabi.200600106
12. Dong, B.; Manolache, S.; Wong, A. C. L.; Denes, F. S. *Polym. Bull.* **2011,** *66,* 517–528. doi:10.1007/s00289-010-0358-y
13. Nguyen, T. D. H. Revêtements polysilazane à activités antibactériennes. Ph.D. Thesis, University of the South, Toulon-Var, France, 2011.
14. Sofia, S. J.; Premnath, V.; Merrill, E. W. *Macromolecules* **1998,** *31,* 5059–5070. doi:10.1021/ma971016l
15. Murthy, R.; Cox, C. D.; Hahn, M. S.; Grunlan, M. A. *Biomacromolecules* **2007,** *8,* 3244–3252. doi:10.1021/bm700543c
16. Chen, H.; Zhang, Z.; Chen, Y.; Brook, M. A.; Sheardown, H. *Biomaterials* **2005,** *26,* 2391–2399. doi:10.1016/j.biomaterials.2004.07.068
17. Kenausis, G. L.; Voros, J.; Elbert, D. L.; Huang, N.; Hofer, R.; Ruiz-Taylor, L.; Textor, M.; Hubbell, J. A.; Spencer, N. D. *J. Phys. Chem. B* **2000,** *104,* 3298–3309. doi:10.1021/jp993359m
18. Ostuni, E.; Chapman, R. G.; Liang, M. N.; Meluleni, G.; Pier, G.; Ingber, D. E.; Whitesides, G. M. *Langmuir* **2001,** *17,* 6336–6343. doi:10.1021/la010552a
19. Huang, N. P.; Michel, R.; Voros, J.; Textor, M.; Hofer, R.; Rossi, A.; Elbert, D. L.; Hubbell, J. A.; Spencer, N. D. *Langmuir* **2001,** *17,* 489–498. doi:10.1021/la000736+
20. Johnston, E. E.; Bryers, J. D.; Ratner, B. D. *Langmuir* **2005,** *21,* 870–881. doi:10.1021/la036274s
21. Cooper, A. I.; DeSimone, J. M. *Curr. Opin. Solid State Mater. Sci.* **1996,** *1,* 761–766. doi:10.1016/S1359-0286(96)80100-8
22. Harrison, K. L.; Johnston, K. P.; Sanchez, I. C. *Langmuir* **1996,** *12,* 2637–2644. doi:10.1021/la9510137
23. Kingshott, P.; Wei, J.; Bagge-Ravn, D.; Gadegaard, N.; Gram, L. *Langmuir* **2003,** *19,* 6912–6921. doi:10.1021/la034032m
24. Lestel, L.; Cheradame, H.; Boileau, S. *Polymer* **1990,** *31,* 1154–1158. doi:10.1016/0032-3861(90)90266-2
25. Chung, D.; Kim, T. G. *J. Ind. Eng. Chem.* **2007,** *13,* 571–577.
26. Benhabbour, S. R.; Sheardown, H.; Adronov, A. *Macromolecules* **2008,** *41,* 4817–4823. doi:10.1021/ma8004586
27. Roosjen, A.; Van der Mei, H. C.; Busscher, H. J.; Norde, W. *Langmuir* **2004,** *20,* 10949–10955. doi:10.1021/la048469l

Beilstein Journal of Nanotechnology

Exploring the retention properties of CaF_2 nanoparticles as possible additives for dental care application with tapping-mode atomic force microscope in liquid

Matthias Wasem*[1], Joachim Köser[2], Sylvia Hess[3], Enrico Gnecco[4] and Ernst Meyer[1]

Full Research Paper

Open Access

Address:
[1]Department of Physics, University of Basel, Klingelbergstrasse 82, Basel 4056, Switzerland, [2]Institute for Chemistry and Bioanalytics, University of Applied Sciences and Arts Northwestern Switzerland, Muttenz 4132, Switzerland, [3]GABA International AG, Grabetsmattweg, 4106 Therwil, Switzerland and [4]Instituto Madrileño de Estudios Avanzados, IMDEA Nanociencia, 28049 Madrid, Spain

Email:
Matthias Wasem* - matthias.wasem@unibas.ch

* Corresponding author

Keywords:
AM-AFM in liquid; nanodentistry; nanoparticles

Beilstein J. Nanotechnol. **2014,** *5,* 36–43.
doi:10.3762/bjnano.5.4

Received: 08 August 2013
Accepted: 10 December 2013
Published: 13 January 2014

This article is part of the Thematic Series "Nanomanipulation and environmental nanotechnology".

Guest Editor: T. Glatzel

Abstract

Amplitude-modulation atomic force microscopy (AM-AFM) is used to determine the retention properties of CaF_2 nanoparticles adsorbed on mica and on tooth enamel in liquid. From the phase-lag of the forced cantilever oscillation the local energy dissipation at the detachment point of the nanoparticle was determined. This enabled us to compare different as-synthesized CaF_2 nanoparticles that vary in shape, size and surface structure. CaF_2 nanoparticles are candidates for additives in dental care products as they could serve as fluorine-releasing containers preventing caries during a cariogenic acid attack on the teeth. We show that the adherence of the nanoparticles is increased on the enamel substrate compared to mica, independently of the substrate roughness, morphology and size of the particles.

Introduction

Amplitude-modulation atomic force microscopy (AM-AFM), also known as tapping mode AFM, is a variant of scanning probe microscopy. In this dynamic technique imaging is achieved while a microcantilever is driven at its resonance frequency and the supported probing tip touches the sample surface at the bottom of each oscillation cycle. This imaging mode offers the opportunity to investigate surface structures with gentle force, which for example is required to investigate polymers or biomolecules. Compared to contact mode AFM the destructive lateral forces are virtually eliminated in tapping mode as the probing tip has a much lower contact time while mapping the surface, which results in a much more gentle

sensing of the investigated surface [1,2]. AM-AFM has the ability to measure simultaneously the surface morphology and the compositional variations of the mapped surface. These variations are detected by recording the phase-lag of the excitation signal with respect to the vibrating tip, which is known as phase imaging technique. These so-generated phase images are closely related to energy dissipation maps [3,4]. While phase imaging in ambient with high quality cantilever Q-factors is well established [5], a comprehensive model of the energy dissipation process in liquid is still missing since the first studies of AM-AFM measurements in liquid [6,7]. Recent studies have related the phase contrast, when measuring in liquid in which low Q-factors are found, to two origins: the excitation of higher eigenmodes and the energy dissipation on the sample surface [8,9].

In this work we show that for surface associated manipulation of nanoparticles in liquid, the phase-lag in AM-AFM is closely related to the retention properties of the adsorbed nanoparticles, i.e., the particle–substrate contact area and the intrinsic chemical affinity between them. This enabled us to qualitatively compare the adhesion strength of as-synthesized CaF_2 nanoparticles adsorbed on mica and on tooth enamel in liquid. Manipulation experiments of nanoparticles are routinely done by using the AFM in the contact mode [10-12]. However some studies have been reported, in which a controlled manipulation of nanoparticles in tapping mode AFM was performed. Sitti et al. used a cantilever probe in the dynamic mode to manipulate as-synthesized latex nanoparticles on Si in ambient [13]. Other authors manipulated antimony nanoparticles [14] and gold nanoparticles [15] on graphite also under ambient conditions. Mougin and co-workers moved as-synthesized and functionalized gold nanoparticles on silicon substrates with dynamic AFM [16]. Darwich et al. investigated the retention of colloidal gold nanoparticles depending on particle–substrate affinity and humidity with tapping mode AFM [17]. In all these studies the major difficulty arises to quantify the dynamic processes during manipulation, i.e., the collision between the probing tip and the particle, the friction between the particles and the substrate, the role of water when measuring in ambient (lubrication, capillary effects, etc.), electrostatics between them, etc. The high surface to volume ratio of nanoparticles makes them very interesting for application in science, technology and medical applications including dentistry [18]. In this context calcium fluoride is of high interest in saliva chemistry and in the context of reducing acid dissolution of teeth [19]. The outermost layer of the teeth, also called enamel, has the purpose to protect the inner sensitive part of the teeth from physical or chemical attacks. It consists of tightly packed hydroxyapatite crystals and has a thickness of up to 2.5 mm. The solubility of enamel depends highly on the pH value [20]. The consumption of acidic beverages directly lowers the pH value in the vicinity of teeth while bacteria in the dental plaque metabolize sugars and lower the pH value on the tooth surface. If the pH drops below a certain threshold value the tooth enamel starts to dissolve. This demineralization process of the enamel is better known as enamel erosion and caries disease. The use of CaF_2 nanoparticles as a source of fluoride in order to prevent caries was already discussed in early studies [19,21,22]. Little research to explore tooth enamel has been done with AFM. Studies investigated the erosion of enamel with AFM based nanoindentation and related the demineralization and remineralization processes to softening of the enamel [23,24]. Another study recorded force–distance curves with AFM tips on etched superficial enamel substrate to examine the softening of enamel [25]. The formation of fluoride-containing nanostructures on tooth enamel upon exposure to a fluorated solution has been observed with AFM in liquid [26]. To the best of our knowledge no manipulation experiment of particles adsorbed on human tooth enamel has been performed so far. The anticaries activity of calcium fluoride nanoparticles is mainly determined by two factors, the solubility of the nanocomposites at a certain pH value and their adhesion strength to the tooth enamel upon application. The solubility of CaF_2 has already been investigated by titration methods with respect to the pH-dependent fluoride release [27]. In this study we focus on exploring the adhesion strength of calcium fluoride nanoparticles adsorbed on mica and on tooth enamel in liquid with AM-AFM.

Theory

As already described above, manipulation experiments in the tapping-mode are difficult to quantify as dynamic and friction processes are involved at the same time. To connect the power dissipation to the particle–substrate interplay we used the work of two earlier studies. To quantify the particles–substrate contact we use the relation derived from Rao et al. [28]. They showed that when performing AM-AFM manipulation experiments with nanoparticles in the raster scan path, the particles are deflected in a direction defined by the geometries of the probing tip, the particles contact area with the substrate and the spacing between consecutive scan lines. If the radius of the nanoparticles is very big compared to the tip radius, and the spacing between the scan lines, b, remains constant, the trajectory angle of the manipulated particle is mainly a function of the intrinsic particle–substrate contact radius R. With exception for the first scan line, the displacement angle of a particle θ with respect to the fast scan axis is given by:

$$\tan\theta = -\frac{b}{R\left(\cos\alpha_0 + \log\tan\frac{\alpha_0}{2}\right)} \quad (1)$$

where α_0 = arcsin [1−(b/R)]. The theoretical predicted deflection angle depending only on the particle-substrate contact radius derived from Equation 1 is illustrated in Figure 1a.

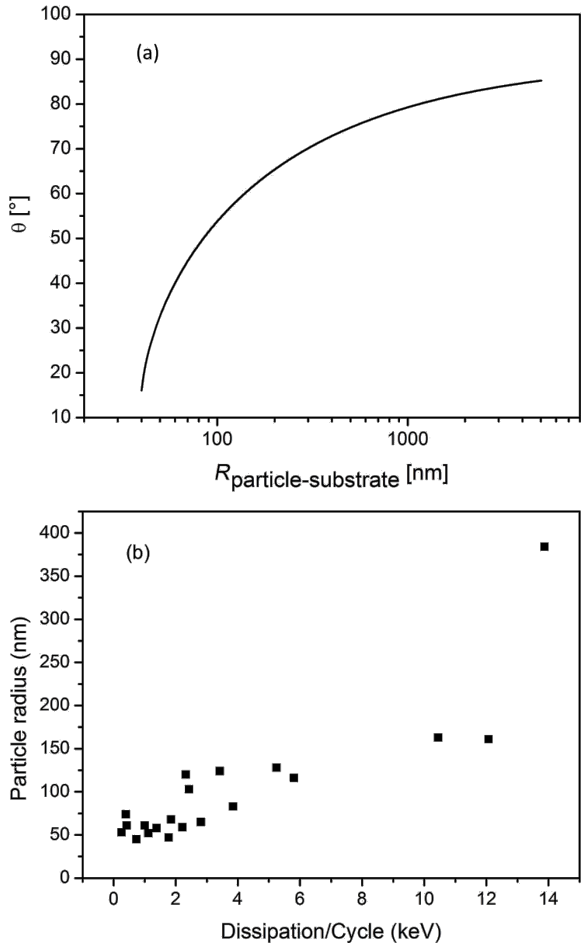

Figure 1: (a) Theoretically predicted trajectory angles of nanoparticles manipulated on an arbitrary surface as a function of the particle–substrate contact radius with b = 39 nm. (b) Calculated particle radius and energy dissipation obtained by using Equation 2 with an experimentally determined phase-lag and trajectory angle of the manipulated particles adsorbed on mica. The amplitude was A = 23 nm, the Q-factor = 7 and A_0 = 1.2A.

By reading out the trajectory angle of the deflected particles we get the particle–substrate contact size distribution. For the case of particles with plane facing adsorbed on smooth and atomically flat substrates, such as mica, the trajectory angle distributions can be approximately regarded as the size distribution of the synthesized particles. In order to calculate the power dissipation from the phase-lag of the cantilever relative to the excitation, we used the method of Cleveland et al. [3]. In this method, in the dynamic steady-state equilibrium, the average rate at which energy is fed into the cantilever must equal the average rate at which energy is dissipated by the cantilever and the tip. With this restriction one can separate the total dissipated power into two terms, $\overline{P_{in}} = \overline{P_0} + \overline{P_{tip}}$. The first term of the dissipated power, $\overline{P_0}$, can be thought as the average power dissipated by the body of the cantilever (i.e., air damping or in our case damping of the cantilever motion in the liquid) and can be modeled by simple viscous damping. The second part, $\overline{P_{tip}}$, corresponds to the power dissipated by tip–sample interactions. If the cantilever has a normal spring constant k and is driven sinusoidally with the amplitude A_0 and drive frequency ω_0, we can calculate the average power dissipated by tip–sample interactions as

$$\overline{P_{tip}} = \frac{1}{2}\frac{kA^2\omega_0}{Q_{cant}}\left[\left(\frac{A_0}{A}\right)\sin(\vartheta) - 1\right] \qquad (2)$$

where A is the damped amplitude at the given set point, Q_{cant} the quality factor of the cantilever and ϑ the phase angle. According to this equation the power lost by tip–sample interaction is proportional to the sine of the phase-lag. It is important to note that Equation 2 allows to calculate the total energy lost by tip–sample interactions but does not reveal how it is lost.

Experimental

Synthesis of CaF_2 nanoparticles

The CaF_2 nanoparticles were synthesized through a procedure called the precipitation method [29]. Particles with defined morphology were prepared at room temperature by preparing a 1:1 volumetric mixture of unbuffered aqueous $CaCl_2$ and NaF salt solutions with specific concentrations. The formation process of the particles was very fast as the solution became rapidly opaque. Generally no differences were observed if particles were assembled overnight or for several days. The formed nanoparticles were purified by centrifugation and washed several times with a saturated solution of calcium fluoride to remove excess salt ions. Subsequently the nanoparticles were vacuum dried, resulting in a white powder, which was stored in a dry and dark environment until use. Scanning electron microscopy (SEM) was used to determine the size and shape of the particles. The three types of CaF_2 nanoparticles examined in this work have been prepared by mixing a) 50 mM NaF and 250 mM $CaCl_2$ (Figure 2a), b) 50 mM NaF and 50 mM $CaCl_2$ (Figure 2b) and c) 75 mM NaF and 1 mM $CaCl_2$ (Figure 2c).

Sample preparation and manipulation experiments with AFM

The adsorption of CaF_2 nanoparticles on the sample surface was performed as follows. An aliquot of the dried nanoparticles was mixed with 200 µL saturated calcium fluoride solution and put in an ultrasonic bath for 20 min to break any aggregated particles. Subsequently, 2 µL were dropped onto the substrate and

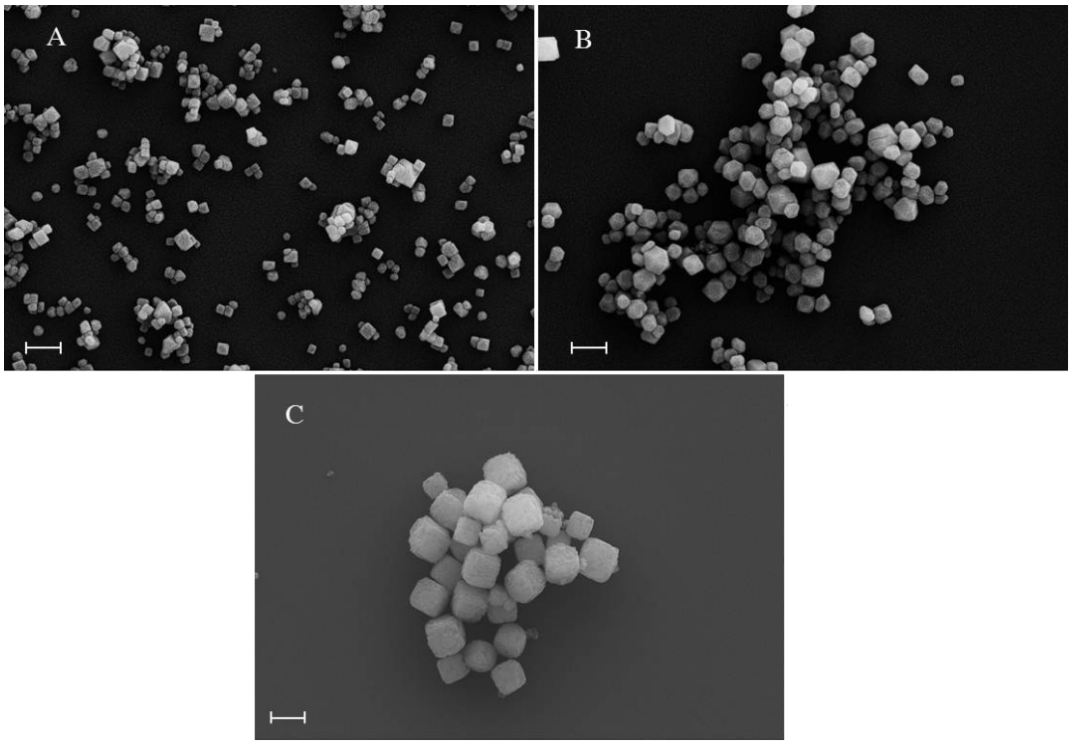

Figure 2: SEM images of the three morphologies of nanoparticles explored in this work. A certain size distribution of the particles was achieved with the synthesis method described in the text. The diameters vary from 50–100 nm for (A), 100–150 nm for (B) and 200–250 nm for (C). The shape varied from cubic (A) to polyhedral (B) and oblate cubic (C). The scale bar for all images is 200 nm.

dried. All measurements were performed in a saturated solution of calcium fluoride with pH 6, to inhibit any change of the adsorbed nanoparticles. The mica substrate was freshly cleaved prior to use. Human wisdom teeth embedded in resin were generously donated from GABA International (Therwil, Switzerland). The enamel was polished with 3 µm and 1 µm diamond paste grain size under constant water cooling. The cleaning procedure of the polished tooth enamel was done as described elsewhere [30]. All specimens were stored in a dust-free box and not further processed. A topography image of nanoparticles (A) adsorbed on enamel is illustrated in Figure 3b.

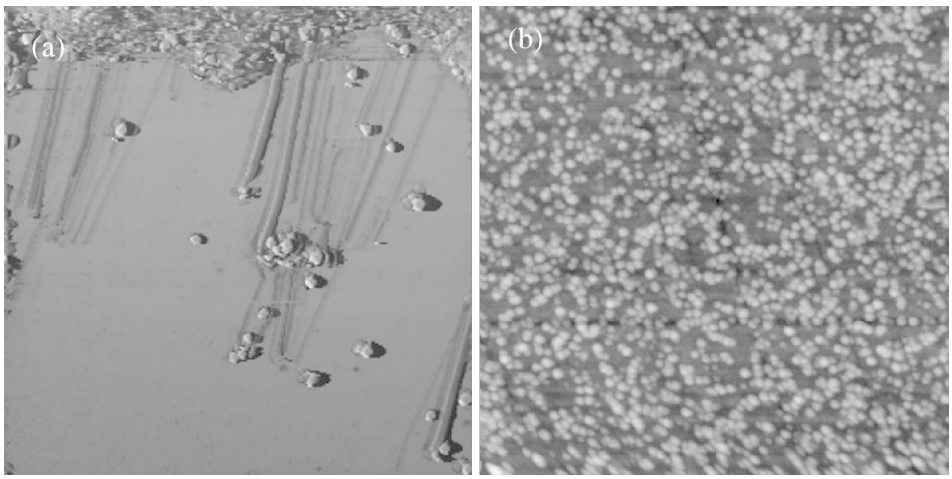

Figure 3: (a) Phase image of nanoparticles (B) adsorbed and manipulated on mica substrate. (b) Topography image of nanoparticles (A) adsorbed on enamel substrate. Scan size is for both images 10 µm.

All imaging and manipulation experiments were performed by using a commercially available AFM (Flex AFM from Nanosurf AG, Switzerland). Rectangular silicon cantilevers with typical resonance frequencies in air and liquid of 160 kHz and 70 kHz, respectively, and spring constants of 45 $N \cdot m^{-1}$ and 7 $N \cdot m^{-1}$, respectively, have been used (PointProbe PPP-NCLPt from Nanosensors AG, Switzerland). A typical phase image obtained after a manipulation experiment is shown in Figure 3a. To compare the manipulation experiments done on mica and on tooth enamel we conducted measurements with comparable amplitudes and set points.

Results and Discussion

To address the calculated power dissipation to the retention of the nanoparticles on a given surface, i.e., the particle–substrate contact area and the chemical interplay between them, we recorded the phase-lag at the point the particles were displaced and their trajectory angle relative to the fast scan direction. In Figure 1b a plot is illustrated for the nanoparticles (A) obtained from one single manipulation experiment. The result was reproducible for all nanoparticles. As discussed above the trajectory angle of manipulated particles is closely related to the nanoparticle–substrate contact area. The determined particle radius from the trajectory angle for the manipulated specimen (A) confirms the radius distribution observed from the SEM images in Figure 2 of r = 50–100 nm. The size distribution of CaF_2 particles synthesized with the precipitation method described above depends on following parameters: the degree of supersaturation of the solution, the spatial concentration distribution and the growth time of the crystals [31]. Not precisely controlling these factors in our synthesis procedure resulted in a certain size distribution of the synthesized particles. As the facets of particles (A) are smooth and plane the particles radius equals the contact radius with the substrate. It also shows that at higher contact radii, more energy is needed to dislocate the particle. The phase-lag correlates with the power that is needed to move the particles. This correlation between energy dissipation and deflection angle was observed for all three kinds of nanoparticles investigated. Manipulation experiments in liquid have the advantage, compared to measurements in ambient, that the retention of adsorbed particles in not dominated by the wetting layer (hydrodynamic drag of water layer), but the intrinsic particle–sample interaction energies. The frequency distribution of the calculated power dissipated for each of the particles enables us to examine the chemical affinity between the calcium fluoride nanoparticles adsorbed on mica and on polished tooth enamel. The energy dissipation histograms obtained for the three nanoparticles are illustrated in Figure 4.

The histograms in Figure 4a show the distribution of the calculated power dissipated for CaF_2 nanoparticles adsorbed on mica. The lowest energy dissipation was found for the specimen (C) with a power dissipation per cycle of the cantilever of around $\overline{P_{tip}}$ = 1 keV/cycle. These particles were the biggest in size that we examined with an approximate diameter of d = 200–250 nm. The fact that they show the least energy that was needed to manipulate them, is related to the rough and spherical surface structure of these particles. Compared to the smaller particles (A) and (B), which have plane and smooth faceting, the high surface roughness leads to a smaller contact area on the substrate. The fact that the lowest energy dissipation was observed for specimen (C) is consistent with the number of asperity contacts in the interface of the particle–substrate system. Comparing particles (A) and (B) we find comparable dissipated powers needed to displace the particles. The broad distribution of the power dissipation for the specimen (A) and especially (B) can be explained by the fact that more conglomerated particles were moved instead of isolated single ones. Nevertheless, the smaller particles with a diameter ranging from 50–150 nm and with smooth and plane surfaces show a higher retention as big particles with rough and spherical facing. The histograms in Figure 4b show the distribution of the calculated power dissipated for nanoparticles adsorbed on polished tooth enamel substrates. The relatively wide distribution of the calculated dissipated energies for all three particles may arise from the inhomogeneous scratch profiles for each of the polished tooth enamel substrates used. Remarkably, the energy dissipation for each of the particles is found to be much higher on enamel than on mica. For particles (C) the power dissipation is found to be up to 10-times higher on tooth enamel. The specimens (A) and (B), which are similar in size and surface structure show an increase in the dissipated power of around 5 to 10 times on tooth enamel compared to the adsorption on mica. The interaction between particles and a substrate is known to depend on the size of the contact area, i.e., the nanoparticle- and substrate surface roughness and geometry. Compared to mica, which is atomically flat, the tooth enamel, which was mechanically polished before use, had a mean square roughness (RMS) ranging between 3.4–4.0 nm. The higher substrate roughness of enamel would lower the particle–substrate contact area. This has been experimentally verified in earlier studies by measuring the pull-off force of nanoparticles attached to a cantilever tip on surfaces of different roughness [32,33]. Recent studies have simulated that the mobility of nanoparticles is enhanced on rough surfaces, compared to smooth ones, if the asperities are much smaller than the particles [34,35]. This phenomenon was explained in terms of less contacting asperities in the substrate–particles interface and hence less adhesion force acting between them. Our experiments show the exact opposite behavior, at a higher substrate roughness we observe a higher retention of the nanoparticles. We explain this in terms of the higher chemical affinity of the

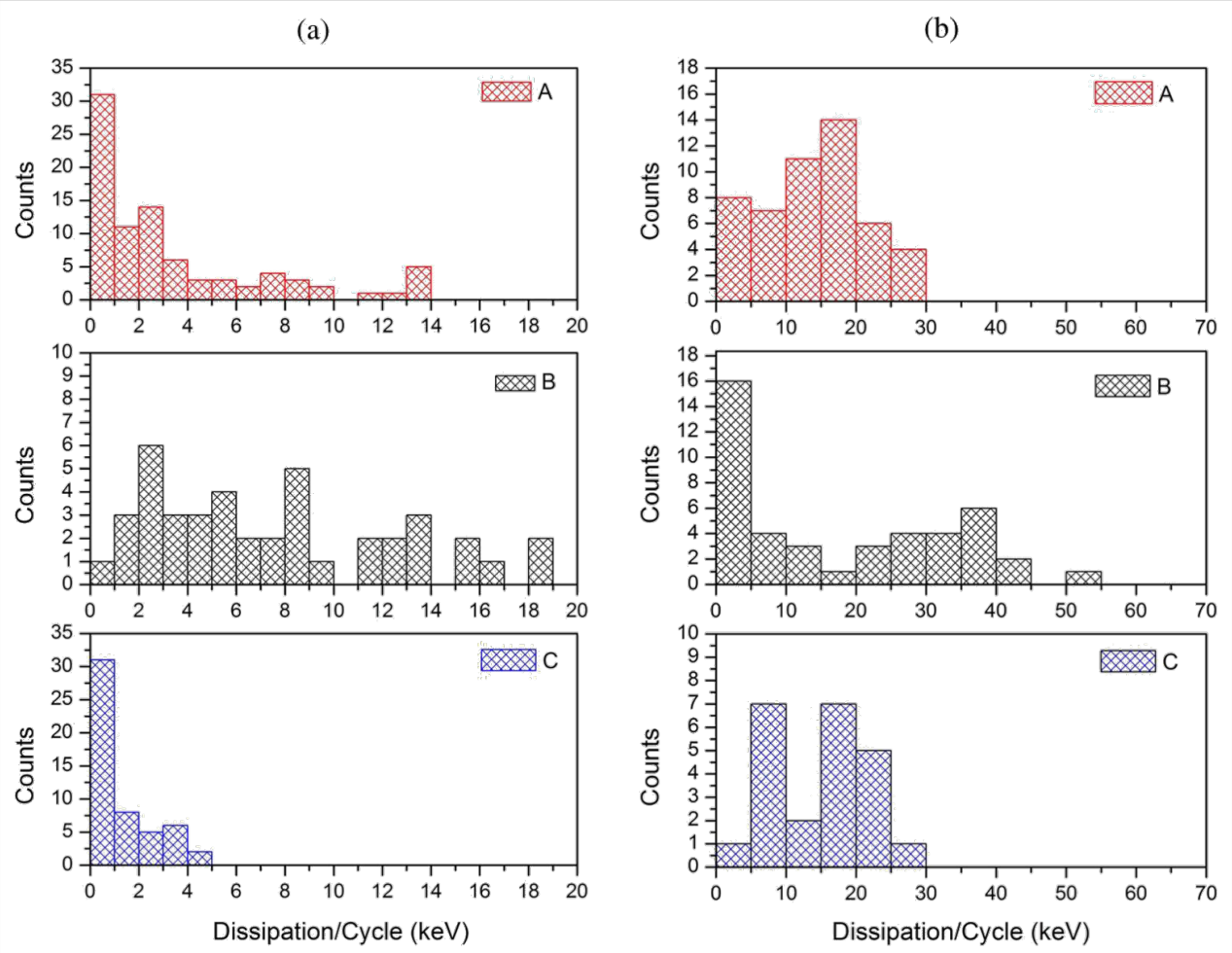

Figure 4: Calculated energy dissipation histograms obtained for the nanoparticles A, B and C from Figure 3 on mica (a) and tooth enamel (b). The dissipated power was calculated per oscillation cycle of the cantilever. Amplitude and set point were comparable for all experiments.

calcium fluoride nanoparticles to the tooth enamel substrate. Earlier studies that examined the enamel surface chemistry at certain pH values that were varied between 2 and 10, have shown that the enamel surface is covered with distinct ionic species depending on the pH value, which come from the enamel and the ionic species present in the liquid [36-38]. In our case, we speculate that the surface polarity of the enamel strongly influenced the retention of the adsorbed CaF_2 nanoparticles. The matching of the polarity of the substrate and the nanoparticle resulted in an increased adhesion strength between the particle and the substrate despite the decreased number of contacting asperities.

Conclusion

To conclude, we compared the retention properties of as-synthesized CaF_2 nanoparticles adsorbed on mica and on polished tooth enamel in liquid. From the phase-lag of the cantilever with respect to the excitation signal we calculated the power dissipation at the point the nanoparticles were mobilized. By comparing the frequency distribution of the obtained dissipated power, we showed that an up to ten times higher retention was observed for particles adsorbed on tooth enamel compared to mica. Although the enamel had an increased surface roughness compared to mica as a result of the mechanical polishing, which resulted in a decreased contact area of the particle with the substrate, more power was needed to dislocate the particles. We relate this to the strong chemical interaction of the CaF_2 nanoparticles with the tooth enamel. Further, we have shown that particles with an ordered, smooth and plane surface structure show a higher retention than rough and spherical ones. Thus, the nano-morphology of particles has a strong influence on the mobility. The evidence that the interplay of calcium fluoride nanoparticles with the tooth enamel is so strong, makes calcium fluoride nanoparticles a promising candidate to be used in dental care products preventing teeth demineralization. Regarding the solubility of the CaF_2 nanoparticles, further experiments are needed to examine how the retention varies with respect to the pH and also solubility test are required to

explore their acid-dependent release of fluorine over time. We showed that AM-AFM is a powerful tool to compare detachment and interaction properties of adsorbates in liquid.

Acknowledgements

We thank W. Tschudin from the Institute of Mineralogy and Petrography at the University of Basel for polishing the teeth. We also acknowledge GABA International for providing the teeth substrates. This work was supported by the Swiss Nanoscience Institute (SNI) as Nano Argovia project and the Swiss National Science Foundation.

References

1. Tamayo, J.; García, R. *Langmuir* **1996,** *12,* 4430–4435. doi:10.1021/la960189l
2. Magonov, S. N.; Elings, V.; Whangbo, M.-H. *Surf. Sci.* **1997,** *375,* L385–L391. doi:10.1016/S0039-6028(96)01591-9
3. Cleveland, J. P.; Anczykowski, B.; Schmid, A. E.; Elings, V. B. *Appl. Phys. Lett.* **1998,** *72,* 2613. doi:10.1063/1.121434
4. Anczykowski, B.; Gotsmann, B.; Fuchs, H.; Cleveland, J. P.; Elings, V. B. *Appl. Surf. Sci.* **1999,** *140,* 376–382. doi:10.1016/S0169-4332(98)00558-3
5. Tamayo, J.; García, R. *Appl. Phys. Lett.* **1998,** *73,* 2926. doi:10.1063/1.122632
6. Hansma, P. K.; Cleveland, J. P.; Radmacher, M.; Walters, D. A.; Hillner, P. E.; Bezanilla, M.; Fritz, M.; Vie, D.; Hansma, H. G.; Prater, C. B.; Massie, J.; Fukunaga, L.; Gurley, J.; Elings, V. *Appl. Phys. Lett.* **1994,** *64,* 1738. doi:10.1063/1.111795
7. Putman, C. A. J.; Van der Werf, K. O.; De Grooth, B. G.; Van Hulst, N. F.; Greve, J. *Appl. Phys. Lett.* **1994,** *64,* 2454. doi:10.1063/1.111597
8. Melcher, J.; Carrasco, C.; Xu, X.; Carrascosa, J. L.; Gómez-Herrero, J.; de Pablo, P. J.; Raman, A. *Proc. Natl. Acad. Sci. U. S. A.* **2009,** *106,* 13655–13660. doi:10.1073/pnas.0902240106
9. Payam, A. F.; Ramos, J. R.; Garcia, R. *ACS Nano* **2012,** *6,* 4663–4670. doi:10.1021/nn2048558
10. Dietzel, D.; Mönninghoff, T.; Jansen, L.; Fuchs, H.; Ritter, C.; Schwarz, U. D.; Schirmeisen, A. *J. Appl. Phys.* **2007,** *102,* 084306. doi:10.1063/1.2798628
11. Palacio, M.; Bhushan, B. *Nanotechnology* **2008,** *19,* 315710. doi:10.1088/0957-4484/19/31/315710
12. Dietzel, D.; Feldmann, M.; Herding, C.; Schwarz, U. D.; Schirmeisen, A. *Tribol. Lett.* **2010,** *39,* 273–281. doi:10.1007/s11249-010-9643-z
13. Sitti, M.; Hashimoto, H. *IEEE/ASME Trans. Mechatronics* **2000,** *5,* 199–211. doi:10.1109/3516.847093
14. Ritter, C.; Heyde, M.; Stegemann, B.; Rademann, K.; Schwarz, U. D. *Phys. Rev. B* **2005,** *71,* 085405. doi:10.1103/PhysRevB.71.085405
15. Paolicelli, G.; Rovatti, M.; Vanossi, A.; Valeri, S. *Appl. Phys. Lett.* **2009,** *95,* 143121. doi:10.1063/1.3238320
16. Mougin, K.; Gnecco, E.; Rao, A.; Cuberes, M. T.; Jayaraman, S.; McFarland, E. W.; Haidara, H.; Meyer, E. *Langmuir* **2008,** *24,* 1577–1581. doi:10.1021/la702921v
17. Darwich, S.; Mougin, K.; Rao, A.; Gnecco, E.; Jayaraman, S.; Haidara, H. *Beilstein J. Nanotechnol.* **2011,** *2,* 85–98. doi:10.3762/bjnano.2.10
18. Uskoković, V.; Bertassoni, L. E. *Materials* **2010,** *3,* 1674–1691. doi:10.3390/ma3031674
19. Xu, H. H. K.; Moreau, J. L.; Sun, L.; Chow, L. C. *J. Dent. Res.* **2010,** *89,* 739–745. doi:10.1177/0022034510364490
20. Larsen, M. J.; Jensen, S. J. *Arch. Oral Biol.* **1994,** *39,* 23–27.
21. Xu, H. H. K.; Weir, M. D.; Sun, L.; Moreau, J. L.; Takagi, S.; Chow, L. C.; Antonucci, J. M. *J. Dent. Res.* **2010,** *89,* 19–28. doi:10.1177/0022034509351969
22. Azami, M.; Jalilifiroozinezhad, S.; Mozafari, M.; Rabiee, M. *Ceram. Int.* **2011,** *37,* 2007–2014. doi:10.1016/j.ceramint.2011.02.025
23. Lippert, F.; Parker, D. M.; Jandt, K. D. *J. Colloid Interface Sci.* **2004,** *280,* 442–448. doi:10.1016/j.jcis.2004.08.016
24. Cross, S. E.; Kreth, J.; Wali, R. P.; Sullivan, R.; Shi, W.; Gimzewski, J. K. *Dent. Mater.* **2009,** *25,* 1517–1526. doi:10.1016/j.dental.2009.07.012
25. Pelin, I. M.; Piednoir, A.; Machon, D.; Farge, P.; Pirat, C.; Ramos, S. M. M. *J. Colloid Interface Sci.* **2012,** *376,* 262–268. doi:10.1016/j.jcis.2012.03.013
26. Petzold, M. *Caries Res.* **2001,** *35* (Suppl 1, Suppl. 1), 45–51. doi:10.1159/000049110
27. Pan, H.-B.; Darvell, B. W. *Arch. Oral Biol.* **2007,** *52,* 861–868. doi:10.1016/j.archoralbio.2007.03.002
28. Rao, A.; Gnecco, E.; Marchetto, D.; Mougin, K.; Schönenberger, M.; Valeri, S.; Meyer, E. *Nanotechnology* **2009,** *20,* 115706. doi:10.1088/0957-4484/20/11/115706
29. Dirksen, J. A.; Ring, T. A. *Chem. Eng. Sci.* **1991,** *46,* 2389–2427. doi:10.1016/0009-2509(91)80035-W
30. Lussi, A.; Jaeggi, T.; Gerber, C.; Megert, B. *Caries Res.* **2004,** *38,* 567–571. doi:10.1159/000080588
31. Chen, J.-F.; Wang, Y.-H.; Guo, F.; Wang, X.-M.; Zheng, C. *Ind. Eng. Chem. Res.* **2000,** *39,* 948–954. doi:10.1021/ie990549a
32. Beach, E. R.; Tormoen, G. W.; Drelich, J.; Han, R. *J. Colloid Interface Sci.* **2002,** *247,* 84–99. doi:10.1006/jcis.2001.8126
33. Götzinger, M.; Peukert, W. *Langmuir* **2004,** *20,* 5298–5303. doi:10.1021/la049914f
34. Korayem, M. H.; Zakeri, M. *Appl. Surf. Sci.* **2011,** *257,* 6503–6513. doi:10.1016/j.apsusc.2011.02.055
35. Klapetek, P.; Valtr, M.; Nečas, D.; Salyk, O.; Dzik, P. *Nanoscale Res. Lett.* **2011,** *6,* No. 514. doi:10.1186/1556-276X-6-514
36. Robinson, C.; Connell, S.; Brookes, S. J.; Kirkham, J.; Shore, R. C.; Smith, D. A. M. *Arch. Oral Biol.* **2005,** *50,* 267–270. doi:10.1016/j.archoralbio.2004.11.017
37. Robinson, C.; Yamamoto, K.; Connell, S. D.; Kirkham, J.; Nakagaki, H.; Smith, A. D. *Eur. J. Oral Sci.* **2006,** *114,* 99–104. doi:10.1111/j.1600-0722.2006.00275.x
38. Harding, I. S.; Rashid, N.; Hing, K. A. *Biomaterials* **2005,** *26,* 6818–6826. doi:10.1016/j.biomaterials.2005.04.060

Beilstein Journal of Nanotechnology

Manipulation of nanoparticles of different shapes inside a scanning electron microscope

Boris Polyakov[1], Sergei Vlassov[*1,2,3], Leonid M. Dorogin[2,3], Jelena Butikova[1], Mikk Antsov[2,3], Sven Oras[2,3], Rünno Lõhmus[2,3] and Ilmar Kink[2,3]

Full Research Paper

Open Access

Address:
[1]Institute of Solid State Physics, University of Latvia, Kengaraga 8, LV-1063, Riga, Latvia, [2]Institute of Physics, University of Tartu, Riia 142, 51014, Tartu, Estonia and [3]Estonian Nanotechnology Competence Center, Riia 142, 51014, Tartu, Estonia

Email:
Sergei Vlassov[*] - vlassovs@ut.ee

* Corresponding author

Keywords:
contact mechanics; nanomanipulation; nanoparticles; nanotribology; scanning electron microscopy (SEM)

Beilstein J. Nanotechnol. **2014,** *5,* 133–140.
doi:10.3762/bjnano.5.13

Received: 30 September 2013
Accepted: 16 January 2014
Published: 05 February 2014

This article is part of the Thematic Series "Nanomanipulation and environmental nanotechnology".

Guest Editor: E. Gnecco

Abstract

In this work polyhedron-like gold and sphere-like silver nanoparticles (NPs) were manipulated on an oxidized Si substrate to study the dependence of the static friction and the contact area on the particle geometry. Measurements were performed inside a scanning electron microscope (SEM) that was equipped with a high-precision XYZ-nanomanipulator. To register the occurring forces a quartz tuning fork (QTF) with a glued sharp probe was used. Contact areas and static friction forces were calculated by using different models and compared with the experimentally measured force. The effect of NP morphology on the nanoscale friction is discussed.

Introduction

The manipulation of nanoparticles (NPs) is a powerful method for the investigation of the mobility of nano-objects on solid substrates and it is contributing to a deeper understanding of nanomechanics and nanotribology [1]. Thanks to the rapid progress in the synthesis of NPs, there is a wide choice of materials, structures, compositions, shapes and coatings of NPs for nanomanipulation experiments. NPs demonstrate many intriguing phenomena, which are important for nanotribology and nanotechnology in general, for example low-temperature melting [2], vanishing friction [3], contact aging [4], etc.

The frictional properties of NPs have been extensively studied in manipulation experiments based on atomic force microscopy (AFM), either in contact mode or dynamic mode [5,6]. Besides the undoubted advantages of AFM manipulation methods, such as a wide choice of materials (not limited to conductive materials), and high resolution and accuracy, they have certain limitations. AFM is used for both displacement and visualization of the initial and the final position of the NPs, but these two procedures cannot be performed simultaneously. Therefore there is no real-time visual feedback in a single line scan

concerning the trajectory of the particle and its type of motion (sliding, rolling or rotation) during the manipulation event. It is possible to extract trajectory and motion type data from complete AFM images as it was recently demonstrated in several works [4,7-9]. However, such a process is time consuming, since it requires a large amount of line scans to be made. The interpretation of the manipulation experiments is still a challenge because of a number of factors that might not be properly defined. Those factors include the morphology of the NP, the real contact area, as well as various diffusion and chemical processes possibly taking place in the vicinity of the NP–substrate interface [10]. For instance, in most of the nanomanipulation experiments NPs are considered to be spherical (described by the diameter only) [9,11-14], and the roughness of the substrate is neglected by assuming it to be atomically flat. Significantly fewer works are dedicated to nonspherical NPs [5,15-18] and nanoscale roughness [10].

The goal of this article is to demonstrate the advantages and to discuss the limitations of a real-time manipulation technique inside a scanning electron microscope (SEM) that is employed for tribological studies of metal NPs. The forces needed to overcome static friction and move individual polyhedron-like Au and sphere-like Ag NPs on an oxidized Si surface are measured and analyzed with respect to the morphology of the NPs.

Experimental

The 150 nm Au NPs (BBI International) were deposited from solution onto oxidized silicon wafers (Semiconductor Wafer Inc., 50 nm of thermal oxide). The samples were annealed for 1 h at 500 °C prior to every experiment to remove the surfactant. Rounded Ag NPs were produced by laser-induced (532 nm, Expla, NL200) partial melting [19] of pentagonal Ag nanowires (Blue Nano), 120 nm in diameter, which were deposited on the oxidized silicon wafer.

High resolution images of the NPs and the traces left after displacement of the NPs were taken inside an FEI Helios Nanolab SEM. Standard contact AFM cantilevers (ATEC-CONT) were used as sharp probes to displace the NPs. The cantilever chip was mounted on a polar-coordinate manipulator Kleindiek MM3A-EM. No force registration was used inside FEI SEM.

Real time manipulations with force registration were carried out inside a Vega-II SBU TESCAN SEM. The experimental set-up comprised an XYZ-nanopositioner (SLC-1720-S, SmarAct) equipped with a custom-made force sensor. The force sensor was made by gluing an electrochemically sharpened tungsten wire or commercial AFM cantilever with a sharp tip (Nanosensor ATEC-CONT cantilevers C = 0.2 N/m) to one prong of a commercially available quartz tuning fork (QTF). The tip of ATEC-CONT cantilevers is tilted about 15 degrees relative to the cantilever, providing visibility of the tip from the top (Figure 1). In the experiments the QTF was driven electrically on its resonance frequency in the self-excitation regime in amplitude-modulation mode. The oscillation parameters of such a system strongly depend on the load that acts on the tip, which enables one to measure the applied force. The signal from the QTF was amplified by a lock-in amplifier (SR830, Stanford Research Systems) and recorded through an ADC–DAC card (NI PCI-6036E, National Instruments). The typical values of the driving voltage were 20–50 mV and the corresponding tip oscillation amplitude was in order of 100 nm. The tip oscillated parallel to the sample surface, i.e., in the shear mode [20]. The QTF force sensors were calibrated on a reference contact mode AFM cantilever (NT-MDT, CSG11), which was previously calibrated by the thermal noise method. A detailed description of calibration procedure is given in Supporting Information File 1.

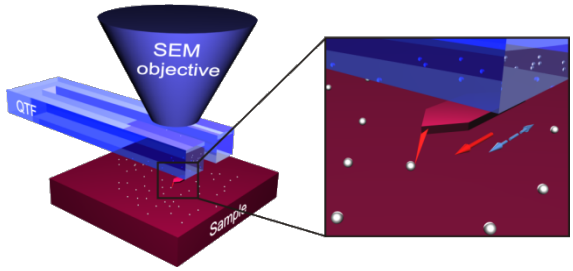

Figure 1: Schematics of the manipulation experiments inside an SEM. Solid arrow indicates the direction of the tip movement. Dashed arrow indicates QTF oscillation direction.

Each manipulation experiment started with a displacement of the NP from its initial position by an abrupt tip motion in the step regime to reduce the initial adhesion, which is known to be time-dependent [4]. The initial displacement was followed by a controlled manipulation of the particle by pushing it with the tip while simultaneously recording the force in the scan regime (a detailed description of SmarAct manipulator regimes is given in Supporting Information File 1). During the manipulation, the tip moved parallel to the surface along a straight line without feedback loop. At the end of every manipulation event the tip was abruptly retracted from the NP to avoid sticking of the particle to the tip. Two different modes of the tip oscillation direction were used in experiments: perpendicular to the manipulation direction and parallel to the manipulation direction.

Results and Discussion

Morphology of the NPs. The shape of the NPs has a direct impact on their tribological properties and can be considered as

a primary factor that determines the NP–substrate contact area and friction. The NPs used in the present experiments exhibited various morphologies, which need to be considered in more detail.

Intact Au NPs deposited on a substrate have well distinguishable facets (Figure 2a) and will be referred to as polyhedron-like. Tetrahedral, decahedral, icosahedral and other shapes can be identified in the SEM image (Figure 2b). Some particles exhibit truncated edges and apexes. Typical morphologies of Au NPs are listed in Table 1. It should be noted, that after the removal of the surfactant by thermal treatment partial rounding of the particles might occur [20].

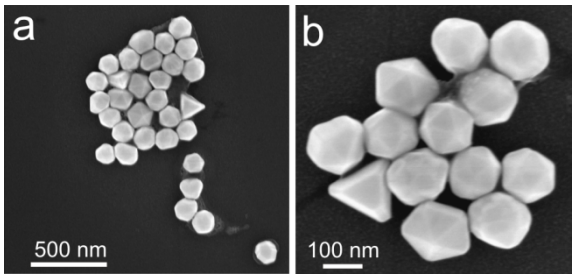

Figure 2: High resolution SEM images of Au NPs (150 nm) of different shape as deposited from a solution.

The morphology of Ag NPs was determined by the conditions of the laser annealing of the target nanowires [21,22]. At a relatively small laser pulse energy, rounded structures formed on both ends of nanowires (Figure 3a). At a higher pulse energy the whole NW melted into separated round NPs due to Plateau–Rayleigh instability [19]. All Ag NPs produced by laser induced melting appear almost spherical in the SEM micrographs (Figure 3b). There are two possible scenarios for the formation of Ag NPs. In the first scenario the molten nanostructures are able to detach from the substrate surface and solidify before contacting the substrate again [21]. In this case the particle shape can be close to ideal sphere. According to another scenario Ag nanostructures melt under the laser irradiation for a short period of time (ns) and then solidify again forming "frozen" droplets on a substrate surface. The frozen droplet model can be applied to determine the geometry of the resulted Ag NP given that the contact angle of NP–substrate interface is known. In this case the real shape of the Ag NP is a truncated sphere.

NP–substrate contact area. Depending on the NP morphology two basic approaches for the determination of the contact area can be distinguished: geometrical and adhesive. The contact area of polyhedron-like Au NPs on a flat substrate can be defined as the area of the facet in contact. It enables to use the

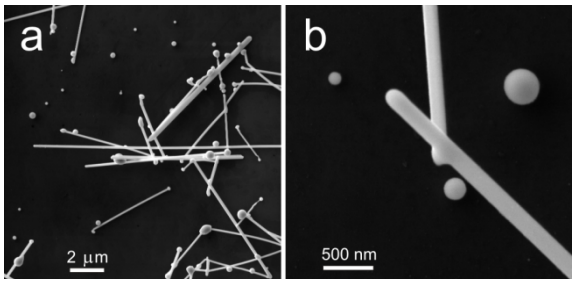

Figure 3: High resolution SEM images of Ag nanowires (diameter 120 nm) after pulsed laser annealing (a). Ag NPs of different size produced by laser annealing (b).

geometrical approach to the contact area for faceted NPs. It should be added that because of the presence of arbitrarily truncated edges and apexes the contact areas of real particles is supposedly lower than the maximal values listed below in Table 1. For frozen-droplet shaped Ag NPs, the contact area A can also be estimated by geometrical considerations for a sphere of radius R and a cutting plane of the contact:

$$A = \pi R^2 \sin^2 \Theta , \quad (1)$$

where Θ is the contact angle for Ag/SiO_2 interface.

As described previously [20], for sphere-like NPs contact mechanics (adhesive contact approach) must be applied. The contact area is typically calculated on the basis of continuum elasticity models for deformable spheres such as the Johnson–Kendall–Roberts (JKR) [23] or the Derjaguin–Müller–Toporov (DMT-M) model [24]. According to Tabor [25], the choice of the most suitable model is determined by the parameter

$$\eta = \left(\frac{16 R \gamma^2}{9 K^2 z_0^3} \right)^{1/3} , \quad (2)$$

where R is the radius of the sphere, γ is the work of adhesion, and z_0 is the equilibrium spacing for the Lennard-Jones potential of the surfaces. K is the combined elastic modulus of the sphere and substrate, defined as

$$K = \frac{4}{3}\left[\left(1-\nu_1^2\right)/E_1 + \left(1-\nu_2^2\right)/E_2 \right]^{-1} ,$$

in which $\nu_{1,2}$ and $E_{1,2}$ are the Poisson ratios and Young moduli of the substrate and the sphere, respectively. For small η, the DMT-M theory is more appropriate [26]. According to the DMT-M model, the contact area A_{DMT} of the sphere on a flat surface is:

$$A_{\mathrm{DMT}} = \pi\left(\frac{2\pi\gamma}{K}\right)^{2/3} R^{4/3}. \quad (3)$$

The DMT-M approach can also be applied for the frozen droplets displaced and rolled from their initial position. For convenience different types of particle geometries and corresponding models are schematically represented in Figure 4.

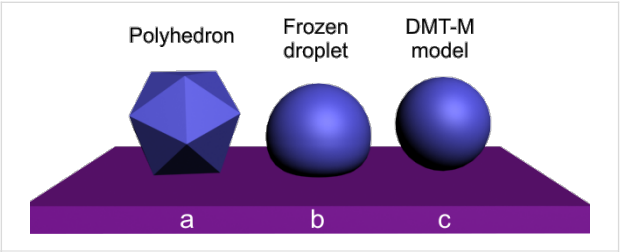

Figure 4: Different models for the estimation of the contact area: facet area of a polyhedron for Au NPs (a), frozen droplet for Ag NPs solidified on a substrate (b), DMT-M model for Ag NPs solidified without contact to a substrate (c).

Real time manipulations of NPs. Au and Ag NPs were manipulated inside a SEM and the lateral force, F_{friction}, that was needed for the displacement of individual particles (i.e., static friction) was measured and analyzed with respect to the NP shape. Visual guiding during the manipulation of the NPs enabled to monitor their trajectory, in order to distinguish between continuous and abrupt motions (jumps), and to correlate the movement of the NPs with the measured tip–NP interaction force.

The first series of measurements was carried out with 19 Au NPs. Figure 5 represents a typical manipulation experiment with Au NPs. The tip displacement was linear in time and the diagram presents the force curve versus time to link the SEM images and the force curve. The initial region of the curve from (a) to (b) corresponds to the tip movement at a constant height above the surface towards the NP and into the contact with the particle. The gradual increase of the force in proximity of (b) is caused by the tip–particle interaction. The peak value at point (b) corresponds to the ultimate force needed to overcome the static friction and to displace the Au particle. Usually, after overcoming the static friction the particle made a jump of a few hundred nanonewtons, and in doing so released the potential energy accumulated during loading. From (c) to (e) the particle moved smoothly in the direction that is indicated by the arrows while only a small tip–particle interaction force was exerted. The static friction in the series was found to be in the range from 50 to 750 nN. In some cases the sensor oscillation amplitude dropped to zero. This drop corresponds to a force higher than 1500–2500 nN (the upper limit depending on the particular sensor). Forces higher than these limits could not be measured due to the limited range of the QTF sensitivity at a given driving voltage.

Another series of experiments was performed with 10 Ag NPs. In general, the behaviour of the Ag NPs during the manipulations was rather similar to that of the Au NPs. A typical manipulation force curve is shown in Figure 6. A force of several hundred nanonewtons was needed to overcome the static friction and to displace a NP (region in proximity of (b) in

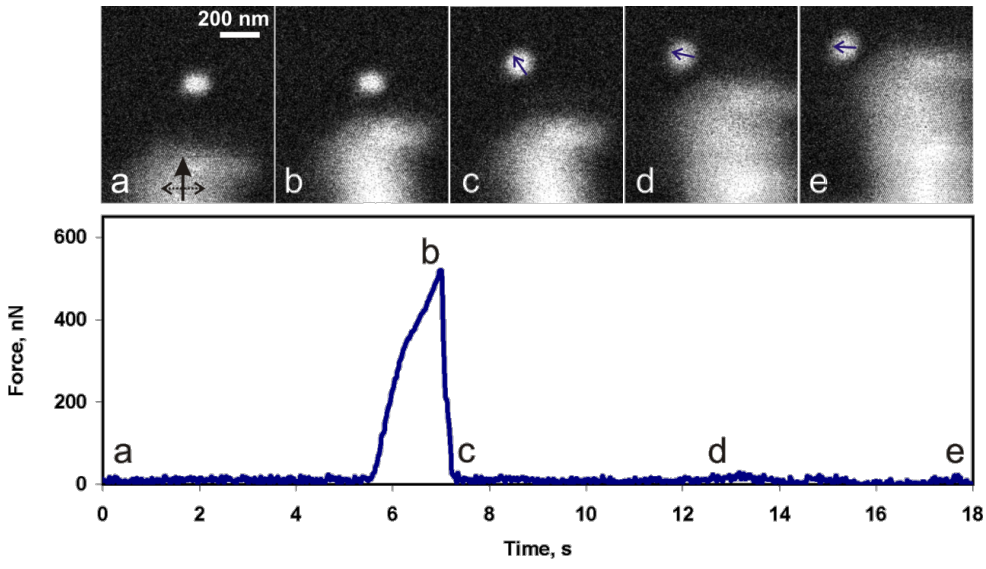

Figure 5: SEM snapshots of the manipulation process of a Au NP by using a tungsten tip, and the corresponding force curve. The black solid arrow in image (a) indicates the movement direction of the tip and dashed arrow shows tip the oscillation direction. The small blue arrows indicate the NP displacement directions (b, c, d).

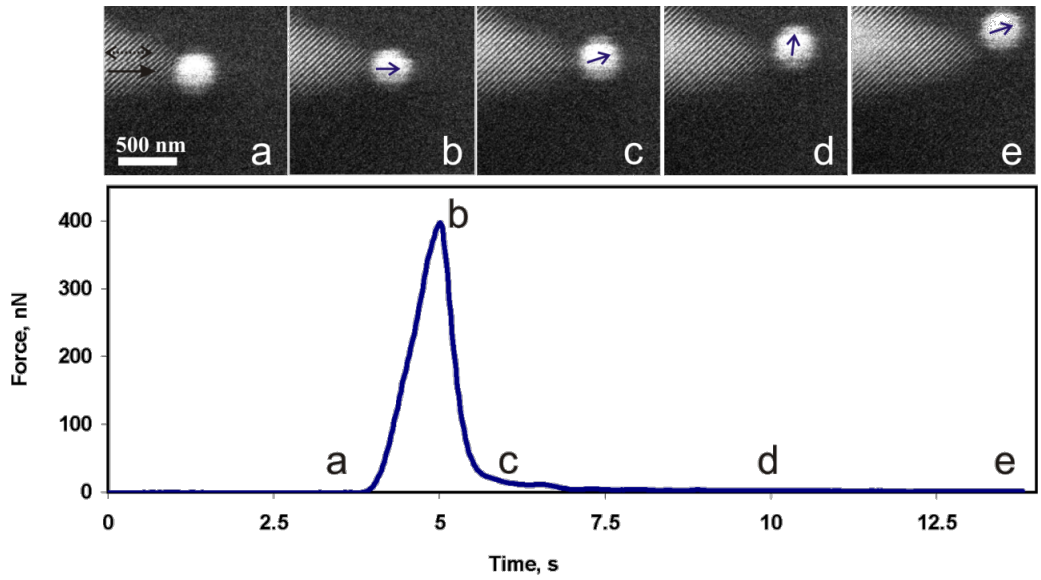

Figure 6: Snapshots of the manipulation of a Ag NP by using an AFM tip, and the corresponding force curve. The black solid arrow in image (a) indicates the tip movement direction and the dashed arrow shows the tip oscillation direction. The small blue arrows indicate NP displacement directions (b, c, d, e).

Figure 6), and only a few nanonewtons was enough to support the motion of the NP (regions (c)–(d)–(e), Figure 6). This finding is in agreement with those of other researchers, who have demonstrated that the kinetic friction is vanishing for clean surfaces in vacuum [3]. A nonstop motion of the NPs during the manipulations was an essential condition for staying in the vanishing friction regime, because rested NPs had a tendency to adhere strongly to the substrate. The static friction in the series was found to range from about 130 to 1880 nN.

The distributions of the static friction values for both polyhedron-like Au NPs and for sphere-like Ag NPs are represented in the form of histograms in Figure 7b. It should be noted that when the tip oscillated perpendicular to the manipulation direction (Figure S5, Supporting Information File 1) the NP often moved aside affected by the tip oscillation (Figure 5). Moreover, the force necessary to displace a NP can be overestimated due to an unaccounted amount of energy dissipated in a shear interaction between the tip and the NP. For the parallel tip oscillation direction (Figure S5, Supporting Information File 1) the NPs usually moved forward (motion in the manipulation direction), however, sometimes the NPs randomly deviated from the forward motion and moved aside (Figure 6). Such events are probably caused by surface defects. In summary, a tip oscillation parallel to the manipulation direction is more preferable for the manipulation of NPs because of the better control over the NP movement and a more accurate estimation of the force.

Static friction analysis. To analyze the results of the experimentally measured static friction force of the NPs, we calculated the friction force values, F_{friction}, by using a simple relation:

$$F_{\text{friction}} = \tau \cdot A\,, \tag{4}$$

where τ is the interfacial shear stress/strength and A is the contact area [26]. The shear strength is defined as an ultimate shear stress τ before the object is displaced, and can be estimated by using the relation $\tau_{\text{theo}} = G^*/Z$ between the theoretical shear strength and the combined shear modulus,

$$G^* = \left[\left(2-\nu_1\right)/G_1 + \left(2-\nu_2\right)/G_2\right]^{-1},$$

where ν is the Poisson ratio and $G_{1,2} = E_{1,2}/2(1 + \nu_{1,2})$ [27,28]. Z is an empirical coefficient that depends on the material and ranges from 5 to 30 [29]. To calculate interfacial shear stress/strength τ for Au NPs the following parameters were used: E_1 = 71.7 GPa, ν_1 = 0.17, E_2 = 78 GPa, ν_2 = 0.36, Z = 30 [4]. The static friction force values for Au NPs of different geometries were calculated according to Equation 1 and presented in Table 1. The detailed calculation is given in Supporting Information File 1.

Analyzing the experimentally measured and calculated static friction force values (Figure 7a and Table 1) it can be seen that

Table 1: Calculated contact areas and static friction forces for 150 nm Au particles of different faceting.

shape	contact area, nm^2	static friction, nN
tetrahedral	9743	2768
decahedral	3652	1038
truncated icosahedral hexagonal facet	3474	987
icosahedral	2693	765
truncated icosahedral pentagonal facet	2301	654

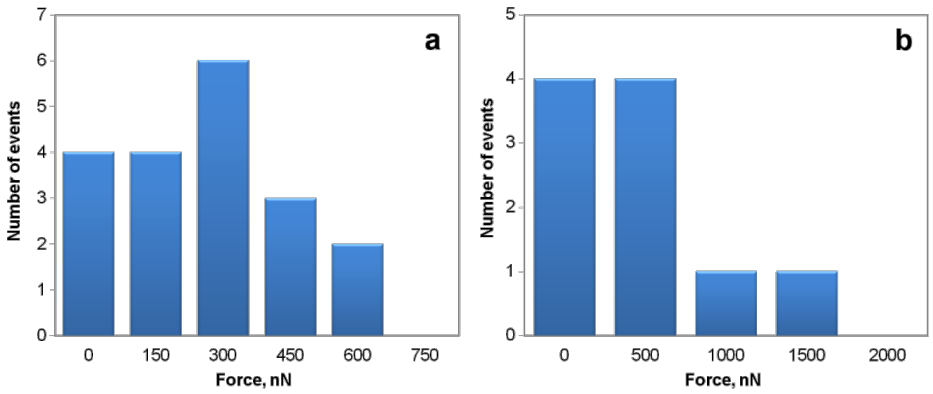

Figure 7: Distribution histogram of static friction force values that were experimentally measured for NPs of different shapes: polyhedron-like Au NPs (a) and for sphere-like Ag NPs (b), respectively.

the experimental friction force values mostly correspond to icosahedral and truncated icosahedral NP shapes.

To evaluate the applicability of the frozen droplet and DMT-M models for Ag NPs we examined the residual traces, which remained after the displacement of 33 NPs inside a high resolution SEM. Figure 8 demonstrates the trace after the first displacement of a NP that rested on the flattened side according to the frozen droplet model (Figure 8a,b) and after the second displacement of a NP that supposedly rested on the round side according to DMT-M model (Figure 8c,d). The contact area for the first NP is ca. 21800 nm^2, and only about 3260 nm^2 for the second particle, which confirms our assumption that the displacement can cause a rolling of NPs from the initial flattened side to a more rounded side (and consequently decreasing the contact area).

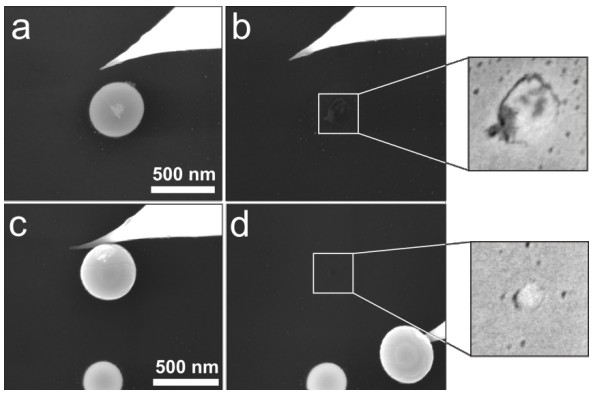

Figure 8: High resolution SEM images of Ag NPs (no force recording during the displacement of the NPs). Traces indicating the contact area after the first (a,b) and the second (c,d) displacement of two different Ag NPs. The corresponding estimated static friction forces are ca. 6190 nN and about 930 nN, respectively.

The experimental data on the static friction forces measured by the QTF sensor (f_{QTF}) and calculated from the diameters of the traces left after the displacement of the NPs (f_{trace}) are shown in Figure 9 along with theoretical curves of the static friction as a function of the particle radius according to the frozen droplet (Equation 1 and Equation 4) and DMT models (Equation 3 and Equation 4). The following parameters were used in the calculations: $\Theta = 123.8°$ [30], $E_1 = 71.7$ GPa, $\nu_1 = 0.17$, $E_2 = 82.5$ GPa [31], $\nu_2 = 0.36$, $\gamma = 50$ mJ/m^2 [4], and $z_0 = 0.3$ nm, $Z = 15$ [29]. When comparing the numerical values of f_{QTF} and f_{trace} one should be aware that due to the differences between the methods only a raw estimation and qualitative conclusions can be derived. The static friction force values of NPs that were displaced for the first time (Figure 9, empty circles) are closer to the frozen droplet model. However, it is evident that the

static friction predicted by the DMT-M model is smaller than the values measured with the QTF for previously displaced NPs (Figure 9, red circles). We suppose that the final shape of NPs was determined by the deviation from a perfect sphere towards an oblate spheroid according to the wettability of the liquid droplet during solidification. An alternative explanation may be the enlargement of the contact area of Ag NPs due to partial melting or enhanced diffusion of atoms caused by the electron beam (e.g., electromigration [32,33]).

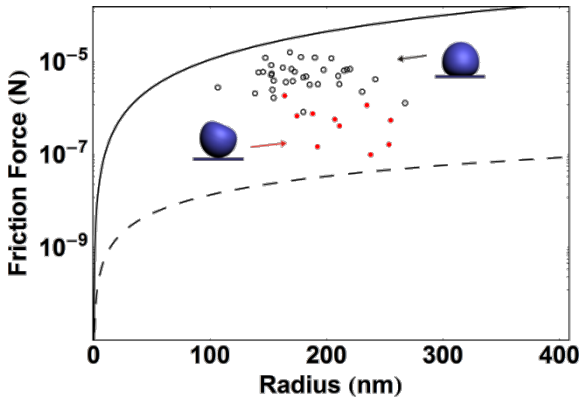

Figure 9: The static friction force of Ag NPs on a Si wafer as a function of the radius of the NPs. The static friction force values experimentally measured by QTF (dots) and calculated from the diameters of visible traces left after the displacement of the particles (circles). The theoretical curves of friction as functions of the radius of the NPs according to the DMT-M model (dashed curve) and frozen droplet model (solid curve).

Limitations of manipulations inside a SEM. At the end we would like to briefly discuss some limitations or drawbacks of inside-SEM nanomanipulations. The scanning rate of the electron beam is limited to a few hertz, therefore only relatively slow processes can be visualized (e.g., the monotonous motion of a NP pushed by the tip). Fast processes such as, for example, jumps of NPs can only be noticed. Another limitation is connected to the resolution of the SEM, which is related to the scanning speed and forces one to make compromises between the accuracies of determination of either the shape or the dynamics of the NPs. The effect of the electron beam on the substrate surface and on the nanostructures should also be taken into account. As it is well known, the melting temperature of the nanostructures decreases when decreasing the diameters of the structures [34,35]. Potentially, a focused e-beam is capable of introducing significant amounts of energy and causing a partial melting of the nanostructures. Additional effects can be an activation of the substrate surface or an electrostatic charging, which can also influence the results of nanotribological experiments [36].

Conclusion

Polyhedron-like Au and sphere-like Ag NPs were manipulated on an oxidized Si substrate inside a SEM with a simultaneous force detection by using a QTF-based sensor. Real time manipulations benefit from a visual guidance of the SEM. This enables revealing the NP trajectories, distinguishing continuous or jumping motions and correlating them with the interaction force between tip and NPs. The contact areas were calculated from geometrical considerations for polyhedron-like NPs. For sphere-like NPs the contact areas were calculated by using DMT-M and frozen droplet models. The recorded static friction force values are in good agreement with the calculated values for both polyhedron-like and sphere-like NPs.

Supporting Information

The Supporting Information contains details of SmarAct manipulator working regimes, the QTF force sensor calibration and calculations of the surface areas for different geometries.

Supporting Information File 1

Additional experimental details.
[http://www.beilstein-journals.org/bjnano/content/supplementary/2190-4286-5-13-S1.pdf]

Acknowledgements

This work was supported by the ESF project Nr. 2013/0202/1DP/1.1.1.2.0/13/APIA/VIAA/010 and EU through the ERDF (Centre of Excellence ‘‘Mesosystems: Theory and Applications’’, TK114). The work was also partly supported by COST Action MP1303 and ETF grants 8420, 9007, Estonian Nanotechnology Competence Centre (EU29996), ERDF ‘‘TRIBOFILM’’3.2.1101.12-0028, ‘‘IRGLASS’’ 3.2.1101.12-0027, ‘‘Nano-Com’’ 3.2.1101.12-0010.

References

1. Gnecco, E.; Meyer, E., Eds. *Fundamentals of Friction and Wear;* Springer: Berlin, Heidelberg, New York, 2007.
2. Wang, N.; Rokhlin, S. I.; Farson, D. F. *Nanotechnology* **2008,** *19,* 415701. doi:10.1088/0957-4484/19/41/415701
3. Dietzel, D.; Ritter, C.; Mönninghoff, T.; Fuchs, H.; Schirmeisen, A.; Schwarz, U. D. *Phys. Rev. Lett.* **2008,** *101,* 125505. doi:10.1103/PhysRevLett.101.125505
4. Kim, S.; Ratchford, D. C.; Li, X. *ACS Nano* **2009,** *3,* 2989–2994. doi:10.1021/nn900606s
5. Darwich, S.; Mougin, K.; Rao, A.; Gnecco, E.; Jayaraman, S.; Haidara, D. *Beilstein J. Nanotechnol.* **2011,** *2,* 85–98. doi:10.3762/bjnano.2.10
6. Mougin, K.; Gnecco, E.; Rao, A.; Cuberes, M.; Jayaraman, S.; McFarland, E. W.; Haidara, H.; Meyer, E. *Langmuir* **2008,** *24,* 1577–1581. doi:10.1021/la702921v

7. Paolicelli, G.; Rovatti, M.; Vanossi, A.; Valeri, S. *Appl. Phys. Lett.* **2009,** *95,* 143121. doi:10.1063/1.3238320
8. Nita, P.; Casado, S.; Dietzel, D.; Schirmeisen, A.; Gnecco, E. *Nanotechnology* **2013,** *24,* 325302. doi:10.1088/0957-4484/24/32/325302
9. Rao, A.; Gnecco, E.; Marchetto, D.; Mougin, K.; Schönenberger, M.; Valeri, S.; Meyer, E. *Nanotechnology* **2009,** *20,* 115706. doi:10.1088/0957-4484/20/11/115706
10. Polyakov, B.; Vlassov, S.; Dorogin, L. M.; Kulis, P.; Kink, I.; Lohmus, R. *Surf. Sci.* **2012,** *606,* 1393–1399. doi:10.1016/j.susc.2012.04.029
11. Resch, R.; Bugacov, A.; Baur, C.; Koel, B. E.; Madhukar, A.; Requicha, A. A. G.; Will, P. *Appl. Phys. A* **1998,** *67,* 265–271. doi:10.1007/s003390050769
12. Sitti, M.; Hashimoto, H. *IEEE/ASME Trans. Mechatronics* **2000,** *5,* 199–211. doi:10.1109/3516.847093
13. Onal, C. D.; Ozcan, O.; Sitti, M. Automated 2-D Nanoparticle Manipulation with an Atomic Force Microscope. International Conference on Robotics and Automation, Kobe, Japan, May 12–17, 2009; .
14. Marz, M.; Sagisaka, K.; Fujita, D. *Beilstein J. Nanotechnol.* **2013,** *4,* 406–417. doi:10.3762/bjnano.4.48
15. Gnecco, E.; Rao, A.; Mougin, K.; Chandrasekar, G.; Meyer, E. *Nanotechnology* **2010,** *21,* 215702. doi:10.1088/0957-4484/21/21/215702
16. Hsieh, S.; Meltzer, S.; Wang, C. R. C.; Requicha, A. A. G.; Thompson, M. E.; Koel, B. E. *J. Phys. Chem. B* **2002,** *106,* 231–234. doi:10.1021/jp012747x
17. Dietzel, D.; Mönninghoff, T.; Jansen, L.; Fuchs, H.; Ritter, C.; Schwarz, U. D.; Schirmeisen, A. *J. Appl. Phys.* **2007,** *102,* 084306. doi:10.1063/1.2798628
18. Gnecco, E. *Beilstein J. Nanotechnol.* **2010,** *1,* 158–162. doi:10.3762/bjnano.1.19
19. Fowlkes, J. D.; Kondic, L.; Diez, J.; Wu, Y.; Rack, P. D. *Nano Lett.* **2011,** *11,* 2478–2485. doi:10.1021/nl200921c
20. Vlassov, S.; Polyakov, B.; Dorogin, L. M.; Löhmus, A.; Romanov, A. E.; Kink, I.; Gnecco, E.; Löhmus, R. *Solid State Commun.* **2011,** *151,* 688–692. doi:10.1016/j.ssc.2011.02.020
21. Habenicht, A.; Olapinski, M.; Burmeister, F.; Leiderer, P.; Boneberg, J. *Science* **2005,** *309,* 2043–2045. doi:10.1126/science.1116505
22. Afkhami, S.; Kondic, L. *Phys. Rev. Lett.* **2013,** *111,* 034501. doi:10.1103/PhysRevLett.111.034501
23. Johnson, K. L.; Kendall, K.; Roberts, A. D. *Proc. R. Soc. London, Ser. A* **1971,** *324,* 301–313. doi:10.1098/rspa.1971.0141
24. Derjaguin, B. V.; Müller, V. M.; Toporov, Yu. P. *J. Colloid Interface Sci.* **1975,** *53,* 314–326. doi:10.1016/0021-9797(75)90018-1
25. Tabor, D. *J. Colloid Interface Sci.* **1977,** *58,* 2–13. doi:10.1016/0021-9797(77)90366-6
26. Carpick, R. W.; Salmeron, M. *Chem. Rev.* **1997,** *97,* 1163–1194. doi:10.1021/cr960068q
27. Timoshenko, S. P.; Goodier, J. N. *Theory of Elasticity;* McGraw-Hill: New York, U.S.A., 1987.
28. Cottrell, A. H. *Dislocations and Plastic Flow in Crystals;* Oxford University Press: Oxford, U.K., 1953.
29. Hirth, J. P.; Lothe, J. *Theory of Dislocations;* Wiley: New York, U.S.A., 1982.
30. Gadre, K. S.; Alford, T. L. *J. Appl. Phys.* **2003,** *93,* 919–923. doi:10.1063/1.1530362
31. Smith, D. R.; Fickett, F. R. *J. Res. Natl. Inst. Stand. Technol.* **1995,** *100,* 119–171. doi:10.6028/jres.100.012
32. Stahlmecke, B.; Meyer zu Heringdorf, F.-J.; Chelaru, L. I.; Horn-von Hoegen, M.; Dumpich, G.; Roos, K. R. *Appl. Phys. Lett.* **2006,** *88,* 053122. doi:10.1063/1.2172012
33. Bellisario, D. O.; Ulissi, Z.; Strano, M. S. *J. Phys. Chem. C* **2013,** *117,* 12373–12378. doi:10.1021/jp4035776
34. Plech, A.; Cerna, R.; Kotaidis, V.; Hudert, F.; Bartels, A.; Dekorsy, T. *Nano Lett.* **2007,** *7,* 1026–1031. doi:10.1021/nl070187t
35. Xiao, S.; Hu, W.; Yang, J. *J. Phys. Chem. B* **2005,** *109,* 20339–20342. doi:10.1021/jp054551t
36. Conache, G.; Ribayrol, A.; Fröberg, L. E.; Borgström, M. T.; Samuelson, L.; Montelius, L.; Pettersson, H.; Gray, S. M. *Phys. Rev. B* **2010,** *82,* 035403. doi:10.1103/PhysRevB.82.035403

License and Terms

Beilstein Journal of Nanotechnology

Single-asperity contact mechanics with positive and negative work of adhesion: Influence of finite-range interactions and a continuum description for the squeeze-out of wetting fluids

Martin H. Müser

Full Research Paper

Open Access

Address:
Jülich Supercomputing Centre, FZ Jülich, 52428 Jülich, Germany

Email:
Martin H. Müser - m.mueser@fz-juelich.de

Keywords:
cohesive zone model; contact mechanics; environmental; fluid squeeze-out; nanomechanics; single-asperity contacts

Beilstein J. Nanotechnol. **2014,** *5,* 419–437.
doi:10.3762/bjnano.5.50

Received: 23 December 2013
Accepted: 12 March 2014
Published: 08 April 2014

This article is part of the Thematic Series "Nanomanipulation and environmental nanotechnology".

Guest Editor: E. Gnecco

Abstract

In this work, single-asperity contact mechanics is investigated for positive and negative work of adhesion $\Delta\gamma$. In the latter case, finite-range repulsion acts in addition to hard-wall constraints. This constitutes a continuum model for a contact immersed in a strongly wetting fluid, which can only be squeezed out in the center of the contact through a sufficiently large normal load F_N. As for positive work of adhesion, two stable solutions can coexist in a finite range of normal loads. The competing solutions can be readily interpreted as contacts with either a load-bearing or a squeezed-out fluid. The possibility for coexistence and the subsequent discontinuous wetting and squeeze-out instabilities depend not only on the Tabor coefficient μ_T but also on the functional form of the finite-range repulsion. For example, coexistence and discontinuous wetting or squeeze-out do not occur when the repulsion decreases exponentially with distance. For positive work of adhesion, the normal displacement mainly depends on F_N, $\Delta\gamma$, and μ_T but – unlike the contact area – barely on the functional form of the finite-range attraction. The results can benefit the interpretation of atomic force microscopy in liquid environments and the modeling of multi-asperity contacts.

Introduction

The continuum description of single-asperity contact mechanics has received much attention in the last few decades. This is in large parts because it describes force-displacement curves rather accurately down to nanometer scales relevant to atomic force microscopy (AFM) [1-3]. The contributions to the linear elasticity of (frictionless) single-asperity contacts most central to this work are the following: Hertz [4] solved the contact mechanics of a parabolic tip pressed against a substrate for

hard-wall repulsion. He found that the contact area A_c and the separation between the two solids d both disappear continuously with $F_N^{2/3}$ as the normal load squeezing the two solids together, F_N, approaches zero. Derjaguin, Muller, and Toporov (DMT) [5] included adhesion as a long-range interaction, in which case adhesion effectively acts as a normal load that is independent of the contact-radius a_c. Johnson, Kendall, and Roberts (JKR) [6] solved the problem for short-range adhesion, for which the attractive surface forces act directly at the contact line. Unlike Hertz and DMT, JKR found finite values for A_c and d at pull off. Tabor [7] introduced a dimensionless parameter, μ_T, now known as Tabor coefficient, allowing one to estimate if a contact is closer to DMT or to JKR theory. He actually recognized that DMT and JKR describe the opposite limits of long- and short-range forces, respectively. This had not been known before but was soon confirmed in numerical simulations by Muller, Yushenko, and Derjaguin [8]. Lastly, Maugis [9] used a cohesive-zone model introduced by Dugdale (MD) and found analytical solutions for intermediate-range adhesion at arbitrary values of μ_T.

Although single-asperity, linearly-elastic, adhesive contacts mechanics is a rather mature field [10], two key issues remain worth addressing: First, only few studies have considered the case of negative work of adhesion [11,12], $\Delta\gamma < 0$, specifically finite-range repulsion between two surfaces acting in addition to hard-wall repulsion. In particular, the concept of the Tabor coefficient has not yet been applied to negative $\Delta\gamma$. Therefore, I investigate if there are different regimes for $\Delta\gamma < 0$ as is the case for contacts with $\Delta\gamma > 0$, which are classified as JKR for large μ_T and as DMT for small μ_T. This includes a study of which parameters determine the behavior near squeeze-out as well as a comparison to the behavior near pull-off for $\Delta\gamma > 0$. For the latter, it is straightforward to deduce from established results how the $a_c(F_N)$ relation depends on the Tabor coefficient in the DMT and the JKR limit. Specifically, $a_c - a_p \propto (F_N + F_p)^\kappa$ for $F_N \geq -F_p$, where F_p and a_p are pull-off force and pull-off radius, respectively. They both depend on μ_T just like the exponent κ, e.g., $a_p > 0$ and $\kappa = 1/2$ in the JKR limit, while $a_p = 0$ and $\kappa = 1/3$ for DMT. In the present comparison of squeeze-out (finite-range repulsion) versus pull-off (finite-range attraction), I also study whether the exponent κ changes continuously between JKR and DMT or discontinuously – as assumed implicitly in the Carpick–Ogletree–Salmeron (COS) model [1].

The second motivation for this paper is that it has not yet been investigated sufficiently how the (precise) functional form for adhesive interactions affects contact mechanics – assuming that all continuum parameters, from normal load to Tabor coefficient, are identical. It is only established that there is little sensitivity in the limits of large and zero Tabor coefficients. Yet, when studying contact-mechanics between macroscopic, adhesive, rough surfaces in the context of continuum-mechanics, one would want to know how to best reach the JKR limit, which appears to be the relevant limit for that application. For example, it is used implicitly in Persson theory for nominally flat, adhesive surfaces [13]. In fact, the current work was initiated by the desire to add adhesion into a Green's function molecular dynamics (GFMD) code used to model the contact between rough surfaces. To model adhesion, one needs to identify a functional form for the finite-range surface forces allowing one to reach the JKR limit in an efficient and well-controlled fashion. It quickly became clear that doing a clean job is not entirely trivial and that modeling single-asperity contacts ought to be better understood first and moreover is interesting in its own right.

The remainder of this paper is organized as follows: I first introduce the model, sketch the numerical methods and discuss difficulties arising in simulations in the limit of large and small Tabor coefficients. Next, I present a brief dimensional analysis motivating the commonly used unit system and the Tabor coefficient. The result section opens with adhesive contacts. There, I reproduce some established results and investigate how sensitive results are on the details of the interaction model. That section also contains a comparison to and an asymptotic analysis of the MD model motivating some minor modifications of the empirical COS equations [1]. Next, results on positive adhesion are presented before the major results are summarized and conclusions are drawn.

Results and Discussion

Definition of the model

In this section, the single-asperity contact problem is introduced. As shown in Figure 1, we consider a stiff, ideally-flat wall positioned in the xy plane at $z = 0$ and a linearly-elastic tip of parabolic shape. Its undeformed surface is given by

$$z(r) = r^2/2R, \tag{1}$$

where R is the radius of curvature and $r = \sqrt{x^2 + y^2}$ the in-plane distance of the center of the tip from the origin of the coordinate system. The elastic displacement of the tip, $u(x,y)$ is formally a function of both in-plane coordinates, although the equilibrium solutions only depend on r. The gap $g(x,y)$ indicates the distance between the deformed tip and the substrate, i.e.,

$$g(x,y) = z\{r(x,y)\} - u(x,y). \tag{2}$$

It is furthermore assumed that the tip cannot penetrate the substrate. This can be stated as a non-holonomic boundary condition

$$g(x,y) \geq 0. \tag{3}$$

Alternatively, one can formally introduce a short-range, hard-wall repulsion [14]

$$V_{\mathrm{sr}} = \lim_{z_{\mathrm{r}}\to 0} \int \mathrm{d}^2 r \left(f_{\mathrm{r}} z_{\mathrm{r}}\right) \exp\left\{-g(x,y)/z_{\mathrm{r}}\right\}, \tag{4}$$

where f_{r} is an arbitrary positive constant of unit force per area. Note that the integrand on the r.h.s. of Equation 4 is zero for finite gaps while it diverges for negative gaps. Depending on the problem, it can be more convenient to use either the non-holonomic boundary condition or the energy-based description of the short-range repulsion.

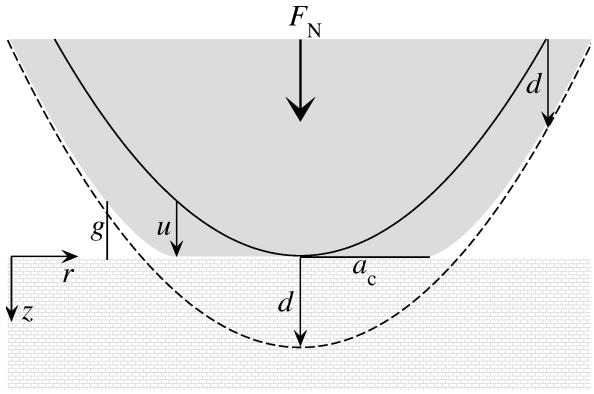

Figure 1: Geometry of the deformed tip (upper grey solid), the substrate (lower solid), and the reference tip (solid line). The dotted line represents a hypothetical tip that is allowed to penetrate the substrate the distance *d* into the substrate without deforming. The following vectors are introduced in the sketch: Normal load F_{N} acting on the center of mass of the tip, the elastic displacement field *u*, and the displacement *d* of the tip's center of mass. In addition, two scalar quantities, namely the contact radius a_{c} and the gap (field) *g* are shown.

This work also considers finite-range adhesive or finite-range repulsive interactions V_{fr}, which only depend on the local gap. The default expression for it is:

$$V_{\mathrm{fr}} = -\Delta\gamma \int \mathrm{d}^2 r \exp\left\{-g(x,y)/z_0\right\}, \tag{5}$$

where $\Delta\gamma$ is the work of adhesion per surface area that is obtained when a flat tip touches the substrate in a continuum description. The choice of the functional dependence of V_{fr} is not motivated by the true functional form for the interactions between any two real solids, but for the moment being, it is a matter of convenience. Alternative interaction models for the integrand are introduced in a seperate section.

An important property of all models for V_{fr} is that the interaction is characterized by a prefactor representing the work of adhesion and a single length scale z_0. The choice of the latter allows one to localize adhesive stress near the contact line through $z_0 \to 0$ or to extend the adhesive interactions to radii much exceeding the contact radius a_{c} for $z_0 \to \infty$. Of course, z_0 can take any value between zero and infinity so that intermediate-range interactions can be modeled as well. Note that V_{fr} and V_{sr} are qualitatively different: The prefactor of the short-range potential is formally zero, because f_{r} is finite and z_{r} very small. In other words, z_{r} represents the size of an "infinitesimally-small" atom whose size is irrelevant on a continuum scale. In contrast, the prefactor of the finite-range potential is considered finite as well as the range of interaction z_0. It represents a "collective" length scale, such as the decay length of density oscillations in the fluid [15] or the radius of gyration of a polymer.

The displacement $u(x,y)$ and other fields (gap and stress) will be expressed not only in real space, but also in Fourier space. This is done most conveniently by using in-plane periodic boundary conditions. The respective boundaries lie at x or $y = \pm L/2$, which should be chosen such that L (the linear dimension of the simulation cell) is much greater than the linear dimension of the contact zone. The latter includes the contact and the area of non-negligible adhesive (or finite-range repulsive forces) stresses. The following convention for the Fourier transform shall be employed

$$\tilde{u}(\mathbf{q}) = \frac{1}{A}\int \mathrm{d}^2 r u(\mathbf{r}) \exp\left\{i\mathbf{q}\cdot\mathbf{r}\right\} \tag{6}$$

$$u(\mathbf{r}) = \sum_{\mathbf{q}} \tilde{u}(\mathbf{q}) \exp\left\{i\mathbf{q}\cdot\mathbf{r}\right\}, \tag{7}$$

where the wave vector components satisfy $q_\alpha = 2\pi n/L$, $A = L^2$ is the integration domain, and n an integer number. With these definitions, one can express the elastic energy of the deformed tip (in the small-slope approximation) as

$$V_{\mathrm{ela}} = \frac{AE}{4}\sum_{\mathbf{q}} q\left|\tilde{u}(\mathbf{q})\right|^2, \tag{8}$$

where E is the effective modulus, $E = E_{\mathrm{Y}}/(1-\nu^2)$, E_{Y} being the Young's modulus and ν the Poisson ratio. The convention of using the symbol E^* for the effective modulus is abandoned for

clarity, because primes will be used later to indicate scaled coordinates and scaled parameters.

Since $\tilde{u}(0)$ can be interpreted as the center of mass mode, the effect of a load (or normal force) exerted on the tip leads to an energy

$$V_{\text{ext}} = -F_{\text{N}}\tilde{u}(0). \tag{9}$$

When solving the contact problem, one seeks to minimize the total energy

$$V_{\text{tot}}\left[u(\mathbf{r})\right] = V_{\text{sr}} + V_{\text{fr}} + V_{\text{ela}} + V_{\text{ext}} \tag{10}$$

with respect to $u(x,y)$, i.e., the solution $u_0(\mathbf{r})$ must satisfy

$$\left.\frac{\delta V_{\text{tot}}\left[u(\mathbf{r})\right]}{\delta u(\mathbf{r})}\right|_{u(\mathbf{r})=u_0(\mathbf{r})} = 0 \tag{11}$$

for each $\mathbf{r}$. Here, δ indicates a functional derivative. In a discrete representation of the problem, $\mathbf{r}$ is an index so that the functional derivative in Equation 11 has to be replaced by a partial derivative.

Alternative interaction models

Throughout this paper, different functional forms for the finite-range interactions between surfaces are considered in addition to the "default" or "exponential" model introduced in Equation 5. Functions similar to the ones used in this work have already been employed for the simulation of mode I fracture or delamination. Depending on the authors, the functions are called the cohesive zone model [16], the crack evolution function [17], or the traction-separation relation [18]. However, it is not clear how the results obtained for mode I fracture geometries relate to Hertzian contacts. This is the main reason why the results obtained within the cohesive zone model cannot be compared in a straightforward fashion to those of the current study.

The additional models in the current work replace the integrand on the r.h.s. of Equation 5 with the following expressions:

$$\nu_{\text{fr}}\left(\frac{g}{z_0}\right) = -\Delta\gamma \times \begin{cases} \exp\left(-g^2/2z_0^2\right) & \text{Gauss modell} \\ 1\Big/\left[1+\left(g/z_0\right)^2\right] & \text{van der Waals modell} \\ \left(1-g/z_0\right)\Theta\left(z_0-g\right) & \text{Maugis–Dugdale model} \end{cases}, \tag{12}$$

where Θ(···) denotes the Heavyside step functions, which is one for positive arguments and zero otherwise. The interaction potentials and their first derivatives are shown in Figure 2.

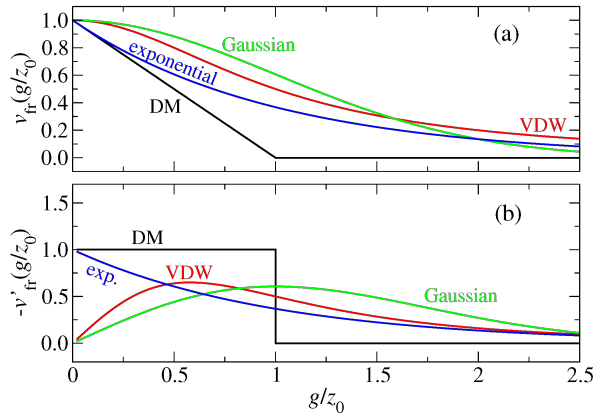

Figure 2: (a) Finite-range surface energies and (b) forces per unit area for the models investigated in this study.

All expressions take the same value, $-\Delta\gamma$, for the adhesive energy when the two surfaces touch, i.e., in each case the work of adhesion is Δγ. In this sense, all four models produce the same continuum limit. However, in two models, namely the Gauss and the van der Waals (VDW) integrands, the derivative $\nu'_{\text{fr}}(g/z_0)$ goes to zero when the two surfaces touch, while it remains finite in the exponential model and the MD model.

As stated before, none of the models are supposed to be highly realistic representations of surface forces, although each model may have its justification. In particular the exponential model follows from the argument that long-range density correlations in fluids are governed by a single length [15]. In a high-density fluid, the correlation length becomes complex [15], which then leads to layering transitions as discussed recently [19]. The VDW model might approximate the long-range van der Waals interactions in a way that Δγ reflects the Hamaker constant. Depending on the confined system in question, other effective interactions might be possible. However, all models represent the feature that surfaces repel upon close approach (i.e., when atoms from opposing surfaces bump into each other, which is implemented through the hard-wall repulsion) and that attraction – or additional repulsion – may occur at finite distance. Continuous short-range repulsive forces are not used here. Doing so would complicate the definition of contact and thus contact radius, which has remained controversial for systems without hard-wall or hard-disk interactions [20-23]. Lastly, the equations to be solved would become very stiff and thus the simulation inefficient if the hard-wall constraint was replaced by potentials with large curvature.

In the context of the squeeze-out of fluids, the MD and the exponential model might not be physically meaningful for small ratios of g/z_0: when one flat solid is placed on top of another flat solid with an infinitesimally small external load (in the absence of a fluid), the two solids would repel, although they "cannot know", away from a contact line, that a fluid wants to penetrate. Nonetheless, the exponential model has been used in early study of squeeze-out of fluids [12]. Forces between two (flat) surfaces in the Gauss and the VDW model are zero either for intimate mecanical contact or at infinite separation.

Dimensional analysis

In this section, I present a simple dimensional analysis of the contact problem. The result of the analysis is a meaningful set of units, which, in similar form, has already been established by Maugis [9]. However, in the present analysis, units are not motivated from the solutions but rather straight from the beginning, i.e., by the expressions defining the model. This is why Maugis' and the present units differ by dimensionless prefactors, which, however, always turn out close to unity. In the subsequent derivation, it is not necessary to know the precise functional dependence of the finite-range forces.

Assume we know the solution $u_0(\mathbf{r})$ minimizing V_{tot} for a given set of parameters defining our model, i.e., $u(\mathbf{r})$ solves the contact problem for a specific set of values for E, R, F_{N}, $\Delta\gamma$, and z_0. It is then possible to "recycle" the shape of the function $u_0(\mathbf{r})$ to solve a different problem defined by different parameters E', R', F'_{N}, $\Delta\gamma'$, and z'_0. Specifically, if each individual summand of $V'_{\text{tot}}\left[u'(\mathbf{r}')\right]$ is identical to the equivalent term in $V_{\text{tot}}[u(\mathbf{r})]$ (up to a multiplicative constant, which can be set to one), then $u'_0(\mathbf{r})$ minimizes $V'_{\text{tot}}\left[u'(\mathbf{r})\right]$ given that $u_0(\mathbf{r})$ minimizes $V_{\text{tot}}[u(\mathbf{r})]$.

The transformation, $u'_0(\mathbf{r}') \equiv tu(\mathbf{r}') = tu_0(s\mathbf{r})$, in which in-plane coordinates are scaled as $\mathbf{r}' \equiv s\mathbf{r}$ and normal coordinates are scaled as $z' = tz$ leaves the shape of the solution unchanged. Of course, $z(\mathbf{r})$ and thus $g(\mathbf{r})$ must be transformed the same way as $u(\mathbf{r})$. Therefore, the radius of curvature of the "new" tip is $R' = s^2R/t$.

Let us investigate how one has to alter each individual term contributing to $V'_{\text{tot}}\left[u'\right]$ so that it matches its equivalent in $V_{\text{tot}}[u]$. (i) The hard-wall repulsive energy V_{fr} is unproblematic. It disappears for the old and the new solution, because of the limit $z_{\text{r}} \to 0$, i.e., $V'_{\text{fr}}\left[u'\right] = 0$. (ii) To recycle the V_{fr} calculation, we need to set $z'_0 = tz_0$. Keeping in mind that $A' = s^2A$, where $A = L^2$ is the original integration domain, it follows that $V'\left[u'\right] = s^2(\Delta\gamma'/\Delta\gamma)V[u]$. (iii) For the calculation of the elastic energy, it is useful to keep in mind that $q' = q/s$ and that $A' = s^2A$. This means that $V'_{\text{ela}}\left[u'\right] = st^2\left(E'/E\right)V_{\text{ela}}\left[u\right]$. (The integer indices enumerating the wave vectors are identical for the original and the new domain.) (iv) Lastly, the load-related energy becomes $V'_{\text{ext}} = t\left(F'_{\text{N}}/F_{\text{N}}\right)V_{\text{ext}}$. In summary, we can recycle our solution with the following substitutions

$$E' = E/st^2 \tag{13}$$

$$R' = s^2R/t \tag{14}$$

$$\Delta\gamma' = \Delta\gamma/s^2 \tag{15}$$

$$z'_0 = tz_0 \tag{16}$$

$$F'_{\text{N}} = F_{\text{N}}/t. \tag{17}$$

Let us first consider the case of no external force, $F_{\text{N}} = 0$, so that we investigate the "intrinsic" system properties. If we use E as the unit of pressure, which is done until further notice, all three remaining parameters defining the system can be expressed to be of unit length, i.e, R, z_0, and $\Delta\gamma/E$. Wether a potential should be classified as short- or long-ranged can only depend on a non-dimensionalized interaction length. This means that z_0 has to be expressed in the two remaining units of length (R and $\Delta\gamma/E$) such that the dimensionless ratio

$$\frac{z_0}{R^{1-\alpha}\left(|\Delta\gamma|/E\right)^{\alpha}} \tag{18}$$

remains unchanged under a scaling transformation.

Let us now chose the radius of curvature as the unit of length, or, alternatively, consider only those scaling transformations that leave R constant. This can be achieved by setting $t = s^2$, which maps an infinite parabola ($x \to z = x^2$) onto itself ($sx \to s^2z$). I note in passing that such a transformation might not be meaningful for a scaling analysis of the contact mechanics of randomly rough surfaces, which will be presented elsewhere.

Inserting the relevant equalities from Equation 13–Equation 17 reveals that choosing $\alpha = 2/3$ leaves the expression in Equation 18 constant. As a consequence, the range of influence of the adhesive term is best quantified by the term

$$\frac{1}{\mu_{\text{T}}} = \frac{z_0}{R^{1/3}\left(|\Delta\gamma|/E\right)^{2/3}}, \tag{19}$$

where μ_T is known as Tabor coefficient – up to a dimensionless, multiplicative constant. It remains invariant under all scaling transformation in Equation 13–Equation 17 leaving the radius of curvature unchanged.

From Equation 19 one can see that we need to send $z_0 \to w^{2/3}z_0$ in order to keep the Tabor coefficient constant when changing $\Delta\gamma/E$ at constant R to $w\Delta\gamma/E$. This in turn implies a transformation of $x \to w^{1/3}x$ for the in-plane coordinates, because R is supposed to remain unchanged. It follows that $a_c(F_N = 0) \to w^{1/3}a_c(F_N = 0)$ and thus $a_c \propto (|\Delta\gamma|/E)^{1/3}$. The unit of a_c can be fixed by multiplying the r.h.s. of this proportionality with $R^{2/3}$. Otherwise the proportionality coefficient can only depend on μ_T, and of course, on the sign of $\Delta\gamma$. Therefore, we can write

$$\frac{a_c\left(F_N=0\right)}{\left(R^2\left|\Delta\gamma\right|/E\right)^{1/3}} = a_{c,T}\left(\mu_T, F_N=0\right), \tag{20}$$

such that the r.h.s. of the equation only depends on the Tabor coefficient and the functional form of the surface interaction. Since we have not used the explicit functional form of our default surface interaction (other than that it depends only on a single length scale), the conclusions drawn in this section extends to any choice for V_{fr} considered in this work.

To include finite loads into the analysis, note that the ratio $F_N/|\Delta\gamma|R$ does not change under the transformation Equation 13–Equation 17. This allows us to express a properly undimensionalized contact radius as a dimensionless function of a properly dimensionless load

$$\frac{a_c\left(F_N\right)}{\left(R^2\left|\Delta\gamma\right|/E\right)^{1/3}} = a_{c,T}\left(\mu_T, F_N/\left|\Delta\gamma\right|R\right). \tag{21}$$

From this last equation, it also becomes clear that the pull-off (or the squeeze-out) force is proportional to $|\Delta\gamma|R$, i.e., by identifying the value of $F_N/|\Delta\gamma|R$ at which the function $a_{c,T}$ takes its minimum value. Therefore, it is most meaningful to normalize the force with $\Delta\gamma R$, unless, of course, $\Delta\gamma = 0$.

The approach is validated in Figure 3. It shows the spatial dependence of the gap for two different parameterizations. Small deviations, which are not visible to the naked eye, occur. They are due to finite-size and discretization effects. For example, the ratio a_c/L is not exactly zero and takes different values for different values of s for a fixed number of points used to represent the elastic surface.

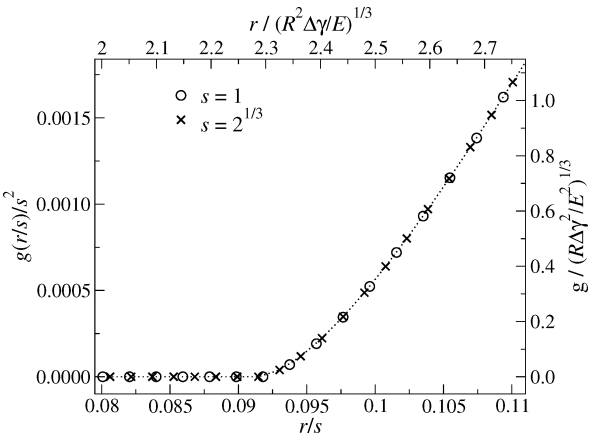

Figure 3: Scaled gap $g(r)$ as a function of scaled distance from origin r for two different parameter realizations related through the scaling transformation Equation 13–Equation 17. Parameters used are $E = L = \mu_T = 1$, $F_N = 1{\cdot}10^{-4}/w$ and $\Delta\gamma = 0.64{\cdot}10^{-4}/w$. The surface is discretized into 512 × 512 elements. Circles $s = 1$ with $w = 1 \to z_0 = 0.0016$, crosses $w = 1/2 \to z_0 = 2^{2/3} \cdot 0.0016$. For the second data set, this implies a scaling factor of $t = 2^{2/3}$ for variables linear in normal coordinates and thus $s = 2^{1/3}$ for variables proportional to in-plane coordinates. The units on the normal side of the axes are in "absolute" units, i.e., $L = 1$. The units on the opposite axes correspond to those that remain invariant under a scaling transformation. The dotted line is drawn to guide the eye.

The normal displacement can be nondimensionalized in a similar fashion as the contact radius, except that it needs to be rescaled with the factor $w^{2/3}$ rather than with $w^{1/3}$. This is why it must obey

$$\frac{d\left(F_N\right)}{R^{1/3}\left(\left|\Delta\gamma\right|/E\right)^{2/3}} = d_T\left(\mu_T, F_N/\left|\Delta\gamma\right|R\right), \tag{22}$$

where all terms on the r.h.s. of the equation are again dimensionless, while those on the l.h.s. are allowed to have units. Thus, displacements and gaps are best represented in units of $R^{1/3}(|\Delta\gamma|/E)^{2/3}$, while contact radii are more meaningfully expressed as multiples of $R^{2/3}(|\Delta\gamma|/E)^{1/3}$. As a result, numbers turn out of order unity when data is represented in these units, unless F_N approaches the pull-off threshold or distinctly exceeds $\Delta\gamma R$.

I conclude this section by summarizing the units used in this work and discuss some of the consequences arising from it: Specifically, the following units are used for:

$$\text{in-plane coordinates:} \qquad \left[x\right] = R^{2/3}\left(\left|\Delta\gamma\right|/E\right)^{1/3} \tag{23}$$

$$\text{out-of-plane coordinates:} \qquad \left[z\right] = R^{1/3}\left(\left|\Delta\gamma\right|/E\right)^{2/3} \tag{24}$$

normal force: $$[F_N] = R|\Delta\gamma| \quad (25)$$

normal pressure: $$[p] = \left(|\Delta\gamma|/R\right)^{1/3} E^{2/3} \quad (26)$$

This list includes a "new" unit of normal stress or pressure, $[p]$, which must be chosen proportional to $[F_N]/[x]^2$ rather than to E so that the regular definition of pressure applies. As noted above, E drops out of the definition of the unit for the normal force, implying that pull-off or squeeze-out forces cannot be functions of E. Instead they must equal $R|\Delta\gamma|$ times dimensionless expressions that can only depend on μ_T, and, of course, on the functional form of the interaction potential. In our units, the well-known $a_c(F_N,E^*,R,\Delta\gamma)$ relations can be simplified to

$$a_c^3 = \frac{3}{4}\left(F_N + 2\pi\right) \quad \text{in DMT limit} \quad (27)$$

$$a_c^3 = \frac{3}{4}\left(F_N + 3\pi + \sqrt{6\pi F_N + 9\pi^2}\right) \quad \text{in JKR limit.} \quad (28)$$

Hertzian contact mechanics is obtained in either limit for $F_N >> 1$. Finally, note that Maugis' choice for units slightly differs from ours in that he used $\pi\Delta\gamma$ rather than $\Delta\gamma$ in Equation 23–Equation 26 and $3E/4$ instead of E. The conversion between Maugis' and our system is summarized in Equation 43–Equation 46.

Numerical analysis

Different methods can be used in the numerical solution of Equation 11. For the present study, Green's function molecular dynamics (GFMD) [24] as described in [25] was employed. The only modification is the implementation of conservative surface forces acting in addition to the boundary condition $g(\mathbf{r}) \geq 0$. Moreover, the results in this work were produced with a serial code with typical run times of a few minutes. I refer to the literature for more details on GFMD [24,25]. Irrespective of the employed code or method, particular precautions, which are worth discussing, need to be taken into account when including adhesion or finite-range repulsion.

When simulating Hertzian contact mechanics, one needs to ensure that the discretization of the lattice Δa satisfies $\Delta a << a_c$. Of course, methods based on spatially varying grids only need to obey that relation near the contact line. In addition, one wants a_c to be much less than the size of the simulation cell, at least in Fourier-based methods, such as GFMD. One then has the sequence of inequalities $\Delta a << a_c << L$. In Hertzian contact mechanics, this is easy to achieve: choosing the discretization such that $\Delta a/a_c = 1/32$ and $a_c/L = 1/8$ already gives accurate results for the contact area, that is, to within less than 0.1% error if the contact area is determined through a fit of the radial pressure profile.

When including adhesion, an additional length enters, namely that associated with the adhesive zone. The additional adhesive radius or skin a_a then needs to be taken into consideration. When the Tabor coefficient is very small, a_a becomes large, and one needs a_a to lie within the simulation cell. A new series of inequalities is obtained: $\Delta a << a_c << a_a << L$. If the normal stress changes smoothly with the gap, i.e., for long-range adhesion, the forces couple predominantly to large wavelength modes. This then results in a simple offset force, as is well known from DMT theory. However, numerical demands can become significant when a_c disappears continuously with decreasing load as in the DMT scenario. The condition $a_c << a_a$ then becomes difficult to satisfy.

In the opposite case of a large Tabor coefficient, a_a is very small, potentially much smaller than a_c. We still need to resolve the adhesive zone sufficiently well, because the stress has to be smooth on the given discretization. One thus obtains the series of inequalities $a << a_a << a_c << L$. In either limit of large or small Tabor coefficient, another inequality needs to be satisfied in addition to those for Hertzian contact mechanics.

While the contact area converges reasonably quickly as the respective inequalities are obeyed, the center-of-mass displacement d, which corresponds to $\tilde{u}(0)$ or $u(r \to \infty)$ only converges slowly. The reason is that the displacement field induced at a given point due to an external force only decays with the inverse distance from that point, i.e.,

$$d \approx u(r) + \frac{c}{r} \quad \text{for} \quad r >> a_c + a_a, \quad (29)$$

where c is a load- and system-dependent constant. Outside of the adhesive zone, this relation can be used, in principle, to extrapolate from finite r to infinite r, i.e., by determining c and d from two measurements taken sufficiently far outside the adhesive zone. In practice, this turns out problematic, because the periodic boundary conditions suppress the $1/r$ corrections near the boundaries.

For Hertzian contacts, it is still possible to use a slightly modified (empirical) correction

$$d \approx 6u_X - 5u_M, \quad (30)$$

where X and M denote the (symmetry) points $(L/2,L/2)$ and $(L/2,0)$ relative to the position of the center of the tip. The same

extrapolation scheme also appears to give quickly converging estimates for the normal displacement for adhesive contact, which is demonstrated in Figure 4.

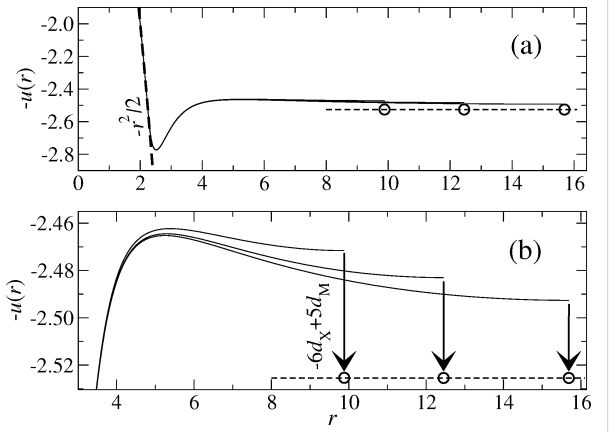

Figure 4: Negative elastic displacement $-u(r)$ (as defined in Figure 1) of a tip with $R = E = 1$ pressed against a rigid substrate at a positive load of $F_N = 1.5625$ for a work of adhesion $\Delta\gamma = 1$ and a Tabor coefficient $\mu_T = 1$ resulting in an exponential decay length of $z_0 = 1$. In each case, the system is discretized into 512 × 512 grid points, but different sizes are used, i.e., $L = L_0$, $L = 2^{1/3}L_0$, $L = 2^{2/3}L_0$ with $L_0 = 9.8825$. Part (a) shows a larger domain including the shape of the tip in form of a dashed line. Part (b) shows a smaller domain and includes a higher-resolution estimate of the displacement at infinite radius R through the extrapolation $6u_X - 5u_M$.

It is worth discussing Figure 4. At the given load, the contact radius is $a_c \approx 2.30$, while it would have been $a_c \approx 1.05$ without adhesion. The displacement curve has a peak at $r = 2.52$ and adhesive effects remain non-negligible all the way up to $r \approx 4$. At that distance the gap starts to be greater than $5z_0$, which means that the adhesive attraction is less than e^{-5} times the value in the contact and its immediate periphery. For distances exceeding $r = 4$, an infinitely large system would then show the displacement given in Equation 29. The periodic boundary conditions suppress this scaling rather strongly, yet, for radii as small as $r = 10$, accurate estimates for d_∞ can be achieved through Equation 30.

Simulations could be made more efficiently by exploiting the radial symmetry of the system. This would allow one to reduce sums over two indices (e.g., q_1 and q_2) to that over one index. However, less is gained than it first might seem. To get a good resolution of the contact area, the one-dimensional (1D) calculation require greater ratios for a_c/a than two-dimensional setups. The reason is that the resolution of the contact area in 1D and in 2D both scale with $1/N$, where N is the number of grid points in the contact. For example, when representing a contact in which for the given discretization $5a < a_c < 6a$ in a 2D system, then a_c is allowed to take the values $\sqrt{5^2+1^2}$, $\sqrt{5^2+2^2}$, $\sqrt{5^2+3^2}$, and $\sqrt{4^2+4^2}$. The maximum distance between two radii thus is $\Delta a_{max} = 0.28$ so that the resolution is $\Delta a_c/a \approx 5/0.28$. To match this in a 1D model, one would need 18 grid points rather than five. Since we need to cover a (square) area of $(2a_c)^2$ in 2D, we thus have a computational overhead of a little more than a factor of 4 compared to 1D. However, the disadvantage of large 1D systems is that the number of iterations to find solutions can be much larger than in 2D. Depending on the nature of the solver, the number of iterations scales as a power law with linear system size. In the given case, where the effective stiffness scales proportional to wave vector q, one would expect a slowing down with $\sqrt{q}$, at least in simple gradient-based minimization such as steepest descent or molecular-dynamics. For this reason, no efforts were made to reduce the dimensionality, although this would have been legitimate for the given problem.

Positive work of adhesion

This section analyzes how the employed models reproduce established results for adhesive single-asperity contacts in the limits of large and small Tabor coefficient. This includes an asymptotic analysis of Maugis' solution of the Dugdale model, which in turn leads to modifications of the equations proposed by Carpick, Ogletree, and Salmeron [1]. The cross-over from JKR to DMT is investigated as well, in particular at zero load and near pull-off, allowing one to identify the model for the surface interaction that is most appropriate for the simulation of (adhesive) multi-asperity contacts.

Zero external load

An external load of $F_N = 0$ is addressed first. The motivation for studying this special case is that one can analyze relatively easily at what Tabor coefficients the DMT and JKR limits start to predict reasonably accurate values for the contact radii and displacements in our various models.

We start our analysis with the pressure distribution of the exponential model, which is depicted in Figure 5 for $\mu_T = 1/4$ and $\mu_T = 4$. It behaves very similar to the MD model, which shall not be shown explicitly. As to be expected, the adhesive load is spread out for $\mu_T = 1/4$ to radii clearly exceeding a_c (all the more as each radius r contributes with a weight proportional to r), while it is rather localized near $r = a_c$ for $\mu_T = 4$. It therefore seems legitimate to call the (net) pressure profile for $\mu_T = 1/4$ DMT-like and JKR-like for $\mu_T = 4$.

The adhesive pressure is calculated from the functional derivative $p_{adh}(x,y) = -\delta V_{fr}/\delta g(x,y)$, where V_{fr} is defined in Equation 5. This can be evaluated to yield

$$p_{adh}(r) = \frac{-\Delta\gamma}{z_0}\exp\{-g(r)/z_0\}, \qquad (31)$$

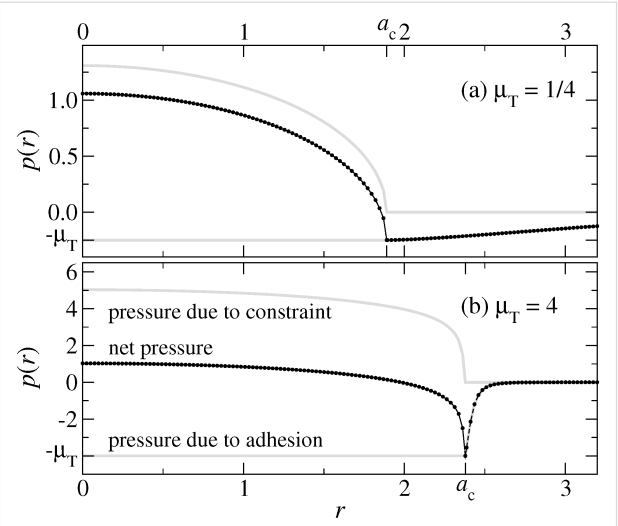

Figure 5: Interfacial pressure on a free, linearly-elastic half space resting at zero external load on a rigid, adhering, parabolic substrate for (a) $\mu_T = 1/4$ and (b) $\mu_T = 4$ in case of the exponential model. In each case, the upper and lower grey lines indicate, respectively, the pressure due to the constraint and that due to adhesion. Contact radii are indicated by a_c. The net pressure is shown by a black line as well as by small circles representing the actual grid points. Units are chosen according to Equation 23–Equation 26.

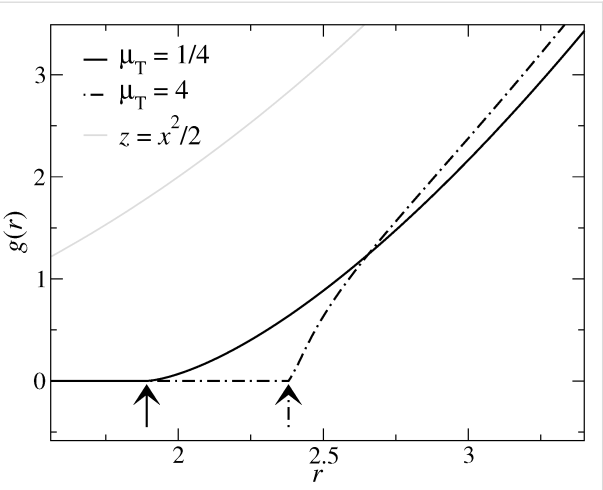

Figure 6: Gap between a rigid, adhesive, parabolic tip and a linearly-elastic half space for two different Tabor coefficients $\mu_T = 1/4$ (solid black line) and $\mu_T = 4$ (broken black line). The gap $z = x^2/2$ of an undeformed half-space is shown in grey for comparison. Arrows indicate contact radii. Units are chosen according to Equation 23–Equation 26.

which becomes $p_{adh}(r < a_c) = -\Delta\gamma/z_0$ within the true contact area. Using Equation 19, one obtains

$$p_{\text{adh}}\left(r<a_{\text{c}}\right)=-\left(\frac{\mu_{\text{T}}^3\Delta\gamma E^2}{R}\right)^{1/3} \quad \text{in physical units} \qquad (32)$$
$$=-\mu_{\text{T}} \quad \text{in our reduced units.}$$

Stress or pressure originating from the constraint $g(x,y) \geq 0$ is computed from the elastic Green's functions.

The well-known qualitative difference for the contact geometry of systems with large ($\mu_T = 4$) and small ($\mu_T = 1/4$) Tabor coefficient is borne out in the radial dependence of the gap $g(r)$. Specifically, Figure 6 reveals that a small Tabor coefficient makes $g(r)$ have a positive curvature at $r \geq a_c$, as in the DMT solution, while it has a negative curvature at $r \geq a_c$, indicative of an adhesive neck, for large μ_T. Figure 6 also shows that the displacement (defined by the difference between the actual gap and the gap in an undeformed contact at $r >> 1$) is smaller for $\mu_T = 4$ than for $\mu_T = 1/4$, although the contact radius is larger for $\mu_T = 4$ than for $\mu_T = 1/4$.

The Gauss model behaves qualitatively different from the exponential model. First, there are no adhesive forces within the contact, but only outside of it, as shown in Figure 7. Second, at $r = a_c$, the total pressure disappears in the Gauss model, while it remains finite in the exponential model. Third, the pressure due to the constraint has finite slope at $r = a_c^-$ in the Gauss model, while the slope diverges in the exponential model (not shown explicitly). All these differences arise because the derivative of $v_{fr}(g/z_0)$ remains finite (i.e., with positive sign) in the exponential model when the gap closes, while $v'_{fr}(g/z_0)$ is zero in the Gauss model.

Another consequence of $p_{adh}(g/z_0)$ having zero slope in the limit of $g \to 0^+$ is that the gap in the Gauss model closes continuously rather than with a discontinuity in its first derivative. This is shown in Figure 8, from where it becomes clear that it is

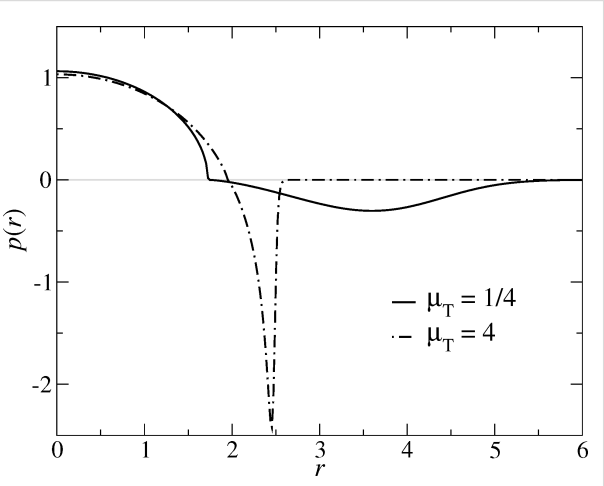

Figure 7: Pressure $p(r)$ in the Gauss model at zero load for two different Tabor coefficients as a function of the in-plane distance r from the center of the contact. The contributions due to the constraint are positive, i.e., above the grey line, while the adhesive forces are negative.

difficult to define good measures for the contact radius. In a linear representation (at low resolution), it seems as if the contact closes with the typical adhesive neck, i.e., in part (a) of Figure 8 the gap appears to close at $r \approx 2.415$. There, the slope of $g(r)$ takes its maximum value, in a very similar fashion as in the JKR limit, or for the exponential model for the same value of $\mu_T = 16$. However, when increasing the magnification, one can see that the contact closes only at $r \approx 1.97$. Unfortunately, the radii where the gap closes to zero, and where $g(r)$ has its maximum do not approach each other quickly when μ_T is increased. Instead, the value of g in the cross-over region in Figure 8b moves to smaller values as μ_T increases. Similar behavior is seen in the VDW model, which is not shown here explicitly.

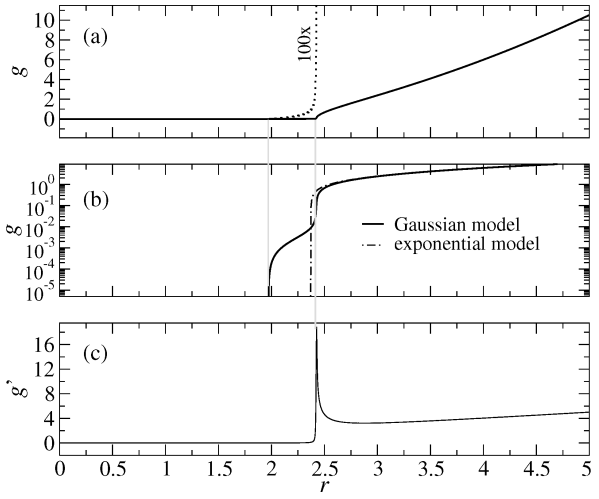

Figure 8: Gap $g(r)$ in linear (a) and logarithmic (b) representation as well as (c) first derivative $g'(r)$ for $\mu_T = 16$ in the Gauss model (straight lines). A higher resolution representation of the gap is given in (a) with a dotted line. The exponential model is shown for comparison in (b). The two thin grey lines are drawn where the gap becomes zero (left line) and where the slope of $g(r)$ takes its maximum value.

Zero-load contact radii for different potentials are depicted in Figure 9 as function of the Tabor coefficient. In the exponential model, the contact radius approaches DMT and JKR limits in a very similar fashion as in the MD model. In a later section on the asymptotic analysis, I find that the MD corrections to the JKR limit are of order $1/\mu_T^2$ for large Tabor coefficients while those to the DMT limit are of order μ_T for small Tabor coefficients. The same scaling of the leading-order corrections is apparently borne out in the exponential model.

Models in which $v_{fr}(g/z_0)$ has zero slope in the origin behave qualitatively different from the MD or the exponential model. They approach the DMT limit for the contact radius fairly

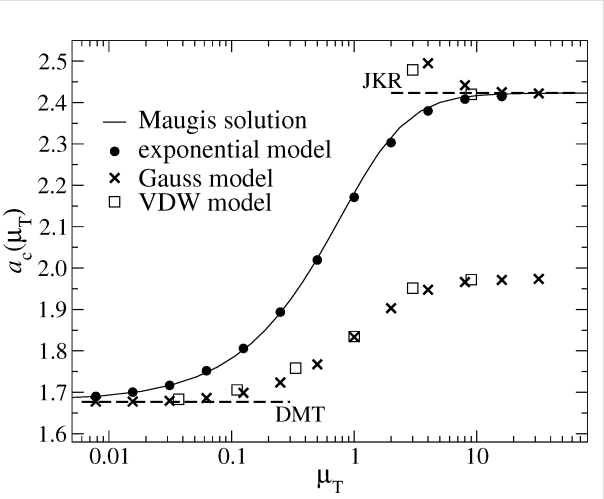

Figure 9: Contact radius a_c at zero external load as a function of the Tabor coefficient μ_T for different model interactions: exponential (full circles), Maugis Dugdale (straight lines), Gauss (crosses), and VDW (open squares). The upper and lower broken line denote the DMT and the JKR limits, respectively. In the Gauss and VDW models, two different definitions are used for a_c: The upper symbols refer to the position where $g'(r)$ reaches a local maximum, while the lower symbols indicate the points of first gap closure ($g = 0$).

quickly, i.e., roughly with $\mu_T^{3/2}$. However, convergence to the JKR limit is poor. The latter can be improved by defining the contact line to be located where $g'(r)$ takes its maximum value. Unfortunately, this definition cannot be universally applied, i.e., only when μ_T is sufficiently large to allow for an adhesive neck to be formed, see also Figure 8. Moreover, in the context of randomly rough surfaces with complicated contact geometries, this last definition of contact would not be practicable.

Unlike the contact radius, the normal displacement d does not suffer from any difficulties to be properly defined. In principle, this could enable one to ascertain $v_{fr}(g)$ from displacement measurements without much ambiguity. However, Figure 10 reveals that the functional form of $d(\mu_T)$ is relatively insensitive to the details of the finite-range interaction, at least, as long as we allow for a redefinition of the Tabor coefficient, such that all curves superimpose at the distance half way between the JKR and the DMT limit. This is in agreement with a work by Tvergaard and Hutchinson [18] who found that $\Delta\gamma$ and the peak stress (which one may losely associate with $\Delta\gamma/z_0$) are the basic parameters for mode I fracture.

Before proceeding to the case of finite load, I wish to comment on the relatively large numerical (GFMD) uncertainties for the displacement at large Tabor coefficients. They stem predominantly from the difficulty to apply the finite-size extrapolation formula, Equation 30, to gaps having adhesive necks. This problem would not be present in large-scale simulations of

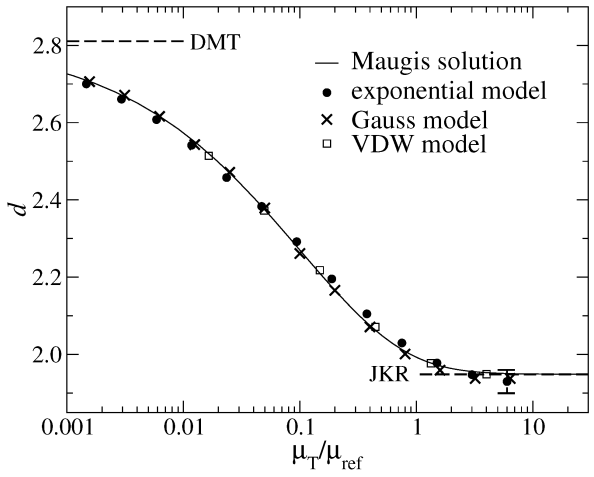

Figure 10: Normal displacement d at zero external load as a function of the Tabor coefficient μ_T for different model interactions: exponential (full circles), Maugis Dugdale (straight lines), Gauss (crosses), and VDW (open squares). The Tabor coefficient was normalized so that all curves superimpose at the "half-way" distance $d = (d_{JKR} + d_{DMT})/2$. The upper and lower broken line denote the DMT and the JKR limits, respectively. Numerical uncertainties arise in the limit of large Tabor coefficients, as indicated by the error bar.

multi-asperity interfaces, because system sizes would automatically be much larger than local contact radii. One may conclude that the use of the exponential model for the study of adhesive multi-asperity contacts appears to be appropriate. The MD model could be used as well, in principle, however, it might induce undesired numerical instabilities due to the discontinuity of $v'(g/z_0)$ at $g = z_0$. The Gauss model can only be taken when the property of interest is related to the gap but not for the calculation of contact area. If one wanted to simulate van der Waals attraction at large μ_T, one might want to replace the VDW model in Equation 12 with $1/(1 + g/z_0)^2$. This dependence makes it possible to determine the contact area meaningfully in the realm of continuum mechanics while using reasonable approximations for van der Waals interactions at large distance.

Finite external load

In most experiments, the Tabor coefficient is kept constant and the normal load is changed. As a result, one obtains the normal displacement $d(F_N)$ as a function of the normal load F_N. In some cases, i.e., for sufficiently large contact radii, an estimate of the contact radius, $a_c(F_N)$, can be obtained as well. One might be tempted to believe that knowing such curves allows one to deduce the surface forces. Here, I want to investigate to what degree such an inversion is possible by studying the sensitivity of the functions $d(F_N)$ and $a_c(F_N)$ to the functional form of the surface interactions. Figure 11 shows the contact radius as a function of the normal load. One can see that the exponential model and the MD model agree very closely, that is, curves almost superimpose for a given Tabor coefficient. This makes it essentially impossible to discriminate between these two forms of interaction experimentally. Likewise, the Gauss and VDW models also coincide for the same Tabor coefficient despite their significant differences at large gaps. Interestingly, the $\mu_T = 1$ curve for VDW and Gauss (both having finite slope potentials at $g = 0$) is akin of the $\mu_T = 1/4$ curves for the MD and the exponential model (both having zero-slope potentials at $g = 0$). This confirms the trend reflected in Figure 9: Surface potentials with zero slope at $g = 0$ make the results move toward the DMT limit.

In contrast to the $a_c(F_N)$ dependence, the normal displacement curve $d(F_N)$ predominantly depends on the Tabor coefficient. Now, all $\mu_T = 1$ curves resemble each other closely, independent of the slope of the surface potential at zero gap. As for the normal displacement, all curves are reasonably close to the JKR limit. Even the $\mu_T = 1/4$ curve lies closer to the JKR than to the DMT line. This is consistent with the results shown in Figure 10, which show that the DMT limit for $d(F_N)$ is only reached at extremely small Tabor coefficients. Figure 12 reveals that it is possible to adjust the free parameters of the MD model to fit $d(F_N)$ curves for a broad variety of surface interactions. However, one should abstain from deducing contact areas based on such fits, as this can result in non-negligible errors. For example, if we only knew the contact area from Maugis' solution, we would be ill-advised to conclude from Figure 12 that the contact area for the $\mu_T = 1$ Gauss model should lie roughly half way between those of the $\mu_T = 1$ and $\mu_T = 4$.

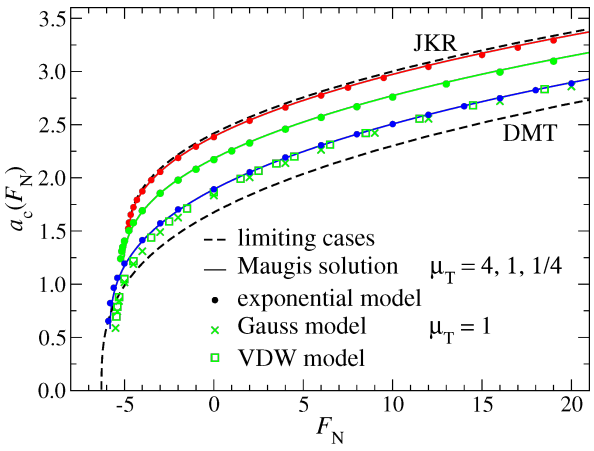

Figure 11: Contact radius a_c as a function of load F_N for the exponential and the MD model using different Tabor coefficients, ranging from $\mu_T \to \infty$ (JKR, top) to $\mu_T = 0$ (DMT, bottom). For the Gauss and VDW models, only $\mu_T = 1$ is shown. Their $a_c(F_N)$ curve is similar to that of the Maugis and the exponential model for $\mu_T = 1/4$. Color coding: $\mu_T = 4$ (red), $\mu_T = 1$ (green), and $\mu_T = 1/4$ (blue).

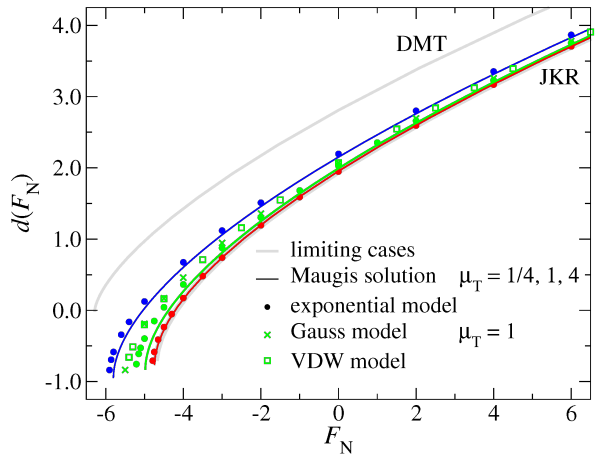

Figure 12: Normal displacement d as a function of load F_L for the exponential and the MD model using different Tabor coefficients, ranging from $\mu_T = 0$ (DMT, top) to $\mu_T \to \infty$ (JKR, bottom). For the Gauss and the exponential model, data is only shown for $\mu_T = 1$. Color coding: $\mu_T = 4$ (red), $\mu_T = 1$ (green), and $\mu_T = 1/4$ (blue).

Comparison to other models and asymptotic analysis

Maugis proposed an analytical solution for the relation between contact radius a_c and normal load F_N in the Dugdale model. It requires the elimination of an auxiliary variable, m, through the self-consistent solution of two coupled non-linear equations. Once a_c and m are found, the displacement d can be readily calculated as well. Using tildes to indicate variables in Maugis' unit system, the relevant equations read:

$$1 = \frac{\tilde{\mu}_T \tilde{a}^2}{2} f(m) + \frac{4\tilde{\mu}_T^2 \tilde{a}}{3} g(m) \tag{33}$$

$$\tilde{F}_N = \tilde{a}^3 - \tilde{\mu}_T \tilde{a}^2 h(m) \tag{34}$$

$$\tilde{d} = \tilde{a}^2 - \tilde{a}\tilde{\mu}_T j(m), \tag{35}$$

where the functions $f(m)$, $g(m)$, $h(m)$, and $j(m)$ are defined as

$$f(m) = \sqrt{m^2 - 1} + \left(m^2 - 2\right)\operatorname{acos}(1/m) \tag{36}$$

$$\approx \begin{cases} \frac{4}{3}\left\{2(m-1)\right\}^{3/2} & \text{for } m \to 1 \\ \frac{\pi}{2}\left(m^2 - 1\right) & \text{for } m \to \infty \end{cases}, \tag{37}$$

$$g(m) = \sqrt{m^2 - 1}\ \operatorname{acos}(1/m) - m + 1 \tag{38}$$

$$\approx \begin{cases} m - 1 & \text{for } m \to 1 \\ \left(\frac{\pi}{2} - 1\right) m & \text{for } m \to \infty \end{cases}, \tag{39}$$

$$h(m) = \sqrt{m^2 - 1} + m^2 \operatorname{acos}(1/m) \tag{40}$$

$$\approx \begin{cases} \left\{8(m-1)\right\}^{1/2} & \text{for } m \to 1 \\ \frac{\pi}{2} m^2 & \text{for } m \to \infty \end{cases}, \tag{41}$$

and

$$j(m) = \sqrt{m^2 - 1}. \tag{42}$$

In each but one (straightforward) case, behavior of the functions for m approaching unity or infinity has been included. They become useful in the limit of large and small Tabor coefficients, respectively.

Conversion back to our unit system can be done using:

$$\mu_T = \left\{2\pi/9\right\}^{1/3} \tilde{\mu}_T \tag{43}$$

$$a = (3\pi/4)^{1/3}\, \tilde{a} \tag{44}$$

$$d = (3\pi/4)^{2/3}\, \tilde{d} \tag{45}$$

$$F_N = \pi \tilde{F}_N. \tag{46}$$

To overcome the need of having to find the self-consistent solution to Maugis' equations, Carpick, Ogletree, and Salmeron (COS) [1] proposed a simple and thus elegant analytical formula for the $a_c(F_N)$ dependence

$$\frac{a_c(F_N, \mu_T)}{a_c(0, \mu_T)} = \left\{\frac{\alpha(\mu_T) + \sqrt{1 + F_N / F_p(\mu_T)}}{1 + \alpha(\mu_T)}\right\}^{2/3}. \tag{47}$$

Schwarz [2] later recognized that the COS description is exact – given proper parameterization – if the interaction between the

surfaces results from the superposition of an infinitesimally short-ranged and an infinitely long-ranged contribution. However, in the given context of one intermediate-range potential, I will treat the COS equation as a guessed approximation containing the correct functional form in the limits of large and small μ_T.

The primary COS equation (Equation 47) is designed such that the contact radius at zero load $a_c(0,\mu_T)$ as well as the pull-off force $F_p(\mu_T)$ can be reproduced exactly. However, approximations to their dependence on μ_T had been provided as well, because no closed-form expression are available. A free parameter remains, $\alpha(\mu_T)$, which can be used to minimize deviations from the exact solution. At large loads, one recovers the well-known $a_c \propto F_N^{1/3}$ scaling, however, not necessarily with the correct prefactor. Another property of the COS approximation is that it does not necessarily contain the correct value of the contact radius at pull-off. Thus, despite predicting the contact radius fairly well, the COS contact radius is not exact in the limit of very large and very small (i.e., pull-off) normal loads. These deficiencies can be improved when parameterizing the COS equation in a slightly different fashion, e.g.,

$$a_c^3\left(F_N,\mu_T\right)=\frac{3}{4}\left(F_N+F_0\left(\mu_T\right)+\alpha\left(\mu_T\right)\sqrt{F_N+F_p\left(\mu_T\right)}\right) \quad (48)$$

with

$$F_0\left(\mu_T\right)=F_p\left(\mu_T\right)+\frac{4}{3}a_c^3\left(0,\mu_T\right). \quad (49)$$

This set of equation ensures that a_c converges to the exact value when $F_N \to \infty$ and $F_N \to -F_p$. The parameter $\alpha(\mu_T)$ can then be adjusted to either yield the correct zero-load contact radius, or to minimize the deviation between approximation and the exact Maugis solution by some other mean. Note that the factors 3/4 in Equation 48 and 4/3 in Equation 49 have to be replaced by unity when working with Maugis' unit system.

I wish to note that including the correct asymptotics in the $a_c(F_N)$ expression does not necessarily improve the fits in the range from slightly above the pull-off force at negative loads to several times the absolute pull-off force. This is demonstrated in Figure 13. Moreover, convergence to the correct $a_c(F_N)$ dependence at large loads is rather slow even when using Equation 49.

It is also possible to constrain the COS relation for the contact radius such that it contains the correct pull-off force and contact radius as well the correct zero-load radius. In either case, relative errors are small, i.e., ≤1% even for $\mu_T \approx 1$, where one is relatively far away from both the DMT and the JKR limit.

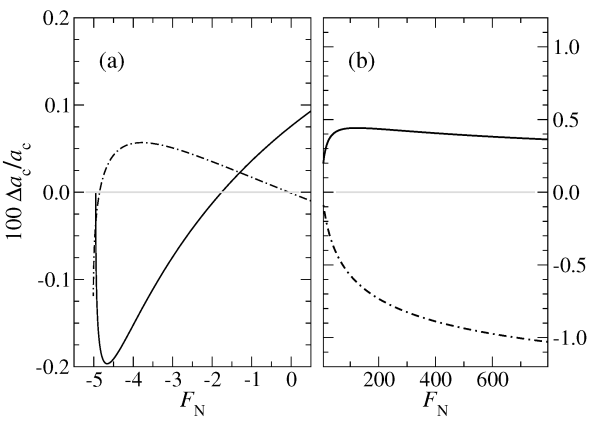

Figure 13: Relative errors in per cent for the contact radius a_c for $\mu_T = 1$ at (a) negative and (b) positive load. The full line indicates the error when using Equation 48, while the dot-dashed line is based on Equation 47. In both cases, the parameter $\alpha(\mu_T)$ was adjusted to minimize the deviation from Maugis solution in the domain $-F_p < F_N < 2F_p$.

Zero load: The asymptotic analysis is readily done for zero loads, because the variable *m* can be directly eliminated in that case. As a result, one obtains

$$\tilde{a}_c\left(F_N=0\right)=\begin{cases}6^{1/3}+O\left(\tilde{\mu}_T^{-2}\right) & \text{for } \tilde{\mu}_T \to \infty \\ 2^{1/3}+O\left(\tilde{\mu}_T\right) & \text{for } \tilde{\mu}_T \to 0\end{cases} \quad (50)$$

and

$$\tilde{d}\left(F_N=0\right)=\begin{cases}\left(4/3\right)^{1/3}+O\left(\tilde{\mu}_T^{-2}\right) & \text{for } \tilde{\mu}_T \to \infty \\ 2^{2/3}+O\left(\tilde{\mu}_T^{1/2}\right) & \text{for } \tilde{\mu}_T \to 0\end{cases}. \quad (51)$$

From the last two equations, one can see – as in Figure 9 and Figure 10 – that the JKR limit is quickly reached as the Tabor coefficient increases. However, convergence to the DMT limit with decreasing $\tilde{\mu}_T$ is rather slow. It is particularly slow for the normal displacement. E.g., to have a maximum error in $a_c(F_N = 0)$ and $d(F_N = 0)$ that is of order 1% with respect to a desired limit, it is sufficient to work with $\tilde{\mu}_T \approx 10$ for JKR, but one needs $\tilde{\mu}_T \approx 10^{-4}$ to approach the DMT limit with similar accuracy. The latter is not problematic for the simulation of multi-asperity contacts, as the system is large by default. However, for single-asperity contacts, large deviations from $\mu_T = 1$ (on a logarithmic scale) are difficult to handle in single-

asperity contact simulations for reasons discussed in the numerical-analysis section.

Knowing the asymptotic behavior of $\tilde{a}_0(\tilde{\mu}_T) = \tilde{a}(\tilde{F}_N = 0, \tilde{\mu}_T)$ and $\tilde{d}_0(\tilde{\mu}_T) = \tilde{d}(\tilde{F}_N = 0, \tilde{\mu}_T)$ with respect to $\tilde{\mu}_T$ allows one to incorporate it in empirical equations for these two quantities. The following equations are found to achieve this and to provide excellent approximations to Maugis' solutions:

$$\tilde{a}_0(\tilde{\mu}_T) \approx \frac{a_{DMT}/\tilde{\mu}_T^2 + c_1/\tilde{\mu}_T + c_2 + a_{JKR}c_3\tilde{\mu}_T^2}{1/\tilde{\mu}_T^2 + c_4 + c_3\tilde{\mu}_T^2} \quad (52)$$

$$\tilde{d}_0(\tilde{\mu}_T) \approx \frac{\left(d_{DMT}/\sqrt{\tilde{\mu}_T} + c_5\right)/\tilde{\mu}_T^{1/3} + c_7\left(c_6 + d_{JKR}\tilde{\mu}_T^2\right)}{\tilde{\mu}_T^{-5/6} + c_7\tilde{\mu}_T^2} \quad (53)$$

Two coefficients in each of the last two equations (c_1, c_2 and c_5, c_6) can be constrained to reproduce the correct asymptotics (and thus be obtained analytically). Two fit parameters remain for contact radius and one for the displacement. The relative errors from the pertinent fits are shown in Figure 14. Compared to an already quite accurate empirical relation proposed by Carpick et al. for $\tilde{a}_0(\tilde{\mu}_T)$, see Eq. (12b) in [1], the new Equation 52 and Equation 53 contain the correct asymptotics and reduces the maximum relative error from 1.5% to 0.3%. The data shown in Figure 14 were obtained with the following numerical values: $c_1 = 4/5$, $c_2 = -1.285$, $c_3 = 4/5$, $c_4 = -0.435$, $c_5 = -3/2$, $c_6 = 0.1845$, and $c_7 = 6.71$.

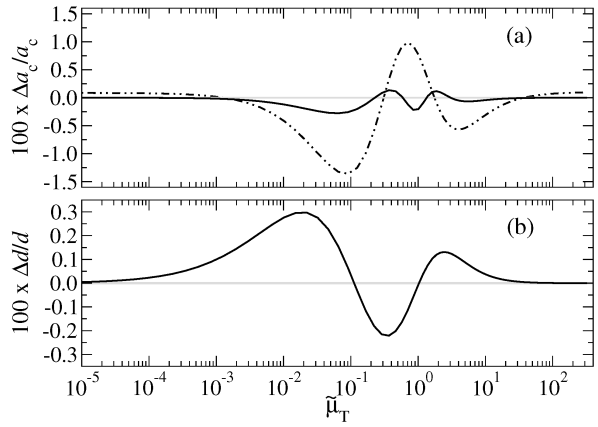

Figure 14: Relative errors in per cent for (a) contact radius and (b) normal displacement at zero normal load. Full lines refer to a fit based on Equation 52 and Equation 53 containing the correct asymptotic limits. The dotted line reflects an empirical fit based on the COS equations.

Asymptotic behavior near pull off: The structure of the COS approximation, Equation 47, and its modified form, Equation 48, indicates that the critical behavior near pull off satisfies $\tilde{a}_c - \tilde{a}_p \propto \left(\tilde{F}_N + \tilde{F}_p\right)^\kappa$, where κ must be either κ = 1/3 as in the DMT limit, or κ = 1/2 as in the JKR limit. However, nothing in the self-consistent solution of Maugis indicates that the exponent κ changes discontinuously from one value to the next as the Tabor coefficient reaches or passes through a critical value. In fact, representing the data from Figure 11 in terms of $\Delta a_c(\Delta F_N)$, as done in Figure 15, shows that κ changes continuously from 1/3 to 1/2 as μ_T increases from 0 to infinity.

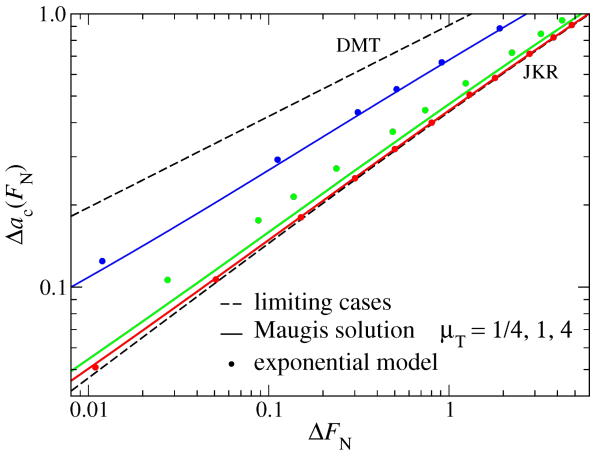

Figure 15: Excess contact radius $\Delta a_c = a_c - a_p$ as a function of the excess load $\Delta F_N = F_N + F_p$ for different values of the Tabor coefficient ranging from $\mu_T = 0$ (DMT, top) to $\mu_T \to \infty$ (JKR, bottom). Here a_c and a_p denote the contact radius at an arbitrary load F_N and the pull-off load F_p, respectively. Deviations between the Maugis solution and the exponential model are particularly obvious for the $\mu_T = 1$ data set. Color coding: $\mu_T = 4$ (red), $\mu_T = 1$ (green), and $\mu_T = 1/4$ (blue).

An analysis for the normal displacement, similar to the one presented in Figure 15 but not shown explicitly here, exhibits a similar trend. The exponent describing $\Delta d = d - d_p$ as a function of $\Delta F_N = F_N + F_p$ crosses over continuously from the DMT to the JKR limit as μ_T increases. However, there is not a one-to-one relation between μ_T and κ. In particular the data sets for $\mu_T = 1$ show relatively large differences between the exponent in the MD model (κ ≈ 0.469) and the exponential model (κ ≈ 0.435).

The insights obtained from Figure 15 can be used, in principle, to further modify the COS approximations, e.g., by replacing the square-root in Equation 48 by some other power or likewise by changing the square-root and the exponent 2/3 on the r.h.s. of Equation 47 in an appropriate fashion. When doing so, the modified version of Equation 48 does not only converge to the correct value at pull-off. It can also be parameterized to yield

the correct asymptotics near pull-off. This results in a further reduction of the mean or overall error by a little more than a factor of two with respect to those shown in Figure 13, however, at the expense of one additional fit variable. Since the main new aspect of this study is concerned with negative work of adhesion and, moreover, both original and modified COS equations are already quite accurate, a more detailed analysis of the adhesive single-asperity contact is not pursued in this work.

Negative work of adhesion

For repulsive contacts, $\Delta\gamma < 0$, there is obviously no finite contact radius at zero normal load $F_N = 0^+$. The repelled rigid tip simply "hovers" at (infinitely) large distance over an undeformed elastic manifold. This is why it is not possible in this case to conduct a zero-load analysis similar to that presented for adhesive contacts. Since Maugis' solution has not yet been extended to repulsive contacts, we are not in a position to compare our data to analytical solutions for negative $\Delta\gamma$. One of the consequences is that the asymptotic analysis must be based on GFMD data, except for $\mu_T \to 0$, for which normal forces couple predominantly to long-wavelength modes so that the Hertz-plus-offset approximation (DMT) should be accurate. Given the close similarity between the exponential and the Maugis–Dugdale model as well as that between the Gauss and the VDW model seen in the last section, the attention is restricted to one potential in each class, i.e., the exponential and the Gauss model.

We start our analysis with the contact radius dependence on load. In analogy to the context of wetting fluids, one may call the force at which a finite value of a_c becomes unstable upon lowering the load the spontaneous wetting force F_{sw}. The force above which a_c can no longer be zero is called the squeeze-out force F_{sq}. If the transition from contact to non-contact is continuous $F_{sw} = F_{sq}$, otherwise $F_{sw} < F_{sq}$. Results are shown in Figure 16.

As is the case for attractive interactions, the contact radius at small loads can be sensitive to both the Tabor coefficient and the choice of the potential. Specifically, the exponential model always shows a continuous transition from finite to zero contact radius (at least for the values of μ_T investigated here), while the Gauss model has either a continuous transition below a critical Tabor coefficient $\mu_T^* \leq 1$ or a discontinuous transition for $\mu_T > \mu_T^*$. The discontinuity of the contact radius for Gauss potentials and sufficiently large Tabor coefficients implies that two solutions may coexist, i.e., one where the two surfaces are separated and one where they touch. However, once F_N exceeds a second threshold force $F_{sq}(\mu_T)$, i.e., the squeeze-out force, only one solution survives, that is, the one with finite contact radius. This can be seen in analogy to adhesive contacts with

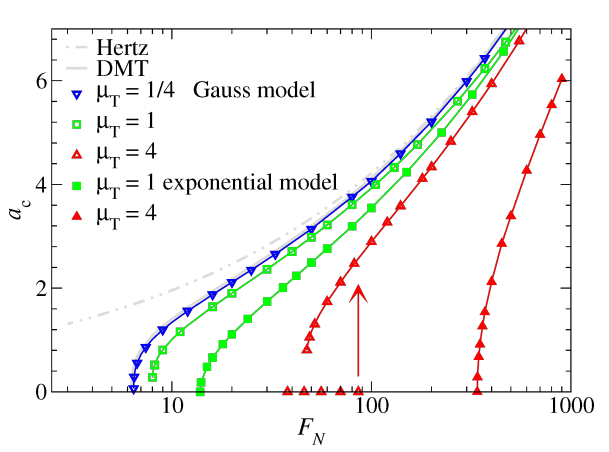

Figure 16: Contact radius a_c as a function of normal force F_N for the exponential (full symbols) and the Gauss (open symbols) model. Lines connect data points (not all shown explicitly). In the case of $\mu_T = 4$ (Gauss model), an arrow indicates where the $a_c = 0$ solution becomes unstable for increasing F_N. Color coding: $\mu_T = 4$ (red), $\mu_T = 1$ (green), and $\mu_T = 1/4$ (blue).

$\mu_T > 0$, where two solutions coexist in a finite interval of forces $-F_p \leq F_N \leq 0$.

As for the $a_c(F_N)$ relation near pull-off in the case of positive work of adhesion, the excess contact radius, $a_c - a_{sw}$, depends as a power law on the excess force, $F_N - F_{sw}$, for $F_N \geq F_{sw}$:

$$a_c - a_{sw} \propto \left(F_N - F_{SW}\right)^{\kappa}. \tag{54}$$

Fits to the $a_c(F_N)$ relation are shown exemplarily for two values of μ_T in Figure 17. Details about the fits to the presented as well

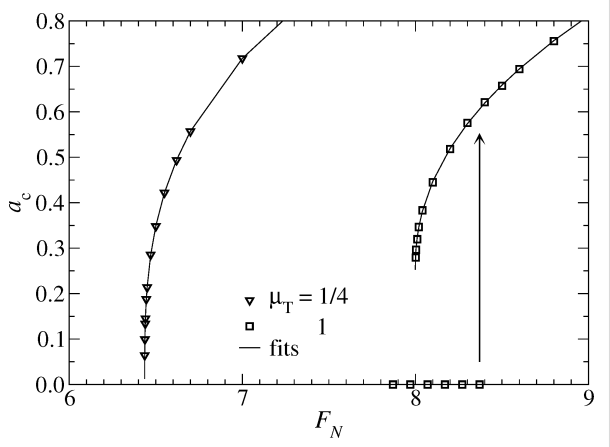

Figure 17: Contact radius a_c as a function of normal force F_N in the vicinity of the spontaneous wetting force F_{sw}. Symbols reflect numerical results while lines are fits according to Equation 54. They terminate at $a_c(F_{sw})$. In the case of $\mu_T = 1$, an arrow indicates where the $a_c = 0$ solution becomes unstable with increasing F_N.

as additional data are summarized in Table 1. As for attractive contacts, it is found that κ changes continuously from $\kappa(\mu_T \to \infty) = 1/2$ to $\kappa(\mu_T \to 0) = 1/3$. For small μ_T , Hertz-plus-offset behavior is reached as evidenced by the observation that c and F_{sw} approach $(3/4)^{1/3}$ and 2π, respectively. However, F_{sw} as well as F_{sq} quickly increase with μ_T for $\mu_T \geq 1$. This latter behavior is different from that of the pull-off F_p force for attractive surfaces, which only varies between 1.5π and 2π in the present unit system. Since the increase of both F_{sw} and F_{sq} is much faster in the exponential model than in the Gauss model, one can conclude that the exponential model converges more quickly to the continuum model than the Gauss model.

Table 1: Results of fits to the data shown in Figure 16. The last digit may not be significant.

model	μ_T	a_{sw}	F_{sw}	F_{sq}	c	κ
Gauss	1/16	0	6.30	6.30	0.91	0.333
	1/4	0.01	6.43	6.44	0.86	0.34
	1	0.25	8.00	8.40	0.56	0.46
	4	0.66	47.3	86	0.30	0.50
exponential	1/16	0	6.38	6.38	0.62	0.35
	1/4	0	6.89	6.89	0.68	0.44
	1	0	13.85	13.85	0.46	0.48
	4	0	339	339	0.28	0.49

As in the case of adhesive interactions, the normal displacement seems less sensitive to both the choice of the potential and the Tabor coefficient than the contact area, unless normal loads are very small, i.e., at loads similar in magnitude or smaller than the squeeze-out load for $\mu_T = 1$. This is demonstrated in Figure 18. It reveals that information on the (effective) near-range surface interactions at small separation are difficult to obtain from experimentally measured load-displacement curves.

I conclude this section with an analysis of the gap profile for repulsive contacts. At large loads, different Tabor parameters and functional forms for finite-range repulsion yield gap profiles that are indistinguishable at small magnification, see Figure 19a. Differences become nevertheless significant at high resolution near the center of the contact. Particularly remarkable is the data set for the Gauss model with $\mu_T = 4$ and its bistability revealed in Figure 19b. For an increasing force, no contact has formed at $F_N = 7.5$. However, when reaching $F_N = 7.5$ from above, contact is formed for radii $r < a_c \approx 1.73$. In the latter case, the gap then quickly increases within $\Delta r \approx 0.1$ to an almost constant value of order $1/\mu_T$ for $r \geq a_c$, as if one had a single confined layer of liquid. For radii $r > a_c^{macro}$, the gap assumes the "macroscopic" behavior. Here, $a_c^{macro} \approx 4$ is the contact radius that one would ascertain from the analysis of

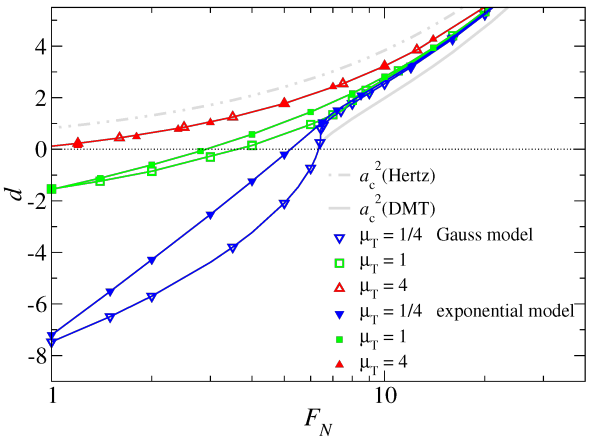

Figure 18: Displacement d as a function of normal force F_N in the vicinity of the spontaneous wetting force F_{sw}. Symbols reflect numerical results. The lines, which connect many data points not explicitly shown, are drawn to guide the eye. The two thick grey lines reflect the square of the contact radius in the Hertz and DMT approximation, respectively. Color coding: $\mu_T = 4$ (red), $\mu_T = 1$ (green), and $\mu_T = 1/4$ (blue).

the gap with low resolution, e.g., via graphical inspection of Figure 19a.

At small loads, the sensitivity of the gap profile on the details of the model become even more apparent. This result, which can be seen in Figure 19c, is expected, since the elasticity of the tip is no longer relevant. Instead, the force-displacement curve is

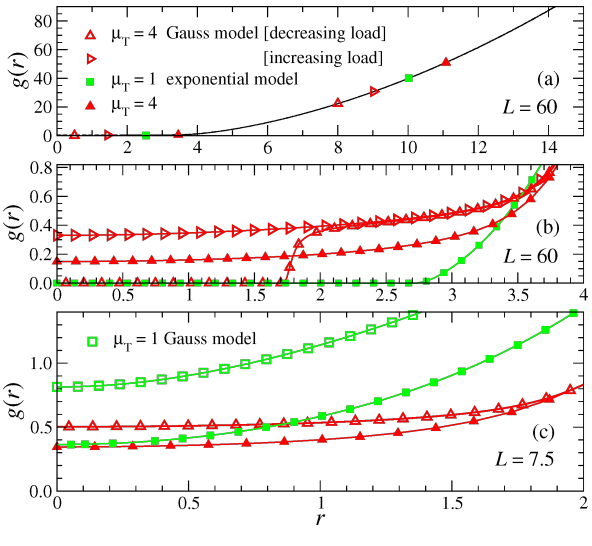

Figure 19: Gap $g(r)$ as a function of the lateral distance from the origin r for a large load $F_N = 60$ (a) and (b) as well as for an intermediate load $F_N = 7.5$ (c). In each case, surfaces repel each other. Graph (b) contains the same data as (a) but has higher resolution. Color coding: $\mu_T = 4$ (red) and $\mu_T = 1$ (green).

predominantly determined by the effective surface interactions, as shown clearly by the $\mu_T = 4$ data sets in Figure 18. They exhibit, to leading order, a $F_N \propto \exp(-d/\zeta)$ relation in the exponential model, and a $F_N \propto \exp(-d^2/\zeta^2)$ relation for the Gauss model, where ζ is inversely proportional to μ_T.

Conclusion

The principle new aspect of this work is the continuum-mechanics based analysis of single-asperity contacts with finite-range repulsion acting in addition to short-range hard-wall repulsion. The analysis is based on the concept of the Tabor coefficient and the repulsion is assumed to arise due to the presence of a strongly wetting fluid. As for attractive single-asperity contacts, it is found that the contact area or the displacement on the normal load depend, to a large degree, not only on the surface energy but also on the Tabor coefficient μ_T. Moreover, for μ_T exceeding a critical value, there may exist a range of loads in which two (meta)stable solutions coexist, i.e., one in which the surfaces touch and one in which a thin gap between the two surfaces remains. When the value for the load is increased above a threshold, the latter solution becomes unstable and the gap disappears. However, in order to obtain this kind of behavior, which is reminiscent of the squeeze-out of a wetting fluid, the finite-range interactions between the contacting surfaces have to be tailored correctly. Using a surface interaction v_{fr}, whose derivative increases monotonically as the gap g approaches zero, such as $v_{fr} \propto \exp(-g/z_0)$, only one stable solution exists for any given normal load. Conversely, when the distance–force dependence is multivalued, as is the case for a $v_{fr} \propto \exp\left(-g^2/2z_0^2\right)$ relation, squeeze-out and spontaneous wetting can be rationalized and thus be modeled in the realm of continuum mechanics – in terms of transitions between (meta)stable solutions. These transitions (similar to instabilities in the Prandtl model [26], in which a particle is dragged with a weak spring through a sinusoidal potential) can occur for solvated tips on surfaces, for example, if the effective tip–surface interactions has zero slope when the surfaces touch, as is the case for $v_{fr} \propto \exp\left(-g^2/2z_0^2\right)$. In reality, the far-field potential may even be oscillatory and evidenced by the squeeze-out of many subsequent layers. Such behavior has been recently observed and linked to the (damped) long-range oscillatory behavior of the density correlations in high-density liquids [15,19].

An interesting consequence of short-range repulsion is that the contact geometry can look similar to that of an adhesive neck. This is shown in Figure 19b for the ($\mu_T = 4$) Gauss model and decreasing load. To improve the visualization, a similar gap geometry is shown again in Figure 20 together with a profile of the finite-range repulsion.

A secondary aspect of this work is devoted to the analysis of how to best reach well-defined asymptotic behavior in numerical simulations of adhesive contact mechanics. It is found that the DMT limit is approached quickest when using attractive potentials whose first derivative disappears as the gap goes to zero, at least if the contact area is the variable of interest. However, these potentials approach the JKR limit only at a rate of $1/\mu_T$ for large μ_T and the contact area becomes difficult to define once $\mu_T \geq 1$. Thus, one is better off using potentials with finite slope in the small-gap limit. They converge in a well-defined fashion with $1/\mu_T^2$ to the JKR limit for large Tabor coefficients. This is supposedly the more relevant limit for adhesive surfaces with self-affine fractal roughness. For the modeling of repulsive surfaces, the situation is more complicated. Formally, the JKR limit is again reached more quickly with models that have finite slope at zero gap. However, these models do not allow one to model the hysteretic response of a confined fluid that results whenever the squeeze-out force exceeds the spontaneous wetting force.

A by-product of this work is a minor modification of the phenomenological description of single-asperity contact mechanics by Carpick, Ogletree, and Salmeron [1]. The COS equations can be parametrized to contain the correct asymptotic behavior for JKR and for DMT limits and also for the superpo-

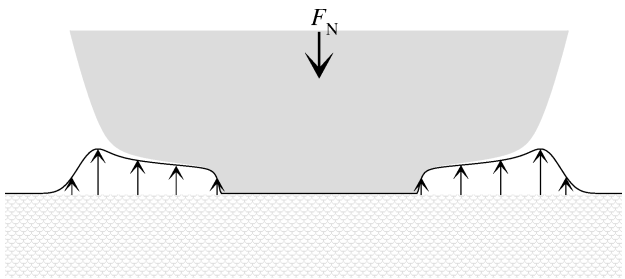

Figure 20: Contact geometry for a Gauss model with finite-range repulsion. Arrows indicate the direction of normal load F_N (thick arrow) and that of the finite-range repulsion (thin arrows) acting in addition to a hard-wall constraint. No adhesive forces between the surfaces are considered.

sition of extremely short- and long-range interfacial interactions, as shown by Schwarz [2]. However, they still have a few formal shortcomings for intermediate-range potentials. For example, the original interpolation of the contact-area-on-load dependence for finite Tabor coefficients recuperates neither Hertzian contact mechanics at large loads with correct prefactors nor the correct contact radii in either DMT or JKR limit at zero normal loads. In this work, I propose to enforce those limits exactly including the correct asymptotics for $a_c(\mu_T,F_N = 0)$ at $\mu_T = 0$ and $\mu_T \to \infty$. By doing so, the maximum error of the $a_c(F_N = 0,\mu_T)$ curve could be reduced from 1.2% to less than 0.3%. A shortcoming of both the original and the new, modified COS equations is that they both assume an asymptotic behavior near pull-off ($F_N \to -F_p$) according to $(a - a_p) \propto (F_p + F_N)^\kappa$, where the exponent takes the JKR value $\kappa = 2/3$ for any non-zero Tabor coefficient. The modified COS equations could thus be improved further if one incorporated the new finding that κ crosses over continuously from 2/3 (exact for JKR) to 1/2 (exact for DMT). However, this does not seem useful in practice. Extreme accuracies (5 digits and more for a_c and F_N) would be needed in measurements to deduce a_p and κ to within one or two digits. Such an accuracy is difficult to achieve both experimentally and numerically. Moreover, the surface energy is not very well defined at small scales, because its precise value depends crucially on roughness down to the atomic scale, see, e.g., [27]. Thus, from a practical point of view, both the original and the modified COS equations are quite reasonable, all the more because the geometry of real tips can deviate quite substantially from a parabola.

This work is concluded with an assessment of what values for μ_T one might expect in AFM or SFA experiments. To come up with a ballpark estimate, the following "typical values" shall be assumed: $\Delta\gamma = 40$ mN ($\Delta\gamma$ can, of course, be close to zero, but much higher, e.g., for two equally charged surfaces in the context of electrochemistry), $E = 5$ GPa (in between soft matter and ceramics), $z_0 = 10$ Å (size of an OMCTS or molten salt molecule), $R = 1$ μm (in between AFM and SFA, precise value not very important, as third root is taken). These numbers lead to $\mu_T = 0.4$, which is close to the interesting "cross-over" regime. Thus, real contacts may span a broad range of values for μ_T. Comparison between theory and experiment may be difficult, in particular because atomic-scale roughness (or even sub-atomic roughness arising from electron orbitals) leads to complicated slip-boundary conditions and slow kinetics. However, given a well-motivated form for the effective interaction between two flat surfaces, it may yet be possible to rationalize and to model, at least on a semi-quantitative level, the interactions of curved surfaces in the presence of a strongly wetting fluid within the presented Tabor-coefficient based framework. Particularly appealing systems may be found in tribo-electrochemical applications, where the surface interactions can be tailored in a quasi-continuous fashion.

Acknowledgements

MHM thanks Sissi de Beer for useful discussions and valuable literature hints. The author furthermore thanks Bo Persson for the request to add adhesion to Green's function molecular dynamics, which ultimately motivated this work.

References

1. Carpick, R. W.; Ogletree, D. F.; Salmeron, M. *J. Colloid Interface Sci.* **1999,** *211,* 395–400. doi:10.1006/jcis.1998.6027
2. Schwarz, U. D. *J. Colloid Interface Sci.* **2003,** *261,* 99–106. doi:10.1016/S0021-9797(03)00049-3
3. Grierson, D. S.; Flater, E. E.; Carpick, R. W. *J. Adhes. Sci. Technol.* **2005,** *19,* 291–311. doi:10.1163/1568561054352685
4. Hertz, G. *J. Reine Angew. Math.* **1881,** *92,* 156. doi:10.1515/crll.1882.92.156
5. Derjaguin, B. V.; Muller, V. M.; Toporov, Yu. P. *J. Colloid Interface Sci.* **1975,** *53,* 314–326. doi:10.1016/0021-9797(75)90018-1
6. Johnson, K. L.; Kendall, K.; Roberts, A. D. *Proc. R. Soc. London, Ser. A* **1971,** *324,* 301–313. doi:10.1098/rspa.1971.0141
7. Tabor, D. *J. Colloid Interface Sci.* **1977,** *58,* 2–13. doi:10.1016/0021-9797(77)90366-6
8. Muller, V. M.; Yushenko, V. S.; Derjaguin, B. V. *J. Colloid Interface Sci.* **1980,** *77,* 91–101. doi:10.1016/0021-9797(80)90419-1
9. Maugis, D. *J. Colloid Interface Sci.* **1992,** *150,* 243–269. doi:10.1016/0021-9797(92)90285-T
10. Barthel, E. *J. Phys. D: Appl. Phys.* **2008,** *41,* 163001. doi:10.1088/0022-3727/41/16/163001
11. Hughes, B. D.; White, L. R. *Q. J. Mech. Appl. Math.* **1979,** *32,* 445–471. doi:10.1093/qjmam/32.4.445
12. Vinogradova, O. I.; Feuillebois, F. *J. Colloid Interface Sci.* **2003,** *268,* 464–475. doi:10.1016/j.jcis.2003.09.002
13. Persson, B. N. J.; Tosatti, E. *J. Chem. Phys.* **2001,** *115,* 5597–5610. doi:10.1063/1.1398300
14. Müser, M. H. *Phys. Rev. Lett.* **2008,** *100,* 055504. doi:10.1103/PhysRevLett.100.055504
15. Fisher, M. E.; Wiodm, B. *J. Chem. Phys.* **1969,** *50,* 3756–3772. doi:10.1063/1.1671624
16. Chandra, N.; Li, H.; Shet, C.; Ghonem, H. *Int. J. Solids Struct.* **2002,** *39,* 2827–2855. doi:10.1016/S0020-7683(02)00149-X
17. Turon, A.; Dáviall, C.; Camanho, P.; Costa, J. *Eng. Fract. Mech.* **2007,** *74,* 1665–1682. doi:10.1016/j.engfracmech.2006.08.025
18. Tvergaard, V.; Hutchinson, J. W. *Int. J. Solids Struct.* **1996,** *33,* 3297–3308. doi:10.1016/0020-7683(95)00261-8
19. Hoth, J.; Hausen, F.; Müser, M. H.; Bennewitz, R. *J. Phys.: Condens. Matter* **2014**. Accepted.
20. Luan, B. Q.; Robbins, M. O. *Nature* **2005,** *435,* 929–932. doi:10.1038/nature03700
21. Mo, Y. F.; Turner, K. T.; Szlufarska, I. *Nature* **2009,** *457,* 1116–1119. doi:10.1038/nature07748
22. Shengfeng, C.; Robbins, M. O. *Tribol. Lett.* **2010,** *39,* 329–348. doi:10.1007/s11249-010-9682-5
23. Eder, S.; Vernes, A.; Vorlaufer, G.; Betz, G. *J. Phys.: Condens. Matter* **2011,** *23,* 175004. doi:10.1088/0953-8984/23/17/175004

24. Campañá, C.; Müser, M. H. *Phys. Rev. B* **2006,** *74,* 075420. doi:10.1103/PhysRevB.74.075420
25. Dapp, W. B.; Lücke, A.; Persson, B. N. J.; Müser, M. H. *Phys. Rev. Lett.* **2012,** *108,* 244301. doi:10.1103/PhysRevLett.108.244301
26. Prandtl, L. *Z. Angew. Math. Mech.* **1928,** *8,* 85–106. doi:10.1002/zamm.19280080202
27. Jacobs, T. D. B.; Ryan, K. E.; Keating, P. L.; Grierson, D. S.; Lefever, J. A.; Turner, K. T.; Harrison, J. A.; Carpick, R. W. *Tribol. Lett.* **2013,** *50,* 81–93. doi:10.1007/s11249-012-0097-3

License and Terms

Beilstein Journal of Nanotechnology

Applicability and costs of nanofiltration in combination with photocatalysis for the treatment of dye house effluents

Wolfgang M. Samhaber[1] and Minh Tan Nguyen[*2]

Full Research Paper

Open Access

Address:
[1]Institute of Process Engineering, Johannes Kepler University Linz, Welser Strasse 42, A-4060 Leonding, Austria and [2]Institute for R&D of Natural Products, Hanoi University of Science and Technology, 1 Dai Co Viet Road, Hanoi, Vietnam

Email:
Minh Tan Nguyen[*] - tan.nguyenminh@hust.edu.vn

* Corresponding author

Keywords:
dye industry effluent; environmental; membrane; nanofiltration; photocatalysis; UV

Beilstein J. Nanotechnol. **2014,** *5,* 476–484.
doi:10.3762/bjnano.5.55

Received: 30 September 2013
Accepted: 21 March 2014
Published: 15 April 2014

This article is part of the Thematic Series "Nanomanipulation and environmental nanotechnology".

Guest Editor: E. Gnecco

Abstract

Nanofiltration (NF) is a capable method for the separation of dyes, which can support and even improve the applicability of photocatalysis in effluent-treatment processes. The membrane process usually will need a special pre-treatment to avoid precipitation and fouling on the membrane surface. Conceptually NF can be applied in the pre-treatment prior to the catalytic reactor or in connection with the reactor to separate the liquid phase from the reaction system and to recycle finely suspended catalysts and/or organic compounds. When concerning such reaction systems on a bigger scale, cost figures will prove the usefulness of those concepts. Different applications of photocatalysis on the lab-scale have been published in recent years. Membrane technology is used almost in all those processes and an overview will be given of those recently published systems that have been reported to be potentially useful for a further scale-up. NF membranes are mostly used for the more sophisticated separation step of these processes and the additional costs of the NF treatment, without any associated equipments, will be described and illustrated. The total specific costs of industrial NF treatment processes in usefully adjusted and designed plants range from 1 to 6 US$/m^3 treated effluent. Combination concepts will have a good precondition for further development and upscaling, if the NF costs discussed here in detail will be, together with the costs of photocatalysis, economically acceptable.

Introduction

Textile processing comprises different operations such as pre-treatment, dyeing, washing of garments, printing and finishing and produces a large amount of polluted effluent. For processing one ton of textile, 230 to 270 m^3 of wastewater has to be treated prior to the release into the environment [1]. Conventional biological treatment plants are not effective in the

removal of colour dye effluents, because of the aromatic structure of the large dye molecules, which provides chemical stability and, thus, also a high resistance to biological degradation. Dyes are made to be stable to light, oxidizing agents, and aerobic digestion to fulfil the quality demands of textile products. Fundamental principles and applications of photocatalytic degradation of dyes in homogeneous or heterogeneous systems can be found in the literature. For example there is an extensive overview given from Mills and Le Hunte [2], a review by Chong et al. [3] about recent developments in photocatalytic water treatment technology, and a short description of fundamentals is given by Rauf and Salman Ashraf 2009 [4].

Results

Conventional concepts of effluent treatment and NF

In the conventional treatment of effluent of the textile industries separation methods like coagulation, flocculation, flotation or sedimentation are used. Process variants concerning the separation of dyes are numerous, but all of them require a final disposal, possibly with a prior on-site storage. The drawbacks of all chemical methods are an additional usage of chemicals, an increased sludge production and often the need to remove additional colour and chemical oxygen demand (COD). Unconventional membrane separation plants with NF filters, in combination with certain pre-treatment steps, are applied in some textile works, but those nanofiltration applications do not yet reflect the state of the art, and are not yet adopted as standard techniques in the dye industry [5]. However, the major drawback of applying membrane processes in wastewater treatment is membrane fouling. Therefore a proper pre-treatment of the feed of a nanofiltration separation is the most important measurement to obtain a successful technical application. Many reports are found in the literature, which deal with possible measures for the prevention of fouling in membrane filtration. One recent review focuses the coagulation in connection with nanofiltration has been published by Zahrim et al. [6]. Flocculation and the separation of flocculated materials can reduce COD and colour to a great extent and, in addition, decrease the fouling rate in a membrane process.

In Figure 1, a schematic overview of possible pre-treatment steps is displayed and it can be recognised that pre-treatment plays an important role but will also be costly when membranes are applied in the wastewater treatment. In the nanofiltration permeate, which constitutes the bigger part of the treated effluent, COD and colour are usually reduced to a great extent. If necessary, an additional NF step can be installed further down-stream as a post-treatment process.

Membrane filtration combined with photocatalysis

Photocatalysis is an advanced method for the degradation of dyes from textile effluent due to its ability to oxidize and to destruct dyes simultaneously while the conventional treatment methods either concentrate or transfer dyes to a solid phase [7-11]. Fundamentally, organic compounds are decomposed by means of reactive species such as hydroxyl radicals ($OH^{\bullet}$), which are generated by UV irradiation of photocatalysts in the reaction system. Commonly applied photocatalysts include TiO_2, ZnO, Fe_2O_3, CdS, GaP and ZnS. Among these, titanium dioxide (TiO_2) has attracted great interest in research and development because of its mechanical properties, chemical and thermal stability and resistance to chemical breakdown, which promote its application in photocatalytic water treatment [7,9,12,13]. Photocatalysts can be used in the form of suspended fine particles or immobilized on various supports. Obviously, photoreactors with a suspended catalysts (or slurry type) are considered to offer greater contacting surfaces between the photocatalysts and the pollutant molecules than reactors working with immobilized photocatalysts. Immobilized catalysts have a defined specific surface area, which is connected with the supporting surface. Photoreactors with suspended catalysts, however, require a separation of the catalyst from the treated effluent.

The combination of photocatalysis and membrane filtration is based on the fact that photocatalysts exhibit an oxidation potential and the membrane separation, especially with nanofiltration membranes, provides the selective separation of pollutants to be retained and removed. Different concepts have been described

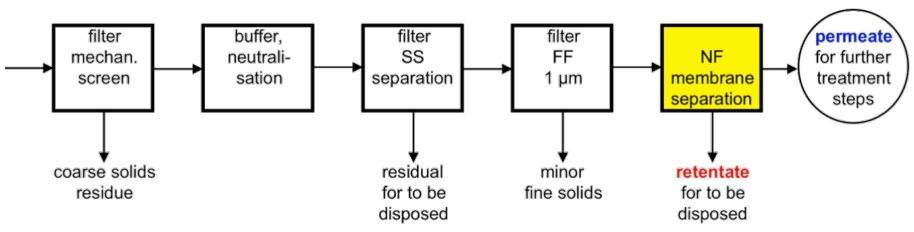

Figure 1: General pre-treatment steps prior to membrane separation.

in literature. The use of particulate catalysts, require a recirculation of the catalyst, and it is in addition necessary to uncouple the hydraulic residence time from the residence time of the organic compounds in the catalytic reactor system, which can be achieved by selective membrane separation [3,10,12,14-16]. Photocatalytic processes have been predominantly selected to be combined with pressure-driven membrane processes such as microfiltration (MF) [17], ultrafiltration (UF) [10,17,18], nanofiltration (NF) [5,10,19-21] and reverse osmosis (RO) [19]. Recently, the combination with membrane distillation (MD) [10,18] has also been proposed for the treatment of dye industry effluents.

Molinari et al. [21] studied the degradation of two commercial azo-dyes, namely Congo red ($C_{32}H_{22}N_6Na_2O_6S_2$) and patent blue ($C_{27}H_{31}N_2NaO_6S_2$), by using TiO_2 Degussa P25 as the photocatalyst in a lab-scale combined system with NF membranes NTR 7410 (Nitto Denko, Tokio) and have observed that it was possible to successfully treat concentrated solutions (500 mg/L) of both dyes by means of a continuous process with a suspended photocatalyst. Damodar et al. [17] have studied the coupling of a MF membrane separation with a photocatalytic laboratory slurry reactor for an advanced treatment of dye effluent and achieved high removal rates (82–100% colour removal, 45–93% TOC removal, and 50–85% COD removal) at optimal initial concentration of reactive black 5 (RB5) in a flat polytetrafluoroethylene (PTFE) MF membrane module submerged into the slurry photocatalytic reactor. Moreover, the submerge membrane concepts enabled long-term test runs. Grzechulska-Damszel et al. [10] investigated the removal of azo dyes (acid red 18, direct green 99 and acid yellow 36) from water in different combined systems: (a) photocatalysis with immobilized catalyst bed/NF and (b) photocatalysis in suspension/UF/MD. Berberidou [19] achieved a complete decolourization of a synthetic dye effluent containing reactive black 5 with a combined system of photocatalysis and RO/NF, as well as a more than 95% reduction of the initial organic content and salinity. Mozia [8] conducted experiments with two combined systems: photocatalysis–ultrafiltration and photocatalysis–membrane distillation for the degradation of acid red 18 in an aqueous solution. Both membrane processes could achieve a separation of TiO_2 from the solution. The MD process separated the model dye completely while the UF process only removed 77% of the dye after 5 h of the irradiation. Photocatalysis and membrane processes in combination can also be accomplished with various photocatalytic membrane reactors (PMRs), many of which have been described in the literature [3,16,17,21]. PMRs can generally be divided into two main groups: fixed-bed photoreactors and slurry batch photoreactors. Molinari et al. [22] compared different PMRs in terms of the position of UV irradiation. Irradiation can take place in the flat sheet membrane cell or in a separated recirculation loop. Different configurations were applied for both fixed-bed photoreactors and slurry batch photoreactors. The authors indicated that an advantage of the system with the suspended photocatalyst over the fixed one is to avoid the risk of a possible membrane oxidation by $OH^{\bullet}$ radical attack, because the photocatalytic reaction is effectively separated from the membrane filtration step.

NF concepts with photocatalysis

To combine a nanofiltration process with photocatalysis there are two basic concepts to consider. NF can be set on the up-stream side or on the down-stream side of the photocatalytic reactor. In Figure 2 the photocatalysis process is shown as the responsible step to achieve or fulfil the main process requirements. The NF step down-stream from the photocatalysis reactor operates for the recycling of catalysts and residual organic compounds and will achieve additional improvements in the quality of the treated effluent streams. The permeate of the NF step can optionally be fed to a reverse osmosis (RO) step in order to separate the salts from the relatively well purified NF permeate stream to produce water for re-use.

Zheng et al. [5] have investigated the colour removal and COD reduction in biologically treated dye effluent. With submerged NF hollow fibres, it was possible to remove 99.3% of colour and 91.5% of COD while maintaining a steady permeat flux of 5.15 $L/m^2 \cdot h$ with an applied trans-membrane pressure of 0.8 bar. Colour compounds of biologically pre-treated effluent could be separated by NF separation, which would enable the combination with a photocatalytic reactor, in which the reject stream could be treated in parallel. From this example, it can be concluded that these concepts require, on the one hand, a feed that is not too highly loaded and has a sufficient transparency for the photocatalytic reaction. On the other hand, the drain from the photocatalysis will possibly contain less fouling matter with the advantage that the NF can be operated with a significant reduction of membrane fouling. The challenge of this concept can further be seen in its highly efficient oxidation. The following NF acts almost solely as a polishing step and possibly for the recovery or recycling of the catalysts. A clear effluent stream with less complex constituents together with a high optical transmission is favourable for such a concept. Finally, it must be kept in mind that the further quality improvements through NF and RO will have to justify the costs of the additional membrane steps down-stream.

Another way of combining NF and photocatalysis is shown in Figure 3. In this schematic block diagram, the NF step is located on the up-stream side of the photocatalysis and therefore the NF is primarily responsible for the separation. In other

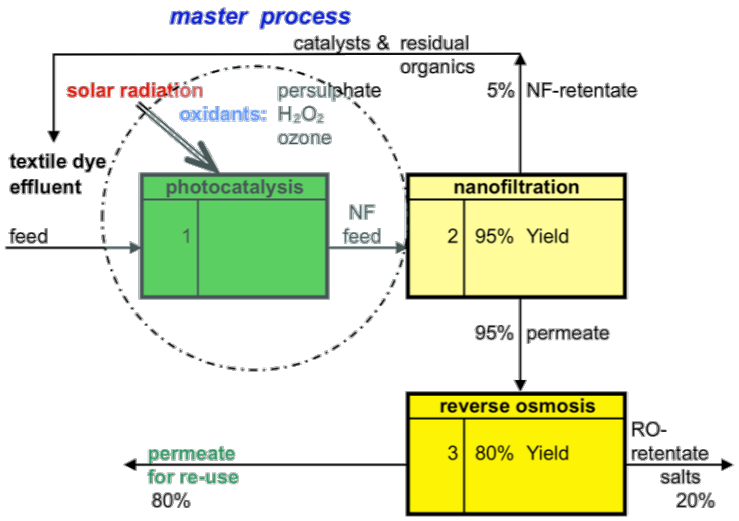

Figure 2: Photocatalysis as the master process responsible for the reduction of organic and fouling matter with a nanofiltration and RO-step for further removal of residual contaminants.

words, NF will be the master process and other processes downstream, such as the photocatalysis, are connected and/or adjusted with or to the NF. Here, photocatalysis acts more or less as a polishing step to reduce residual colour compounds, which are contained in the NF permeate. This concept is comparable with a general NF treatment concept at the source, and therefore, the feed has to be pre-treated in order to avoid membrane fouling as mentioned previously. Fouling of membranes is often a weakness of the membrane process and the development of a proper pre-treatment recipe is therefore a challenging task as described earlier.

The retained dyes and organic matter are separated and represent the concentrate or retentate stream, which have to be treated further and finally disposed according to local regulations. The permeate stream, which is already reduced in colour and in dissolved organic compounds, is post-treated in the photocatalysis, which can again be classified as a polishing step.

A more sophisticated concept is shown in Figure 4. A submerged UF membrane is used to keep the nano-sized catalyst particles within the UV-radiated reaction chamber. A

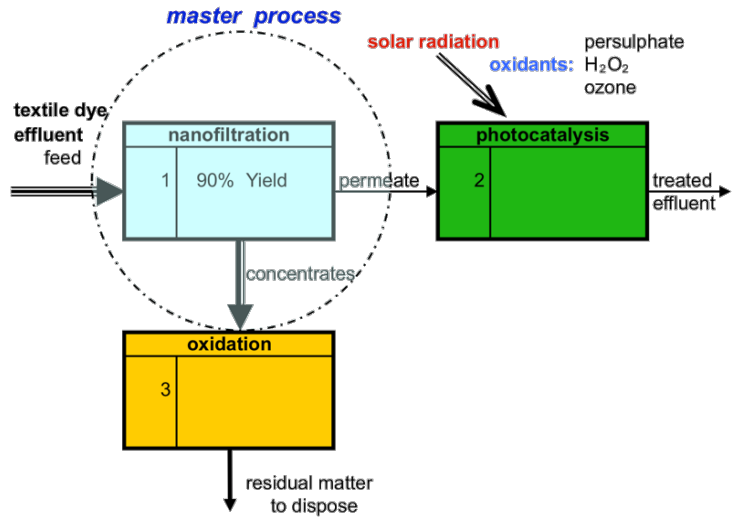

Figure 3: Nanofiltration as the master process responsible for the major reduction of colour and organic compounds, while photocatalysis acts as a polishing step.

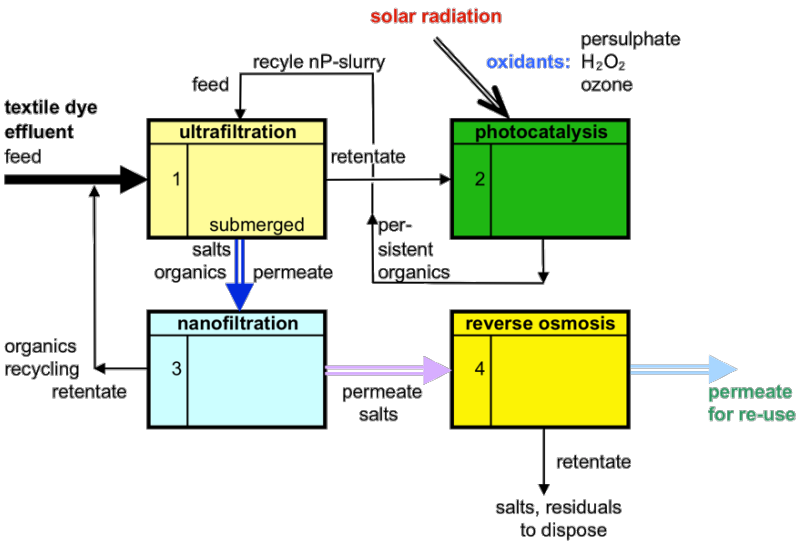

Figure 4: Photocatalysis combined with a submerged UF separation and a down-stream NF and RO treatment.

comparable system is described by Patsios et al. [23] for the continuous degradation of humic acids. In a heterogeneous catalysis with TiO_2 the successful removal of 5 to 10 mg/L humic acid from a synthetic effluent, without any reject stream, was demonstrated.

If effluent of the dye industry is processed, there will be organic colour and inorganic salts in the feed stream. In the backflow of the photocatalytic system, compounds of not yet reacted or oxidized organic matter are collected. The UF retentate is returned back to the photocatalytic reaction system. The UF permeate will be used as the feed to the down-stream NF separation step. Retained compounds from the nanofiltration will be recycled to the UF feed. The NF step should be arranged in such a way, that the residence time of persistent organic compounds could be increased within the system. The NF permeate again can be treated optionally to separate salts and minor residuals down-stream within an RO step. The main feed of the dye effluent will need respective pre-treatment, after which the effluent stream has to be transparent and clarified and to contain only a minor content of dyes and dissolved organic compounds. The photocatalytic process can be carried out almost without a rejected fraction and no further disposal of residual matters.

Estimation of NF costs

The synergies of applying nanofiltration in combination with photocatalysis must justify the additional costs. As we have seen, NF can be a pre-treatment step to increase the effectiveness of the photocatalysis or can act as a post-treatment after the photocatalysis, for a further reduction of colour and COD. In both process concepts, the NF will contribute significantly to the dye separation, but it will also be a major contribution in the treatment costs. For a rough and a quick estimation of these costs, a simple approach will be described and demonstrated in an example. The described procedure is based on the authors experiences in the realization of NF-plants for the production of dyes and chemicals and for the pre-treatment of wastewater in the 1980s and 1990s, within the dye division of Sandoz, as well as for intermediates and solvents isolation for DSM and Evonik in recent years. According to those experiences, the costs of the NF treatment can be attributed to the membrane replacement costs, which directly depend on the required membrane area and therefore, on the size of the plant that is used for the treatment process. When membrane plants are applied, it is a challenge to keep membrane costs low, because of the frequent need for membrane replacement that is associated with these applications. Membrane costs in industrial applications are in the range of 10 to 20% of the total equipment costs. In wastewater treatment the maximum affordable membrane replacement costs (MRC) are, as a rule, less than 10% of the equipment costs.

The annual operating costs, as given in Table 1, are between 204 and 408 US$, which is roughly seven times the assumed membrane replacement costs (MRC) of 30 to 60 US$ per m^2 of the spirally wound membrane elements used in the focused treatment plant. The estimated figures of fixed and variable costs are empirical cost data collected from NF membrane plants with membrane areas from 100 to 500 m^2 with a cost accuracy of ±30%, depending on the quality, technical performance and efficiency of the separation. Based on the figures of Table 1, we can roughly estimate the operating cost of an NF application, which has to achieve a given through-put of

Table 1: Compilation of costs in multiples of membrane replacement costs.

specific membrane replacement costs (sMRC) for spiral membrane elements		30–60 US$/m^2
volumetric permeate capacity		5–30 L/m^2·h
assumed membrane life time (MLT)		1 a
fixed costs	amortization	2.55 × MRC
	maintenance (20% of amortization)	0.50 × MRC
	total fixed costs	3.05 × MRC
variable costs	membrane costs	1.00 × MRC
	energy costs	0.50 × MRC
	cleaning (CIP) costs	0.25 × MRC
	labour costs	2.00 × MRC
	total variable costs	3.75 × MRC
total operating costs		**6.80 × MRC**

permeate. The permeate flux indicated in Table 1 as the volumetric specific permeate capacity, which empirically will be in the range between 10 to 30 L/m^2·h for an NF-application.

A short example illustrates this cost estimation procedure. The first steps of this approach are shown in Table 2. We assume an application with a treatment capacity of 20 m^3/d and 200 d per year of operation. For cleaning (CIP) 4 h per day is set and the net operating time per day results in 20 h. With the assumed 200 operating days per year, we get the specific permeate capacity between 200 and 600 L/m^2·d or, when calculated for one year, of 40 to 120 m^3/(m^2·a). Depreciation and maintenance costs incur independently of the operatinal status of the plant. That is, no matter whether or not there is a demand to treat effluents, the periodical CIP is included in the maintenance cost, which is required, even if the membrane plant is not in operation.

As for the amortization period, we have generously taken a 10-year period, which might not be generally applicable depending on local situations or financial regulations. Figure 5 is a compilation of empirical data of realized membrane plants with different module configurations such as tubular, plate and frame, or spiral wound. The given specific equipment costs are the turn-key costs of frame-mounted separation plants, including the CIP system, without the costs for local installation of buffer tanks and all out-side the battery limits of the separation plant, which are considered to be ex-works prices. From Figure 5 we can now take the estimated purchase price for the equipment cost, based on the necessary plant size, which is defined by the membrane area needed for the filtration process and based on the design output mentioned previously.

The required plant size in our example is defined with a 100 m^2 membrane area. As we are using spiral wound configuration,

Table 2: Cost estimation example based on Table 1 for a treatment capacity of 20 m^3 dye effluent per day at an assumed operation time of 200 days per year.

dye effluent	20 m^3/d
specific permeate capacity	10 L/(m^2·h)
operation	20 h/d
specific permeate capacity per day	200 L/(m^2·d)
resulting size of NF plant	100 m^2 (membrane area size, MAS)
sMRC	30–60 US$/m^2 (mean value: 45 US$/m^2)
membrane lifetime	1 a
total sMRC (100 m^2 MAS)	3,000–6,000 US$/a
cost estimation of Table 1 (365 d/a operation)	6.80 × MRC
fixed costs (Table 1)	3.05 × MRC
variable costs (Table 1) for 200 d/a	2.05 × MRC (= 200/365 × 3.75 MRC)
total operating costs	**15,300–30,600 US$/a (= 5.10 × MRC)**

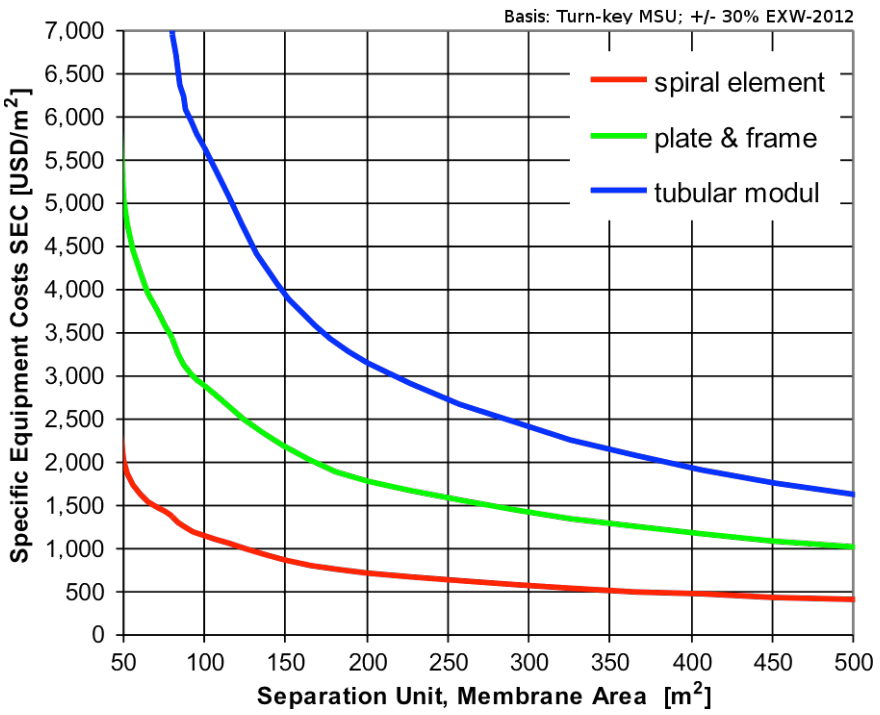

Figure 5: Specific equipment cost (SEC) per m^2 of membrane area.

the specific equipment costs can be taken from Figure 5 to be about 1,150 US$/$m^2$, which results in an equipment purchase price of 115,000 US$ (±30% depending quality of materials, instrumentation, control devices and process automation standards, etc.). As calculated in Table 2, the total operating cost will be 15,300 US$ (for 3,000 US$ membrane replacement cost) or 30,600 US$ (for 6,000 US$ MRC), respectively. With those figures we can calculate the treatment cost of one cubic metre of dye effluent, which results, depending again on the respective membrane replacement cost, in the range between 3.83 and 7.66 US$/$m^3$.

Influences on NF treatment costs

The daily required effluent treatment capacity and time for membrane cleaning together with the main specific permeate flux, should be taken for the preliminary fixing of the NF plant size, as illustrated in the previous example, whereby influences in flux performances are not taken in consideration. With the amortization costs the invested capital of a plant, which can be estimated on the basis of the plant size, will be paid off over a certain period time. The number of years for paying off the capital expenditures is one cost sensitive factor and another is given with the yearly operating hours. This influence affects to a great extent the total specific treatment costs. The total mean treatment cost (MRC = 45 US$/$m^2$) can be calculated as 5.74 US$/$m^3$, for our example of a NF treatment plant with a capacity of 20 m^3 dye effluent per day and with an assumed membrane flux of 10 L/m^2·h and 200 operating days per year, which means that 4,000 m^3 would be treated during one year. Those treatment costs would be decreased to 4.20 US$ /m^3 if the plant could be operated the whole year with a total treatment capacity of 7,300 m^3. The number of treatment days per year, which represents a significant influence in the treatment costs too, is shown in Figure 6.

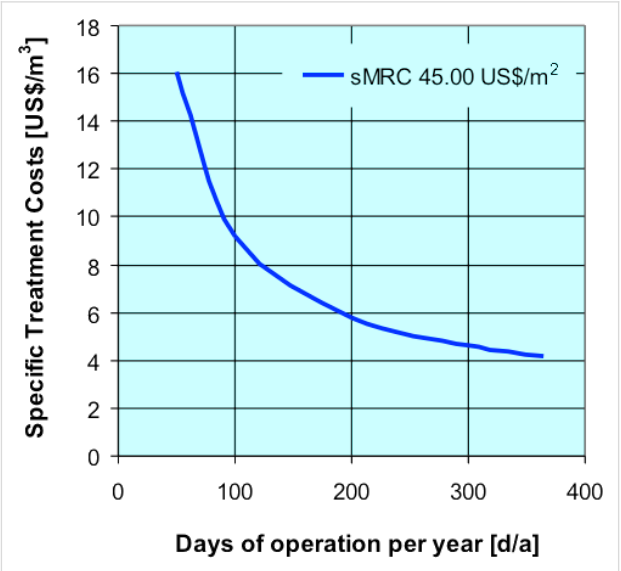

Figure 6: Total specific treatment costs of dye industry effluent versus the operating time in d/a with a mean MRC value of 45 US$/$m^2$.

Even a well-performing plant has to be preferably operated round the year for a profitable application. A treatment plan over the year is needed to reduce down-time periods and overcapacities of treatment plants. Overcapacities and long down-times can kill the economic benefits of a projected treatment plant. Alongside these effects, CIP time and/or membrane cleaning times, together with the achievable permeate fluxes, will have an additional influence on the demandable sizes of the membrane plant areas and represent therefore another significant factor in the separation plant and costs. In Figure 7, the total specific treatment costs in US$ per treated cubic metre effluent is shown versus the mean plant permeate flux which can be achieved in the considered treatment process. In Figure 5, the dependence of the specific investment or equipment costs versus the membrane areas or plant sizes is displayed. Taking into account this and an assumed amortization period of 10 years, the total specific treatment costs are calculated for an assumed 365 days per year operation, and for plant capacities of 20 m^3/d and 100 m^3/d. In Figure 7, the resulting treatment costs in US$ per cubic metre of dye effluent are outlined versus the achievable mean permeate flux of the NF process.

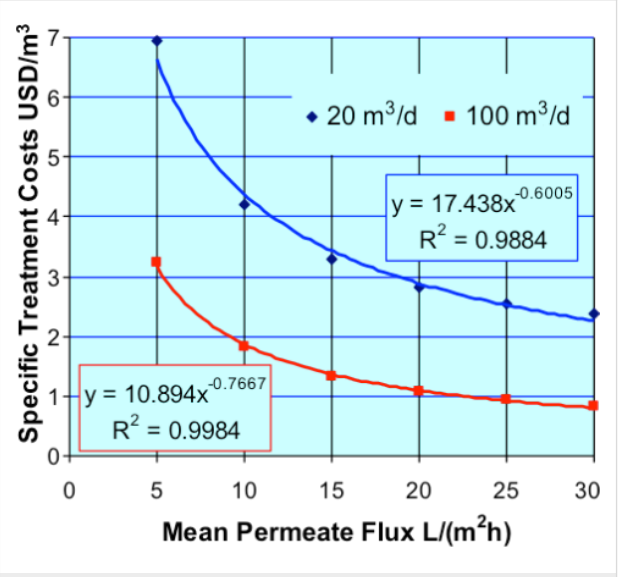

Figure 7: Specific total operating costs, treatment capacity 20 m^3/d and 100 m^3/d, 365 days per year treatment operation.

Discussion

Focusing on industrial applications it is a rule that costs are associated almost directly with the numbers of treatment steps involved. To combine different treatment steps it is important to learn about the strengths and weaknesses of the single steps to be able to evaluate the opportunity of a certain combination. In our case photocatalysis is used to degrade compounds in the effluent. The nanofiltration is used to isolate compounds selectively from the effluent. The combination of the two has to ensure the required removal of dyes from the effluent, without generating a reject stream which would again require a further treatment step or has to be finally disposed. The assessment of the applicability of nanofiltration in combination with photocatalysis is clearly given in the treatment application, if the constituents of effluents can be rejected or isolated by the nanofiltration as well as properly degraded by the photocatalysis.

The costs of the nanofiltration separation, which have to be taken in account, dependent on different empirical factors, which can be obtained from respective experiences or have to be specifically collected through lab and/or pilot tests, which should be done preferably in combination with the projected photocatalytic reactor. Regarding the cost calculation of nanofiltration, assumptions were made, which are based as far as possible on practical experiences. The expected specific treatment costs lie in the range between 1 and 6 US$ per m^3 of treated effluent depending on plant size, quality of effluent to be treated and required treatment limits.

Conclusion

The combination of NF with photocatalysis is capable of increasing the efficiency of the dye degradation process. NF possesses the ability to reject organic colour compounds in the pre-treatment, as well in the post-treatment. Photocatalysis needs a more transparent system and therefore lower concentration of dyes to be effectively applied. Despite their application potential NF membrane processes are not a common technology in dye works, yet. Promising laboratory results of NF separation are not easily transferred to industrial applications, and it has to be kept in mind that membrane processes are seldom stand-alone solutions and additional investment costs for industrial plants that include the necessary pre-treatment equipment can be high.

Considering the treatment of dye effluents, there is a possibility to set the treatment at the source to avoid the disadvantage of a dilution of dyes being treated. Previously many dyehouses discharged their effluents to the main sewer and, as a consequence, the treatment of the collected dye effluents had to be carried out in large-volume tanks. Secondly various residual dyes from different sources have to be separated or oxidized more or less at the end of the pipe after a biological treatment step to fulfil regulations or to achieve an almost colourless effluent. The treatment of diluted systems after the biological degradation, also described as effluent polishing, can be carried out conventionally through natural UV-radiation in large surface ponds or, with reduced area demands, in photocatalytic systems, in which the so-called advanced oxidation processes

are conducted. The photocatalytic systems exhibit higher efficiencies and shorter residence times and nanofiltration can contribute by almost completely rejecting organic compounds, which are not readily degraded within the given hydraulic residence time in the photocatalysis. However, a nanofiltration down-stream of the photocatalytic reaction will be a major cost factor. The exclusive costs of NF will range from 1 to 6 US$ per m^3 of treated effluent. But as a result, NF will ascertain high qualities of the treated effluents and can be synergistically combined with a photocatalytic degradation facility.

References

1. Tahri, N.; Masmoudi, G.; Ellouze, E.; Jrad, A.; Drogui, P.; Ben Amar, R. *J. Cleaner Prod.* **2012,** *33,* 226–235. doi:10.1016/j.jclepro.2012.03.025
2. Mills, A.; Le Hunte, S. *J. Photochem. Photobiol., A: Chem.* **1997,** *108,* 1–35. doi:10.1016/S1010-6030(97)00118-4
3. Chong, M. N.; Jin, B.; Chow, C. W. K.; Saint, C. *Water Res.* **2010,** *44,* 2997–3027. doi:10.1016/j.watres.2010.02.039
4. Rauf, M. A.; Salman Ashraf, S. *Chem. Eng. J.* **2009,** *151,* 10–18. doi:10.1016/j.cej.2009.02.026
5. Zheng, Y.; Yu, S.; Shuai, S.; Zhou, Q.; Cheng, Q.; Liu, M.; Gao, C. *Desalination* **2013,** *314,* 89–95. doi:10.1016/j.desal.2013.01.004
6. Zahrim, A. Y.; Tizaoui, C.; Hilal, N. *Desalination* **2011,** *266,* 1–16. doi:10.1016/j.desal.2010.08.012
7. Kumar, A.; Pratibha, C.; Verma, P. *Global J. Environ. Res.* **2011,** *5,* 46–52.
8. Mozia, S. *Sep. Purif. Technol.* **2010,** *73,* 71–91. doi:10.1016/j.seppur.2010.03.021
9. Malato, S.; Fernández-Ibáñez, P.; Maldonado, M. I.; Blanco, J.; Gernjak, W. *Catal. Today* **2009,** *147,* 1–59. doi:10.1016/j.cattod.2009.06.018
10. Grzechulska-Damszel, J.; Mozia, S.; Morawski, W. A. *Catal. Today* **2010,** *156,* 295–300. doi:10.1016/j.cattod.2010.06.033
11. Sanches, S.; Penetra, A.; Rodrigues, A.; Cardoso, V. V.; Ferreira, E.; Benoliel, M. J.; Barreto Crespo, M. T.; Crespo, J. G.; Pereira, V. J. *Sep. Purif. Technol.* **2013,** *115,* 73–82. doi:10.1016/j.seppur.2013.04.044
12. Choo, K.-H.; Chang, D.-I.; Park, K.-W.; Kim, M.-H. *J. Hazard. Mater.* **2008,** *152,* 183–190. doi:10.1016/j.jhazmat.2007.06.117
13. Lee, S.-A.; Choo, K.-H.; Lee, C.-H.; Lee, H.-I.; Hyeon, T.; Choi, W.; Kwon, H.-H. *Ind. Eng. Chem. Res.* **2001,** *40,* 1712–1719. doi:10.1021/ie000738p
14. Augugliaro, V.; García-López, E.; Loddo, V.; Malato-Rodríguez, S.; Maldonado, I.; Marcì, G.; Molinari, R.; Palmisano, L. *Sol. Energy* **2005,** *79,* 402–408. doi:10.1016/j.solener.2005.02.020
15. Le-Clech, P.; Lee, E.-K.; Chen, V. *Water Res.* **2006,** *40,* 323–330. doi:10.1016/j.watres.2005.11.011
16. Martínez, F.; López-Muñoz, M. J.; Aguado, J.; Melero, J. A.; Arsuaga, J.; Sotto, A.; Molina, R.; Segura, Y.; Pariente, M. I.; Revilla, A.; Cerro, L.; Carenas, G. *Water Res.* **2013,** *47,* 5647–5658. doi:10.1016/j.watres.2013.06.045
17. Damodar, R. A.; You, S.-J.; Ou, S.-H. *Sep. Purif. Technol.* **2010,** *76,* 64–71. doi:10.1016/j.seppur.2010.09.021
18. Mozia, S.; Tomaszewska, M.; Morawski, A. W. *Desalination* **2006,** *198,* 183–190. doi:10.1016/j.desal.2006.01.024
19. Berberidou, C.; Avlonitis, S.; Poulios, I. *Desalination* **2009,** *249,* 1099–1106. doi:10.1016/j.desal.2009.06.045
20. Grzechulska-Damszel, J.; Morawski, A. W. *Asia-Pac. J. Chem. Eng.* **2009,** *4,* 239–245. doi:10.1002/apj.238
21. Molinari, R.; Pirillo, F.; Falco, M.; Loddo, V.; Palmisano, L. *Chem. Eng. Process.* **2004,** *43,* 1103–1114. doi:10.1016/j.cep.2004.01.008
22. Molinari, R.; Borgese, M.; Drioli, E.; Palmisano, L.; Schiavello, M. *Catal. Today* **2002,** *75,* 77–85. doi:10.1016/S0920-5861(02)00047-0
23. Patsios, S. I.; Sarasidis, V. C.; Karabelas, A. J. *Sep. Purif. Technol.* **2013,** *104,* 333–341. doi:10.1016/j.seppur.2012.11.033

License and Terms

Beilstein Journal of Nanotechnology

Pyrite nanoparticles as a Fenton-like reagent for in situ remediation of organic pollutants

Carolina Gil-Lozano*[1], Elisabeth Losa-Adams[1], Alfonso F.-Dávila[2] and Luis Gago-Duport[1]

Full Research Paper

Open Access

Address:
[1]Departamento de Geociencias Marinas, Universidad de Vigo, Lagoas Marcosende, 36310-Vigo, Spain and [2]Carl Sagan Center, SETI Institute, 189 Bernardo Avenue, Suite 100, Mountain View, CA 94043, USA

Email:
Carolina Gil-Lozano* - karolina_gil@uvigo.es

* Corresponding author

Keywords:
copper phthalocyanine; Fenton-like reagent; hydrogen peroxide; nanoparticles; pyrite

Beilstein J. Nanotechnol. **2014,** *5,* 855–864.
doi:10.3762/bjnano.5.97

Received: 15 February 2014
Accepted: 15 May 2014
Published: 16 June 2014

This article is part of the Thematic Series "Nanomanipulation and environmental nanotechnology".

Guest Editor: E. Gnecco

Abstract

The Fenton reaction is the most widely used advanced oxidation process (AOP) for wastewater treatment. This study reports on the use of pyrite nanoparticles and microparticles as Fenton reagents for the oxidative degradation of copper phthalocyanine (CuPc) as a representative contaminant. Upon oxidative dissolution in water, pyrite (FeS_2) particles can generate H_2O_2 at their surface while simultaneously promoting recycling of Fe^{3+} into Fe^{2+} and vice versa. Pyrite nanoparticles were synthesized by the hot injection method. The use of a high concentration of precursors gave individual nanoparticles (diameter: 20 nm) with broader crystallinity at the outer interfaces, providing a greater number of surface defects, which is advantageous for generating H_2O_2. Batch reactions were run to monitor the kinetics of CuPc degradation in real time and the amount of H_2O_2. A markedly greater degradation of CuPc was achieved with nanoparticles as compared to microparticles: at low loadings (0.08 mg/L) and 20 h reaction time, the former enabled 60% CuPc removal, whereas the latter enabled only 7% removal. These results confirm that the use of low concentrations of synthetic nanoparticles can be a cost effective alternative to conventional Fenton procedures for use in wastewater treatment, avoiding the potential risks caused by the release of heavy metals upon dissolution of natural pyrites.

Introduction

There has been growing interest in nanomaterials for green environmental remediation. For example, catalytically active synthetic nanoparticles inspired by natural minerals have been combined with in situ advanced oxidation processes (AOPs) as a potential strategy to remediate contaminants [1-3]. These AOPs generate hydroxyl radicals ($OH^{\bullet}$) that trigger the formation of other reactive intermediates (e.g., $HO_2^{\bullet}$ and $O_2^{\bullet-}$). Due to their high oxidation potential (E^0 = 2.8 V), hydroxyl radicals attack most organic pollutants with rate constants in the order of 10^6 to 10^9 $M^{-1}{\cdot}s^{-1}$ [4,5]. In practice, the formation of $OH^{\bullet}$ to

degrade organic compounds involves the iron (Fe^{2+} and Fe^{3+}) catalysed decomposition of H_2O_2; this transformation is known as the Fenton reaction [6]. A major drawback of conventional Fenton chemistry for wastewater treatment is that it requires a continuous supply of H_2O_2 under strict pH control, to limit the precipitation of iron oxyhydroxides. However, this control makes the process difficult and cost expensive.

Green nanotechnology can be used in various industrial and in situ remediation processes and can be an effective option for wastewater treatment. Several studies have recently reported the capacity of mineral suspensions (e.g., silicates, oxides and sulfides) to continuously generate H_2O_2 at surface defect sites [7-14]. Since the catalytic performance of the particles depends on the surface area-to-volume ratio (i.e., better performance is enabled by higher ratios), nanoparticles are typically expected to be more reactive than microparticles. Following this logic, and given the fact that pyrite microparticles have already been explored in Fenton chemistry [15], we sought to explore pyrite nanoparticles as heterogeneous catalysts for Fenton-like systems. Pyrite, the most abundant iron sulfide in the crust of Earth, releases Fe^{2+} and H^+ upon oxidative dissolution. As such, it has been used with H_2O_2 as a Fenton catalyst for the degradation of several organic pollutants, including trinitrotoluene, carbon tetrachloride and diclofenac [16-19]. Several recent studies have reported that pyrite can spontaneously produce H_2O_2 via catalytic dissociation of O_2 and H_2O with iron surface sites [7,8,10,12-14]. Albeit the use of pyrite alone as Fenton reagent (i.e., without externally added H_2O_2) has been demonstrated for lactate degradation [15], this approach remains poorly studied and, to the best of our knowledge, has never been used to remove dyes from textile wastewater.

In this work, we compared synthetic pyrite nanoparticles to naturally derived pyrite microparticles for their efficiency in the oxidative degradation of copper phthalocyanine (CuPc), a representative dye that has a metallic ring structure. Phthalocyanines are widely used in the textile industry and can provoke carcinogenesis. However, removal of metallocyanines is difficult because of their resistance towards oxidative degradation as well as their low biodegradability. To this end, we performed real time experiments to determine the degradation rate of CuPc induced by H_2O_2 generated at the surface of the pyrite nanoparticles or microparticles, using UV–vis adsorption spectroscopy and H_2O_2 sensors.

Results

Structural aspects of the pyrite nanoparticles

The pyrite nanoparticles were analyzed at bulk level by XRD to evaluate the possible formation of secondary phases (Figure 1). As shown in the XRD pattern, the only observable Bragg reflections correspond to lattice planes of the cubic structure of pyrite (JCPDS card no. 42-1340). A moderate amount of background is also present in the pattern, where it is especially marked at the tail of the intensity distribution. This type of broadening is a characteristic indicator that coherent X-ray diffraction is occurring in finite-size domains (e.g., sub-grains). The average size of the crystalline domains (as calculated by Rietveld analysis) was 20 nm, which is consistent with the HR-TEM observation of the individual particles.

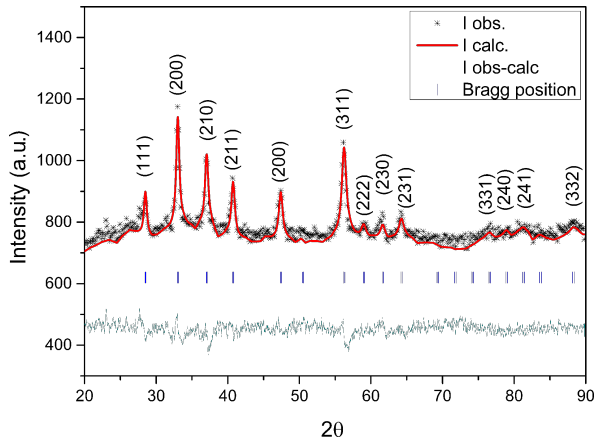

Figure 1: XRD pattern of the nanoparticles, indicating that pyrite was the only crystalline phase resulting from the synthesis. Rietveld analysis of the reflection broadening gave an average crystallite size of 20 nm.

The TEM micrographs of the nanoparticles are shown in Figure 2. The upper left panel (Figure 2a) corresponds to a low-magnification image that shows the typical arrangement of nanocrystals obtained in our syntheses. The nanoparticles tended to aggregate, forming polydisperse clusters of rounded particles ranging in size from 20 nm (individual nanoparticle) to 150 nm (largest cluster). At the initial stages of the process, the clusters were polycrystalline, as indicated by the SAED pattern (Figure 2b). However, as crystallization progressed, some of the particles tended to reorganize, giving rise to single-crystal domains that extended to several particles. This feature is observable in the HR-TEM image (Figure 2c), in which two particles have self-assembled and their lattice fringes, corresponding to the (200) planes, exhibit coherent interference domains. This fact is also confirmed by the FFT superposition of the two particles (inset), which reveals that the diffraction spots have identical orientation. Interestingly, individual particles were surrounded by an amorphous layer (thickness: ca. 2 to 3 nm), suggesting that crystallization had begun upon nucleation of an amorphous precursor and subsequently followed some type of structural reorganization associated with high-energy surfaces between adjacent particles [20-22]. Similar textures have been observed in other syntheses, especially when

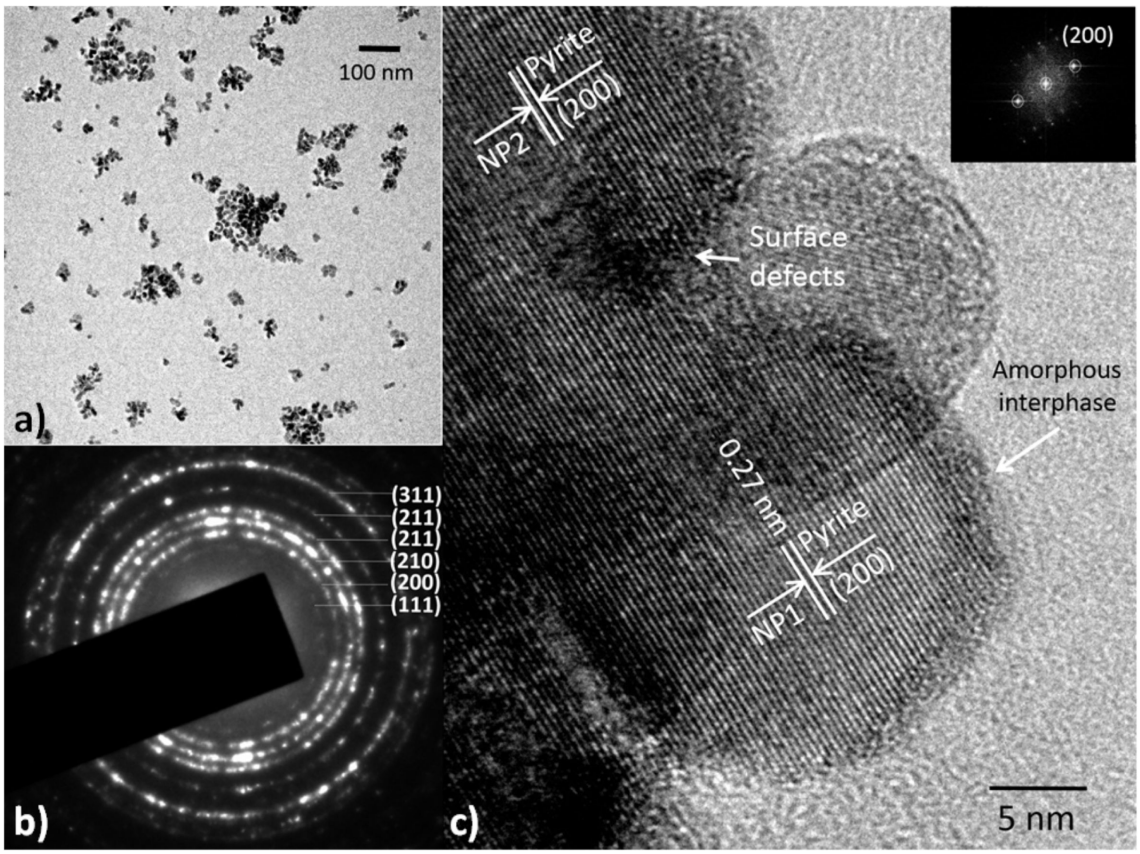

Figure 2: a) TEM image of the typical distribution of the nanoparticles, comprising polycrystalline aggregates of pyrite. b) SAED pattern of the nanoparticles. c) HR-TEM image showing the structure of the nanoparticles. Individual nanoparticles tended to self-assemble, thereby forming finite-size crystalline domains extended over several particles. The surface of the nanoparticles always appeared to be surrounded by an amorphous layer.

high concentrations of precursors were employed [23-26]. This factor can be a limitation when high crystallinity is required; in such cases, use of low reagent concentrations or surfactants is often required to keep the particles apart. However, for the purposes of our work, the formation of interphases with numerous defects is advantageous, since the generation of H_2O_2 relies precisely on the presence of these defect sites.

Kinetics of H_2O_2 generation and CuPc decoloration

Effect of pyrite particle surface area on reactivity

In order to evaluate the influence of the pyrite particle surface area on the amount of H_2O_2 generated and on the dye decoloration (degradation) pathway, we performed kinetic experiments with dispersions of pyrite nanoparticles or microparticles (Figure 3, see section Experimental below). The same initial particle loading (0.08 g/L) and dye concentration (0.1 mg/L) were used. When nanoparticles were employed (Figure 3, curve a), the amount of H_2O_2 detected by the sensor oscillated, rose to a maximum value of 1.4 μM, rapidly decreased to zero and finally, plateaued at 0.2 μM within ca. 10 h. The oscillatory trend and the rapid decrease in H_2O_2 levels suggest that with the nanoparticles, nearly all the generated H_2O_2 had been immediately transformed into less stable free radical species, in a process catalyzed by the Fe^{2+} ions released during their rapid dissolution. However, the microparticles gave vastly distinct results: the H_2O_2 was generated much more slowly, and gradually accumulated in solution (Figure 3, curve b). This observation suggests a less efficient conversion of H_2O_2 into free radicals, which would be consistent with a lower rate of iron delivery to solution than in the case of the nanoparticles. This hypothesis is consistent with PHREEQC calculations [27] of the total iron [Fe^{2+} + Fe^{3+}] released (Figure 3, inset) in each case, using the rate expression of Williamson and Rimstidt [28]. The reactive surface was estimated by the geometrical model assuming cubes of 20 nm for nanoparticles and 1.4 μm for microparticles.

The degradation efficiency in each case is shown in Figure 4. During the start-up period (about 5 to 6 h), decomposition was very similar in each reaction, with a rate constant of $k_1 = 0.004\ h^{-1}$. Afterwards, the rate constant in the nanoparticle

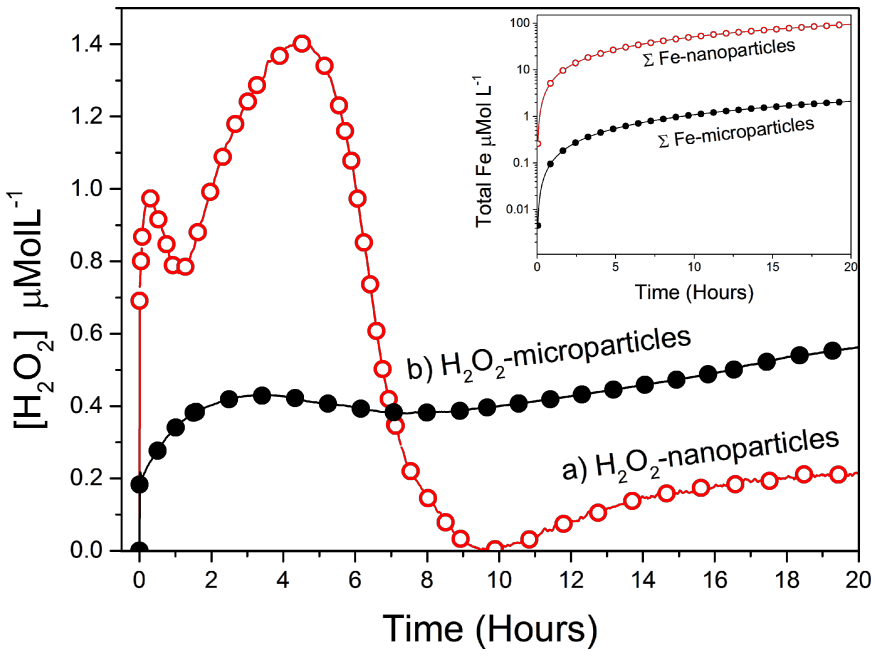

Figure 3: Plot of H_2O_2 concentration over time for suspensions of: a) pyrite nanoparticles or b) pyrite microparticles, at loadings of 0.08 g/L. Inset: Plot of PHREEQC calculations of total iron [Fe^{2+} + Fe^{3+}] delivered in each case, assuming cubes of 20 nm for nanoparticles and 1.4 µm for microparticles.

reaction increased to k_2 = 0.07 h^{-1}, which in terms of degradation efficiency ([1 − (C/C_0)] × 100%) represents a final value ca. 8 times higher than in the microparticle experiments.

Effect of pyrite particle loading and phthalocyanine concentration

The influence of the initial mass of pyrite on the CuPc degradation was assessed by performing experiments with nanoparticles at three different loadings. As shown in Figure 5, even small differences on pyrite loadings prompted changes in the degradation efficiency of CuPc, with the higher loading corresponding to a faster CuPc decomposition (k_1 = 0.07 h^{-1} at 0.08 g/L, k_2 = 0.04 h^{-1} at 0.04 g/L and k_3 = 0.003 h^{-1} at 0.02 g/L) and consequently leading to more efficient degradation (the higher loading experiment was about 8 times more efficient).

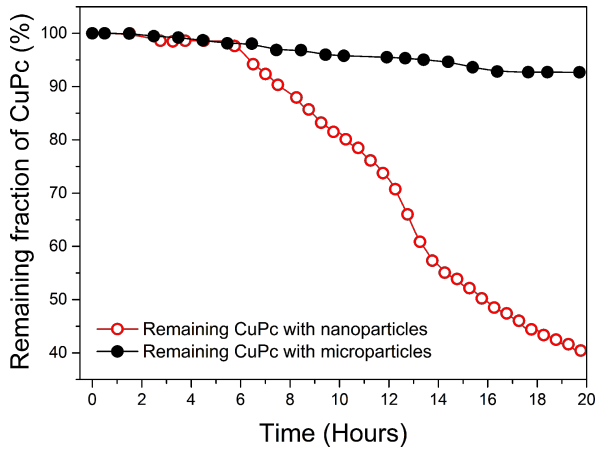

Figure 4: Rate of CuPc decoloration (initial concentration: 0.1 mg/L) in suspensions of pyrite nanoparticles (average size: 20 nm; red circles) or microparticles (average size: 1.4 µm; black circles), at loadings of 0.08 g/L.

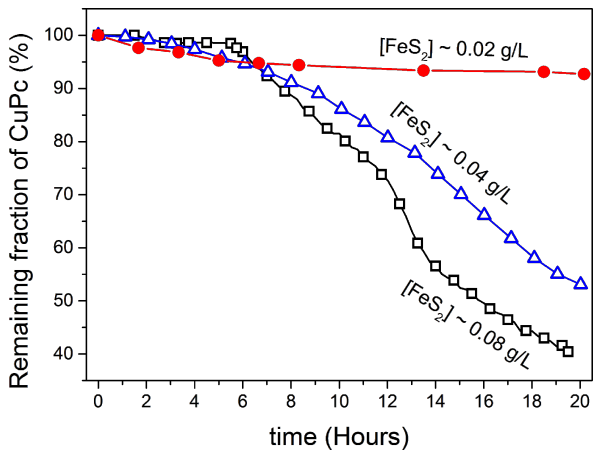

Figure 5: Effect of pyrite nanoparticle loading on the rate of CuPc decoloration. ([CuPc]$_0$ = 0.1 mg/L, loadings values are marked in the curves).

We also evaluated the influence of the initial concentration of CuPc on its degradation. The results are plotted in Figure 6, in which the curves represent the fraction of remaining contaminant (C/C_0) obtained with pyrite nanoparticles (Figure 6a) or microparticles (Figure 6b). In both cases, the degradation proceeded much more quickly at lower levels of dye (nanoparticles: ca. 4 times; microparticles: ca. 2 times), corroborating previous reports of delayed degradation at higher dye concentrations [29]. Nevertheless, experiments with a relatively concentrated dye solution (5 mg/L) and low nanoparticle loading (0.08 g/L) still gave a degradation efficiency of 17% within 20 h.

The use of pyrite nanoparticles for CuPc degradation acidified the system. In the performed experiments, the pH usually attains a final value of the order of 4–5, where Fenton reaction is far more efficient. Consequently, special pH control is not required. This it shown in Figure 7, for experiments performed with two different concentration values of dye and pyrite nanoparticle loads.

We used high performance liquid chromatography (HPLC) to identify byproducts generated during degradation. The chromatogram of unreacted dye was employed as control (Figure 8) and showed a single peak in the UV region with a retention time of 2.42 minutes. After 27 h of reaction with nanoparticles, the chromatogram exhibited seven new peaks (retention times: 1.56, 3.01, 3.56, 4.24, 5.71, 6.31 and 9.12 minutes, respectively) and an appreciable decrease in the intensity of peak corresponding to the dye (at 2.42 minutes). The peak at 5.71 minutes, which is associated with phthalamines, a diagnostic species for the oxidative destruction of phthalocyanines [30], showed a λ_{max} of 217 nm.

Discussion

There have been previous reports on the surface generation of H_2O_2 upon oxidative dissolution of pyrite [7,8,10,12-14]. This reactivity, coupled with the iron delivery and the decrease in pH that occur upon dissolution of pyrite, are the reasons that this mineral is ideal for use in wastewater treatments. Furthermore, in the present work, we have demonstrated

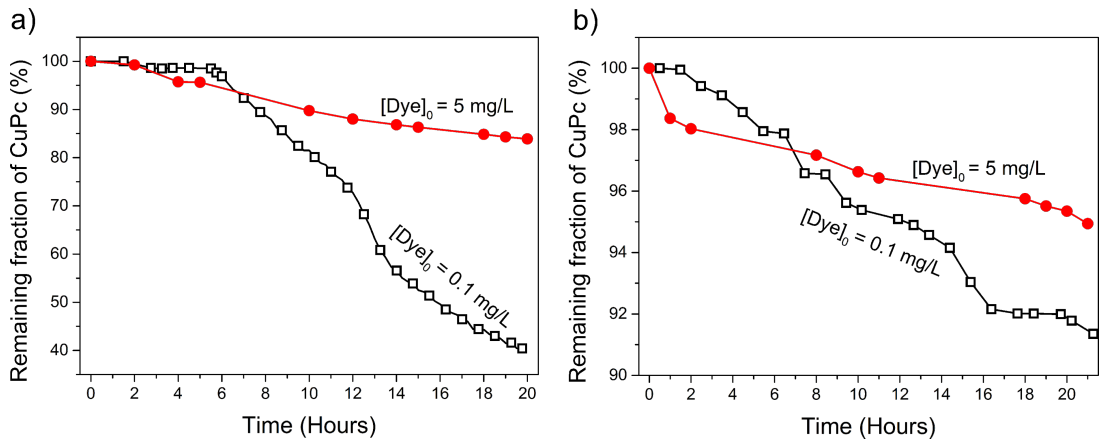

Figure 6: Decoloration rate at different initial concentrations of CuPc in suspensions of pyrite a) nanoparticles or b) microparticles, at loadings of 0.08 g/L.

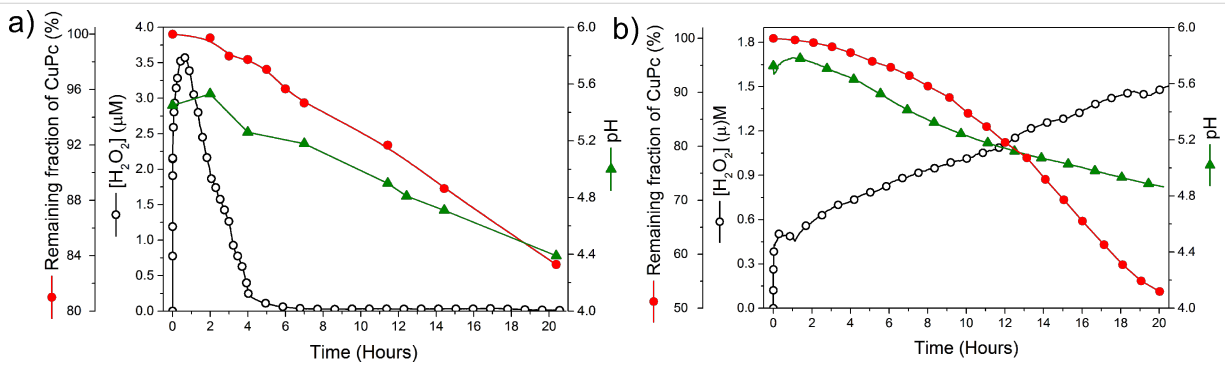

Figure 7: The pH and H_2O_2 evolution in CuPc solutions with pyrite nanoparticles (a) $[CuPc]_0$ = 5 mg/L at 0.06 g/L loading (b) $[CuPc]_0$ = 0.1 mg/L at 0.04 g/L loading.

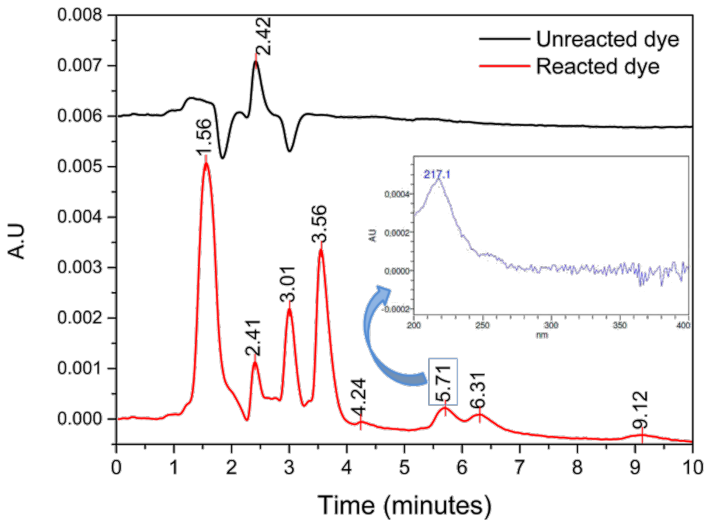

Figure 8: a) HPLC Chromatograms (UV detection: 219 nm) of untreated dye, and of dye treated with suspensions of nanoparticles for 27 h. b) UV-vis spectrum of the peak at 5.7 minutes (λ_{max}: 217 nm).

the efficiency of pyrite at breaking down the ring of CuPc, which we confirmed through the HPLC identification of sulfophthalimide, the most common oxidative byproduct of this dye [30]. Practical interest in pyrite as a Fenton-type reagent depends on its capability to efficiently and sustainably generate H_2O_2 for oxidative degradation of contaminants. Figure 9 summarizes the proposed reaction mechanisms which are involved in the H_2O_2 generation and in the subsequent degradation of CuPc by the hydroxyl radical [29].

Although the mechanism of H_2O_2 generation remains controversial [7,10-15,31,32], researchers agree that this product is afforded by reaction of iron defect sites at the pyrite surface with adsorbed oxygen and water, according to Equation 1 and Equation 2, below. This chemistry involves the intermediate generation of $O_2^{\bullet-}$ from dissociative adsorption of $O_{2(g)}$ at the pyrite surface:

$$\equiv \mathrm{pyFe}^{2+} + \mathrm{O}_{2(g)ads} \rightarrow \equiv \mathrm{pyFe}^{3+} + \mathrm{O}_2^{\bullet-} \qquad (1)$$

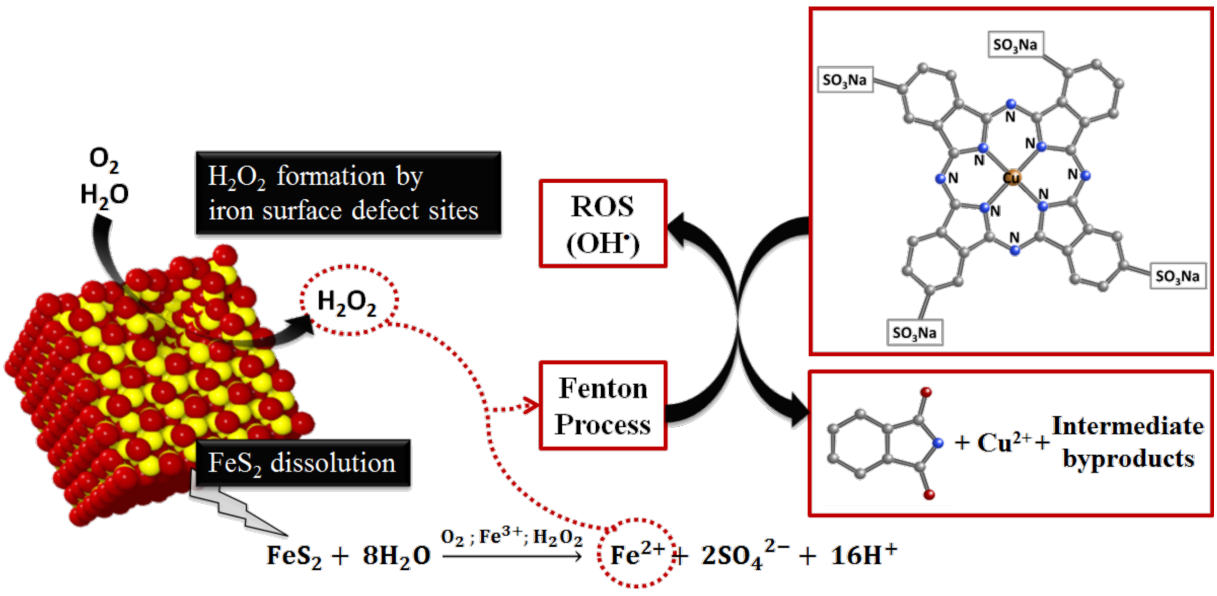

Figure 9: Proposed reaction mechanisms for the generation of H_2O_2 and for the oxidative degradation of CuPc by $OH^{\bullet}$.

$$\equiv \mathrm{pyFe^{2+}} + \mathrm{O_2^{\bullet -}} + 2\mathrm{H^+} \rightarrow \equiv \mathrm{pyFe^{3+}} + \mathrm{H_2O_{2\,ads}} \quad (2)$$

The adsorbed H_2O_2 is then released into the solution. Simultaneously, the amount of Fe^{2+} required for the Fenton reaction to occur is supplied to the solution by oxidative dissolution of pyrite in the presence of O_2(aq), according to Equation 3:

$$2\mathrm{FeS} + 7\mathrm{O_{2(aq)}} + \mathrm{H_2O} \rightarrow 2\mathrm{Fe^{2+}} + 4\mathrm{SO_4^{2-}} + 4\mathrm{H^+} \quad (3)$$

At this moment, Fe^{2+} starts to catalyze the decomposition of H_2O_2 into $OH^{\bullet}$ and other reactive oxygen species involved in the oxidation of organics pollutants, according to the Fenton chain-reaction sequence, described by Equations 4 to 7, below [33].

$$\mathrm{Fe^{2+}} + \mathrm{H_2O_2} \rightarrow \mathrm{Fe^{3+}} + \mathrm{HO^-} + \mathrm{OH^{\bullet}} \quad k_1 = 70\ \mathrm{M^{-1}s^{-1}} \quad (4)$$

$$\mathrm{Fe^{3+}} + \mathrm{H_2O_2} \rightarrow \mathrm{Fe\text{-}OOH^{2+}} + \mathrm{H^+} \quad (5)$$

$$\mathrm{Fe\text{-}OOH^{2+}} \rightarrow \mathrm{HOO^{\bullet}} + \mathrm{Fe^{2+}} \quad k_{5-6} = 0.001 - 0.02\ \mathrm{M^{-1}s^{-1}} \quad (6)$$

$$2\mathrm{OOH^{\bullet}} \rightarrow \mathrm{O_2} + \mathrm{H_2O} \quad k_7 = 8.6\times10^5\ \mathrm{M^{-1}s^{-1}} \quad (7)$$

In this sequence, Equation 5 and Equation 6 are the slowest and diminish the recycling between Fe^{2+} and Fe^{3+}. Consequently, they form the rate-limiting step in the generation of free radical species and decrease the efficiency of the oxidative degradation of contaminants. When pyrite is used as iron source for heterogeneous catalysis, an additional mechanism for the Fe^{2+} regeneration occurs through Equation 8:

$$\mathrm{FeS_2} + 14\mathrm{Fe^{3+}} + 8\mathrm{H_2O} \rightarrow 15\mathrm{Fe^{2+}} + 16\mathrm{H^+} + 2\mathrm{SO_4^{2-}} \quad (8)$$

This drives the oxidation of pyrite by Fe^{3+}, thereby releasing Fe^{2+} and consequently, accelerating the degradation of H_2O_2 through Equation 4. As shown above, Equation 3 and Equation 8 both release protons, promoting acidification simultaneously to the delivery of iron into solution.

The rate expressions associated to Equation 3 and Equation 8 are, respectively [28]:

$$\mathrm{rate}\left(\mathrm{O_2}\right) = \mathrm{SA}\left(\frac{m}{m_0}\right)^{0.67} 10^{-8.1}\left[\mathrm{O_2}\right]^{0.5}\left[\mathrm{H^+}\right]^{-0.11} \quad (9)$$

$$\mathrm{rate}\left(\mathrm{Fe^{3+}}\right) = \mathrm{SA}\left(\frac{m}{m_0}\right)^{0.67} 10^{-6.07}\left[\mathrm{Fe^{3+}}\right]^{0.93}\left[\mathrm{Fe^{2+}}\right]^{-0.4} \quad (10)$$

Both equations depend on the reactive surface, SA (1/dm). Since H_2O_2 is also formed by reactions at the surface, the dye degradation efficiency is expected to increase with a greater surface area (i.e., smaller particles should give better results). We assessed this hypothesis by performing batch experiments to compare the degradation behavior of nanoparticles with that of microparticles (Figure 3 and Figure 4).

As expected, the nanoparticles gave strikingly better results than the microparticles. At low loading (0.08 mg/L) and 20 h reaction time, the former enabled 60% CuPc removal, whereas the latter enabled only 7% removal. As such, the H_2O_2 was consumed far more quickly when nanoparticles were used. This can be explained by the fact that the greater surface area of the nanoparticles not only provides more sites for H_2O_2 generation, but also leads to faster oxidative dissolution of the pyrite itself, as this rate is proportional (in mass terms) to the reactive surface area. Thus, the nanoparticles rapidly supply the solution with iron, which induces the rapid transformation of H_2O_2 into $OH^{\bullet}$ radicals, according to the Fenton reaction scheme. The dye concentration was indirectly proportional to the degradation rate (Figure 6), indicating that the best catalytic activities were reached by using dilution procedures that provide low concentrations of contaminant. Moreover, the system does not require a pH control to degrade CuPc (Figure 7).

Conclusion

We evaluated the use of synthetic pyrite nanoparticles and naturally derived pyrite microparticles for Fenton-like oxidative degradation of the dye CuPc as representative industrial contaminant. Since pyrite spontaneously and sustainably releases H_2O_2 upon surface reaction with adsorbed $O_{2(g)}$ and H_2O, it might prove invaluable for Fenton-like treatment of wastewater, obviating the need for external addition of H_2O_2. Furthermore, dissolution of pyrite in water promotes the recycling of Fe^{2+} into Fe^{3+} and vice versa, triggering Fenton production of $HO^{\bullet}$, the primary species responsible for oxidative degradation of the pollutant. Our results with the synthetic pyrite nanoparticles demonstrate that H_2O_2 is indeed generated by iron disulfide, in the absence of trace compounds founds in natural pyrite.

Our kinetics analysis showed that the pyrite nanoparticles enabled a ca. 8 times greater efficiency of pollutant removal than did the microparticles. The use of synthetic pyrite nanoparticles avoids the dangers of heavy metal release that often occurs upon dissolution of naturally occurring (i.e., mineral derived) pyrites. Furthermore, the low required loadings of these nanoparticles make this procedure even more environmentally friendly. Lastly, since the process does not require UV-illumination or pH constraints, it may serve as a cheap alternative to conventional Fenton approaches for the selective oxidation of pollutant dyes.

Experimental

Chemicals

Copper phthalocyanine-3, 4′, 4′′, 4′′′- tetrasulfonic acid tetrasodium salt (85%), oleylamine (OA, 70%), sulfur (99.99%) and toluene (99.8% anhydrous) were purchased from Sigma Aldrich. Ferrous chloride tetrahydrate ($FeCl_2{\cdot}4H_2O$, 99%) was purchased from Fluka. Absolute ethanol was purchased from Quimivita. All chemicals were used as received without any further purification. Aqueous suspensions of pyrite were prepared using deionized water (resistivity: ca. 18 MΩ·cm) purified in a Milli-Q system at an initial pH of about 5.5.

Synthesis of pyrite nanoparticles

Pyrite nanocrystals were synthesized by the hot injection method [26,34]. The experiments were performed in a three-neck flask connected to a reflux condenser. The device was heated by an electric mantle temperature-probe controlled. Sulfur and $FeCl_2{\cdot}4H_2O$ were used as starting materials. Briefly, 0.4 mmol of $FeCl_2{\cdot}4H_2O$ were dehydrated and dissolved in 6 mL of OA under N_2 atmosphere. The resulting solution was maintained at 100 °C for 1 h, until an Fe–OA complex was formed. A solution of 2.4 mmol of sulfur in 6 mL of OA (to achieve an Fe/S molar ratio of 1:6) was injected, heated to 220 °C and allowed to react for 20 min. The mixed solution was cooled to room temperature. Nanocrystals were dispersed and separated by centrifugation and re-dissolving with several aliquots of a 1:1 toluene/ethanol solution.

Preparation of pyrite microparticles

Natural pyrite cubes (Logroño, Spain) were milled using a diamond disk and sieved (63 μm) to obtain pyrite powder. The resulting particles presented an average diameter of 1.4 μm (laser diffraction particle size analyzer, LS13320) and a specific surface area (BET) of 1.46 m^2/g. Prior to use, the pyrite samples were cleaned by sonication in ethanol (96%), HCl (0.25 M) and deoxygenated water, and then dried under vacuum, purged with N_2 and finally, stored in a glove box (N_2 atmosphere) until use.

Characterization

The nanoparticles were characterized by high-resolution transmission electron microscopy (HR-TEM), selected area electron diffraction (SAED) and X-ray diffraction (XRD). The TEM studies were done on a JEOL JEM-3011 microscope with accelerating voltage of 200 kV. The XRD analysis of the nanoparticles and the microparticles was done on a Philips diffractometer with a graphite monochromator and Cu Kα radiation (1.54 Å). Indexing of pyrite reflections were done using the JCPDS 00-042-1340 card (FeS_2 [pyrite]). Further, Rietveld refinements were performed to rule out the presence of other crystalline iron sulfides (e.g., marcasite, pyrrhotite and troilite) and to calculate the average values of crystallite size and microstrain (according to the Scherrer method [35]).

Experimental set-up

Kinetic experiments were conducted in stirred glass reactors under ambient conditions (i.e., open to atmosphere and at room temperature [22 ± 2 °C]; K-type thermocouple). Pyrite powder was deposited onto silicone strips as a thin film of particles, and the strips were then adhered to the inner reactor walls. The pH was monitored by a glass pH-meter (Vernier FPH-BTA) with an Ag/AgCl reference electrode.

The temporal change in the H_2O_2 concentration in solution was monitored by an amperometric microsensor (ISO-HPO-100, World Precision Instruments, Inc.). These sensors contain a flexible, activated carbon-fiber sensing electrode coated with a proprietary membrane that enhances the low detection limit (LDL) of H_2O_2 to a value of 10 nM (ten times lower than in the bare Pt electrode; LDL: 0.1 μM) with a response time of less than 5 s. The signal was amplified with a picoamperemeter (Apollo 4000 Free Radical Analyzer, World Precision Instruments). Measurements were taken by using a polarization voltage of 0.4 V versus an Ag/AgCl reference electrode.

Simultaneous to H_2O_2 generation, the decoloration (degradation) of CuPc was monitored by tracking the absorbance at 630 nm, using fiber optic UV–vis spectrometry (Black-comet, Stellarnet). A liquid waveguide capillary flow cell (LWCC; path length: 250 cm; WPI), was connected to the batch reactor by a peristaltic pump (masterflex pump system, Cole-Parner Instrument Co; see Figure 10). Alternatively, when the initial dye concentration was too high (i.e. when it led to saturation in the Vis spectra obtained with the LWCC), a standard quartz cuvette (path length: 1 cm) was used and the decoloration of the dye was done measuring aliquots at different times of the process.

The degradation of CuPc was analyzed by high performance liquid chromatography (HPLC; Waters Alliance 2975 equipped

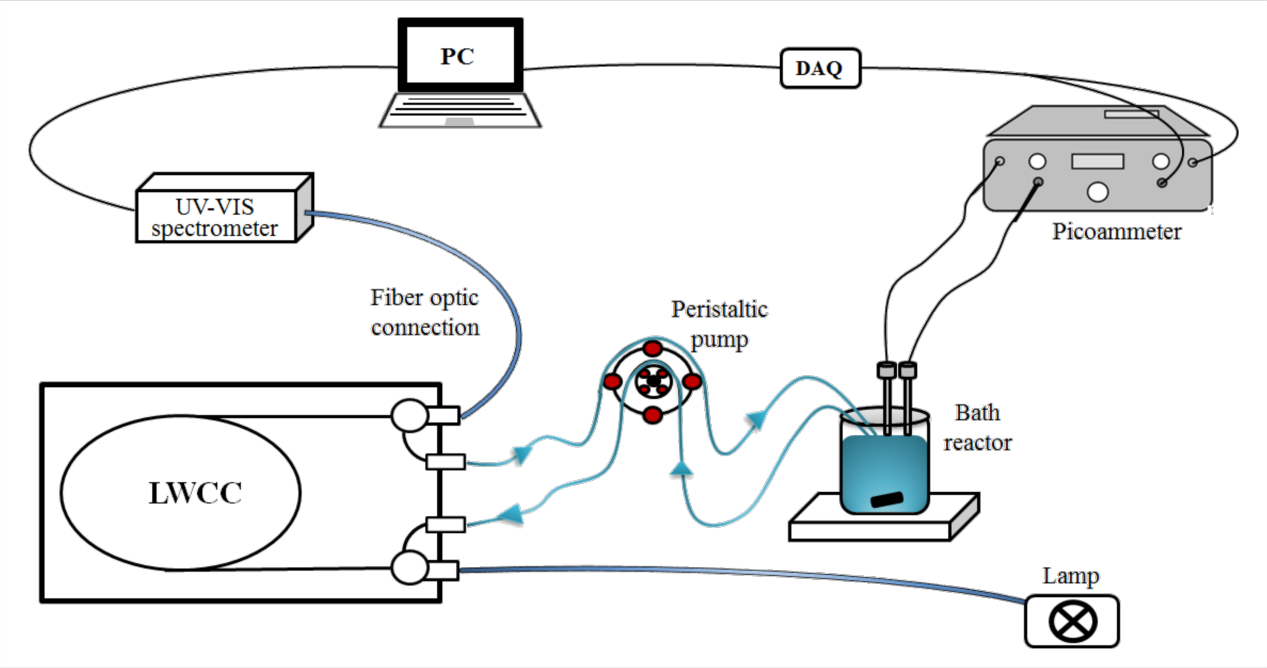

Figure 10: Experimental set-up using a liquid waveguide capillary flow cell (LWCC).

with a Waters 996 Photodiode Array Detector; UV–vis detection), using a C8 column (Waters Symmetry: 150 × 4.6 mm, 3.5 µm). The mobile phases were 0.1% aq phosphoric acid (A), and acetonitrile (B), run in a linear gradient (80:20, v/v) at a flow rate of 1 mL/min.

Acknowledgements

This research was funded by the Spanish Ministry of Science and Innovation as part of the MICINN-FEDER Project CGL2011-30079. The authors would like to thank doctoral student Ruth Otero Lorenzo (Department of Applied Physics, University of Vigo), for her help and advice in the synthesis of pyrite nanoparticles, and Dr. José Benito Rodríguez (C.A.C.T.I. research institute), for his help in the HR-TEM analyses.

Finally, we thank the anonymous referees for their thorough review and highly appreciate the comments and suggestions, which significantly contributed to improving the quality of the publication.

References

1. Garrido-Ramírez, E. G.; Theng, B. K. G.; Mora, M. L. *Appl. Clay Sci.* **2010,** *47,* 182–192. doi:10.1016/j.clay.2009.11.044
2. Kamat, P. V.; Meisel, D. *C. R. Chim.* **2003,** *6,* 999–1007. doi:10.1016/j.crci.2003.06.005
3. Valdés-Solís, T.; Valle-Vigón, P.; Álvarez, S.; Marbán, G.; Fuertes, A. B. *Catal. Commun.* **2007,** *8,* 2037–2042. doi:10.1016/j.catcom.2007.03.030
4. Andreozzi, R.; Caprio, V.; Insola, A.; Marotta, R. *Catal. Today* **1999,** *53,* 51–59. doi:10.1016/S0920-5861(99)00102-9
5. Farhataziz; Ross, A. B. Hydroxyl Radical and Perhydroxyl Radical and Their Radical Ions. In *Selected Specific Rates of Reactions of Transients from Water in Aqueous Solution;* Anbar, M., Ed.; Nat. Stand. Ref. Data Ser., Nat. Bur. Stand. (U.S.), Vol. 59; U.S. Government Printing Office: Washington, DC, USA, 1977.
6. Walling, C. *Acc. Chem. Res.* **1975,** *8,* 125–131. doi:10.1021/ar50088a003
7. Borda, J. M.; Elsetinow, R. A.; Strongin, R. D.; Schoonen, M. A. *Geochim. Cosmochim. Acta* **2003,** *67,* 935–939. doi:10.1016/S0016-7037(02)01222-X
8. Cohn, C. A.; Mueller, S.; Wimmer, E.; Leifer, N.; Greenbaum, S.; Strongin, D.; Schoonen, M. A. A. *Geochem. Trans.* **2006,** *7,* No. 3. doi:10.1186/1467-4866-7-3
9. Gournis, D.; Karakassides, M. A.; Petridis, D. *Phys. Chem. Miner.* **2002,** *29,* 155–158. doi:10.1007/s002690100215
10. Javadi Nooshabadi, A.; Larsson, A.-C.; Kota, H. R. *Miner. Eng.* **2013,** *49,* 128–134. doi:10.1016/j.mineng.2013.05.016
11. Javadi Nooshabadi, A.; Hanumantha Rao, K. *Hydrometallurgy* **2014,** *141,* 82–88. doi:10.1016/j.hydromet.2013.10.011
12. Schoonen, M. A. A.; Harrington, A. D.; Laffers, R.; Strongin, D. R. *Geochim. Cosmochim. Acta* **2010,** *74,* 4971–4987. doi:10.1016/j.gca.2010.05.028
13. Xu, J.; Sahai, N.; Eggleston, C. M.; Schoonen, M. A. A. *Earth Planet. Sci. Lett.* **2013,** *363,* 156–167. doi:10.1016/j.epsl.2012.12.008
14. Davila, A. F.; Fairén, A. G.; Gago-Duport, L.; Stoker, C.; Amils, R.; Bonaccorsi, R.; Zavaleta, J.; Lim, D.; Schulze-Makuch, D.; McKay, C. P. *Earth Planet. Sci. Lett.* **2008,** *272,* 456–463. doi:10.1016/j.epsl.2008.05.015
15. Wang, W.; Qu, Y.; Yang, B.; Liu, X.; Su, W. *Chemosphere* **2012,** *86,* 376–382. doi:10.1016/j.chemosphere.2011.10.026
16. Arienzo, M. *Chemosphere* **1999,** *39,* 1629–1638. doi:10.1016/S0045-6535(99)00061-2

17. Matta, R.; Hanna, K.; Chiron, S. *Sci. Total Environ.* **2007,** *385,* 242–251. doi:10.1016/j.scitotenv.2007.06.030
18. Che, H.; Lee, W. *Chemosphere* **2011,** *82,* 1103–1108. doi:10.1016/j.chemosphere.2010.12.002
19. Bae, S.; Kim, D.; Lee, W. *Appl. Catal., B: Environ.* **2013,** *134–135,* 93–102. doi:10.1016/j.apcatb.2012.12.031
20. Li, M.-L.; Yao, Q.-Z.; Zhou, G.-T.; Qu, X.-F.; Mu, C.-F.; Fu, S.-Q. *CrystEngComm* **2011,** *13,* 5936–5942. doi:10.1039/c1ce05478c
21. Lucas, J. M.; Tuan, C.-C.; Lounis, S. D.; Britt, D. K.; Qiao, R.; Yang, W.; Lanzara, A.; Alivisatos, A. P. *Chem. Mater.* **2013,** *25,* 1615–1620. doi:10.1021/cm304152b
22. Bai, Y.; Yeom, J.; Yang, M.; Cha, S.-H.; Sun, K.; Kotov, N. A. *J. Phys. Chem. C* **2013,** *117,* 2567–2573. doi:10.1021/jp3111106
23. Xuefeng, Q.; Yi, X.; Yitai, Q. *Mater. Lett.* **2001,** *48,* 109–111. doi:10.1016/S0167-577X(00)00288-3
24. Kar, S.; Chaudhuri, S. *Chem. Phys. Lett.* **2004,** *398,* 22–26. doi:10.1016/j.cplett.2004.09.028
25. Wang, D.-W.; Wang, Q.-H.; Wang, T.-M. *CrystEngComm* **2010,** *12,* 755–761. doi:10.1039/b917941k
26. Li, W.; Döblinger, M.; Vaneski, A.; Rogach, A. L.; Jäckel, F.; Feldmann, J. *J. Mater. Chem.* **2011,** *21,* 17946–17952. doi:10.1039/c1jm13336e
27. Parkhurst D. L.; Appelo C. A. J. *User's guide to PHREEQC (Version 2);* Water-Resources Investigations Report 99-4259; U.S. Geological Survey Publications, 1999.
28. Williamson, M. A.; Rimstidt, J. D. *Geochim. Cosmochim. Acta* **1994,** *58,* 5443–5454. doi:10.1016/0016-7037(94)90241-0
29. Shu, H.-Y.; Chang, M.-C. *J. Hazard. Mater.* **2005,** *125,* 96–101. doi:10.1016/j.jhazmat.2005.05.016
30. Matthews, R. D. Transformation and Decolorization of Reactive Phthalocyanine Dyes. Ph.D. Thesis, Georgia Institute of Technology, Atlanta, GA, USA, 2003.
31. Jones, G. C.; van Hille, R. P.; Harrison, S. T. L. *Appl. Microbiol. Biotechnol.* **2013,** *97,* 2735–2742. doi:10.1007/s00253-012-4116-y
32. Weerasooriya, R.; Makehelwala, M.; Bandara, A. *Colloids Surf., A* **2010,** *367,* 65–69. doi:10.1016/j.colsurfa.2010.06.023
33. Navalon, S.; Alvaro, M.; Garcia, H. *Appl. Catal., B: Environ.* **2010,** *99,* 1–26. doi:10.1016/j.apcatb.2010.07.006
34. Lin, Y.-Y.; Wang, D.-Y.; Yen, H.-C.; Chen, H.-L.; Chen, C.-C.; Chen, C.-M.; Tang, C.-Y.; Chen, C.-W. *Nanotechnology* **2009,** *20,* 405207. doi:10.1088/0957-4484/20/40/405207
35. Scherrer, P. *Nachr. Ges. Wiss. Goettingen, Math.-Phys. Kl.* **1918,** *26,* 98–100. http://www.digizeitschriften.de/dms/resolveppn/?PPN=GDZPPN002505045

License and Terms

BEILSTEIN JOURNAL OF NANOTECHNOLOGY

DFT study of binding and electron transfer from colorless aromatic pollutants to a TiO_2 nanocluster: Application to photocatalytic degradation under visible light irradiation

Corneliu I. Oprea, Petre Panait and Mihai A. Gîrțu*

Full Research Paper

Open Access

Address:
Department of Physics, Ovidius University of Constanța, Constanța 900527, Romania

Email:
Mihai A. Gîrțu* - mihai.girtu@univ-ovidius.ro

* Corresponding author

Keywords:
colorless aromatic pollutants; density functional theory; photocatalytic degradation; titanium dioxide; visible light irradiation

Beilstein J. Nanotechnol. **2014,** *5,* 1016–1030.
doi:10.3762/bjnano.5.115

Received: 09 February 2014
Accepted: 10 June 2014
Published: 11 July 2014

This article is part of the Thematic Series "Nanomanipulation and environmental nanotechnology".

Guest Editor: E. Gnecco

Abstract

We report results of density functional theory (DFT) calculations on some colorless aromatic systems adsorbed on a TiO_2 nanocluster, in order to explain experimental results regarding the photocatalytic degradation of these pollutants under visible light irradiation. Based on our modeling, we are able to clarify why transparent pollutants can degrade under visible light in the presence of a catalyst that absorbs only in the UV, to explain experimental data regarding differences in the efficiency of the degradation process, and to state the key requirements for effective water-cleaning. For that purpose, we analyze the absorption spectrum of the free and adsorbed molecules, the binding configurations, the matching of the energy levels with the oxide catalyst and the likelihood of the charge-transfer to the substrate. The comparison between several colorless aniline and phenolic systems allows a correlation between the chemical structure and the degradation rate of these pollutants.

Introduction

Titania, TiO_2, has been widely used as photocatalyst for environmental applications [1-6], particularly for waste water purification. Due to its large band gap TiO_2 absorbs only UV radiation, a fact that limits the efficiency and keeps the costs of the photocatalytic degradation of environmental pollutants high. To be used under visible light irradiation, in the range of wavelengths where the solar spectrum has its maximum, the electronic band structure of the photocatalyst has to be modified in various ways [6]. Alternative approaches to the modification of the TiO_2 photocatalyst are the self-sensitized degradation of

dyes which absorb visible light [7,8] and the photocatalytic degradation of colorless organic compounds by formation of a charge-transfer-complex, CTC [9,10]. The assumption of a surface CTC in the visible light catalysis was supported by subsequent work on various other types of systems, such as phenolic compounds [11,12], fluoroquinolone antibacterial agents [13], and various colorless aromatic pollutants [14].

Despite the extensive experimental work, the role of the key factors that influence the microscopic mechanism of the photocatalytic processes is not entirely understood. Our goal is to answer a few key questions, regarding photocatalytic degradation: i) Why can transparent pollutants degrade under visible light in the presence of a catalyst that absorbs only in the UV? ii) Why are some pollutants degraded more efficiently than others? iii) What are the requirements for an effective water-cleaning process? To answer these questions we start from an analogy with the photoelectrochemical Grätzel cells [15,16]. We argue here that efficient photocatalytic degradation of pollutants under visible light irradiation has to meet similar requirements to the ones of the dyes in Grätzel cells. In particular, the anchoring mode of the pollutant to the TiO_2 surface influences the electron transfer [17]. The most commonly used anchoring group is the carboxylic acid group (–COOH) [16]. It ensures strong binding of the dye on the surface and promotes the charge transfer. The anchoring of the salicylate group on TiO_2 has also been studied [18,19]. At the surface, both substituent groups of a benzene derivative are involved in the complexation of colloidal titanium dioxide [18]. This results in the formation of a six-atom ring with a chelating type of bonding to the same Ti(IV) ion. Similarly, the binding of the salicylic acid to titania was thought as bidentate chelate through the oxygen atoms of –OH and of –OCOH [14,20].

Theoretically, density functional theory (DFT) calculations showed [21-23] that the binding of the carboxy group to titania is bidentate bridging, with the monodentate anchoring being less stable [24-27]. The higher performance of the dyes with both carboxy and hydroxy anchoring groups [28] has led us to revisit earlier studies of a dye with three types of anchoring groups: –OH, –COOH and $–SO_3H$ [29,30]. We showed that although the salicylate does use both the carboxy and hydroxy substituent groups, the binding configuration is not bidentate chelate, as previously thought [14,18-20].

Building upon the experience gained while modeling materials for photoelectrochemical cells, we report here results of DFT and time dependent DFT (TD-DFT) calculations performed on several colorless aromatic pollutants, as well as complex systems consisting of benzene derivatives adsorbed on a TiO_2 nanocluster. To answer the questions raised above we determine the electronic structure and the optical spectra of the pollutant itself, and find where the deprotonation is more likely to take place. We also simulate the pollutant–catalyst system to analyze the binding configurations. We discuss the energy level alignment between the pollutant and the catalyst as well as the charge transfer between the pollutants and the oxide. We compare our theoretical results with the experimental data available, particularly with the work of Wang et al. [14] on phenol (Ph), benzoic acid (BA), *p*-hydroxybenzoic acid (pHBA) and salicylic acid (SA), which attempted a correlation between the efficiency of photocatalytic degradation and the chemical structure of the pollutants over TiO_2.

Results and Discussion

This section is divided in five parts. The first describes the computational details whereas the second focuses on the optimized geometry and electronic structure of the free pollutants. The third subsection presents the binding of the pollutants to the titania nanocluster, the fourth presents the optical properties of the adsorbed pollutants, and the last subsection attempts to explain the experimental data as well as the key requirements for efficient photodegradation based on theoretical arguments.

Computational details

The structures of all pollutants were optimized in neutral as well as deprotonated forms, using DFT [31-33], with the B3LYP exchange–correlation functional [34,35] and the double-ζ DZVP basis set including polarization functions for the valence electrons [36] of the free pollutants. In the case of the more complex pollutant–catalyst system the less demanding 3-21G(d) basis set was used for geometry optimization. All optimized structures were checked for stability by means of vibrational analyses. Time-dependent DFT [37] calculations of the molecular orbitals and the electronic transitions were performed in water by means of the polarizable continuum model (PCM) [38,39]. We used the same B3LYP functional and TZVP basis sets [36]. In the case of the pollutants adsorbed on the catalyst, the electronic states were accurately computed by using DZVP basis sets [40]. The Gaussian03 package [41] was used in all calculations.

Free pollutants – electronic structure and optical properties

During the photocatalytic degradation the benzene derivatives (phenol, Ph, benzoic acid, BA, *p*-hydroxybenzoic acid, pHBA, and salicylic acid, SA) undergo various processes, including deprotonation. We first perform a comparative analysis of the likelihood of the deprotonation process. For that, we found the optimized geometries and determined the total energy for all four aromatic pollutants in neutral and their deprotonated forms. The simulations of the deprotonated forms were performed by

taking away a proton from the anchoring group, as it generally happens when the molecule is bound to the substrate. The optimized structures are shown in Figure 1.

Obvious differences between the geometries of the neutral and deprotonated forms are observed for salicylic acid. In the case of doubly deprotonated SA the carboxy group moves away from the plane of the aromatic ring by 86.2°, whereas for the form that is singly deprotonated at the carboxy group the torsion angle is 48.7°. A more careful analysis also reveals some slight differences between the bond lengths and some small distortions of the bond angles but these aspects are not of crucial importance in the following. The key question is at which anchoring group the deprotonation is more likely to take place. To find the answer we can look at the total energy of the pollutants as well as at the proton affinity, *PA*, equal to the difference between the energy of the deprotonated form and the energy of the neutral compound [42], reported in Table 1. For both pollutants, the lowest energy between the two singly deprotonated forms is obtained when the hydrogen atom of the carboxy group is removed.

The DFT calculated energies of the key molecular orbitals of the pollutants in neutral and deprotonated forms are represented in the diagram shown in Figure 2. To put everything in perspective we also represented the results of DFT calculations

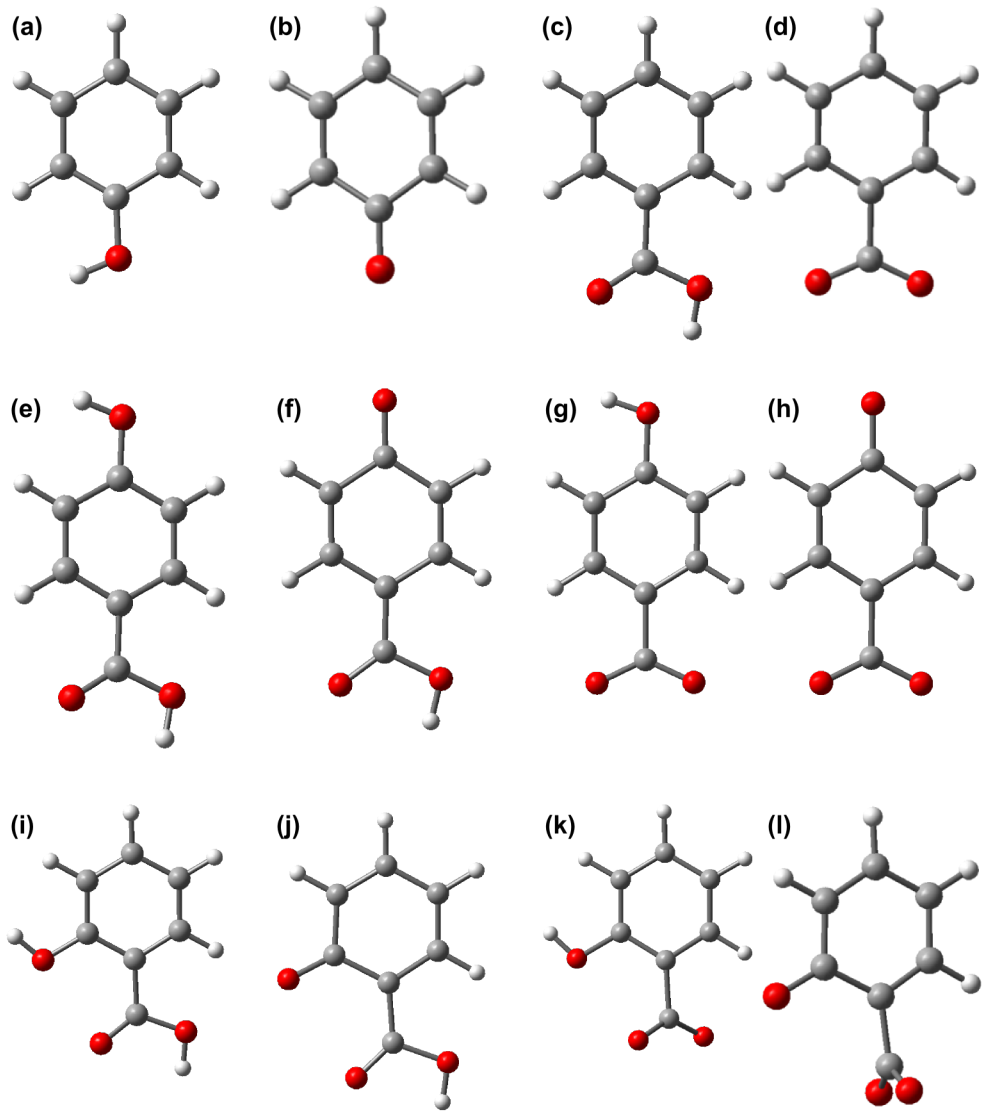

Figure 1: Optimized structure of pollutants in neutral and deprotonated forms calculated at DFT/B3LYP/DZVP level: a) neutral and b) deprotonated Ph, c) neutral and d) deprotonated BA, e) neutral, f) and g) deprotonated, h) doubly deprotonated pHBA, i) neutral, j) and k) deprotonated, l) doubly deprotonated SA.

Table 1: Proton affinities of pHBA and SA in neutral and various deprotonated forms, in water, based on DFT calculations at B3LYP/TZVP level. The labeling corresponds to the one used in Figure 1.

pHBA	(e)	(f)	(g)	(h)
PA (eV)	—	12.97	12.81	26.00
SA	(i)	(j)	(k)	(l)
PA (eV)	—	13.01	12.78	26.09

for TiO_2 clusters [23], particularly the edges of the valence and conduction bands of titania. As discussed in [23,43], and the references therein, DFT calculations on finite size clusters tend to overestimate the gap with respect to the experimental values. It can be seen that the energy difference between the lowest unoccupied molecular orbital (LUMO) and the highest occupied molecular orbital (HOMO) is larger for all pollutants than the calculated band gap of the semiconductor. As a result, the absorption spectra of the free pollutants have peaks further in the UV region than the catalyst. Another important observation is related to the energy level alignment between the pollutants and the catalyst. As all LUMOs of the pollutants are above the conduction band edge of TiO_2, the charge transfer to the semiconductor is possible. We note that the energies of the deprotonated forms are shifted upwards with respect to the neutral pollutants, as expected due to the missing proton.

The electronic spectra of the pollutants, simulated by TD-DFT calculations, are displayed in Figure 3. The spectra are all in the UV, as expected since the pollutants are all colorless, and in agreement with the results of DFT calculations presented in Figure 2. The energy of the electronic transitions, obtained by TD-DFT is a better indicator of the gap than the LUMO–HOMO energy difference determined by DFT [23].

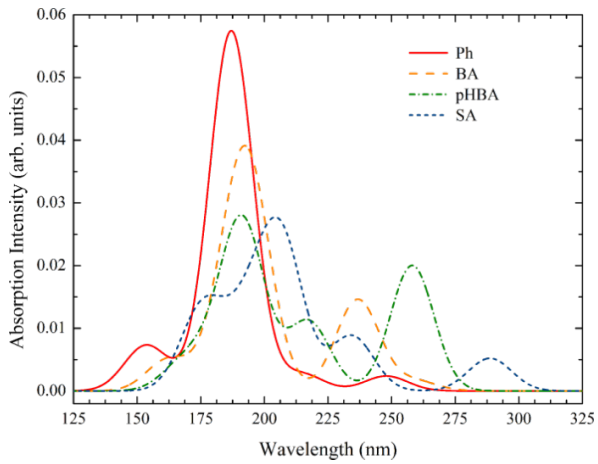

Figure 3: Simulated UV–vis absorption spectra of the first 10 transitions for neutral pollutants in water, calculated by TD-DFT. The spectral lines were convoluted with Gaussian distributions of 20 nm linewidth at half maximum.

Of all pollutants, salicylic acid has peaks at higher wavelengths, just below 300 nm. The spectrum of Ph has a HOMO→LUMO transition at 248 nm, a HOMO→LUMO+1 transition at 215 nm and HOMO−1→LUMO transitions at 187 nm. In the case of BA the transitions are at 259 nm (HOMO→LUMO), 237 nm (HOMO−1→LUMO), and 192 nm (HOMO→LUMO+1). Similarly, for pHBA we found transitions at 258 nm (HOMO→LUMO), 217 nm (HOMO→LUMO+1), and 191 nm (HOMO−1→LUMO+1). Finally, in the case of SA the spec-

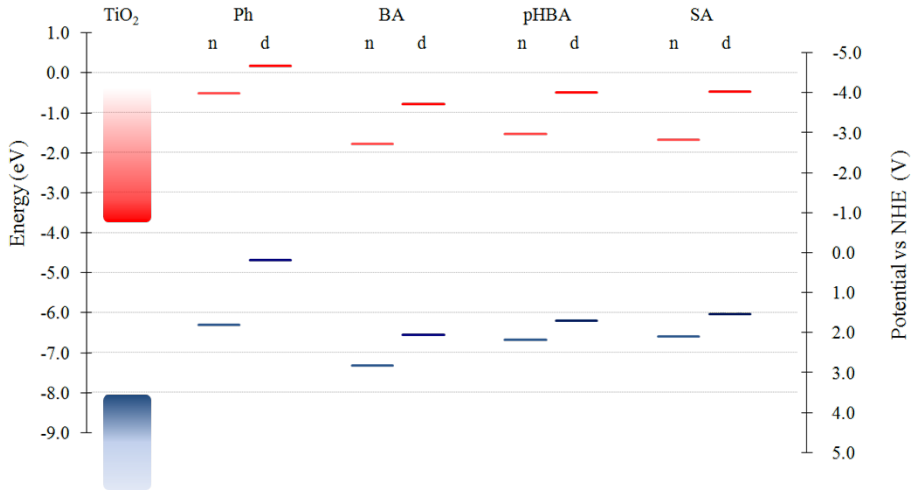

Figure 2: Diagram of energy with respect to vacuum as well as potential versus the normal hydrogen electrode (NHE) of pollutants in both neutral and deprotonated forms, calculated at DFT/B3LYP/TZVP level in solution. In the case of pHBA and SA the deprotonation is on the carboxy group.

trum is closest to the visible range: 289 nm (HOMO→LUMO), 234 nm (HOMO−1→LUMO), and 207 nm (HOMO→LUMO+1). All transitions have π–π* character, for all pollutants. The HOMO→LUMO transitions are weak, the most intense peaks being located for all four compounds in the range of 187–207 nm. These strong transitions involve levels just below HOMO and/or just above LUMO.

Before ending this section we present in Figure 4 the key molecular orbitals of the pollutants, as they will be useful in identifying in a later section the MOs of the complex pollutant–catalyst system.

Pollutant adsorption – binding configurations

As argued in the Introduction, the anchoring modes of the pollutants to the catalyst surface are of crucial importance for the charge transfer. But before discussing adsorption, a few comments regarding the titania cluster are in place. We model TiO_2 nanoparticles by a geometry optimized cluster with the molecular formula $Ti_{24}O_{50}H_4$. Prior to optimization, the cluster was cut from the experimental anatase structure with (101) and (001) surfaces [44]. The optimization led to some slight distortions from the lattice geometry, which lowered the surface energy. To prevent the occurrence of dangling bonds for some peripheric oxygen atoms and to avoid the problem of the surface states in the gap [45] we introduced four hydrogen atoms [29,46]. The resulting $Ti_{24}O_{50}H_4$ cluster has a length of 12.76 Å and a width of 7.39 Å and provides a reasonable compromise between accuracy and computational costs given the small size of the pollutant molecules [29]. One last comment on this topic is related to the nature of the states in the valence and conduction band of titania. The valence band is dominated by the contributions from the p orbitals of oxygen, whereas the conduction band is dominated by the d orbitals of the Ti atoms [29,46].

We start our discussion of adsorption with Ph, which, after deprotonation, can bind to the (101) surface of the substrate through the oxygen atom. This is shown in Figure 5, which displays the optimized structure resulting from the DFT calculations. We note that the geometry optimization was performed for all pollutants starting with the molecule distanced from the

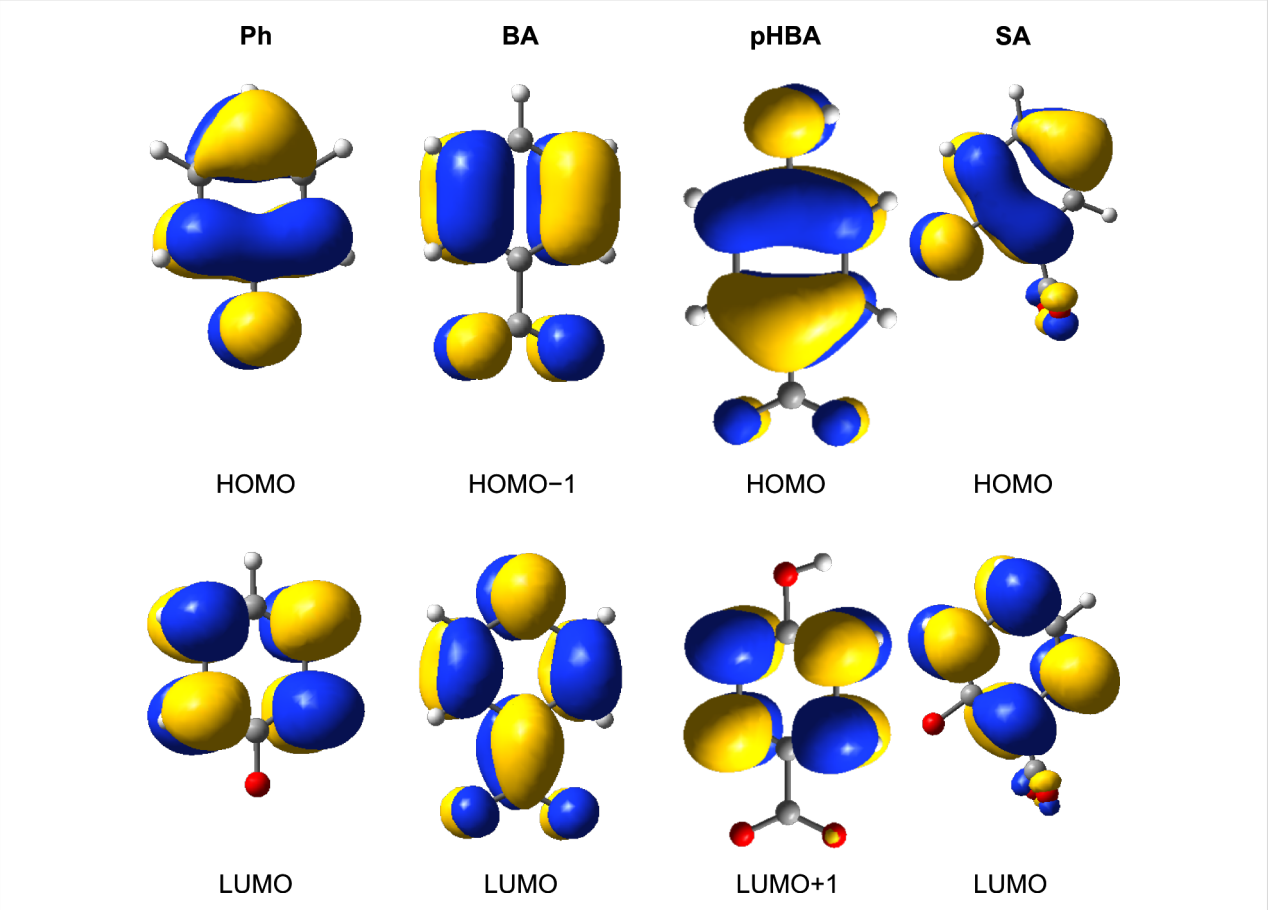

Figure 4: Isodensity surfaces (0.03 *e*/bohr^3) of the key molecular orbitals of the deprotonated pollutants, calculated at DFT/B3LYP/ TZVP level in water. In the case of pHBA and SA the deprotonation is on the carboxy group.

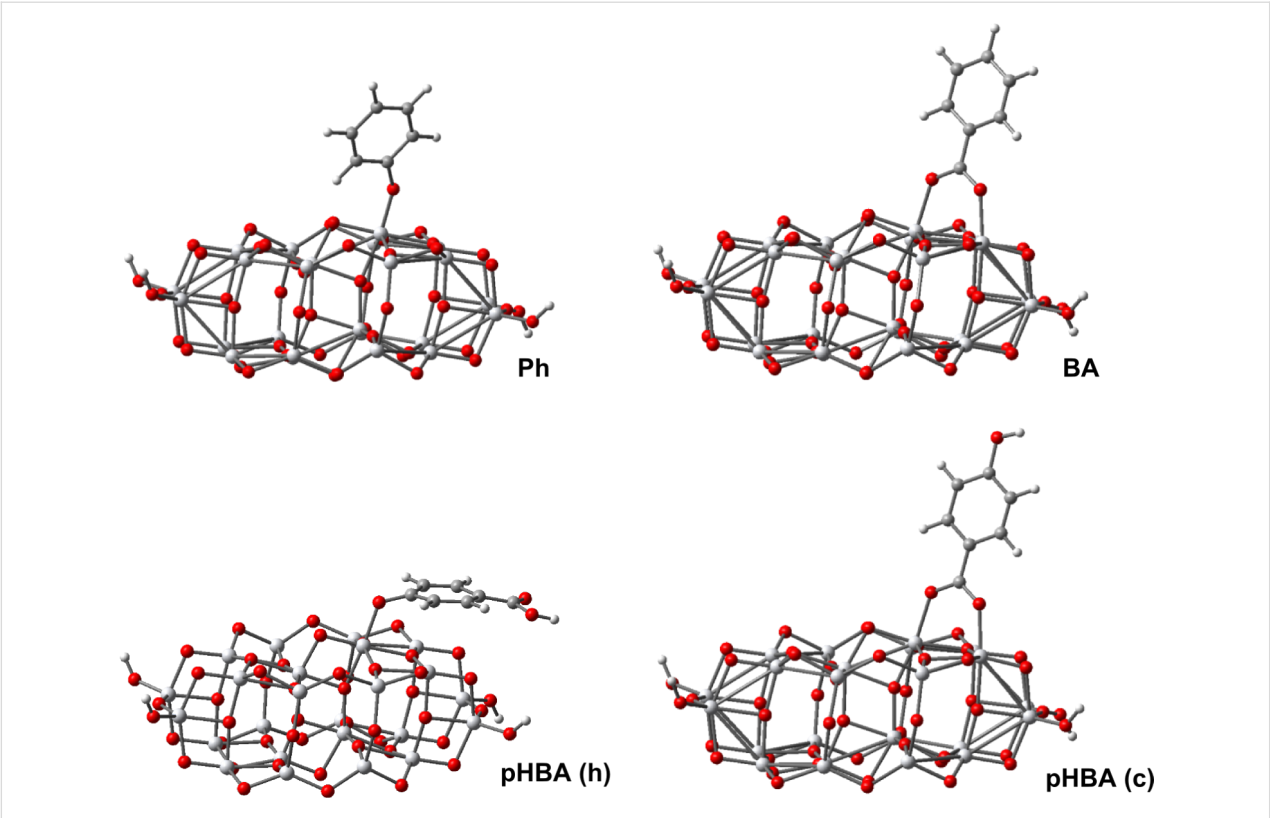

Figure 5: Optimized geometry of the pollutant-catalyst systems calculated at DFT/B3LYP/3-21G* level; pHBA is anchored either through the hydroxy (h) or the carboxy (c) groups.

cluster. The final geometry with pollutants bound to the Ti atoms of the (101) surface was robust with respect to variations in the initial configuration. The distances and angles relevant to the binding of Ph to the titania cluster are reported in Table 2. The dihedral angle τ, which is measured between the plane of the ring and the surface of the cluster (defined by three adjacent Ti ions), is 71.1° tilted away from the normal plane.

In the case of BA, the adsorption is through the carboxy group. Experimental studies have shown that carboxylic acid groups can have various binding configurations with the Ti(IV) ions, ranging from monodentate ester-like binding [47], bidentate bridging [48], or both bidentate chelate and bridging [49,50]. However, theoretical calculations demonstrated that the preferred anchoring is bidentate bridging, with one proton transferred to a nearby surface oxygen [22,24-26]. Our calculations for BA are consistent with these earlier results, the bidentate bridging being the preferred adsorption mode, as shown in Figure 5b. The Ti–O bond distances reported in Table 2, are different, 2.058 Å and 1.991 Å the axis of the molecule being slightly tilted. The dihedral angle is 86.1° almost perpendicular to the surface of the catalyst.

Table 2: Bond distances and bond angles relevant to the binding of the pollutants to the catalyst, after geometry optimization at DFT/B3LYP/3-21G* level; pHBA is anchored either through the hydroxy (h) or the carboxy (c) groups.

parameter	Ph	BA	pHBA (h)	pHBA (c)
r(Ti–O)	1.835 Å	—	1.940 Å	—
r(Ti–O1)	—	2.058 Å	—	2.049 Å
r(Ti–O2)	—	1.991 Å	—	1.985 Å
θ(Ti–O–C)	145.5°	—	120.2°	—
θ(Ti–O1–C)	—	128.3°	—	128.7°
θ(Ti–O2–C)	—	131.0°	—	131.0°
τ	71.1°	86.1°	13.6°	84.0°

For pHBA there are two possible anchors, one is the carboxy group, as in the case of BA, the other is the hydroxy group as for Ph. Our simulations provided different total energies for the two cases, the preferred binding being through the carboxy group, by an energy difference of about 1 eV. Such a result is not a surprise, as the strength of the mechanical adhesion is higher when two Ti–O bonds are involved instead of just one [45]. We also note the different orientation of the aromatic ring in the two cases. When the binding is through the carboxy group the aromatic ring is almost perpendicular to the surface of the catalyst ($\tau = 84.0°$). In contrast, when the binding is of the (h)-type the ring is tilted almost parallel to the surface ($\tau = 13.6°$), reminding of π stacking interactions.

In the case of SA adsorbed on TiO_2 previous studies claimed that in the salicylate complex formed at the interface both substituent groups are involved, which leads to the formation of a six-atom ring with a chelating type of bonding to the same titanium ion [18,19]. Similarly, the binding of SA was thought as bidentate chelate through the oxygen atoms of –OH and of –COOH [14,20]. In a previous paper [29] we showed that for Mordant Yellow-10 anchoring through the SA part can lead to three binding modes, depending on the degree of deprotonation, but none of them was bidentate chelate. Returning to the present study, for SA we performed geometry optimization calculations in three cases. We deprotonated the carboxy group, case (c), the hydroxy group, case (h), and both, case (c&h), when we left one proton to find its equilibrium position on the TiO_2 surface. All these cases are illustrated in Figure 6 and Table 3.

The first question to answer is which of the three types of anchoring is most stable. Our DFT calculations showed the most stable configuration is (c&h). At about 0.58 eV higher lies the SA deprotonated at the hydroxy group (h), followed at 1.18 eV by the configuration obtained by deprotonation of the carboxy group (c). Consequently, we confirm our previous calculation on Mordant Yellow 10, showing that the deprotonation of both groups lowers the energy the most, allowing for stable 'mechanical' structures with three pillars of unequal bond lengths to three different but adjacent Ti(IV) ions. The shortest bond length is the one to the oxygen of the hydroxy group. The triple binding is allowed by a rotation of $\tau' = 62.0°$ of the $–COO^-$ group with respect to the aromatic plane. On the other hand, the benzene ring encloses a dihedral angle of 72.0° with the plane of the surface.

Next, when the deprotonation takes place at the hydroxy group alone, a second bond is formed through the oxygen atom of the carboxy group and the third is a hydrogen bond involving the same carboxy group. We clearly demonstrate that the 'common

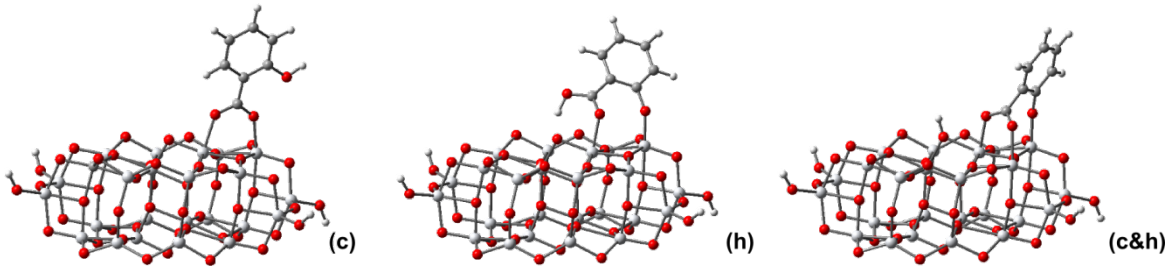

Figure 6: Optimized geometry of SA adsorbed on titania, calculated at DFT/B3LYP/3-21G* level.

Table 3: Distances and angles relevant to the binding of SA to the catalyst, after geometry optimization at DFT/B3LYP/3-21G* level.

parameter	SA (c)	SA (h)	SA (c&h)
r(Ti–O)	—	1.850 Å	1.830 Å
r(Ti–O1)	2.051 Å	—	2.017 Å
r(Ti–O2)	1.969 Å	2.031 Å	2.036 Å
r(O–H)	—	1.112 Å/1.386 Å	—
θ(Ti–O–C)	—	146.0°	163.2°
θ(Ti–O1–C)	128.1°	123.6°	121.2°
θ(Ti–O2–C)	133.0°	—	125.0°
τ	84.8°	45.0°	72.0°
τ′	—	24.6°	62.0°

knowledge' that the binding configuration is in a six ring chelate, suggested by infrared spectroscopy measurements [19,20] or simply assumed by other authors [14,18], is wrong. There are two direct bonds to two different Ti(IV) ions and one indirect bond to an oxygen through the H atom. Again, the third bond is allowed by a rotation of the $–COO^–$ group by $\tau' = 24.6°$. Overall, the plane of the ring is tilted by 45.0° with respect to the surface of the catalyst. The last case involves only the usual bidentate bridging through the carboxy group. This anchoring configuration is overall similar to what we observed for BA and pHBA (c), with comparable bond lengths, bond angles and dihedral angles.

Adsorbed pollutants – optical properties

We recall our conclusion drawn based on Figure 2 and Figure 3, that the absorption bands of the free pollutants are situated further into the UV region than those of the catalyst. In contrast, the TD-DFT simulated optical spectra of the pollutants adsorbed onto the catalyst, displayed in Figure 7, show for all compounds a strong shift toward higher wavelengths. This red-shift is what makes possible the photocatalysis under visible light irradiation. In order to better understand why this red-shift takes place, it is useful to plot the densities of states for all adsorbed pollutants. But before that we take a more careful look at Figure 7.

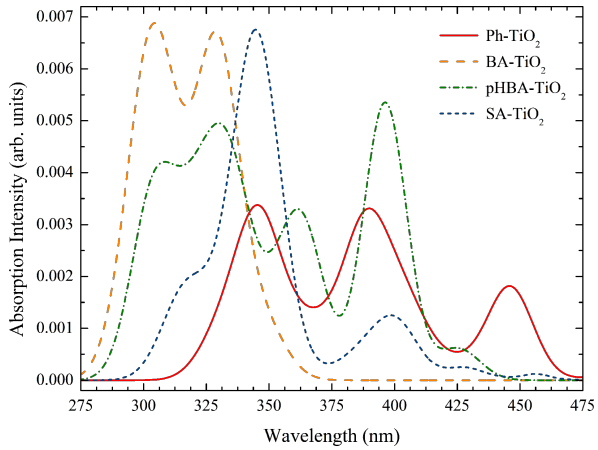

Figure 7: Simulated UV–vis absorption spectra of the pollutants bound to the TiO_2 cluster, calculated by TD-DFT in water. The spectral lines were convoluted with Gaussian distributions of 20 nm linewidth at half maximum.

The first (low energy/high wavelength) bands correspond for all systems to HOMO→LUMO transitions. However, these transitions have very small oscillator strengths, as it can be seen in Table 4. For instance, the only adsorbed pollutant with a band beyond the blue region of the spectrum is Ph, whose first transition is at 524 nm, but the intensity is extremely weak. The stronger UV–vis absorption bands of the adsorbed pollutants are

Table 4: Wavelength, oscillator strength and character of the most intense optical transition for the four pollutants adsorbed on the catalyst, calculated at TD-DFT/B3LYP/DZVP level in water.

pollutant	λ (nm)	*f*	character
Ph/$Ti_{24}O_{50}H_4$	524	0.0002	HOMO→LUMO
	445	0.034	HOMO→LUMO+2
	387	0.038	HOMO→LUMO+13
	345	0.029	HOMO→LUMO+36
BA/$Ti_{24}O_{50}H_4$	354	0.001	HOMO→LUMO
	348	0.019	HOMO−1→LUMO
	330	0.115	HOMO−1→LUMO+2
	306	0.041	HOMO−1→LUMO+4
pHBA/$Ti_{24}O_{50}H_4$ (c)	425	0.013	HOMO→LUMO
	396	0.114	HOMO→LUMO+2
	365	0.040	HOMO→LUMO+6
	335	0.055	HOMO→LUMO+13
	303	0.018	HOMO→LUMO+29
SA/$Ti_{24}O_{50}H_4$ (c&h)	454	0.002	HOMO→LUMO
	428	0.004	HOMO→LUMO+2
	399	0.014	HOMO→LUMO+8
	346	0.047	HOMO→LUMO+19
	319	0.008	HOMO−1→LUMO+6

located below 475 nm. Except for BA, whose key orbital seems to be HOMO-1, for the other adsorbed pollutants the transitions with noticeable oscillator strengths are from the HOMO to states above the conduction band edge, such as LUMO+2.

For the adsorbed Ph we observe three major peaks, one in the visible range, at 445 nm, the other two in the UV range. In the case of the pHBA on the TiO_2 nanocluster, the HOMO→LUMO band at 425 nm has a significant intensity, still much smaller than the next. At the limit of the visible range there is a transition at 396 nm, from HOMO to LUMO+2. When bound to the titania cluster, SA has two weak bands in the visible range and stronger absorption in the UV. Finally, the adsorbed BA has only absorption bands in the UV.

In order to better understand the electronic spectra we looked at the electronic density of the key molecular orbitals, displayed in Figure 8. As expected, the HOMOs have most of the charge located on the pollutant, whereas the LUMOs correspond to the conduction band edge of the catalyst. The excited state of the adsorbed pollutant, identified by comparison with the electron densities of the free pollutants represented in Figure 4, is situated deep into the conduction band for all compounds. For instance, in the case of BA/$Ti_{24}O_{50}H_4$ the corresponding MO is the 52nd from the LUMO, whereas in the other cases there are more than 80 states between the conduction band edge of titania and the excited state of the pollutant. Of crucial importance in the absorption spectra are the MOs mentioned in the transitions reported in Table 4. A common feature of these orbitals is the

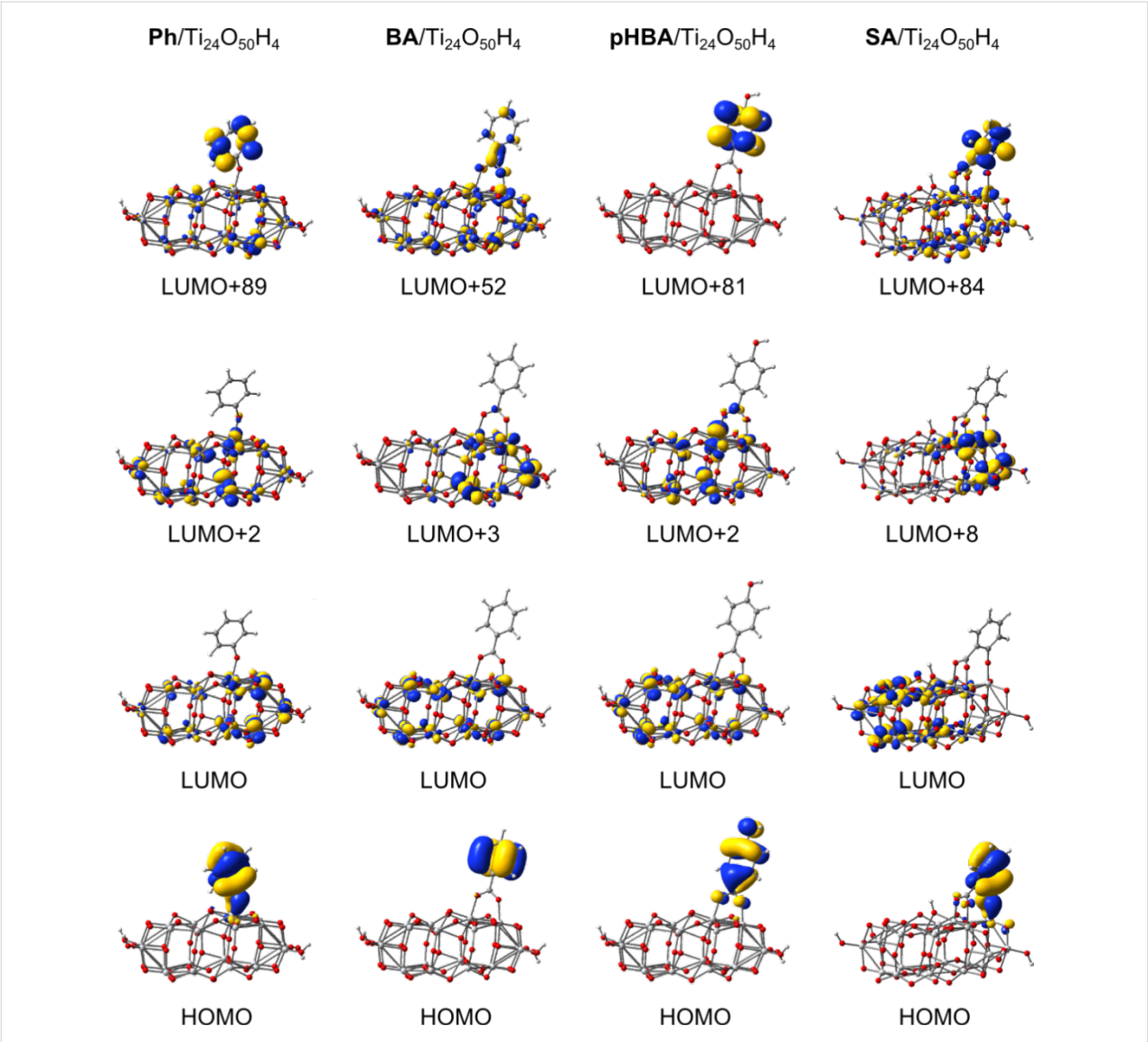

Figure 8: Isodensity surfaces (0.03 *e*/bohr^3) of the key molecular orbitals of the deprotonated and adsorbed forms of pollutants, calculated at DFT/B3LYP/DZVP level in water.

mixed character, the electron density extending from the semiconductor onto the pollutant, as it can be seen from the second row of Figure 8. In fact, it is this delocalization of the charge from the pollutant onto the catalyst in the case of the HOMOs as well as from the semiconductor to the adsorbed molecule, in the case of higher empty states, that make possible the higher wavelength electronic transitions and the absorption in the visible range. Although taken separately both the pollutants and the catalyst absorb in the UV, the states with mixed character lead to allowed optical transitions.

We can even better understand these concepts looking at the density of states (DOS) for the adsorbed pollutants presented in Figure 9. For all four systems, the densities of states have some common features. For instance, the edge of the p-type valence band is located just above −7.9 eV, whereas the d-type conduction band edge is situated just below −3.7 eV. We note that the DFT calculated gap of about 4.2 eV for TiO_2 is overestimated with respect to the experimental value [23,43].

Common to all compounds is that in the gap, significantly higher than the valence band edge, there are two occupied states, HOMO−1 and HOMO, well localized on the pollutants. These two orbitals are separated by about 0.7 eV for three of the four systems, the only exception being BA, for which the two states are almost degenerate (the energy difference is only 0.08 eV). For the three systems for which the HOMO−1 is significantly below the HOMO, only the HOMO plays an

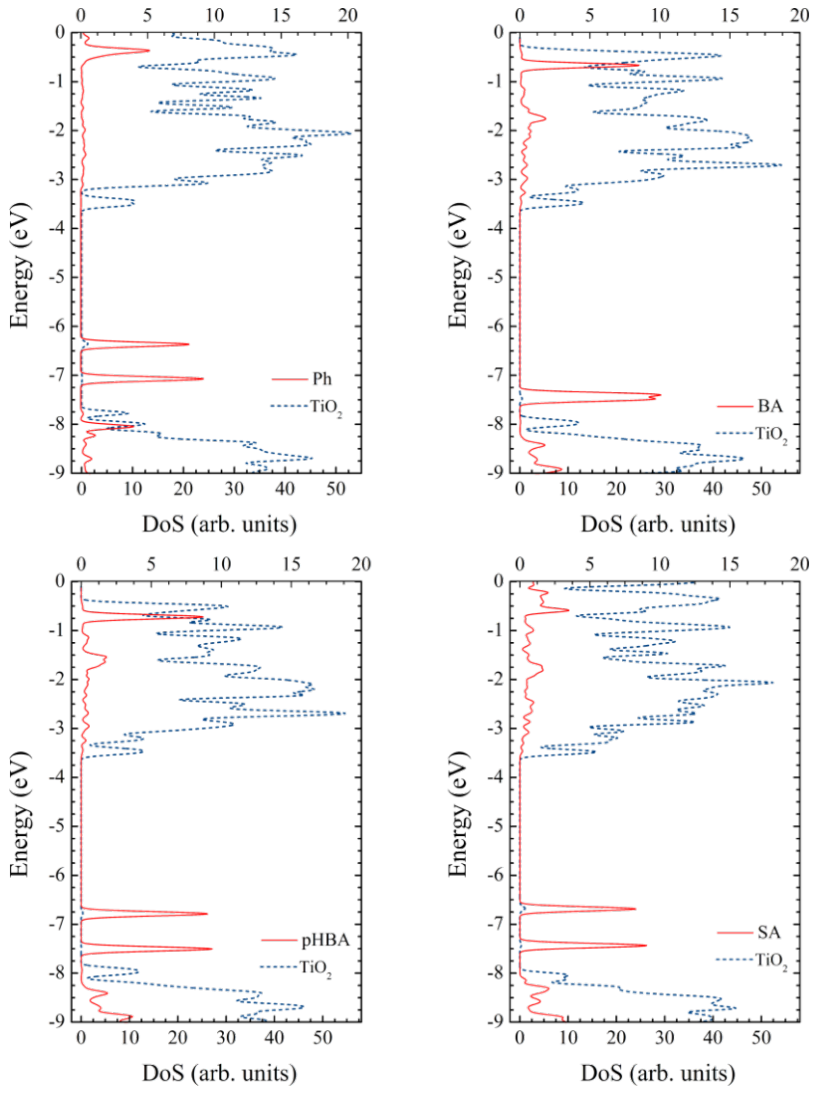

Figure 9: Density of states of the pollutant–catalyst complex systems, calculated at the DFT/B3LYP/DZVP level in water. Bottom scale is for the contribution of the $Ti_{24}O_{50}H_4$ nanocluster (dotted line) whereas the top scale for the contribution of the pollutant (continues line). For all systems, the edge of the p-type valence band of the semiconductor is located at about −7.9 eV, whereas the d-type conduction band edge is situated at about −3.7 eV. The HOMOs of the pollutant are located in the gap of the semiconductor.

important role in the optical spectra. In the fourth case, both HOMO−1 and HOMO can play a role but lying lower in energy, closer to the valence band edge, the energy difference is high and the transitions are in the UV. The energies of the HOMOs are: −6.36 eV, −7.39 eV, −6.78 eV and −6.68 eV for the complex systems with adsorbed Ph, BA, pHBA, and SA, respectively.

In line with the previous discussion, important to note is the mixed character of the states involved in the optical transitions. Looking carefully at the density of states, we can observe that the HOMOs have some small contribution from the catalyst and, similarly, the key states in the conduction band have a small contribution from the pollutant. The weak DOS peaks in the conduction band (note the different scale used) correspond to states with π* character and with sizeable electron density distributed over the pollutant, as shown in Figure 8.

For a more quantitative image we report in Table 5 the contributions to the electron density of the MOs involved in the optical transitions. This way we can see that the charge of the HOMOs is not entirely distributed on the pollutant. While BA keeps over 99% of the charge, the other pass more than 13%, 3%, and 11% (for Ph, pHBA, and SA, respectively) to titania. In the conduction band, the picture reverses, as most of the charge is on titania. However, even in this case there are states with a sizeable charge located on the pollutant.

Table 5: Contributions of pollutant, anchor group, and substrate, in %, to the electron density of MOs involved in lowest electronic transitions, calculated at DFT/B3LYP/DZVP level.

MO	pollutant	anchor	$Ti_{24}O_{50}H_4$
phenol			
HOMO	86.95	19.09	13.05
LUMO	0.14	0.02	99.86
LUMO+2	1.29	0.63	98.71
LUMO+89	42.65	0.01	57.35
benzoic acid			
HOMO	99.58	0.67	0.42
LUMO	0.57	0.38	99.43
LUMO+2	0.15	0.01	99.85
LUMO+52	11.41	4.61	88.59
***p*-hydroxybenzoic acid**			
HOMO	96.29	8.86	3.71
LUMO	0.45	0.29	99.55
LUMO+2	0.04	0.001	99.96
LUMO+81	91.59	0.32	8.41
salicylic acid			
HOMO	88.33	21.84	11.67
LUMO	0.27	0.14	99.73
LUMO+8	2.48	1.49	97.52
LUMO+84	31.81	2.38	68.18

The data reported in Table 5 allow us to draw additional conclusions regarding the likelihood of the electron transfer. In Marcus' theory of the electron transfer [51-53] an important factor in the expression of the electron transfer rate is the electronic matrix element describing the electronic coupling between the excited state of the pollutant and a state in the conduction band of the catalyst. When the orbitals of the two separate components are known, an indicator of the strength of the matrix element may be the overlap between those states. When the orbitals of the entire system are available, as it is the case in our work, we can alternatively look at the degree of mixing indicated by the electron density present on each component and at the electron density on the anchoring group that binds the pollutant to the surface of the catalyst. Taking another look at Figure 8, we note that the flow of charge from the pollutant to the catalyst has to take place through the anchor. If the electron density on the anchor is high in the donor state, the tendency for charge transfer has to be stronger. The states with little density on the atoms of the anchoring group (such as the HOMO of pHBA/TiO_2, which has a nodal plane through the center of the carboxy group), are less likely to favor a charge transfer. Table 5 reports electron densities on the anchoring group for each pollutant–catalyst system. Comparing the MOs involved in the main optical transitions, LUMO+2 for Ph and LUMO+8 for SA, we see that the percentage of the charge localized on the pollutant and on the anchoring group is about two times larger for SA, suggesting a more efficient charge transfer.

One last comment in this section refers to the role of the vibronic coupling effects on the charge transfer to the TiO_2 cluster. In the case of Grätzel cells it has been shown [54,55] that the kinetics of the electron transfer from an excited dye to the titania nanoparticle may be influenced by the vibrational motion of nuclei. The vibronic perturbation, due to the interplay of electron–electron interactions and the internal vibrations of the benzene derivative, may facilitate the charge transfer also in the case of photocatalytic degradation of the pollutants studied here.

Discussion and comparison with experimental data

In this section we compare our theoretical results with the experimental data available, particularly with the work of Wang

et al. [14], who showed that BA can hardly be degraded and, for the other three, the order of the degradation efficiency is: SA > Ph > pHBA. The questions we attempt to answer are: Why do some pollutants degrade faster than others? What are the requirements for an efficient photocatalytic degradation of the pollutants under visible light irradiation? We base our answer on an analogy with the photoelectrochemical Grätzel cells [15,16]. An efficient photocatalytic degradation under exposure to visible light requires: i) strong adsorption of the pollutant to the catalyst, ii) intense absorption of the pollutant or the combined pollutant–catalyst system in the visible range of the spectrum, iii) proper energy level alignment of the excited state of the pollutant and the conduction band edge of the catalyst, and iv) fast charge transfer from the pollutant to the catalyst. Other requirements would regard the chemical reactions that take place after the charge transfer but we will not address those issues here.

Starting with the first criterion, all four pollutants studied here can bind to the catalyst. However, the strength of the bond is not the same, as at one limit SA can exhibit a triple bond, whereas Ph can form only a single bond. Binding through the carboxy group is most likely bidentate bridging, in agreement with various theoretical observations [22,24-26,29,46] and in contrast to some other opinions [56]. Also, the binding of SA involves both substituent groups, but does not lead to the formation of a six-atom ring with a chelating type of bonding to the same Ti(IV) ion, as previously considered [14,18-20,57]. Instead, the proton migrates on the surface leaving all three oxygen atoms available for bonds to three adjacent Ti ions. Moreover, even if the proton were kept by the carboxy group, the binding would still not be chelate and an additional H-bond would be formed.

Checking the four colorless pollutants studied here against the second criterion, we note that BA/TiO_2 has extremely poor absorption in the visible range. The other systems have some absorption bands at low wavelengths, due to the mixed character of the key MOs. For instance the HOMOs, localized mostly on the pollutant, have some small contribution from the catalyst, whereas for some states in the conduction band the situation is reversed. As a consequence, low energy transitions that were forbidden become allowed. Based strictly on the absorption (see Figure 7) we would be led to the conclusion that adsorbed Ph should degrade faster than SA (which has weak bands at 454 nm and 428 nm) and pHBA (425 nm).

The third criterion, asking that the excited state of the pollutant lies higher than the conduction band edge of the catalyst, is met by all four pollutants. Here, an observation regarding a running controversy may be useful, especially as it paves the way for the discussion of the next criterion. Using arguments based on Marcus' theory of electron transfer and making some simplifying assumptions, it was suggested [58] that the larger the 'driving force' (i.e., the difference in energy between the excited state of the molecule and the conduction band edge of the semiconductor) the higher the injection rate. However, there are some experimental observations [29,59-62] backed by some arguments derived through molecular modeling [29,46], which contradict this claim, suggesting that in practice a large driving force is not necessarily a guarantee for high electron transfer rates.

The forth criterion, requiring a fast charge transfer from the pollutant to the substrate, is more difficult to analyze. One of the factors that influence the transfer rate is the matrix element, which, in turn, can be correlated with the overlap integral between the two states. The emphasis on the orbital overlap was underlined long ago [63] suggesting that the π^* orbitals of the carboxy group would promote rapid electron injection into the conduction band of TiO_2, due to its d-symmetry, but not that of SnO_2 or ZnO, which have predominantly s-character. Keeping in mind that for Grätzel cells the charge transfer is optimized in the case of a strong overlap between the dye and the semiconductor [18], which is favored by the presence of charge on the anchor, by analogy, in the case of the pollutant–catalyst system, the electron density on the binding group can provide some information regarding the likelihood of the charge flow. We found that such a comparison favors SA against Ph and both against pHBA.

A summary of the present discussion is displayed schematically in Figure 10. The left panel shows the density of states and reveals the mixed character of the key orbitals, such that, due to charge delocalization optical transitions in the visible become possible. The diagram in the central panel illustrates the energy level alignment and the position of the MOs involved in the excitation by absorption of visible light and in the electron transfer from the pollutant to the catalyst. Although typically the 'driving force' for the charge transfer is defined [53,58] as the difference between the energies of the excited state (LUMO+84, in our case) and of the conduction band edge (LUMO), here it may be more meaningful to consider the LUMO+8 orbital, which is much closer in energy and has a higher overlap with the LUMO. In the right panel the corresponding molecular orbitals are grouped to point out the electro-optical processes but they also presented the unusual anchoring, the charge delocalization as well as the pathways for charge flow.

Summing up, after checking whether the initial requirements for efficient photocatalytic degradation are met, we found that BA

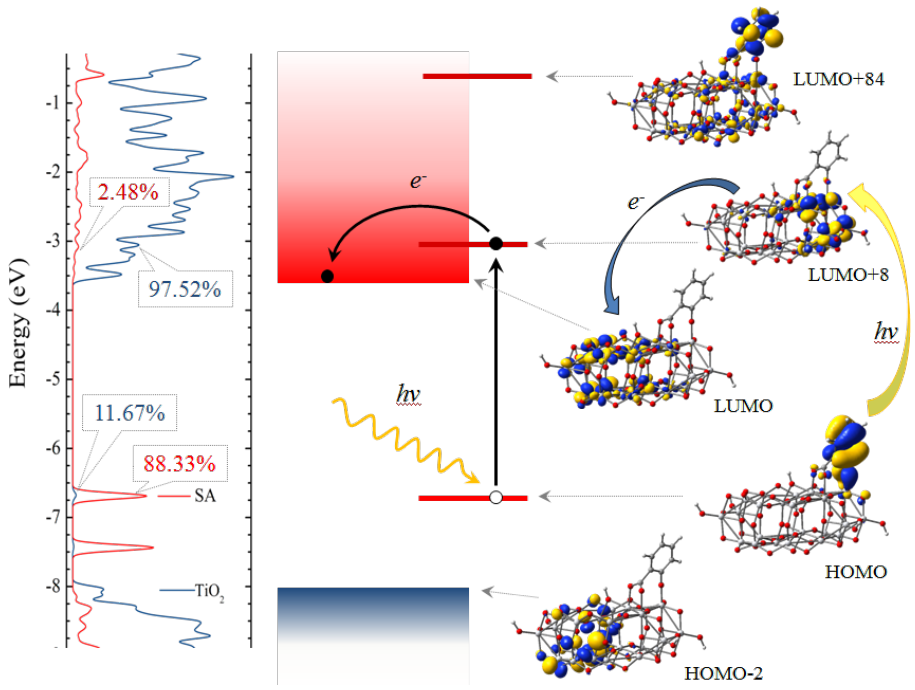

Figure 10: Schematic illustration of electro-optical processes that initiate the photocatalytic degradation of transparent pollutants on titania: (left) density of states, revealing the mixed character of the key MOs, (center) diagram showing the energy level alignment, the photoexcitation and the charge transfer, and (right) the molecular orbitals, showing the anchoring geometry and the charge localization.

is disqualified by the poor absorption in the visible range. Of the other three, Ph has strongest optical absorption but it is outperformed by SA likely due to a more efficient electron transfer. We have to state that our approach cannot quantify the four different criteria discussed. Although the comparison with the experimental data is only qualitative, the present approach can explain some of the main features of the degradation curves observed.

Conclusion

We reported results of DFT and TD-DFT calculations performed on several transparent aromatic pollutants as well as complex systems consisting of the benzene derivatives adsorbed on a TiO_2 nanocluster. Our goal was to answer questions such as: Why can colorless pollutants degrade under visible light? Why do some pollutants degrade faster than others? To answer such questions we determined the electronic structure and the optical spectra of the pollutant itself and found where the deprotonation is more likely to take place. We optimized the geometry of pollutant–catalyst systems and shed some new light on the binding configurations of the benzene derivatives onto titania. We were able to dispel some misconceptions regarding the monodentate binding of the carboxy group, six-ring chelate binding of the salicylic acid. We demonstrated that the optimal binding configuration is bidentate bridging for the carboxy group and tridentate to adjacent titanium ions for SA.

We explained why transparent pollutants adsorbed onto a catalyst that absorbs only in the UV can degrade under visible light based on the mixed character of the key MOs involved in optical transitions. These orbitals are delocalized on both the pollutant and the catalyst such that some low energy transitions that were forbidden become allowed. We attempted to explain the experimental facts which state that the efficiency of degradation under visible light irradiation decreases in the sequence SA > Ph > pHBA > BA. Thus, analyzing the pollutants against some requirements for efficient photocatalytic degradation, we found that BA has no absorption in the visible range even bound to the catalyst. Ph has best light absorption but weakest anchoring, pHBA has very weak electron density on the anchor, which hinders the charge transfer, and that SA has strongest binding and offers the best pathways for charge flow.

Acknowledgements

The authors acknowledge partial financial support from SNSF and UEFISCDI under the Romanian-Swiss Research Programme, through the joint grant RSRP #IZERO-142144/1 and PN-II-ID-RSRP-1/2012.

References

1. Fujishima, A.; Zhang, X.; Tryk, D. A. *Surf. Sci. Rep.* **2008,** *63,* 515–582. doi:10.1016/j.surfrep.2008.10.001

2. Frank, S. N.; Bard, A. J. *J. Am. Chem. Soc.* **1977,** *99,* 4667–4675. doi:10.1021/ja00456a024
3. Hoffmann, M. R.; Martin, S. T.; Choi, W.; Bahnemann, D. W. *Chem. Rev.* **1995,** *95,* 69–96. doi:10.1021/cr00033a004
4. Linsebigler, A. L.; Lu, G.; Yates, J. T. *Chem. Rev.* **1995,** *95,* 735–758. doi:10.1021/cr00035a013
5. Friedmann, D.; Mendive, C.; Bahnemann, D. *Appl. Catal., B: Environ.* **2010,** *99,* 398–406. doi:10.1016/j.apcatb.2010.05.014
6. Kumar, S. G.; Devi, L. G. *J. Phys. Chem. A* **2011,** *115,* 13211–13241. doi:10.1021/jp204364a
7. Liu, G.; Li, X.; Zhao, J.; Hidaka, H.; Serpone, N. *Environ. Sci. Technol.* **2000,** *34,* 3982–3990. doi:10.1021/es001064c
8. Chen, C.; Li, X.; Ma, W.; Zhao, J.; Hidaka, H.; Serpone, N. *J. Phys. Chem. B* **2002,** *106,* 318–324. doi:10.1021/jp0119025
9. Agrios, A. G.; Gray, K. A.; Weitz, E. *Langmuir* **2003,** *19,* 1402–1409. doi:10.1021/la026397x
10. Agrios, A. G.; Gray, K. A.; Weitz, E. *Langmuir* **2004,** *20,* 5911–5917. doi:10.1021/la036165d
11. Kim, S.; Choi, W. *J. Phys. Chem. B* **2005,** *109,* 5143–5149. doi:10.1021/jp045806q
12. Li, M.; Tang, P.; Hong, Z.; Wang, M. *Colloids Surf., A* **2008,** *318,* 285–290. doi:10.1016/j.colsurfa.2008.01.001
13. Paul, T.; Miller, P.; Strathmann, T. J. *Environ. Sci. Technol.* **2007,** *41,* 4720–4727. doi:10.1021/es070097q
14. Wang, N.; Zhu, L.; Huang, Y.; She, Y.; Yu, Y.; Tang, H. *J. Catal.* **2009,** *266,* 199–206. doi:10.1016/j.jcat.2009.06.006
15. Grätzel, M. *Nature* **2001,** *414,* 338–344. doi:10.1038/35104607
16. Hagfeldt, A.; Boschloo, G.; Sun, L.; Kloo, L.; Pettersson, H. *Chem. Rev.* **2010,** *110,* 6595–6663. doi:10.1021/cr900356p
17. Lungu, J.; Oprea, C. I.; Dumbrava, A.; Enache, I.; Georgescu, A.; Rădulescu, C.; Ioniță, I.; Cimpoca, G. V.; Gîrțu, M. A. *J. Optoelectron. Adv. Mater.* **2010,** *12,* 1969–1975.
18. Moser, J.; Punchihewa, S.; Infelta, P. P.; Gratzel, M. *Langmuir* **1991,** *7,* 3012–3018. doi:10.1021/la00060a018
19. Tunesi, S.; Anderson, M. A. *Langmuir* **1992,** *8,* 487–495. doi:10.1021/la00038a030
20. Tunesi, S.; Anderson, M. *J. Phys. Chem.* **1991,** *95,* 3399–3405. doi:10.1021/j100161a078
21. Vittadini, A.; Selloni, A.; Rotzinger, F. P.; Grätzel, M. *J. Phys. Chem. B* **2000,** *104,* 1300–1306. doi:10.1021/jp993583b
22. Pastore, M.; De Angelis, F. *Phys. Chem. Chem. Phys.* **2012,** *14,* 920–928. doi:10.1039/c1cp22663k
23. De Angelis, F.; Fantacci, S.; Selloni, A. *Nanotechnology* **2008,** *19,* 424002. doi:10.1088/0957-4484/19/42/424002
24. Srinivas, K.; Yesudas, K.; Bhanuprakash, K.; Rao, V. J.; Giribabu, L. *J. Phys. Chem. C* **2009,** *113,* 20117–20126. doi:10.1021/jp907498e
25. León, C. P.; Kador, L.; Peng, B.; Thelakkat, M. *J. Phys. Chem. B* **2006,** *110,* 8723–8730. doi:10.1021/jp0561827
26. Martsinovich, N.; Troisi, A. *J. Phys. Chem. C* **2011,** *115,* 11781–11792. doi:10.1021/jp2026847
27. Hagberg, D. P.; Yum, J. H.; Lee, H. J.; De Angelis, F.; Marinado, T.; Martin Karlsson, K.; Humphry-Baker, R.; Sun, L.; Hagfeldt, A.; Grätzel, M.; Nazeeruddin, M. K. *J. Am. Chem. Soc.* **2008,** *130,* 6259–6266. doi:10.1021/ja800066y
28. Chen, Y.-S.; Li, C.; Zeng, Z.-H.; Wang, W.-B.; Wang, X.-S.; Zhang, B.-W. *J. Mater. Chem.* **2005,** *15,* 1654–1661. doi:10.1039/b418906j
29. Oprea, C. I.; Dumbravă, A.; Enache, I.; Lungu, J.; Georgescu, A.; Moscalu, F.; Oprea, C.; Gîrțu, M. A. *Phys. Status Solidi A* **2011,** *208,* 2467–2477. doi:10.1002/pssa.201127083
30. Oprea, C. I.; Panait, P.; Lungu, J.; Stamate, D.; Dumbravă, A.; Cimpoesu, F.; Gîrțu, M. A. *Int. J. Photoenergy* **2013,** 893850. doi:10.1155/2013/893850
31. Hohenberg, P.; Kohn, W. *Phys. Rev.* **1964,** *136,* B864–B871. doi:10.1103/PhysRev.136.B864
32. Kohn, W.; Sham, L. J. *Phys. Rev.* **1965,** *140,* A1133–A1138. doi:10.1103/PhysRev.140.A1133
33. Parr, R. G.; Yang, W. *Density-Functional Theory of Atoms and Molecules;* Oxford University Press: New York, 1989.
34. Becke, A. D. *J. Chem. Phys.* **1993,** *98,* 5648–5652. doi:10.1063/1.464913
35. Lee, C.; Yang, W.; Parr, R. G. *Phys. Rev. B* **1988,** *37,* 785–789. doi:10.1103/PhysRevB.37.785
36. Rassolov, V. A.; Ratner, M. A.; Pople, J. A.; Redfern, P. C.; Curtiss, L. A. *J. Comput. Chem.* **2001,** *22,* 976–984. doi:10.1002/jcc.1058
37. Casida, M. E.; Jamorski, C.; Casida, K. C.; Salahub, D. R. *J. Chem. Phys.* **1998,** *108,* 4439–4449. doi:10.1063/1.475855
38. Barone, V.; Cossi, M. *J. Phys. Chem. A* **1998,** *102,* 1995–2001. doi:10.1021/jp9716997
39. Tomasi, J.; Mennucci, B.; Cammi, R. *Chem. Rev.* **2005,** *105,* 2999–3094. doi:10.1021/cr9904009
40. Godbout, N.; Salahub, D. R.; Andzelm, J.; Wimmer, E. *Can. J. Chem.* **1992,** *70,* 560–571. doi:10.1139/v92-079
41. *Gaussian 03,* Revision C.02; Gaussian Inc.: Wallingford, CT, 2004.
42. Wang, Z.; Chu, I. K.; Rodriquez, C. F.; Hopkinson, A. C.; Michael Siu, K. W. *J. Phys. Chem. A* **1999,** *103,* 8700–8705. doi:10.1021/jp9914976
43. Lundqvist, M. J.; Nilsing, M.; Persson, P.; Lunell, S. *Int. J. Quantum Chem.* **2006,** *106,* 3214–3234. doi:10.1002/qua.21088
44. Selloni, A. *Nat. Mater.* **2008,** *7,* 613–615. doi:10.1038/nmat2241
45. Wahab, H. S.; Bredow, T.; Aliwi, S. M. *Chem. Phys.* **2008,** *353,* 93–103. doi:10.1016/j.chemphys.2008.07.017
46. Oprea, C. I.; Panait, P.; Cimpoesu, F.; Ferbinteanu, M.; Gîrțu, M. A. *Materials* **2013,** *6,* 2372–2392. doi:10.3390/ma6062372
47. Falaras, P. *Sol. Energy Mater. Sol. Cells* **1998,** *53,* 163–175. doi:10.1016/S0927-0248(98)00023-3
48. Duffy, N. W.; Dobson, K. D.; Gordon, K. C.; Robinson, B. H.; McQuillan, A. J. *Chem. Phys. Lett.* **1997,** *266,* 451–455. doi:10.1016/S0009-2614(97)00035-3
49. Ma, T.; Inoue, K.; Yao, K.; Noma, H.; Shuji, T.; Abe, E.; Yu, J.; Wang, X.; Zhang, B. *J. Electroanal. Chem.* **2002,** *537,* 31–38. doi:10.1016/S0022-0728(02)01225-1
50. Weng, Y.-X.; Li, L.; Liu, Y.; Wang, L.; Yang, G.-Z. *J. Phys. Chem. B* **2003,** *107,* 4356–4363. doi:10.1021/jp022534n
51. Marcus, R. A.; Sutin, N. *Biochim. Biophys. Acta* **1985,** *811,* 265–322. doi:10.1016/0304-4173(85)90014-X
52. Gao, Y. Q.; Georgievskii, Y.; Marcus, R. A. *J. Chem. Phys.* **2000,** *112,* 3358–3369. doi:10.1063/1.480918
53. Pelet, S.; Moser, J.-E.; Grätzel, M. *J. Phys. Chem. B* **2000,** *104,* 1791–1795. doi:10.1021/jp9934477
54. Minaev, B. F.; Minaeva, V. A.; Baryshnikov, G. V.; Girtu, M. A.; Agren, H. *Russ. J. Appl. Chem.* **2009,** *82,* 1211–1221. doi:10.1134/S1070427209070106
55. Baryshnikov, G. V.; Minaev, B. F.; Minaeva, V. A. *Opt. Spectrosc.* **2011,** *110,* 393–400. doi:10.1134/S0030400X10061025
56. Tachikawa, T.; Yoshida, A.; Tojo, S.; Sugimoto, A.; Fujitsuka, M.; Majima, T. *Chem.–Eur. J.* **2004,** *10,* 5345–5353. doi:10.1002/chem.200400516

57. Tachikawa, T.; Tojo, S.; Fujitsuka, M.; Majima, T. *Chem. Phys. Lett.* **2004,** *392,* 50–54. doi:10.1016/j.cplett.2004.04.115
58. Anderson, N. A.; Lian, T. *Coord. Chem. Rev.* **2004,** *248,* 1231–1246. doi:10.1016/j.ccr.2004.03.029
59. Hara, K.; Sato, T.; Katoh, R.; Furube, A.; Ohga, Y.; Shinpo, A.; Suga, S.; Sayama, K.; Sugihara, H.; Arakawa, H. *J. Phys. Chem. B* **2003,** *107,* 597–606. doi:10.1021/jp026963x
60. Zhang, X.; Zhang, J.-J.; Xia, Y.-Y. *J. Photochem. Photobiol., A: Chem.* **2008,** *194,* 167–172. doi:10.1016/j.jphotochem.2007.08.004
61. Sánchez-de-Armas, R.; San Miguel, M. Á.; Oviedo, J.; Sanz, J. F. *Phys. Chem. Chem. Phys.* **2012,** *14,* 225–233. doi:10.1039/c1cp22058f
62. Chen, R.; Yang, X.; Tian, H.; Wang, X.; Hagfeldt, A.; Sun, L. *Chem. Mater.* **2007,** *19,* 4007–4015. doi:10.1021/cm070617g
63. Anderson, S.; Constable, E. C.; Dare-Edwards, M. P.; Goodenough, J. B.; Hamnett, A.; Seddon, K. R.; Wright, R. D. *Nature* **1979,** *280,* 571–573. doi:10.1038/280571a0

License and Terms

BEILSTEIN JOURNAL OF NANOTECHNOLOGY

Direct nanoscale observations of the coupled dissolution of calcite and dolomite and the precipitation of gypsum

Francesco G. Offeddu*[1], Jordi Cama[1], Josep M. Soler[1] and Christine V. Putnis[2]

Full Research Paper

Open Access

Address:
[1]Institute of Environmental Assessment and Water Research (IDAEA), CSIC, Jordi Girona 18-26, 08034 Barcelona, Catalonia, Spain and [2]Institut für Mineralogie, University of Münster, Corrensstrasse 24 D-48149, Münster, Germany

Email:
Francesco G. Offeddu* - francesco.offeddu@idaea.csic.es

* Corresponding author

Keywords:
atomic force microscopy (AFM); calcite; dissolution–precipitation; dolomite; gypsum

Beilstein J. Nanotechnol. **2014,** *5,* 1245–1253.
doi:10.3762/bjnano.5.138

Received: 21 March 2014
Accepted: 21 July 2014
Published: 11 August 2014

This article is part of the Thematic Series "Nanomanipulation and environmental nanotechnology".

Guest Editor: T. Glatzel

Abstract

In-situ atomic force microscopy (AFM) experiments were performed to study the overall process of dissolution of common carbonate minerals (calcite and dolomite) and precipitation of gypsum in Na_2SO_4 and $CaSO_4$ solutions with pH values ranging from 2 to 6 at room temperature (23 ± 1 °C). The dissolution of the carbonate minerals took place at the (104) cleavage surfaces in sulfate-rich solutions undersaturated with respect to gypsum, by the formation of characteristic rhombohedral-shaped etch pits. Rounding of the etch pit corners was observed as solutions approached close-to-equilibrium conditions with respect to calcite. The calculated dissolution rates of calcite at pH 4.8 and 5.6 agreed with the values reported in the literature. When using solutions previously equilibrated with respect to gypsum, gypsum precipitation coupled with calcite dissolution showed short gypsum nucleation induction times. The gypsum precipitate quickly coated the calcite surface, forming arrow-like forms parallel to the crystallographic orientations of the calcite etch pits. Gypsum precipitation coupled with dolomite dissolution was slower than that of calcite, indicating the dissolution rate to be the rate-controlling step. The resulting gypsum coating partially covered the surface during the experimental duration of a few hours.

Introduction

The overall process of dissolution of carbonate minerals and precipitation of gypsum is relevant in environmental settings, such as the treatment of acid mine drainage (AMD), geological CO_2 sequestration and monument preservation. The use of limestone (calcite) in the treatment of AMD with elevated concentrations of heavy metals and sulfate is common [1-5]. The purpose is to retain metals and neutralize acidity by means of the so-called anoxic limestone drain (ALD) [1-5]. AMD, flowing through benches filled with calcite gravel, dissolves limestone and thereby increases the Ca^{2+} concentration, alkalinity and pH. Because, in general, AMD contains high concentrations of sulfate and metal ions, the dissolution of calcite initi-

ates a coupled reaction chain that allows the system to precipitate sulfate as gypsum and metals (Al^{3+} and Fe^{3+}) as hydroxides:

$$\begin{aligned} CaCO_3 + 2H^+ &\rightarrow Ca^{2+} + 2HCO_3^- \\ Ca^{2+} + SO_4^{2-} + 2H_2O &\rightarrow CaSO_4 \cdot 2H_2O \downarrow \\ Me^{3+} + 3H_2O &\rightarrow Me(OH)_3 \downarrow + 3H^+ \end{aligned} \quad (1)$$

Such coupled processes, in which the dissolution of one phase produces a supersaturation of another phase in the fluid at the mineral-fluid interface and the new phase can precipitate, are well-documented [6-8].

AMD treatment becomes ineffective as soon as the precipitated hydroxides and/or gypsum fully coat the limestone surface and impede further dissolution of calcite. This mechanism is known as passivation or armoring [3,9-16]. While metal phases tend to precipitate between the calcite grains, gypsum tends to precipitate strongly adhered on the dissolving calcite surface, which is the main mechanism responsible for surface passivation [14-17]. This strong attachment of gypsum to the calcite surface results from crystallographic continuity between the two phases, namely "lattice matching" as pointed out by Booth et al. [18]. The fact that the crystallographic structure of gypsum and calcite exhibits parallel rows of cations and anions, and the cation–cation spacing for both minerals is 4.99 Å suggests a favourable overgrowth of the gypsum (010) plane on top of a calcite cleavage surface.

In the context of geological CO_2 sequestration, the interaction between the acidic sulfate-rich brines and carbonate minerals of the reservoir rock promotes calcite dissolution and gypsum precipitation [18-22]. The effect of acid rain on historical monuments, buildings and statue degradation results from the dissolution of limestone by rain containing dissolved atmospheric SO_2 and the subsequent precipitation of gypsum [23-25]. Large amounts of synthetic gypsum can precipitate during industrial processes involving the reaction between calcite and sulfuric acid [26].

The motivation of this study is to learn about the overall process of calcium carbonate mineral (calcite and dolomite) dissolution and gypsum precipitation in acid sulfate solutions at the micro–nanoscale by means of in-situ atomic force microscopy (AFM) experiments. This approach allows for a visualization of the processes occurring at the reacting carbonate surface.

In the literature, many studies deal with carbonate mineral reactivity [27-37]. In particular, the study of calcite dissolution and gypsum precipitation by Booth et al. [18] is relevant for our experimental AFM study as the authors provided SEM and AFM observations (in situ and ex situ) of the overall process of gypsum coating on calcite (causing passivation or armoring) at pH 1 and 2 in mixed HCl and Li_2SO_4 solutions. They reported on i) the reduction of calcite reactivity due to the gypsum coating, ii) the shape of gypsum crystals (rows parallel to the flux) and iii) the relation between anions and cations of the lattices of both calcite and gypsum. It is suggested that the likely match between cations favors the epitaxial overgrowth of the gypsum (010) face on top of the calcite cleavage plane.

In this study we attempt to enhance the current knowledge about the complementary processes of calcite/dolomite dissolution and gypsum precipitation. Two types of solution were used: (1) acid sulfate solution (Na_2SO_4) undersaturated with respect to gypsum and (2) acid sulfate solution ($CaSO_4$) equilibrated with respect to gypsum. The experimental pH ranged from approximately 2 to 6 and the in-situ AFM experiments were run at ambient temperature (23 ± 1°C) and pressure.

Experimental

The experiments were carried out by using a Digital Instruments (Bruker) Nanoscope III AFM equipped with a fluid cell sealed with an O-ring (50 µL volume), in contact mode using Si_3N_4 tips (Bruker, NP-S20) at room temperature (23 ± 1 °C). The scanning frequency was about 3 Hz and the image resolution was of 256 lines per scan, giving an average scan time of one image about every 100 seconds. The scan size ranged from 1 × 1 μm^2 to 15 × 15 μm^2. Images were analyzed with WSxM free software [38].

Single fragments of calcite (Iceland Spar, Chihuahua, Mexico) and crystalline dolomite (Eugui, Navarra, Spain) of approximately 4 × 3 × 1 mm (crystal volume ≈ 12 mm^3) were cleaved immediately prior to experiments and attached to a fixed and oriented Teflon holder with commercial conductive carbon cement (CCC) and mounted in the fluid cell. The cleavage surface of calcite and dolomite is the (104) surface.

Acid solutions were prepared immediately before the experiments by adding the appropriate amounts of reactive analytical grade, $CaSO_4 \cdot 2H_2O$ (Merck pro analysis) and Na_2SO_4 (Grüssing purity 98%), to Millipore MQ water (resistivity = 18 MΩ·cm) (Table 1). The solution pH was adjusted to the chosen pH (approximately from 2 to 6) by adding concentrated H_2SO_4. Measurements of the pH were carried out by using a InoLab pH meter, equipped with a WTW Sentix 21 electrode calibrated with an accuracy of ±0.02 pH units. The electrode was calibrated with Crison buffer solutions at pH 4 and 7. The saturation index (SI) with respect to gypsum and

Table 1: Experimental conditions.

experiment	substrate	pH	electrolyte	Ca_{inp} [mol/L]	Na_{inp} [mol/L]	SO_{4inp} [mol/L]	SI calcite	SI gypsum
cal14	calcite	2.23	Na_2SO_4	—	5.42E−02	3.10E−02	—	—
cal12	calcite	2.20	Na_2SO_4	—	4.62E−02	2.70E−02	—	—
cal9	calcite	2.18	$CaSO_4$	1.60E−02	—	2.50E−02	−11.0	0.05
cal10	calcite	2.18	$CaSO_4$	1.60E−02	—	2.50E−02	−11.0	0.05
dol6	dolomite	2.11	Na_2SO_4	—	1.02E−02	1.00E−02	—	—
dol3	dolomite	2.11	Na_2SO_4	—	2.62E−02	1.80E−02	—	—
dol4	dolomite	2.18	$CaSO_4$	1.60E−02	—	2.50E−02	−11.0	0.05
dol1	dolomite	2.14	Na_2SO_4	—	5.02E−02	3.00E−02	—	—
cal19	calcite	3.37	Na_2SO_4	—	5.56E−02	2.70E−02	—	—
cal8	calcite	3.06	$CaSO_4$	1.50E−02	—	1.60E−02	−9.2	0.00
cal21	calcite	2.92	Na_2SO_4	—	1.12E−02	6.00E−03	—	—
dol5	dolomite	3.00	$CaSO_4$	1.50E−02	—	1.60E−02	−9.2	0.00
dol7	dolomite	3.00	Na_2SO_4	—	2.70E−02	1.40E−02	—	—
cal4	calcite	4.08	$CaSO_4$	1.50E−02	—	1.50E−02	−7.1	−0.01
cal2	calcite	4.03	Na_2SO_4	—	1.12E−02	6.00E−03	—	—
cal6	calcite	4.80	$CaSO_4$	1.50E−02	—	1.50E−02	−5.7	−0.02
cal3	calcite	5.82	$CaSO_4$	1.50E−02	—	1.50E−02	−3.7	−0.02

calcite of the input solutions was calculated by using the PhreeqC code and the PhreeqC database [39].

The experimental strategy consisted of three stages. First, prior to each in-situ experiment an in-air image of a selected region of the cleaved surface was taken to examine the initial topography and surface features of interest (flat/rough areas, steps terraces and edges; Figure 1a and Figure 1d). Secondly, after an appropriate region of the cleavage surface was selected, the Millipore MQ water was injected by using a syringe to fill the available volume of the fluid cell containing the sample (ca. 38 μL) and flow over the mineral surface. Renovation of the Millipore MQ water was performed after each sequential image capture (ca. 1.5 min) to ensure a similar bulk solution concentration as the reaction took place during the experiment and prevent a saturation of the solution during the reaction (close-to-equilibrium approach). During this stage the calcite dissolution rate, R_{AFM} (mol·cm^{-2}·s^{-1}), was obtained from the dissolved volume of calcite created by the etch pits (as described by Urosevic et al. [37]):

$$R_{AFM} = \Delta V \cdot N_{pit} / V_{cal} \cdot (t_2 - t_1) \quad (2)$$

$$\Delta V = (w_2 \cdot u_2 - w_1 \cdot u_1) \cdot h \quad (3)$$

where ΔV is the increase in dissolved volume of an etch pit between t_2 and t_1 in two sequential images, w, u and h are the width, length and depth, respectively, of an etch pit (h remains constant at ca. 0.3 nm), N_{pit} is the average number of etch pits per cm^2, and V_{cal} is the molar volume of calcite (31.20 cm^3·mol^{-1}). By using sequential images, the pit expansion rate, R_s (nm·s^{-1}), was also calculated from the variation in length of the etch pit sides (Δw or Δu) over time ($R_s = \Delta w/(t_2 - t_1)$). Likewise, the step velocity, R_T (nm·s^{-1}), was calculated from the increase in terrace width (ΔL) over time ($R_T = \Delta L/(t_2 - t_1)$). After the conclusion of mineral dissolution in Millipore MQ water, the third stage started as the cell was filled with the chosen sulfate-rich acid solution in order to promote the precipitation of gypsum. During this stage, solution renovation was not allowed. Hence, the solution saturation state approached an equilibrium with respect to the dissolving carbonate mineral.

Micro-Raman analysis was used to identify the newly precipitated sulfate phases on the calcite and dolomite cleavage surfaces. Micro-Raman spectra were obtained by using a dispersive spectrophotometer Jobin-Yvon LabRam HR 800 with 532 nm light for sample excitation and a CCD detector cooled to −70 °C. The laser power used was between 0.5 and 4 mW. The spectrophotometer was coupled to an optical microscope Olympus BXFM with 50× and 100× objectives. The samples were dried before measurement.

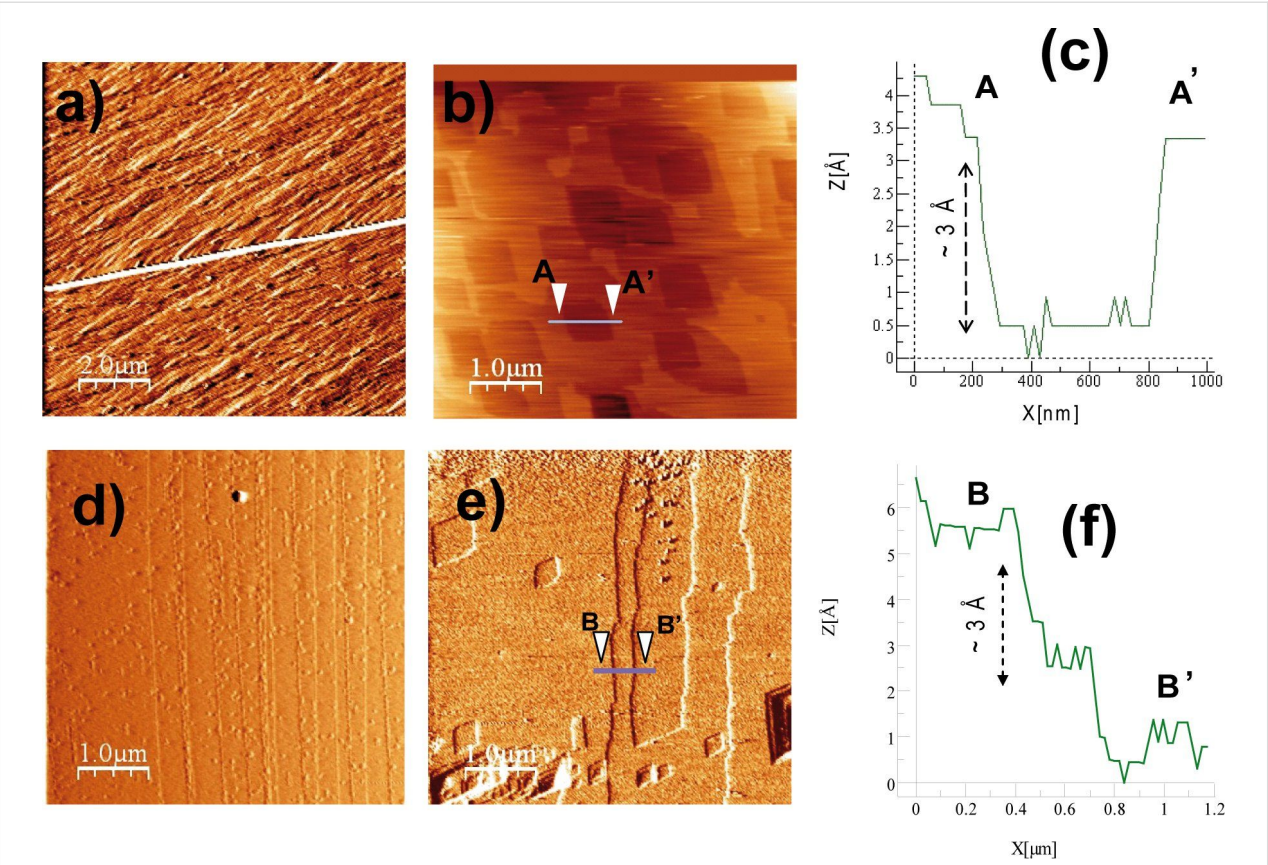

Figure 1: AFM deflection images of calcite cleavage surfaces. Top row: a) image in air shows the initial flat surface with a topographic variation that ranges over 2 nm. The white line across the image corresponds to a terrace; b) same surface region with some drift after 300 s in Millipore MQ water showing a high density of etch pits homogeneously distributed and c) depth profile of an etch pit section. Bottom row: d) image in air shows the initial flat surface with a topographic variation that ranges over 4 nm and e) same surface region after 240 s in Millipore MQ water showing the random formation of etch pits and f) depth profile of a step edge section shown by the arrows in e).

Results and Discussion

Dissolution of calcite

Dissolution of the (104) calcite surface in Millipore MQ water was readily observed. Figure 1b and Figure 1c show the formation of shallow (depth ≈ 0.3 nm ≈ calcite unit cell) and deep rhombohedral etch pits all over the surface [19,30,36,40]. The ratio between the etch pit rhombus diagonals was 0.71 ± 0.02, which is similar to that reported by Pérez-Garrido et al. [41]. Etch pit merging and formation of trenches or steps were observed (Figure 1b and Figure 1e). The number of etch pits per square centimeter of surface (N_{pit}) varied from 8×10^7 (only etch pits, Figure 1b) to 5×10^8 (etch pits and steps, Figure 1e) in scanned flat regions with similar initial roughness. The measured calcite dissolution rate, R_{AFM}, was 1.45×10^{-10} mol·cm^{-2}·s^{-1}, which agrees with that at nearly neutral pH reported elsewhere [19,42,43]. The etch pit expansion rate, R_s, was measured to be 1.82 ± 0.12 nm·s^{-1} and falls within the range of those calculated for deionized water by Jordan and Rammensee (velocity of slow step 0.5 ± 0.2 nm/s and of fast steps 2.5 ± 0.5 nm/s) [44].

Interaction between the acidic sulfate-rich solutions and the calcite cleavage surface (solution injected and not renewed) induced faster dissolution than in Millipore MQ water. A massive nucleation of new rhombohedral etch pits took place at pH 4.80 after solution injection, in contrast to the fairly regular distribution of etch pits in Millipore MQ water (Figure 2). At pH 4.80 R_{AFM} was 5.50×10^{-10} mol·cm^{-2}·s^{-1}, which is faster than that at pH 7, and agrees with the expected rate at pH 5 and 25 °C [19].

In the experiments with Na_2SO_4 solution (Figure 3a; solution injected and not renewed) the dissolution of the calcite cleavage surface was taking place such that equilibrium with respect to calcite was being approached. It was observed that the shape of newly formed rhombohedral etch pits was changing with time as the solution approached equilibrium with respect to calcite. The evolving shape was characterized by rounding of the obtuse–obtuse corner (Figure 3b–d). According to Teng et al. [45] and Teng [46] the retreat velocities of acute and obtuse steps do not show a linear dependence on supersaturation. In

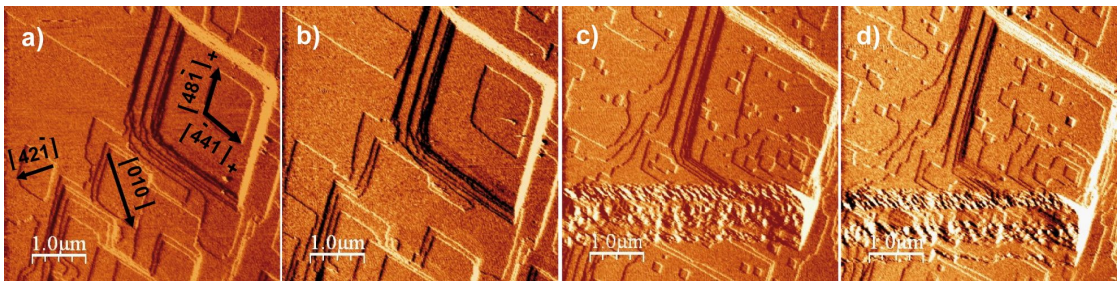

Figure 2: Sequential AFM deflection images of the reacted calcite (104) surface: initially in Millipore MQ water (a and b) and acid solution (pH 4.80) (c and d). Etch pits developed and spread. As pH was decreased to 4.80, a large population of etch pits suddenly formed. Rhombohedra formed along the $[48\bar{1}]^+$ and $[\bar{4}11]^+$ directions with the long and short diagonals parallel to [010] and $[42\bar{1}]$, respectively.

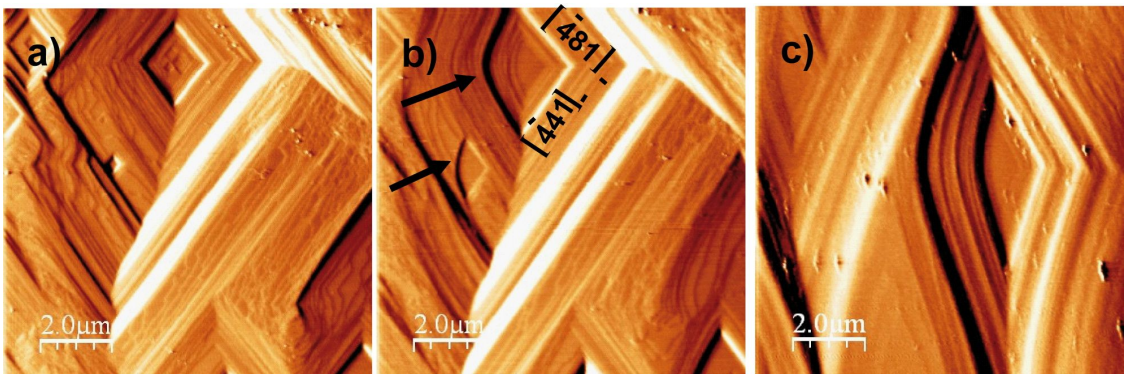

Figure 3: Sequential AFM deflection images of the reacted calcite cleavage surface in contact with Na_2SO_4 solution: a) characteristic morphology of rhombohedral etch pits (after acid injection, pH 4.08) and b) rounding of the obtuse–obtuse corner of the rhombohedral etch pits (shown by arrows) after 12 min, and c) rhombohedral etch pit with elongated shape after 43 min with a short/long diagonal ratio of 0.35 ± 0.02.

addition, several studies have shown that the velocities of acute and obtuse step spreading have different sensitivities to the solute activity ratios in the solution [32,36,47]. Calcite dissolution continuously took place during the solution saturation state drift. This implies a change in Gibbs energy along the experimental runs. As pointed out by Stipps et al. and de Leeuw et al. [48,49] the observed distortion of the etch pit shape (Figure 3b and Figure 3c) likely corresponds to an increase in the difference of velocities between obtuse and acute steps.

Dissolution of dolomite

Dolomite dissolution experiments were carried out similarly to those of calcite. First, dolomite dissolved in Millipore MQ water, and then, the reaction took place in sulfate-rich solutions at pH 2 and 3 (Table 1). Contrary to calcite dissolution, when dolomite reacted in Millipore MQ water, a nucleation of etch pits was not observed for approximately 25 min. Only, at specific surface localities, step retreat was observed (Figure 4a), allowing the calculation of the retreat velocity R_S, considered to be the average retreat velocity of non-crystallographically equivalent steps (Figure 4b and Figure 4c), which was 0.14 ± 0.03 nm·s^{-1}. This value is not far from the etch spreading rate of 0.09 ± 0.01 nm·s^{-1} reported by Urosevic et al. [37] and is about one order of magnitude lower than the etch pit expansion rate of calcite obtained in this study.

As dolomite reacted in acid solution, etch pit nucleation of isolated etch pits was observed over the cleavage surface after 10 min. Single etch pits presented an elongated rhombohedral shape (Figure 5a). As the surface kept dissolving for 8 h, etch pit nucleation occurred all over the surface. Lack of sequential images for this long run prevented us from calculating R_{AFM} under acid conditions (Figure 5b). The formed etch pits showed the typical rhombohedral shape as expect from carbonate mineral dissolution [37].

Coupled dissolution of calcite and dolomite and precipitation of gypsum

As the calcite (104) cleavage surface reacted with the pH 2 solution equilibrated with respect to gypsum, gypsum precipitation was readily observed (Figure 6). Micro-Raman analyses of the retrieved reacted samples confirmed the presence of gypsum. Gypsum nucleation took place uniformly all over the calcite surface immediately after the acid solution interacted

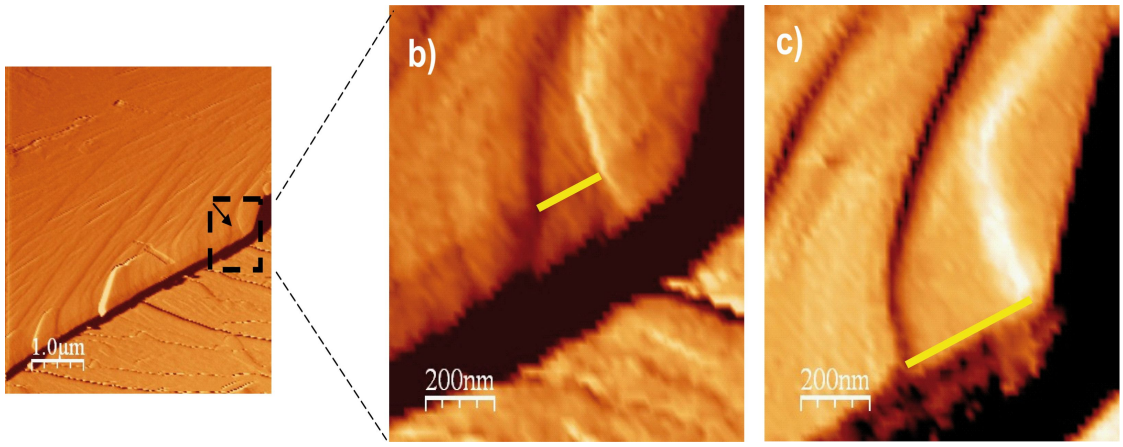

Figure 4: AFM deflection images of dolomite dissolution in Millipore MQ water: a) in air image of the dolomite (010) surface (exp. dol 1 in Table 1). Selected squared region in (a) to calculate the step-retreat rate based on the variation in length with time of the pointed terrace. The sequential images in b) and c) after 7.5 and 11.5 min respectively, show the consequent terrace evolution.

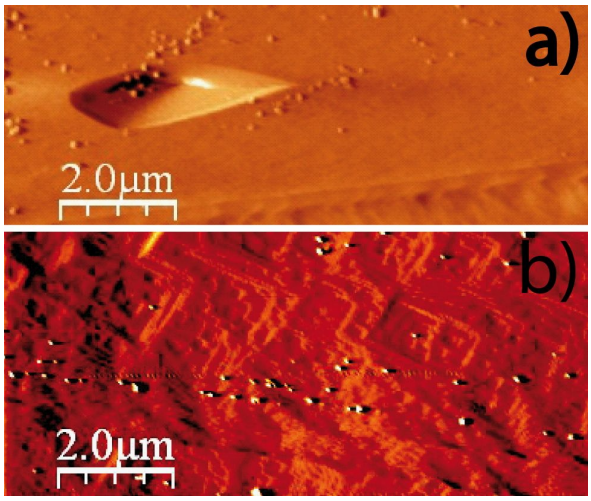

Figure 5: AFM deflection images of the reacted dolomite (104) cleavage surface in acid Na_2SO_4 solutions: a) after 10 min in pH 2, isolated etch pits were observed and b) in pH 3, nucleation of etch pits was observed all over the surface after 8 h.

with the dissolving cleavage surface (Figure 6a and Figure 6b). At pH 2, the gypsum precipitation induction time was slower than 100 s (time between two sequential image captures). The epitaxially grown gypsum crystals displayed an elongated (arrow-like) shape, consistent with their crystallographic monoclinic form, usually presented as tabular crystals, with the long and short sides parallel to the calcite $[\bar{4}41]$ and $[48\bar{1}]$ directions, respectively (Figure 6a and Figure 6c).

This crystal morphology was observed by Booth et al. [18]. 3-D images of the arrow-shaped gypsum crystals showed that the formed gypsum crystals, which entirely coated the cleavage surface, were slightly tilted (ca. 1°) with respect to the calcite (104) cleavage surface. The lack of a reference surface on the calcite substrate and the fast-formed gypsum coating prevented the calculation of gypsum growth rates at the pH range studied. Gypsum precipitation ceased as Ca release from calcite dissolution stopped. This was most likely because calcite dissolution stopped as either the entire calcite surface was totally passi-

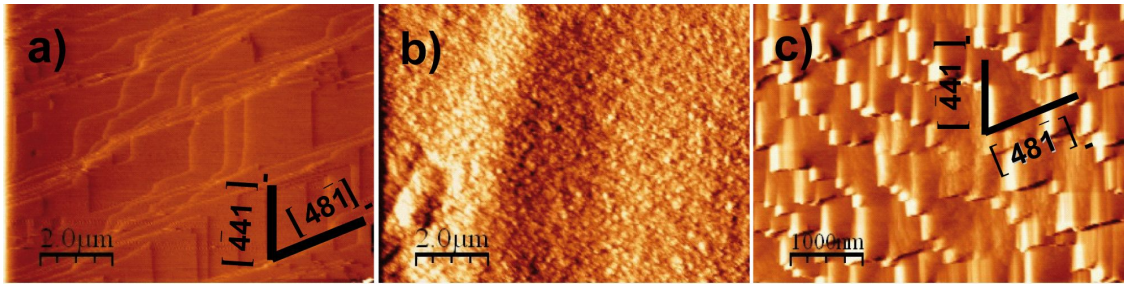

Figure 6: AFM deflection images of reacting (104) calcite surface: a) dissolution in Millipore MQ water; b) after injecting a solution in equilibrium with gypsum at pH 2.18, gypsum precipitation starts (1.5 min) and c) gypsum arrows grow laterally and coalesce (41 min).

vated impeding ion release through the gypsum layer, or because equilibrium with respect to calcite was achieved.

In experiments in which calcite dissolved at pH ≥ 3 in gypsum equilibrated solutions, the gypsum induction time was longer than 240 s, indicating slower gypsum growth than that at pH 2 due to slower calcite dissolution. Gypsum also grew epitaxially over the entire surface and, in general, the crystals showed the arrow-like shape (Figure 7a). In some Na_2SO_4 experiments, however, gypsum precipitation occurred non-uniformly over the cleavage surface, taking place at specific localities, mostly at step edges, and forming individual protuberances (spikes),

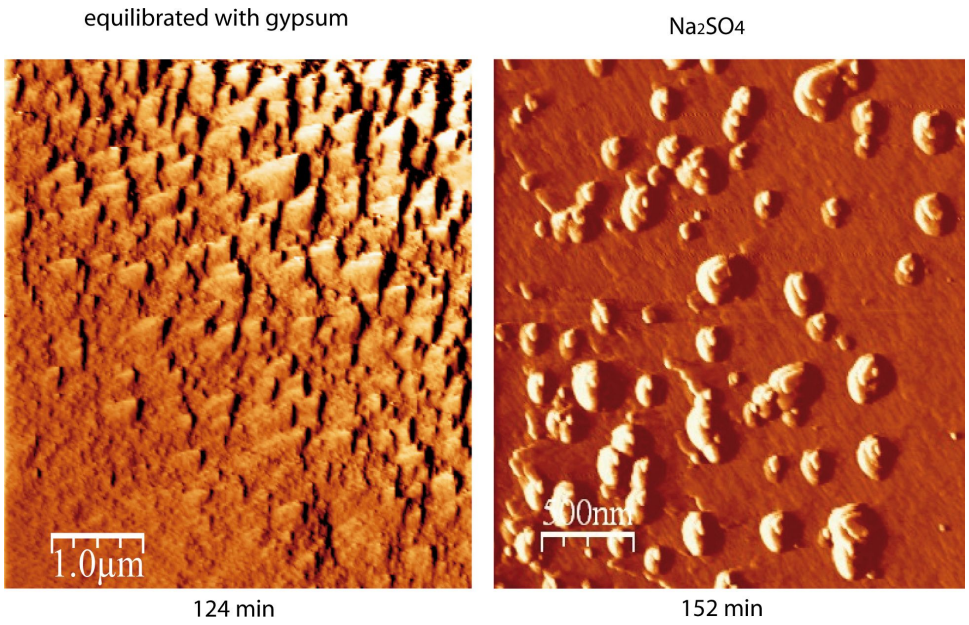

Figure 7: Gypsum precipitation on a calcite surface at pH 3: a) Experiment with gypsum equilibrated $CaSO_4$ solution: homogeneous, arrow-type gypsum growth on the cleavage calcite surface; b) Experiment with Na_2SO_4 solution: random protuberances over the calcite surface.

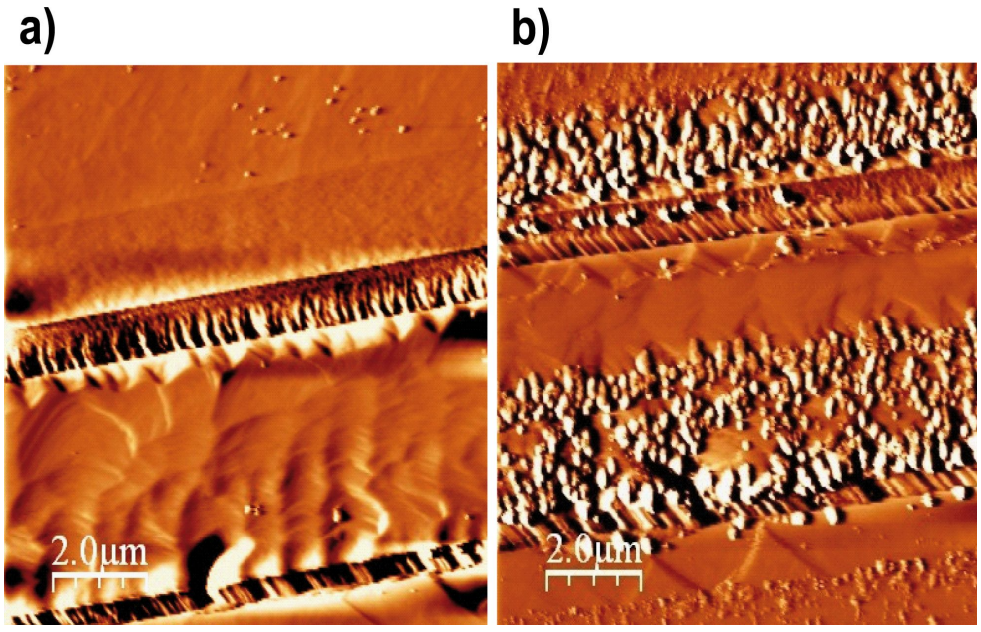

Figure 8: Sequential AFM deflection images of reacted dolomite surface in pH 3 (H_2SO_4) in solution equilibrated with respect to gypsum: a) after 4 h, shallow and deep etch pits are visible on the dolomite surface and b) after 6 h, gypsum precipitated mainly along the step edges.

suggesting preferential sites for the formation of these nuclei (Figure 7b).

When the cleaved dolomite surface was the substrate, gypsum precipitation from dolomite dissolution was slower than that from calcite dissolution at the same pH. Micro-Raman analyses of the reacted fragments at pH 2 and 3 confirmed precipitated gypsum at the dolomite cleavage surfaces. Gypsum precipitation occurred on the previously etch pitted dolomite surface after about 6 h, and again it was difficult to establish an induction time. Epitaxial growth was observed to be non-uniform over the surface (Figure 8), taking place on preferential surface regions, such as step and terrace edges, and areas with marked roughness. This behavior suggests that gypsum precipitation on dolomite cleavage surfaces was favored at highly reactive surface regions, where dolomite dissolution and hence element release was highest. After 8 h of reaction time, dolomite passivation was still only partial with etch pitted regions still visible, in contrast to the full gypsum armoring on the calcite surface.

Conclusion

In-situ atomic force microscopy was used to investigate the coupled processes of carbonate mineral dissolution and gypsum precipitation in acid sulfate-rich solutions in solutions both undersaturated and in equilibrium with respect to gypsum at room temperature.

Dissolution of calcite and dolomite occurred forming the characteristic rhombohedral etch pits. Calcite dissolution rates measured at nearly neutral pH and pH of 4.80 agreed with VSI-measured rates [19]. The calcite etch pit expansion rate and the dolomite step retreat velocity were calculated in near neutral pH (Millipore MQ water), the latter being about one order of magnitude lower than the former. Precipitation occurred as a result of the carbonate mineral dissolution. Therefore, as in acidic pH conditions calcite dissolution rates were faster than those of dolomite, gypsum precipitation was correspondingly faster in the calcite dissolution experiments. Epitaxial growth was the growth mechanism as observed by Booth et al. [18], and gypsum nucleation induction times were shorter in the calcite dissolution experiments. In the case of calcite dissolution in gypsum-equilibrated solutions, gypsum nucleation occurred immediately and surface coating was uniform all over the calcite surface, yielding a total calcite passivation. Arrow-shaped gypsum crystals evolved along the etch pit crystallographic directions ($[\bar{4}41]$ and $[48\bar{1}]$). In Na_2SO_4 solutions undersaturated with respect to gypsum, precipitation occurred via the formation of isolated growth protuberances randomly distributed over the cleavage surface. In the case of dolomite dissolution in gypsum-equilibrated solutions, gypsum precipitation was favored at highly reactive surface regions (step and terrace edges) and rough regions. Gypsum partially coated the dolomite surface during the experimental runs.

In all experiments gypsum precipitation resulted from a two-step process: 1. The calcite or dolomite dissolved, as observed in the regular formation of rhombohedral etch pits and step retreat, thereby releasing Ca^{2+} or Ca^{2+} and Mg^{2+} ions to solution. 2. The solution at the mineral–solution interface became supersaturated with respect to gypsum, which then precipitated. These two processes were coupled at the interface and continued as long as Ca^{2+} was being released.

Acknowledgements

This work was partially funded by project CGL2010-20984-C02-01 from the Spanish Government and the EU initial training network Delta-Min (Mechanisms of mineral replacement reactions, Grant PITN-GA-2008-215360). FGO was supported by a JAE-Predoc grant under the Program “Junta para la Ampliación de Estudios”. We would like to thank Veronika Rapelius (Münster University) for laboratory assistance and Tariq Jawhari Colin (Centres Científics i Tecnològics - Barcelona University) for assistance during the micro-Raman measurements. Ignasi Casanova (Polytechnic University of Catalonia) and Encarnación Ruiz Agudo (Department of Mineralogy and Petrology, University of Granada) are thanked for the assistance during AFM measurements.

References

1. Hedin, R. S.; Watzlaf, G. R.; Nairn, R. W. J. *Environ. Manage.* **1994,** *23,* 1338–1345.
2. Kleinmann, R. L. P.; Hedin, R. S.; Nairn, R. W. Treatment of mine drainage by anoxic limestone drains and constructed wetlands. In *Acidic Mining Lakes;* Geller, W.; Klapper, H.; Salomons, W., Eds.; Springer: Berlin, Germany, 1998; pp 303–319. doi:10.1007/978-3-642-71954-7_16
3. Cravotta, C. A., III; Trahan, M. K. *Appl. Geochem.* **1999,** *14,* 581–606. doi:10.1016/S0883-2927(98)00066-3
4. Cravotta, C. A. *J. Environ. Qual.* **2003,** *32,* 1277–1289. doi:10.2134/jeq2003.1277
5. Johnson, D. B.; Hallberg, K. B. *Sci. Total Environ.* **2005,** *338,* 3–14. doi:10.1016/j.scitotenv.2004.09.002
6. Putnis, A. *Mineral. Mag.* **2002,** *66,* 689–708. doi:10.1180/0026461026650056
7. Putnis, A.; Putnis, C. V. *J. Solid State Chem.* **2007,** *180,* 1783–1786. doi:10.1016/j.jssc.2007.03.023
8. Putnis, C. V.; Ruiz-Agudo, E. *Elements* **2013,** *9,* 177–182. doi:10.2113/gselements.9.3.177
9. Pearson, F. H.; McDonnell, A. J. *J. Environ. Eng. Div. (Am. Soc. Civ. Eng.)* **1975,** *101,* 139–158.
10. Santoro, L.; Valpolicelli, G.; Caprio, V. *Water Res.* **1987,** *21,* 641–647. doi:10.1016/0043-1354(87)90074-1
11. Wilkins, S. J.; Compton, R. G.; Taylor, M. A.; Viles, H. A. *J. Colloid Interface Sci.* **2001,** *236,* 354–361. doi:10.1006/jcis.2000.7418

12. Hammarstrom, J.; Sibrell, P. L.; Belkin, H. E. *Appl. Geochem.* **2003,** *18,* 1705–1721. doi:10.1016/S0883-2927(03)00105-7
13. Watzlaf, G. R.; Schroeder, K. T.; Kleinmann, R. L. P.; Kairies, C. L.; Nairn, R. W.; Street, W. B. *The passive treatment of Coal Mine Drainage. U.S. Department of Energy DOE/NET-2004/1202;* National Technical Information Service: Springfield, VA, USA, 2004; pp 1–72.
14. Soler, J. M.; Boi, M.; Mogollon, J. L.; Cama, J.; Ayora, C.; Nico, P. S.; Tamura, N.; Kunz, M. *Appl. Geochem.* **2008,** *23,* 3579–3588. doi:10.1016/j.apgeochem.2008.08.011
15. Offeddu, F. G.; Cama, J.; Soler, J. M.; Ayora, C. *Geochim. Cosmochim. Acta* **2009,** *73,* A964.
16. Offeddu, F. G.; Cama, J.; Soler, J.; Ganor, J.; Casanova, I.; Putnis, C. V.; Putnis, A. *Macla* **2011,** *15,* 155–156.
17. Huminicki, D. M. C.; Rimstidt, J. D. *Appl. Geochem.* **2009,** *24,* 1626–1634. doi:10.1016/j.apgeochem.2009.04.032
18. Booth, J.; Hong, Q.; Compton, R. G.; Prout, K.; Payne, R. M. *J. Colloid Interface Sci.* **1997,** *192,* 207–214. doi:10.1006/jcis.1997.4978
19. Atanassova, R.; Cama, J.; Soler, J. M.; Offeddu, F. G.; Queralt, I. *Eur. J. Mineral.* **2013,** *25,* 331–351.
20. Dávila, G.; Luquot, L.; Cama, J.; Soler, J. Interaction between the Hontomín cap rock and CO_2-rich brine during geological CO_2 sequestration. In *Proceedings of European Mineralogical Congress,* Frankfurt, Germany, Sept 2–6, 2012; 2012.
21. García-Rios, M.; Luquot, L.; Soler, J. M.; Cama, J. *Procedia Earth Planet. Sci.* **2013,** *7,* 109–112. doi:10.1016/j.proeps.2013.03.013
22. García-Rios, M.; Dávila, G.; Offeddu, F. G.; Soler, J. M.; Cama, J. *Macla* **2011,** *15,* 93–94.
23. Kloppmann, W.; Bromblet, P.; Vallet, J. M.; Vergès-Belmin, V.; Rolland, O.; Guerrot, C.; Gosselin, C. *Sci. Total Environ.* **2011,** *409,* 1658–1669. doi:10.1016/j.scitotenv.2011.01.008
24. Sánchez, J. S.; Romaní, J. R. V.; Alves, C. *Constr. Build. Mater.* **2011,** *25,* 813–822. doi:10.1016/j.conbuildmat.2010.07.001
25. Walker, R. A.; Wilson, K.; Lee, A. F.; Woodford, J.; Grassian, V. H.; Baltrusaitis, J.; Rubasinghege, G.; Cibin, G.; Dent, A. *Sci. Rep.* **2012,** *2,* No. 880. doi:10.1038/srep00880
26. Bard, F.; Bilal, E. *Carpathian J. Earth Environ. Sci.* **2011,** *6,* 241–250.
27. Hillner, P. E.; Manne, S.; Gratz, A. J.; Hansma, P. K. *Ultramicroscopy* **1992,** *44,* 1387–1393.
28. Shindo, H.; Ohashi, M. *Appl. Phys. A* **1998,** *66,* S487–S490. doi:10.1007/s003390051188
29. Arvidson, R. S.; Collier, M.; Davis, K. J.; Vinson, M. D.; Amonette, J. E.; Luttge, A. *Geochim. Cosmochim. Acta* **2006,** *70,* 583–594. doi:10.1016/j.gca.2005.10.005
30. Harstad, A. O.; Stipp, S. L. S. *Geochim. Cosmochim. Acta* **2007,** *71,* 56–70. doi:10.1016/j.gca.2006.07.037
31. Astilleros, J. M.; Fernández-Díaz, L.; Putnis, A. *Chem. Geol.* **2010,** *271,* 52–58. doi:10.1016/j.chemgeo.2009.12.011
32. Larsen, K.; Bechgaard, K.; Stipp, S. L. S. *Geochim. Cosmochim. Acta* **2010,** *74,* 2099–2109. doi:10.1016/j.gca.2009.12.028
33. Ruiz-Agudo, E.; Kowacz, M.; Putnis, V. C.; Putnis, A. *Geochim. Cosmochim. Acta* **2010,** *74,* 1256–1267. doi:10.1016/j.gca.2009.11.004
34. Pina, C. M.; Pimentel, C.; García-Merino, M. *Surf. Sci.* **2010,** *604,* 1877–1881. doi:10.1016/j.susc.2010.07.019
35. Hövelmann, J.; Putnis, C. V.; Ruiz-Agudo, E.; Austrheim, H. *Environ. Sci. Technol.* **2012,** *46,* 5253–5260. doi:10.1021/es300403n
36. Ruiz-Agudo, E.; Putnis, C. V. *Mineral. Mag.* **2012,** *76,* 227–253. doi:10.1180/minmag.2012.076.1.227
37. Urosevic, M.; Rodriguez-Navarro, C.; Putnis, C. V.; Cardell, C.; Putnis, A.; Ruiz-Agudo, E. *Geochim. Cosmochim. Acta* **2012,** *80,* 1–13. doi:10.1016/j.gca.2011.11.036
38. Horcas, I.; Fernández, R.; Gómez-Rodríguez, J. M.; Colchero, J.; Gómez-Herrero, J.; Baro, A. M. *Rev. Sci. Instrum.* **2007,** *78,* 013705. doi:10.1063/1.2432410
39. Parkhurst, D. L.; Appelo, C. A. J. User's guide to PHREEQC (Version 2). *Water-Resources Investigations Report 99-4259;* U.S. Geological Survery Publications, 1999.
40. MacInnis, I. N.; Brantley, S. L. *Geochim. Cosmochim. Acta* **1992,** *56,* 1113–1126. doi:10.1016/0016-7037(92)90049-O
41. Pérez-Garrido, C.; Fernández-Díaz, L.; Pina, C. M.; Prieto, M. *Surf. Sci.* **2007,** *601,* 5499–5509. doi:10.1016/j.susc.2007.09.021
42. De Giudici, G. *Am. Mineral.* **2002,** *87,* 1279–1285.
43. Duckworth, O. W.; Martin, S. *Am. Mineral.* **2004,** *89,* 554–563.
44. Jordan, G.; Rammensee, W. *Geochim. Cosmochim. Acta* **1998,** *62,* 941–947. doi:10.1016/S0016-7037(98)00030-1
45. Teng, H. H.; Dove, P. M.; DeYoreo, J. J. *Geochim. Cosmochim. Acta* **1999,** *63,* 2507–2512. doi:10.1016/S0016-7037(99)00103-9
46. Teng, H. H. *Geochim. Cosmochim. Acta* **2004,** *68,* 253–262. doi:10.1016/S0016-7037(03)00423-X
47. Stack, A. G.; Grantham, M. C. *Cryst. Growth Des.* **2010,** *10,* 1409–1413. doi:10.1021/cg901395z
48. Stipp, S. L. S.; Eggleston, C. M.; Nielsen, B. S. *Geochim. Cosmochim. Acta* **1994,** *58,* 3023–3033. doi:10.1016/0016-7037(94)90176-7
49. de Leeuw, N. H.; Parker, S. C.; Harding, J. H. *Phys. Rev. B* **1999,** *60,* 13792–13799. doi:10.1103/PhysRevB.60.13792

License and Terms

BEILSTEIN JOURNAL OF NANOTECHNOLOGY

Effects of palladium on the optical and hydrogen sensing characteristics of Pd-doped ZnO nanoparticles

Anh-Thu Thi Do*, Hong Thai Giang, Thu Thi Do, Ngan Quang Pham and Giang Truong Ho

Full Research Paper

Open Access

Address:
Institute of Materials Science, Vietnam Academy of Science and Technology, 18 Hoang Quoc Viet, Caugiay, Hanoi, Vietnam; Tel.: +84-43-7569318; Fax: +84-43-8360705

Email:
Anh-Thu Thi Do* - thudta@ims.vast.ac.vn; Thu Thi Do - thudta@ims.vast.ac.vn

* Corresponding author

Keywords:
carrier dynamics; hydrogen sensing; Pd-doped ZnO; photoluminescence; sensor

Beilstein J. Nanotechnol. **2014,** *5,* 1261–1267.
doi:10.3762/bjnano.5.140

Received: 13 February 2014
Accepted: 14 July 2014
Published: 13 August 2014

This article is part of the Thematic Series "Nanomanipulation and environmental nanotechnology".

Guest Editor: E. Gnecco

Abstract

The effect of palladium doping of zinc oxide nanoparticles on the photoluminescence (PL) properties and hydrogen sensing characteristics of gas sensors is investigated. The PL intensity shows that the carrier dynamics coincides with the buildup of the Pd-related green emission. The comparison between the deep level emission and the gas sensing response characteristics allows us to suggest that the dissociation of hydrogen takes place at Pd_{Zn}-vacancies ($[Pd^{2+}(4d^9)]$). The design of this sensor allows for a continuous monitoring in the range of 0–100% LEL H_2 concentration with high sensitivity and selectivity.

Introduction

Semiconductor zinc oxides (ZnO) nanocrystals are not only interesting for fundamental physics, but they are also important for both optoelectronic and emerging electronic device applications, in particular for hydrogen sensing [1-6]. The key features and availability of ZnO nanocrystals in distributed discrete gas sensing devices crucially depend on the growth conditions. These conditions strongly influence their size, uniformity and defects. Optical properties and gas sensing characteristics in ZnO nanostructures are mainly expected to differ in terms of their quality from those in bulk materials. In ZnO bulk material, the sensitivity and selectivity are not sufficiently high. ZnO nanocrystals possess a large surface atom/bulk atom ratio [7], which corresponds to a higher sensitivity, thermal stability [8], compatibility with other nanodevices, and are potentially the best gas sensors. Oxides cannot easily distinguish between different types of gases, but the addition of certain noble metals as dopants can promote the gas-sensing performance [9-11]. Noble metal dopants in ZnO can modify the optical and electric properties of ZnO, which influence the sensitive performance [10,12]. Palladium, a 4d metal, is taken as an impurity in ZnO. This is most likely caused by their special electronic configuration, i.e., 4d. Due to the sensitivity of the palladium ions with

deep holes on singly ionized oxygen interstitials, Zn anti-site vacancies, and oxygen vacancies, it is of interest to find out whether Pd incorporated in ZnO significantly improves sensitivity and specificity for hydrogen [13,14].

In this work, we have successfully synthesized Pd-doped ZnO nanoparticles for an application as gas sensors by a low-temperature wet-chemical process. Photoluminescence (PL) measurements at room temperature are then carried out in order to determine the role of vacancies, trapping levels, and the transition shift of the PL emission maximum in these samples. In order to study and optimize the four main factors affecting the ability of hydrogen sensors, typical sensors based on ZnO nanoparticles have been designed. The hydrogen gas sensor based on Pd-doped ZnO shows a relative fast response compared with the undoped sample. We also investigated the hydrogen sensing characteristics of these catalytic gas sensors in the measurement chamber containing hydrogen in air, with concentrations of 25–100% of the lower explosive limit (LEL), which is the minimum concentration of vapor or gas in air below which flame propagation does not occur on contact with a source of ignition [15]. The value of 25–100% LEL is equivalent to about 10,000–40,000 ppm. An existing correlation between the PL emissions and hydrogen sensing characteristics of these gas sensors will also be discussed.

Results and Discussion

X-ray diffraction patterns of ZnO and Pd/ZnO nanoparticles are presented in Figure 1. All the XRD peaks are indexed by a hexagonal wurtzite phase of ZnO (JCPDS card no. 36-1451). The results show that the Pd-doped ZnO sample has a better crystallinity, higher intensity and smaller peak width than those of the pure ZnO sample at 700 °C for 2 hours. For the Pd/ZnO sample, crystalline phases of ZnO and Pd are found to be coexisting. This revealed that metallic Pd nanoparticles are dispersed in the ZnO matrix. The crystallite sizes estimated for the same samples from Scherrer's formula by using the full width at half maximum (FWHM) [16] from the XRD patterns is in the range of 12 nm to 20 nm, giving average sizes of ZnO and Pd/ZnO samples of 16.2 and 16.5 nm from all the peaks, respectively.

A more precise determination of the primary particle size is inevitably be accompanied by a significant error due to their aggregate nature and the formation of polycrystalline nanoparticles. Consequently, other methods were used to evaluate the particle size. This includes the Brunauer–Emmett–Teller (BET) surface area analysis and the Barrett–Joyner–Halenda (BJH) pore size and volume analysis. The obtained isotherms of the ZnO and Pd/ZnO samples prepared in ethanol (Figure 2) correspond to a type III isotherm in the Brunauer classification [17,18], which is characterized by the hysteresis loop, and it

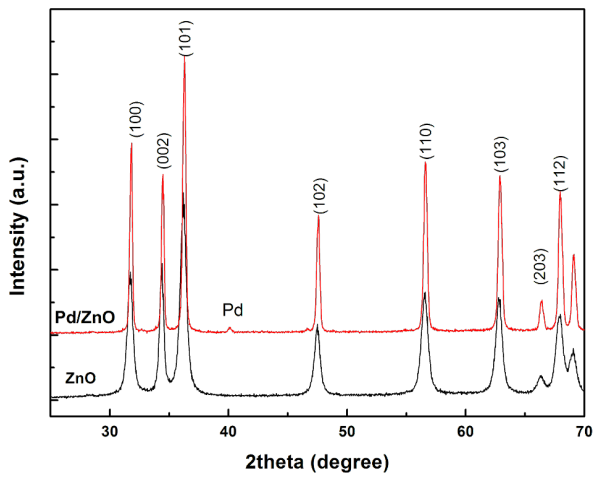

Figure 1: X-ray diffraction patterns of ZnO and Pd/ZnO nanopowders.

does not exhibit any limiting adsorption at high relative pressures. The specific BET surface area of the ZnO and Pd/ZnO samples were determined to be 37.5 and 34.32 m^2/g, respectively, the calculated BJH pore sizes were 8.7 and 10.6 nm. Based on the measured BET surface area the size of the ZnO and Pd/ZnO samples was estimated to be 28 nm and 31 nm, respectively. Thus, BET data satisfactorily correlate with XRD results, and the discrepancy between BET and XRD data can be explained by the complicated geometry of the polycrystalline nanoparticles mentioned above.

To explore the effect of Pd on the optical properties of ZnO nanoparticles, photoluminescence (PL) spectra were measured. Figure 3 shows the PL spectra of ZnO and Pd/ZnO samples with a 325 nm excitation at room temperature. For the ZnO sample a Gaussian fitting analysis shows that the broad emission band is a superimposition of three major peaks, one broad emission with a peak at around 408 nm, a second emission band at 517 nm, and a third emission band at around 570 nm. The UV emission peak at about 408 nm (3.03 eV) corresponds to the near-band-edge emission of the ZnO crystal. The origins of this visible emission have been the subject of a long-standing controversy. It has been attributed to the transition between the electron near the conduction band and the deeply trapped hole, which is an oxygen/zinc vacancy containing no electrons [19,20]. It is also attributed to the transition between donor–acceptor pairs.

In the Pd/ZnO sample, the excitonic band-edge emission completely vanished or was indistinct, while the structured green luminescence band and the transition shift of the emission maximum to higher energies was clearly visible. The second peak at 517 nm increased and the third peak at around 570 nm decreased. Interestingly, the obtained result is

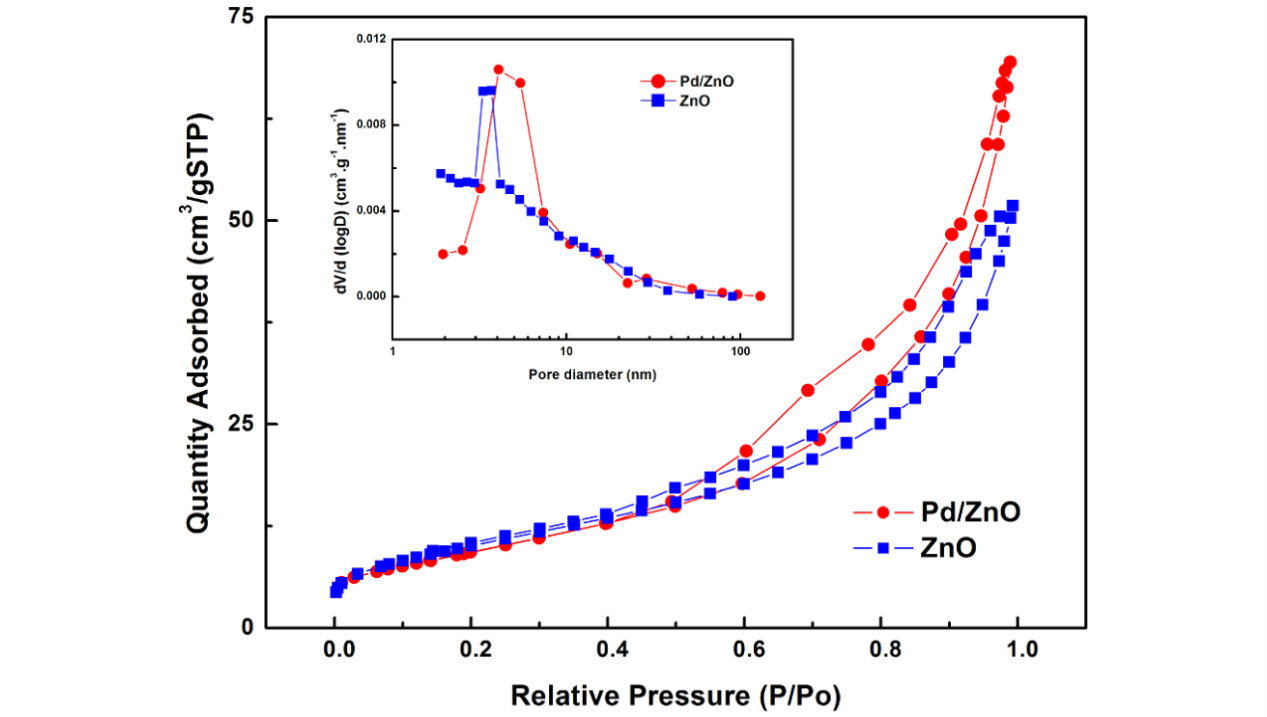

Figure 2: Typical nitrogen adsorption–desorption isotherm and BJH pore size distribution plots (inset) of ZnO and Pd/ZnO nanoparticles.

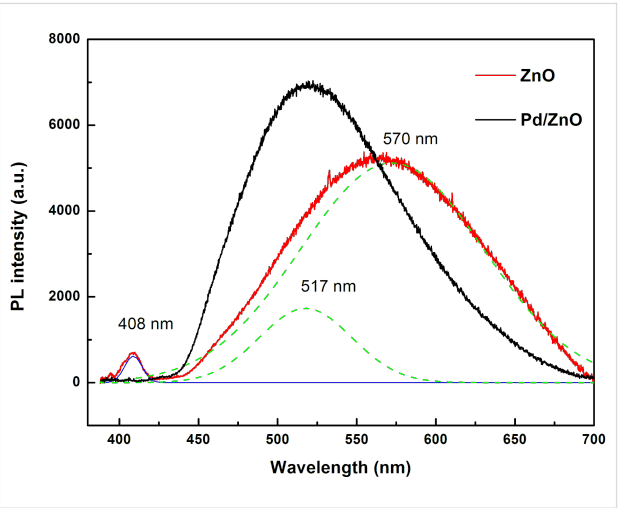

Figure 3: PL spectra of ZnO and Pd/ZnO nanoparticles at room temperature.

confirmed by the similarity of the luminescence bands of ZnO and ZnO:Cu [19-21]. The fine structure is assigned to the longitudinal optical phonon replica with an energy spacing of about 72 meV. This suggests that a green luminescence band originates from palladium ions, which replace zinc and always occur in ZnO in a small amount. The dominant peak at 517 nm corresponds to the exciton transition from the ground-state electronic subband to the ground-state of Pd in replacing Zn sites (i.e., Pd_{Zn} vacancies). The excited state of Pd_{Zn} originates from a hole bound to $4d^{10}$ shells or an intermediately bound exciton to a neutral d^9 configuration due to the hybridization of the Pd4d states with the Zn4s states at the bottom of the conduction band. The electron capture takes place at the neutral Pd_{Zn} center (i.e., $[Pd^{2+}(4d^9)]$), and the hole is captured by the potential created by the tenth electron to form the $[Pd^{+}(4d^9+e), h]$ state.

We now discuss the hydrogen sensing characteristics of catalytic gas sensors based on ZnO nanoparticles. For convenience, the fabricated sensors are denoted according to the used sensitive material. that is, sensor 1, ZnO and sensor 2, Pd/ZnO–0.5 wt % Pd. The characteristics of the sensor were examined in a measurement chamber containing hydrogen in the air at 25% of the lower explosive limit concentration (LEL) with a flow speed of 100 mL/min, at a temperature of 30 °C, and a relative humidity of 65% RH. To keep the operating temperature of the sensor in the range of 200–300 °C, an applied voltage $V_{applied}$ of 1.7 V and a current of about 120 mA are required. The obtained linear curve implied that it is possible to control the operating temperature by turning the applied voltage. To study the role of the Pd catalyst in the ZnO nanoparticles on the sensitivity of the sensor, the sensor output signal was measured as a function of the operating temperature of the sensor in 25% of the LEL concentration of hydrogen. The temperature of the microheater is tuned by changing the voltage $V_{applied}$. The temperature dependence of the sensor sensitivity (through voltage V_{out}) is shown in Figure 4a.

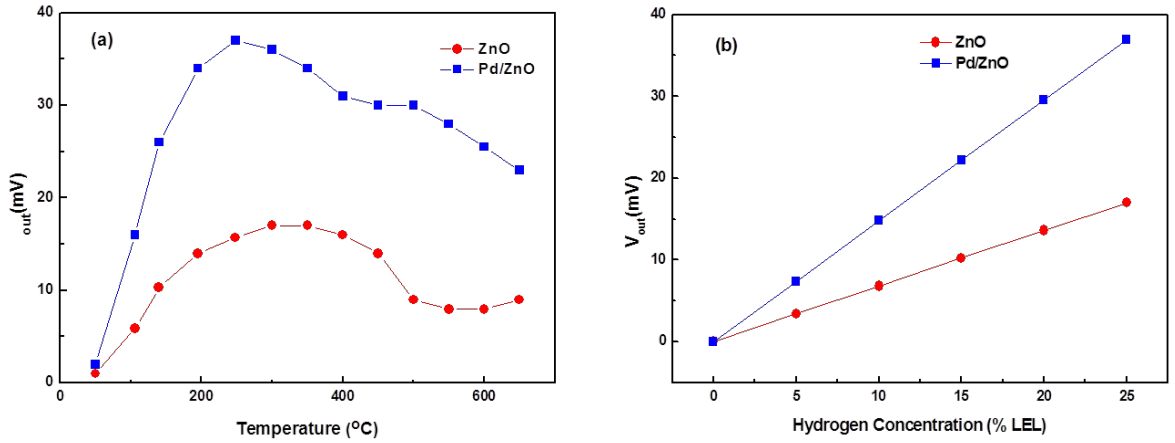

Figure 4: Dependence of (a) the operating temperature on the sensor sensitivity and (b) the hydrogen concentration on the sensor sensitivity (b).

These results indicate that the sensors have the greatest sensitivity within an operating temperature range of 200–300 °C. Among the measured sensors, the highest sensitivity was found with the Pd/ZnO sample. The values of the output voltage maximum, V_{out}, were 17 and 37 mV for ZnO and Pd/ZnO samples, respectively. An operating temperature of 250 °C was selected to investigate the gas-sensitive characteristics of the Pd/ZnO sensor. With a flow speed of 100 mL/min and a relative humidity of 65% RH, the linear dependence of the sensitivity of the Pd/ZnO-based sensor on hydrogen concentrations in the range of 0–25% LEL was observed as shown in Figure 4b.

The gas sensing mechanism usually accepted for semiconductor sensors explains the functionality due to reactions of hydrogen with the adsorbed oxygen species (i.e., O^{2-} or O^{-}) on the surface of the oxide, which liberate free electrons and H_2O thereby changing the conductivity of the material. The sensing mechanism for H_2 at 250 °C can be explained by the Pd metal particles on the surface of ZnO, which act as a catalyst. They dissociate hydrogen molecules into highly reactive atoms, which spread out on the surface of the semiconductor ZnO particles and reduce the potential barrier between the particles. In addition, the greater sensitivity to hydrogen can be explained because the oxidation of dissociated hydrogen is faster and more efficient than the decomposition and oxidation of hydrocarbons [22]. Moreover, as shown in Figure 3, the losing near-band-edge emission and transition shift of green luminescence band are due to Pd_{Zn}-vacancies. This allows us to note the correlation between the deep-level emission and the gas-sensing response characteristics of these samples. We suggest that the dissociation of hydrogen takes place at Pd_{Zn}-vacancies (i.e, $[Pd^{2+}(4d^9)]$) and may be expressed as,

$$H_2 + [Pd^{2+}(4d^9)] + H_2 \rightarrow 4H[Pd^{+}(4d^9 + e)] \quad (1)$$

Then, the oxidation of dissociated hydrogen happens according to the reaction,

$$4H[Pd^{+}(4d^9 + e)] + O_2{}^{-}{}_{(ads)} \rightarrow 2H_2O + [Pd^{2+}(4d^9)] \quad (2)$$

Similar results, viz. that the concentration of vacancies in turn controls the gas sensing characteristics, have been reported in ZnO films [23]. The sensitivity and selectivity characteristics of the gas sensor are associated with the deep hole-trap states and vacancies on the ZnO surface by the electron transfer mechanism [23,24]. The Pd metal nanoparticles modify the charge density on the ZnO surface, so that the incident electric field is changed [25], which not only affects the emission but also changes the oxygen adsorption and desorption of the gas sensors based on Pd/ZnO nanocrystals.

For gas selectivity of the sensor based on Pd/ZnO nanoparticles, the sensitivity of the ZnO– 0.5 wt % Pd sensor depends on the operating temperature. This is shown in Figure 5 for 1 vol % of hydrogen, H_2, carbon monoxide, CO, and for propane, C_3H_8. The comparison of the specificity of the sensor for the studied gases at 250 °C shows that the sensor is highly sensitive to H_2 and less sensitive to CO and C_3H_8. Gas specificity of the sensor is evaluated in terms of the ratio of the sensitivity of the sensor for a particular gas and the sensitivity for other gases when compared under identical conditions ($K_{gas/different\ gas}$). At 250 °C, we found the ratios of $K_{H2/CO}$ = 11.5, and $K_{H2/C3H8}$ = 5.1. This confirms that the produced sensors display

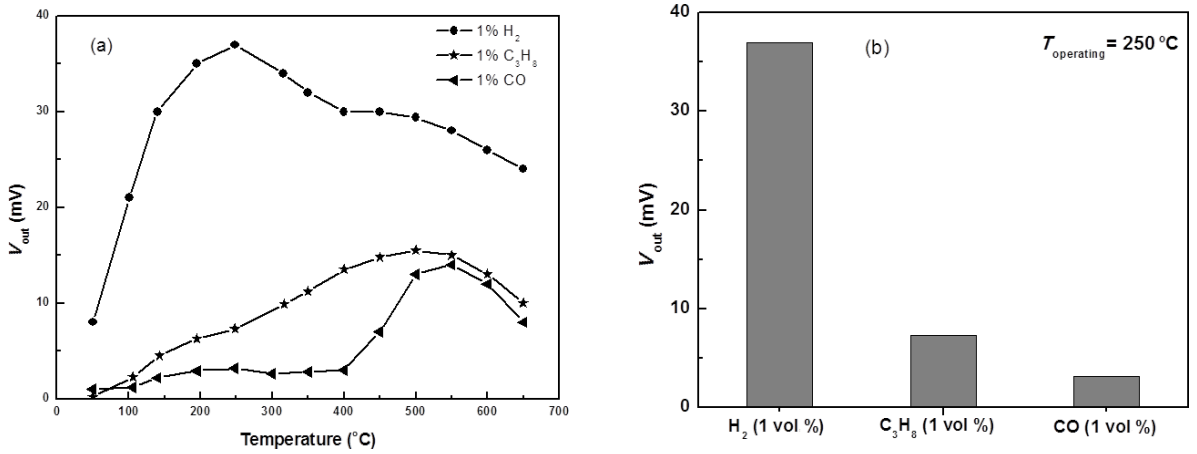

Figure 5: The operating temperature-dependence of (a) the sensitivity and (b) the specificity of the Pd/ZnO sample at 1 vol % of H_2, CO and C_3H_8 with a humidity of 65% RH.

a good specificity for H_2 compared to the cases of CO and C_3H_8. In fact, the effects of these gases on the hydrogen specificity of the sensor is insignificant because the concentration of CO in air is usually very low (<100 ppm), much smaller than a concentration value of 1 vol % (ca. 10,000 ppm).

Figure 6 shows the characteristic of the sensor response to the H_2 concentration of 25% LEL at 250 °C. The results show that the response time of the sensor is in the range of 10–20 s and the recovery time is around 10 s. Thus, this sensor is quite suitable for designing portable equipment as well as online control equipment to measure H_2 concentrations in the range of 0–100% LEL.

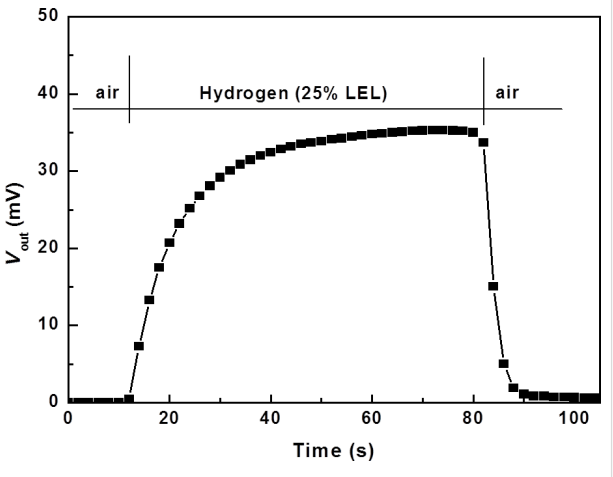

Figure 6: Response characteristics of the hydrogen sensor based on Pd/ZnO nanoparticles.

Finally, to examine the stability of the sensor over time, the measured value of the sensor is recorded every day under two atmospheric conditions, namely, in air and in H_2 concentrations of 25% LEL. The monitoring was carried out for 60 days, the results show that the sensor is rather stable with measured values fluctuated in the range of ±3 mV (Figure 7a). The stability of the sensor was also investigated by measuring a cycle at different concentrations of H_2 (as shown in Figure 7b). For each concentration of H_2, measurements were performed twice with an interval time of 20 minutes to minimize the effect of the previous measurements. The results show that the measured values are stable.

Conclusion

ZnO and Pd/ZnO (with 0.5 wt % Pd) nanoparticles with a nanoscale particle size of 16.2 and 16.5 nm and with a large specific surface area of 37.5 and 34.32 m^2/g, respectively, were prepared by wet chemical methods for gas sensor fabrication. The PL spectra at room temperature show that the carrier dynamics coincides with the buildup of the Pd-related green emission. A novel gas sensor based on 0.5 wt % Pd mixed with ZnO nanoparticles exhibited a high response to hydrogen at a relatively low temperature, from 200 to 300 °C, and the best operating temperature of the sensor is at 250 °C. We also showed that a qualitative correlation exists between the deep level emission and the gas sensing response characteristics of these samples. We suggest that the dissociation of hydrogen takes place at Pd_{Zn}-vacancies ($[Pd^{2+}(4d^9)]$). The design of sensors as a catalytic membrane and Wheatstone bridge measurements allow for the continuous monitoring of the H_2 concentration in the range of 0–100% LEL with high sensitivity and selectivity.

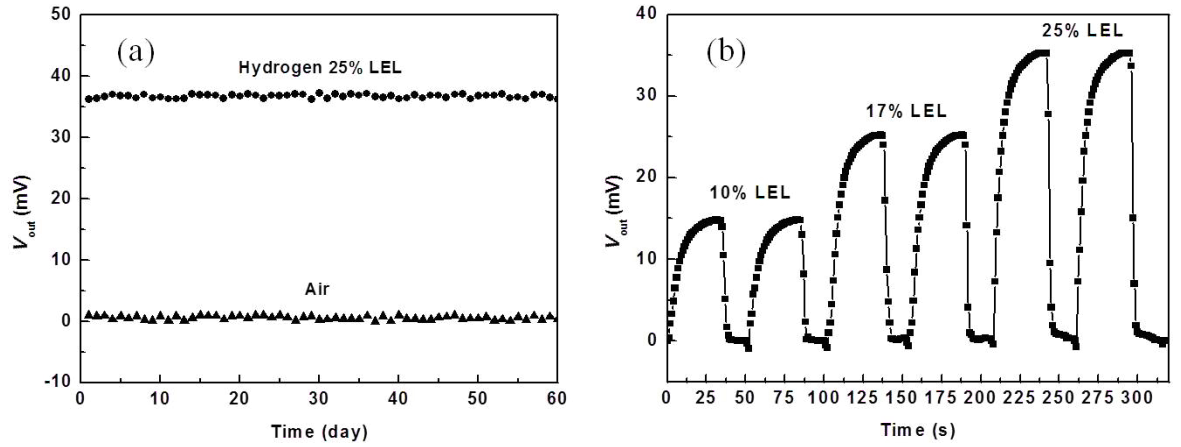

Figure 7: Stability over time of the investigated sensor as a function of (a) time and (b) in hydrogen atmosphere.

Experimental

ZnO nanopowders were synthesized by a wet chemical method with zinc acetate dihydrate, $Zn(CH_3COO)_2{\cdot}2H_2O$, sodium hydroxide, NaOH, and absolute ethanol (analytical reagents, Merck) as starting materials. In a typical procedure, 1.314 g of zinc acetate was dissolved in 300 mL solvent in a three-necked flask under stirring at 60 °C. 0.48 g of sodium hydroxide was added into this solution. After stirring for several minutes, a white precipitate appeared. The solution was stirred at 60 °C for 1 hour. After washing several times with distilled water and absolute ethanol, the particles were dried at 80 °C for 12 h. Pd-doping samples (Pd/ZnO) were obtained by mixing ZnO nanopowder with palladium chloride (Pd content in the sample is of 0.5 wt %). All samples were calcined at 700 °C for 2 hours to decompose the original chloride to obtain Pd/ZnO. The hydrogen sensors were improved on a pellistor gas sensor [26], which consisted of two resistors with R = 500 Ohm, two platinum coils. Their thick membrane (about 10 μm) of ZnO pastes with/without Pd was coated onto one platinum coil (activated bead). Al_2O_3 paste was coated onto the last coil. The temperature of the beads is controlled by the operational electrical current passed through the platinum coils. At high temperatures the chemisorbed hydrogen molecules on the surface catalyst are oxidized with adsorbed oxygen to form water. The heat of combustion raises the temperature of the activated bead, which in turn changes the resistance of the activated coil. This creates an imbalance in the Wheatstone bridge circuit. In this case, the offset voltage is measured as the signal instead of resistance or conductivity values.

The temperature of the sensor was controlled by a UDP-1501 power supply (Unicorn, Korea) connected with a computer, and data were recorded automatically by using a Keithley model DMM-2700.

Crystalline phase analyses of synthesized samples were characterized by powder X-ray diffraction (XRD) with a Siemens D5000 diffractometer by using CuK_α radiation. Morphologies of the samples were obtained by a Field Emission Scanning Electron Microscope (FE-SEM), Hitachi S-4800S. The specific surface areas of the prepared samples were determined by the BET (Brunauer–Emmett–Teller) method on a micromeritics system - AutoChem II 2920. The photoluminescence (PL) signals were dispersed by using an 1800 grating monochromator (Horiba iHR550) and then detected by means of a thermoelectrically cooled Si-CCD camera (Synapse).

References

1. Mitra, P.; Chatterjee, A. P.; Maiti, H. S. *Mater. Lett.* **1998,** *35,* 33–38. doi:10.1016/S0167-577X(97)00215-2
2. Chatterjee, P.; Mitra, P.; Mukhopadhyay, A. K. *J. Mater. Sci.* **1999,** *34,* 4225–4231. doi:10.1023/A:1004694501646
3. Wang, H. T.; Kang, B. S.; Ren, F.; Tien, L. C.; Sadik, P. W.; Norton, D. P.; Pearton, S. J.; Lin, L. *Appl. Phys. Lett.* **2005,** *86,* 243503. doi:10.1063/1.1949707
4. Tien, L. C.; Sadik, P. W.; Norton, D. P.; Voss, L. F.; Pearton, S. J.; Wang, H. T.; Kang, B. S.; Ren, F.; Jun, J.; Lin, J. *Appl. Phys. Lett.* **2005,** *87,* 222106. doi:10.1063/1.2136070
5. Verhelst, S.; Sierens, R. *Int. J. Hydrogen Energy* **2006,** *26,* 987–990. doi:10.1016/S0360-3199(01)00026-X
6. Bévenot, X.; Trouillet, A.; Veillas, C.; Gagnaire, H.; Clément, M. *Sens. Actuators, B* **2000,** *67,* 57–67. doi:10.1016/S0925-4005(00)00407-X
7. Wan, Q.; Li, Q. H.; Chen, Y. J.; Wang, T. H.; He, X. L.; Li, J. P.; Lin, C. L. *Appl. Phys. Lett.* **2004,** *84,* 3654–3656. doi:10.1063/1.1738932
8. Yonenaga, I. *Phys. B (Amsterdam, Neth.)* **2001,** *308–310,* 1150–1152. doi:10.1016/S0921-4526(01)00922-X
9. Liu, Z.; Li, J.; Ya, J.; Xin, Y.; Jin, Z. *Mater. Lett.* **2008,** *62,* 1190–1193. doi:10.1016/j.matlet.2007.08.010
10. Pawinrat, P.; Mekasuwandumrong, O.; Panpranot, J. *Catal. Commun.* **2009,** *10,* 1380–1385. doi:10.1016/j.catcom.2009.03.002

11. Zeng, H.; Cai, W.; Liu, P.; Xu, X.; Zhou, H.; Klingshirn, C.; Kalt, H. *ACS Nano* **2008,** *2,* 1661–1670. doi:10.1021/nn800353q
12. Georgekutty, R.; Seer, M. K.; Pillai, S. C. *J. Phys. Chem. C* **2008,** *112,* 13563–13570. doi:10.1021/jp802729a
13. Hayakawa, I.; Iwamoto, Y.; Kikuta, K.; Hirano, S. *Sens. Actuators, B* **2000,** *62,* 55–60. doi:10.1016/S0925-4005(99)00303-2
14. Lupan, O.; Chai, G.; Chow, L. *Microelectron. Eng.* **2008,** *85,* 2220–2225. doi:10.1016/j.mee.2008.06.021
15. Reese, C. D.; Eidson, J. V. *Handbook of OSHA Construction Safety and Health;* Lewis Publishers: New York, NY, USA, 1999.
16. Yen, W. M.; Shionoya, S.; Yamamoto, H., Eds. *Phosphor Handbook;* CRC Press: Boca Raton, FL, USA, 1998.
17. Gregg, S. J.; Sing, K. S. W. *Adsorption, Surface Area and Porosity,* 2nd ed.; Academic Press: London, U.K., 1982.
18. Yu, J. C.; Xu, A.; Zhang, L.; Song, R.; Wu, L. *J. Phys. Chem. B* **2004,** *108,* 64–70. doi:10.1021/jp035340w
19. Garces, N. Y.; Wang, L.; Bai, L.; Giles, N. C.; Halliburton, L. E.; Cantwell, G. *Appl. Phys. Lett.* **2002,** *81,* 622–624. doi:10.1063/1.1494125
20. Schmidt-Mende, L.; MacManus-Driscoll, J. L. *Mater. Today* **2007,** *10,* 40–48. doi:10.1016/S1369-7021(07)70078-0
21. Xing, G.; Xing, G.; Li, M.; Sie, E. J.; Wang, D.; Sulistio, A.; Ye, Q.-l.; Hon Alfred Huan, C.; Wu, T.; Sum, T. C. *Appl. Phys. Lett.* **2011,** *98,* 102105. doi:10.1063/1.3558912
22. Heiland, G.; Kohl, D. Physical and Chemical Aspects of Oxidic Semiconductor Gas Sensors. In *Chemical Sensor Technology;* Seiyama, T., Ed.; Kodansha: Tokyo, Japan, 1988; Vol. 1, pp 15–38. doi:10.1016/B978-0-444-98901-7.50007-5
23. Pati, S.; Majumder, S. B.; Banerji, P. *J. Alloys Compd.* **2012,** *541,* 376–379. doi:10.1016/j.jallcom.2012.07.014
24. Alenezi, M. R.; Henley, S. J.; Emerson, N. G.; Silva, S. R. P. *Nanoscale* **2014,** *6,* 235–247. doi:10.1039/c3nr04519f
25. Zhang, D.; Wang, P.; Murakami, R.-i.; Song, X. *Appl. Phys. Lett.* **2010,** *96,* 233114. doi:10.1063/1.3442916
26. Hübert, T.; Boon-Brett, L.; Black, G.; Banach, U. *Sens. Actuators, B* **2011,** *157,* 329–352. doi:10.1016/j.snb.2011.04.070

License and Terms

BEILSTEIN JOURNAL OF NANOTECHNOLOGY

In situ observation of biotite (001) surface dissolution at pH 1 and 9.5 by advanced optical microscopy

Chiara Cappelli*[1], Daniel Lamarca-Irisarri[1], Jordi Camas[2], F. Javier Huertas[1] and Alexander E. S. Van Driessche*[3]

Full Research Paper

Open Access

Address:
[1]Instituto Andaluz de Ciencias de la Tierra (IACT - CSIC-Universidad de Granada), Avda. de las Palmeras 4, 18100 Armilla, Granada, Spain, [2]Institute of Environmental Assessment and Water Research (IDAEA), CSIC, Jordi Girona 18–26, 08034 Barcelona, Spain and [3]Structural Biology Brussel, VUB, Pleinlaan 2, 1050 Brussels, Belgium

Email:
Chiara Cappelli* - chiaracappelli@ugr.es;
Alexander E. S. Van Driessche* - alvdries@vub.ac.be

* Corresponding author

Keywords:
biotite; dissolution mechanism; environmental; in situ observation; pH effect

Beilstein J. Nanotechnol. **2015,** *6,* 665–673.
doi:10.3762/bjnano.6.67

Received: 02 June 2014
Accepted: 12 February 2015
Published: 05 March 2015

This article is part of the Thematic Series "Nanomanipulation and environmental nanotechnology".

Guest Editor: E. Gnecco

Abstract

Laser confocal differential interference contrast microscopy (LCM-DIM) allows for the study of the reactivity of surface minerals with slow dissolution rates (e.g., phyllosilicates). With this technique, it is possible to carry out in situ inspection of the reacting surface in a broad range of pH, ionic strength and temperature providing useful information to help unravel the dissolution mechanisms of phyllosilicates. In this work, LCM-DIM was used to study the mechanisms controlling the biotite (001) surface dissolution at pH 1 (11 and 25 °C) and pH 9.5 (50 °C). Step edges are the preferential sites of dissolution and lead to step retreat, regardless of the solution pH. At pH 1, layer swelling and peeling takes place, whereas at pH 9.5 fibrous structures (streaks) form at the step edges. Confocal Raman spectroscopy characterization of the reacted surface could not confirm if the formation of a secondary phase was responsible for the presence of these structures.

Introduction

The study of the reactivity of silicate minerals is essential to understand numerous bio-geochemical processes. Silicate weathering plays an important role in the carbon cycle, the formation of soil and the nutrition of plants [1]. Moreover, the release of cations from silicates and the high cation-exchange capacity of some phyllosilicates contribute to the pH stability of natural waters, the mobility of metals and the control of potentially toxic elements [2,3].

Flow-through reactors filled with powdered samples are frequently used to study the reaction mechanisms of mica dissolution and possible formation of new phases [3-9]. In this type of experiment, the full control over the parameters that influence the reactions (e.g., flow rate, pH, temperature and solution composition) allows one to quantify the mineral dissolution rates and the study of the reaction mechanisms under a wide range of experimental conditions. However, this experimental approach is rather unapt to deal with the reactivity of each crystal face, elucidate the face-specific dissolution–precipitation mechanisms and determine the specific location of the secondary mineral formation. In the last decades, the use of several advanced microscope techniques has allowed for the inspection of the mineral surfaces with high spatial resolution to explore morphological and topographical changes during the alteration process. Atomic force microscopy (AFM) is often employed to characterize reactive surface areas of silicate minerals in situ. For example, dissolution features and precipitation phases can be identified for a field of view that ranges from hundreds of nanometers to 120 micrometers with Angstrom resolution in the vertical plane [1,10-21]. Likewise, ex situ observations of micro-topographic changes on silicate surfaces over larger fields of view (90–2000 μm) are possible with nanometer-scale vertical resolution by using vertical scanning interferometry (VSI) [22-25]. Recently, Tsukamoto and coworkers designed a high-resolution phase shifting interferometer (PSI) that allows for the in situ measurement of extremely low surface dissolution (and growth) rates of minerals while submerged in aqueous solutions [26-30]. With the progress of these techniques our understanding of the mechanisms of the surface reactivity of phyllosilicates has greatly improved.

Although great progress at the experimental and theoretical front has been achieved, further investigations are needed to determine the precise mechanisms of phyllosilicate weathering (especially for low-reactivity conditions) and to integrate them with the new insights of theoretical models developed in the last decade. The main goal of the present work is to show the capability of the confocal differential interference contrast microscopy (LCM-DIM) to study phyllosilicate dissolution in situ. As mentioned above the capability of the AFM and VSI techniques to study mineral reactivity is remarkable, but each one alone shows some limitations [31]. AFM allows for the high-resolution characterization of surface features at the monolayer range but over narrow fields of view, preventing to investigate surface phenomena at the mesoscale. In the case of VSI, the field of view is wider and long in situ observations are possible. However, measurements are highly sensitive to small fluctuations of temperature and air bubbles. Instead, in situ measurements under different solution pH, temperature, flow rate, and pressure by using flow-through cells can be performed with LCM-DIM with a vertical resolution of about 1 nm over a wide field of view (ca. 0.3–2 mm). Although it only provides qualitative height information [31], morphological changes on mineral surfaces are suitably monitored. Additionally, owing to the relatively fast data acquisition (ca. 9.6 s to scan an area of 800×800 μm^2 [31]) and acquired stability, LCM-DIM allows for a stable surface monitoring over long time spans (up to months). AFM, VSI/PSI and LCM-DIM techniques are therefore complementary, and with the latter technique precise information of surface reactivity of slow dissolving minerals at the micro- and meso-scales over long time can be obtained.

In this study we investigate the reactivity of the cleaved biotite (001) surface, at pH 1 and pH ca. 9.5, by using in situ flow-through LCM-DIM experiments, combined with phase shifting interferometry (PSI). The experimental results are discussed considering the most relevant theories on mineral/solution interface processes, i.e., step wave model, dissolution/re-precipitation and leached layer mechanisms [22,32-37].

Results and Discussion

Figure 1a shows LCM-DIM images of a freshly cleaved biotite (001) surface with visible terrace limits. The darker the outline (i.e., contrast), the higher the step. The same surface reacted for ca. 17 h at pH 1 and 25 °C shows edge retreat, layer swelling and peeling (Figure 1b), the latter processes being a consequence of biotite dissolution.

Aldushin et al. [10] suggested that the reaction front on the phlogopite surface was caused by the exchange of interlayer K^+ ions, by octylammonium ions and reported a retreat rate of about 4×10^{-4} μm/s at the initial stage, which decreased to 1×10^{-4} μm/s and about 3×10^{-5} μm/s for phlogopite dissolution at 20 °C and pH 7. Cappelli et al. [38] reported rates of 7.5×10^{-4} and 3.5×10^{-3} μm/s for biotite (001) surface retreat of low steps at 11.5 and 25 °C and pH 1, respectively. Although the rates of Aldushin et al. at pH 7 are slower than the rates at pH 1 measured by Cappelli et al., it is insufficient to discard that an exchange between Na^+ and K^+ is not involved in the fast edge retreat observed on the biotite (001) surface, similarly to that reported by Sánchez-Pastor et al. [21] for phlogopite. However, additional interferometry observations of biotite surfaces reacted with inorganic and organic acids over a wide temperature range (data not shown, in preparation) point to a retreat of low steps due to dissolution rather than ion exchange.

In the case of macrosteps, monolayers or bunches of layers spread while the position of the macrostep remains apparently unchanged (Figure 1). This peculiar behavior is related to the presence of steps with different height on the basal surface. As described in Cappelli et al. [38], while low steps clearly retreat,

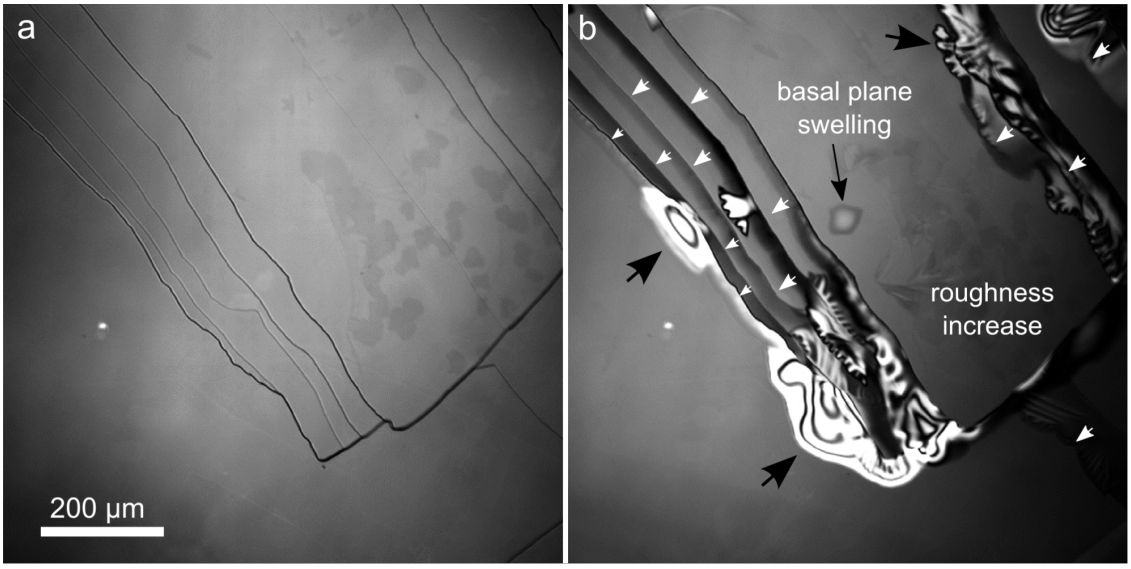

Figure 1: LCM-DIM images of a) freshly cleaved biotite (001) surface and b) the same surface after about 17 h of reaction at pH 1 and 25.0 °C. Upper layers appear in some areas "overexposed" (white zones) owing to layer breaking and curling (peeling process) after swelling. Black arrows indicate areas with layer swelling and peeling, and white arrows indicate the dissolution direction (see text).

leaving fresh unaltered surface, the position of high steps does not change, as only dissolution of the upper layers occurs. Indeed a series of time-lapsed LCM-DIM images (Figure 2a) shows that only upper layers dissolve from high steps while these macrosteps do not lose their initial position (darker areas, Figure 2b) and low steps move across the surface creating fresh biotite surface. Dissolution fronts (f_1–f_5) propagate following a semicircular pattern, indicating that the dissolution rate is similar in all crystallographic directions. Interestingly, new dissolution fronts break away from slower moving step edges (white arrows, Figure 2b), indicating that upper layers move faster than lower ones. Basal plane swelling and a general increase of roughness were also observed.

Figure 1 and Figure 2 show that step edges do not dissolve uniformly except in the case of low steps. Cappelli et al. [38]

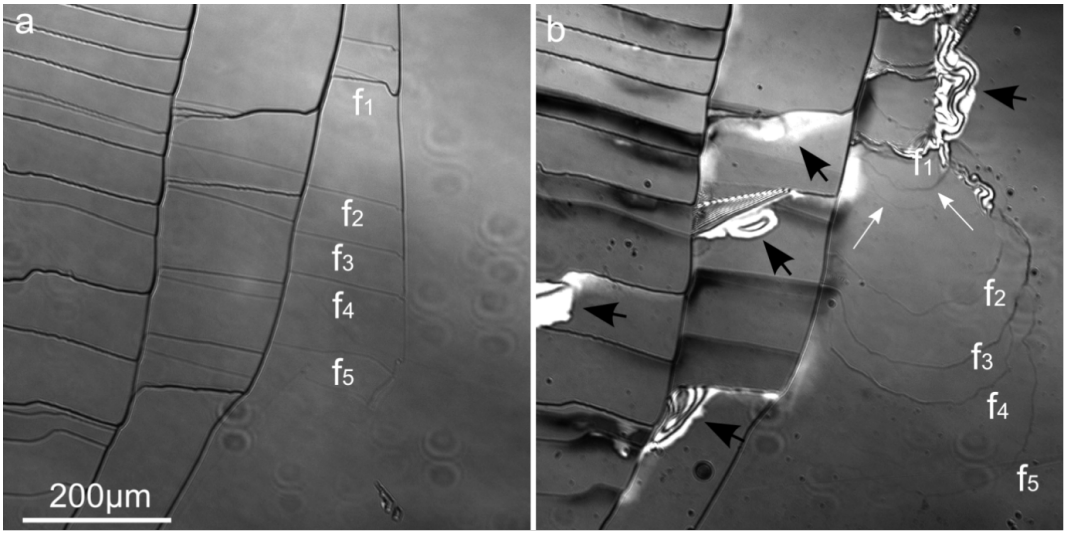

Figure 2: LCM-DIM images: a) freshly cleaved biotite (001) surface and b) the same surface after about 63 h at pH 1 and at 11.5 °C. Black arrows indicate swelling and peeling layers. White arrows indicate new dissolution fronts breaking away from slower moving step edges. Darker areas in b) correspond to higher steps whose upper layers are dissolving. Lower steps (f_1–f_5) move across the surface following a semi-circular pattern and creating unaltered biotite surface. The pale elliptic structures are dust particles derived from the objective lens.

observed that the retreat rate changes with the step thickness, being higher for low steps. Likewise, in this study, it is observed that the dissolution started at specific locations. These observations are in accordance with the results of recent studies that argue about the validity of an average dissolution rate value for complex minerals [32,33]. The novel concept of a rate spectrum was introduced for the complex anisotropic dissolution of mineral surfaces; this implies the existence of a surface energy distribution. In agreement with the above consideration the variability of biotite reactivity is an intrinsic factor of its crystalline anisotropy, i.e., surface energy variance, and thermodynamic parameters, such as activation energy, are not representative of the overall mineral dissolution process. For this reason the activation energy value reported in Cappelli et al. [38] would be part of a probability distribution and could only be associated to the low step retreat.

In the same way biotite step-edge alteration can be reviewed based on the theory of dissolution/re-precipitation for silicate weathering [35,36,39,40]. Based on the results of other studies [11,20,41-43], in our previous work [38] we proposed that layer swelling and peeling likely occurred in three consecutive steps: (1) initial leaching of interlayer and octahedral cations from the biotite structure; (2) hydrolysis of the Si–O–Si and Si–O–Al groups of the tetrahedral sheet, responsible for the layer expansion and (3) re-polymerization of Si–OH groups to form Si–O–Si that might cause layer contraction by expulsion of water. In a new concept of the mineral/solution interface processes [36] the formation of the so called leached layer, due to the loss of octahedral and interlayer cations, is substituted by the existence of a dissolution/re-precipitation interface at which amorphous silica-rich surface layers form [40]. The always stoichiometric dissolution of the mineral is followed by the precipitation of a secondary phase in spite of an undersaturated bulk solution with respect to that secondary phase [36]. In agreement with this theory the increase of layer thickness could correspond to the newly formed silica layer. Yet, layer curling and peeling, observed also in previous studies [43,44], are not fully accounted for by this model.

At basic pH, dissolution also occurred through edge retreat. However, while at acidic pH precipitation of new phases was not observed, at basic pH the dissolution of the biotite (001) surface produced new structures, namely streaks, that grew from step edges and were associated with precipitation (Figure 3). During the early stage of dissolution streaks developed close to steps edges, spreading thereafter over the entire (001) surface (Figure 4). Sánchez-Pastor et al. [21] reported the formation of streaks with heights of 200 nm on phlogopite surfaces during dissolution at room temperature. These streaks were described as irregular swelling structures (bulge-type

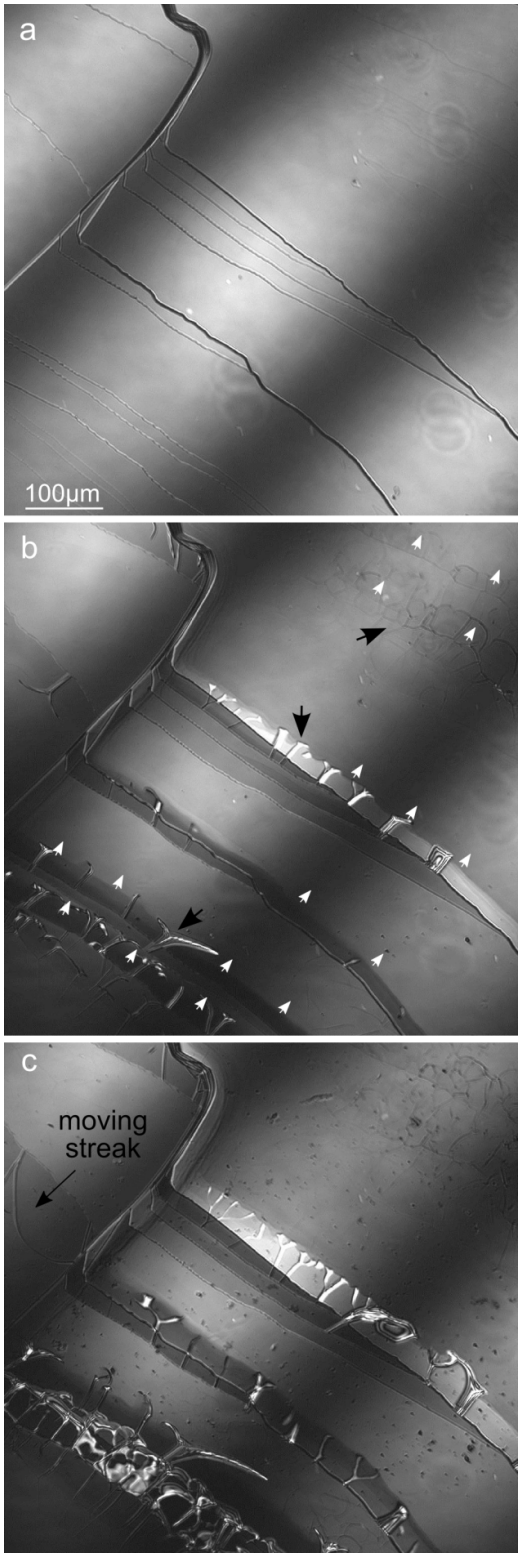

Figure 3: LCM-DIM images: a) freshly cleaved biotite (001) surface; b) same surface after about 33 h and c) after about 51 h at pH 9.5 and 50 °C. White arrows and black arrows in b) indicate edge retreat and streaks, respectively. Streaks formed (b) and grew (c) from steps edge.

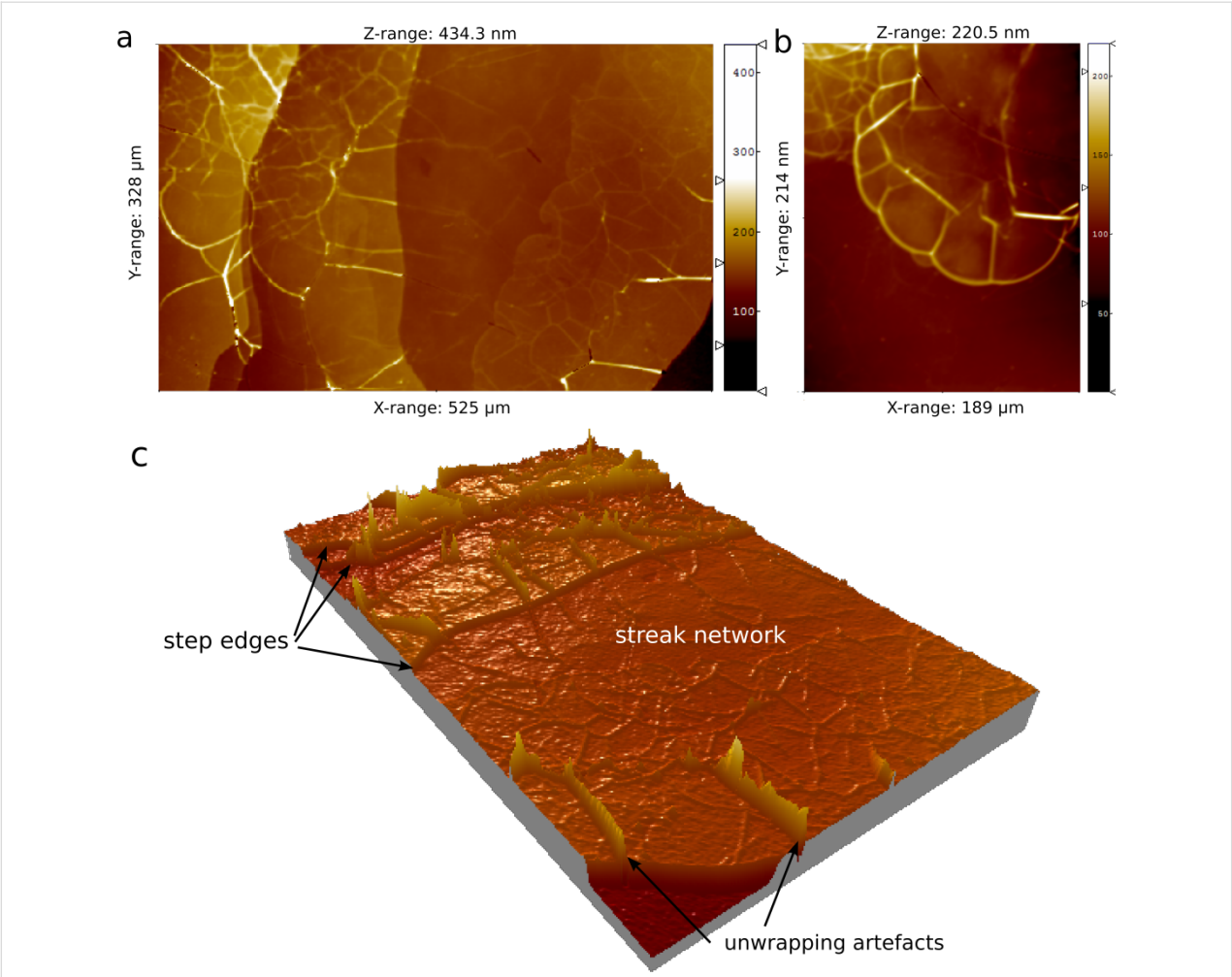

Figure 4: Unwrapped phase shift interferograms of a reacted biotite (001) surface at pH 9.5 and 50 °C after about 3 d: a) 2D image that shows high (80–100 nm) and low (8–10 nm) streaks, which spread from step edges; b) 2D image that shows low streaks in more detail; c) 3D image of a).

shapes). Their formation was associated with an excess of water uptake influenced by local variations of the TOT-layer charge. Likewise, Aldushin et al. [10] observed bulge formation (with heights up to 50 nm) on phlogopite induced by octylammonium–K^+ exchange, arguing that these swelling structures reorganized themselves in new configurations after some reaction time. A similar behaviour was observed in our experiments in which some streaks started to move after an induction time and changed their arrangement (Figure 3). The streaks developed as fiber-type structures with heights that ranged between 10 and 100 nm (measured by PSI with a Linnik configuration; Figure 4). Extensive evidence exists about mica transformation and formation of secondary phases during weathering over a wide range of experimental conditions [3,5,6,19,45,46]. Hu et al. [45] observed the formation of "fibrous illite structures" when biotite reacted in 1 mol·L^{-1} NaCl solution and high temperature (acidic hydrothermal conditions). Shao et al. [47] observed the formation of fibrous illite phases on reacted phlogopite surfaces in presence of organic acids under geologic CO_2 sequestration conditions (95 °C and 102 bar). Based on AFM observations, the authors argued that nano-particles can migrate over mineral surfaces (in particular from edge to basal surface) [46].

To identify the nature of the streak structures, the reacted biotite surface was analysed by confocal Raman spectroscopy. The spectra of the unreacted (001) basal surface and that of the reacted surface with the streaks only showed biotite peaks (Figure 5). However, it should be noted that, owing to the penetration depth (ca. 100 µm) of Raman spectroscopy and the consequent strong "background" signal from the bulk biotite phase with respect to the weak signal from the secondary phase(s), we cannot confirm nor refute the presence of new mineral phase(s). In addition, the measured chemical composition of the output solution of an experiment conducted at pH 9.5 shows a deficit in aqueous Al and Fe, as well as a higher

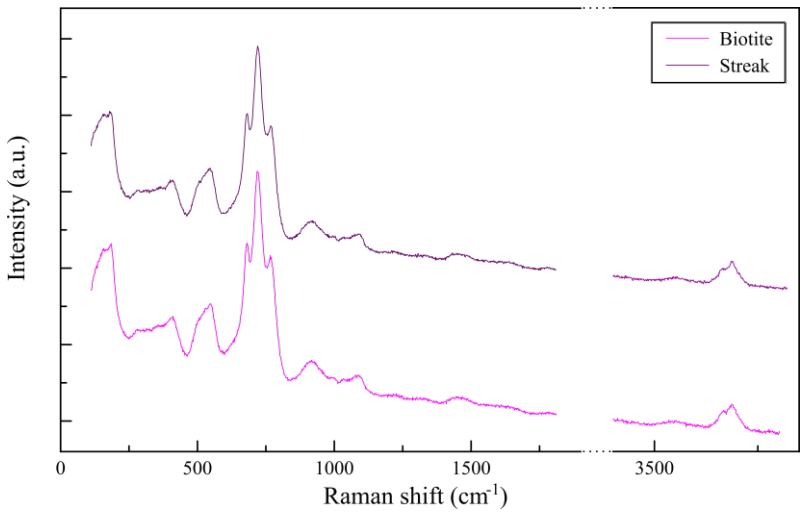

Figure 5: Comparison of characteristic Raman spectra of the (001) biotite surface and that of a streak formed at pH 9.5 and 50 °C. No differences between both spectra are detected.

Mg concentration than that of Si (Table 1). The calculated saturation index (SI) values show that iron oxyhydroxide (goethite) or aluminum oxyhydroxide (boehmite), as well as some Mg-bearing aluminosilicate minerals (talc, phlogopite and saponite) could precipitate (SI > 0, Table 2).

Table 1: Cation concentrations (μmol·L^{-1}) of the output solution at pH 9.5 and 50 °C (d.l.: detection limit).

element	run 1 μmol·L^{-1}	run 2 μmol·L^{-1}
Si	27.8	26.0
Al	<d.l.	1.5
Fe	4.5	3.6
Mg	16.9	16.5

Table 2: PHREEQC saturation indexes calculated with the measured composition of the output solution at pH 9.5 and 50 C.

phase	SI
boehmite	−2.94
brucite	2.81
$Fe(OH)_3$	0.11
goethite	4.91
muscovite	−16.13
nontronite-Na	−0.64
phlogopite	7.56
quartz	−3.59
saponite-Na	7.34
sepiolite	−0.78
SiO_2(am)	−4.71
talc	5.12

Although the derivation of the surface charge of multi-oxide silicates as a function of pH is complex and requires the knowledge of all zero point charge parameters (e.g., isoelectric point, point of zero net proton charge, point of zero salt effect) for an unambiguous description of biotite surface chemistry [48], in general, the alkali treatment of silicate mineral affects the variable surface charge in a way that reactivity towards charged and polar compounds should increase (increase in surface acidity) [49]. This could be responsible for the initial adsorption of particles along the edge surface, where a variable charge is present. Precipitates would then grow and expand on the biotite (001) surface forming a fiber-like structure. Similarly, Johnsson et al. [50] observed small fibrous structures by using AFM on muscovite basal surface after two days of reaction time at pH 5.7 at 22 °C. After ten days of reaction the fibers formed a network with a height of 8–12 Å, covering 20% of the sample surface.

Although the formation of oxides, hydroxides and aluminosilicate phases is likely to occur at the expense of biotite dissolution at basic pH, additional experiments are necessary to confirm or refute precipitation of secondary phases.

Conclusion

In situ LCM-DIM inspection, of the reacted biotite (001) surfaces has shown the differences between the basal surface reactivity in acidic (pH 1) and basic (pH 9.5) solutions. In both pH values step edges are preferential sites of dissolution, leading to step retreat. Layer swelling and peeling occur in acidic pH, while at basic pH fibrous structures (streaks) formed

at step edges, whose temporal evolution was monitored in situ by LCM-DIM. Precipitation appears to be responsible for the formation of streaks.

The experimental approach based on LCM-DIM is a promising technique to study in situ the surface alteration of mica (and other minerals) over a wide range of solution composition and temperature. The obtained (001) surface data at the mesoscale complements with that acquired at higher resolution scale by AFM and VSI/PSI in shorter experimental runs, as well as with that from long batch and flow-through experiments, which do not provide direct information on the occurring mineral surface mechanisms.

A promising future perspective involves the integration of a micro-Raman spectrometer to the LCM-DIM setup to provide simultaneous acquirement of the surface topography and chemistry during mineral (phyllosilicate) weathering.

Experimental

In situ flow-through experiments

Changes of the biotite (001) cleavage surface topography were monitored in situ by employing laser confocal microscopy with differential interference contrast microscopy (LCM-DIM, Figure 6a). This advanced optical system is a combination of two microscopy techniques: a confocal system (FV300, Olympus) is attached to an inverted optical microscope (IX70, Olympus) and a Nomarski prism is introduced into the optical path. A curve-matched thermistor and two Peltier elements were employed to precisely control the temperature of the flow-through observation cell (Figure 6b,c). A detailed description of this experimental setup can be found in previous publications [38,51].

The biotite sample used in the present work was from Bancroft-Ontario, Canada and was purchased from Ward's Natural Science Establishment. Its composition was reported by Turpault and Trotignon [43]. Biotite flakes with (001) cleavage surfaces of ca. 2 × 8 mm^2 and between 0.08 and 0.15 mm in thickness reacted with solutions of pH 1 (0.1 $mol{\cdot}L^{-1}$ HNO_3 and 0.01 $mol{\cdot}L^{-1}$ $NaNO_3$) at 11 and 25 °C and pH 9.5 (0.01 $mol{\cdot}L^{-1}$ $Na_2B_4O_7{\cdot}10H_2O$ and 0.022 $mol{\cdot}L^{-1}$ NaOH) at 50 °C. All solutions were prepared from ultrapure grade chemicals.

The biotite flakes were fixed parallel to the (001) surface on the bottom of the fissure of a custom-made Teflon flow-through cell by a silicone adhesive. The flow cell was a rectangular prism with a volume of 0.08 cm^3 (Figure 6c). A small channel on each side of the cell allowed the reacting solution to circulate at a constant flow rate (0.03–0.07 $mL{\cdot}min^{-1}$), yielding a residence time of approximately 3 to 8 min. The Teflon reactor was carefully sealed with a cover glass glued with high vacuum grease (Dow Corning). The duration of the experiments varied

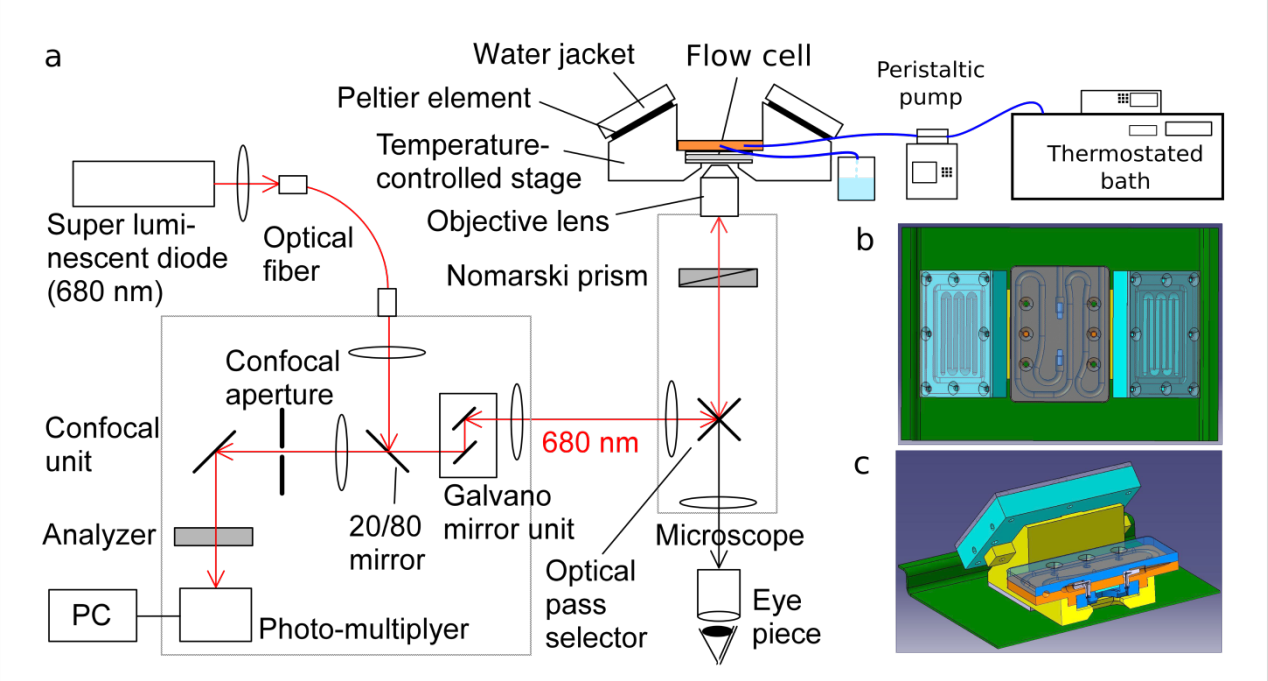

Figure 6: Schematic representation of the experimental setup: (a) Laser confocal differential intereference contrast microscope, (b) top view, and (c) a cross-sectional view of the temperature-controlled observation flow cell.

from 2 h to 3 d according to the experimental conditions. Images of the (001) cleavage surface were taken every 20 s to 15 min with a capture time of 9.6 s.

Solution analysis

The chemical composition of the input and output solutions of the basic pH experiment was determined. Si concentration was determined by colorimetry, using the molybdate blue method [52] with a UV–vis spectrophotometer (Perkin Elmer Lambda 25). The detection limit was 5 ppb and the uncertainty was less than 3%. Al concentration was measured by fluorimetry using lumogallion as complexing agent [53] with a FluoDia T70 high-temperature fluorescence microplate reader fluorimeter. The detection limit was 2 ppb and the uncertainty was less than 5%. Mg concentration was determined by ion chromatography using a Methrohm 883 Basic IC plus with a Metrosep C3 column. The detection limit and the uncertainty were 0.5 ppb and 3%, respectively. Fe concentration was determined by colorimetry, measuring the absorption of the red complex that Fe(II) forms with 1,10-phenanthroline [54,55]. The detection limit was 0.2 ppm and the uncertainty was less than 3%. The pH value was measured by using Crison combination electrodes, calibrated with pH 2, 7 and 9.2 buffer solutions (accuracy ±0.02 pH units).

Ex situ sample characterization

Raman spectroscopy coupled to a confocal microscope was used to examine ex situ the chemical composition of the reacted biotite (001) surface to identify possible newly formed phase(s). A lab-RAM spectrometer with backscattering geometry was employed to collect the spectra. A diode laser (λ = 525 nm) exited the surface and the emitted waves were detected with a Peltier cooled charge-coupled device (CCD) (1064 × 256 pixel) [56]. Signal averaging of three spectra was performed with a time acquisition of 300 s.

Solution saturation state

Table 2 shows the saturation indexes (SI) of the output solution of the experiment run at pH 9.5 and 50 °C collected between 48 h and the end of the experiment (about 69 h) that were calculated by using the PHREEQC code and the thermodynamic data base LLNL [57]:

$$\mathrm{SI} = \log \frac{\mathrm{IAP}}{K},$$

where K is the equilibrium constant for the mineral dissolution reaction and IAP is the corresponding ion activity product [43]. The concentration of NO_3^- and Na^+ was fixed to be 0.01 M and 0.04 M, respectively. Due to the high sodium concentration with respect to potassium, the K^+ concentration could not be measured due to overlapping cation peaks. Therefore, K^+ concentration was assumed to be stoichiometric with respect to Si released.

Acknowledgements

Financial support was obtained from Projects CGL2008-01652 and CGL2011-22567 (Plan Nacional I+D and EU). C.C. benefitted from a FPU grant (MEC), and A.E.S.V.D. is grateful for the support by the Consolider-Ingenio 2010 project "Factoría Española de Cristalización" and Belgian PROgramme de Développement d'Expériences scientifiques under Contract ESA AO-2004-070. FJH, amdg.

References

1. Haward, S. J.; Smits, M. M.; Ragnarsdóttir, K. V.; Leake, J. R.; Banwart, S. A.; McMaster, T. J. *Geochim. Cosmochim. Acta* **2011,** *75,* 6870–6881. doi:10.1016/j.gca.2011.09.010
2. Kalinowski, B. E.; Schweda, P. *Geochim. Cosmochim. Acta* **1996,** *60,* 367–385. doi:10.1016/0016-7037(95)00411-4
3. Malmström, M.; Banwart, S. *Geochim. Cosmochim. Acta* **1997,** *61,* 2779–2799. doi:10.1016/S0016-7037(97)00093-8
4. Malmström, M.; Banwart, S.; Lewenhagen, J.; Duro, L.; Bruno, J. *J. Contam. Hydrol.* **1996,** *21,* 201–213. doi:10.1016/0169-7722(95)00047-X
5. Murakami, T.; Utsunomiya, S.; Yokoyama, T.; Kasama, T. *Am. Mineral.* **2003,** *88,* 377–386.
6. Samson, S. D.; Nagy, K. L.; Cotton, W. B., III. *Geochim. Cosmochim. Acta* **2005,** *69,* 399–413. doi:10.1016/j.gca.2004.07.005
7. Taylor, A. S.; Blum, J. D.; Lasaga, A. C.; MacInnis, I. N. *Geochim. Cosmochim. Acta* **2000,** *64,* 1191–1208. doi:10.1016/S0016-7037(99)00369-5
8. Clemency, C. V.; Lin, F.-C. *Clays Clay Miner.* **1981,** *29,* 107–112. doi:10.1346/CCMN.1981.0290204
9. Kuwahara, Y.; Aoki, Y. *Clays Clay Miner.* **1995,** *43,* 39–50. doi:10.1346/CCMN.1995.0430105
10. Aldushin, K.; Jordan, G.; Aldushina, E.; Schmahl, W. W. *Clays Clay Miner.* **2007,** *55,* 339–347. doi:10.1346/CCMN.2007.0550401
11. Aldushin, K.; Jordan, G.; Schmahl, W. W. *Geochim. Cosmochim. Acta* **2006,** *70,* 4380–4391. doi:10.1016/j.gca.2006.04.015
12. Baba, M.; Kakitani, S.; Ishii, H.; Okuno, T. *Chem. Phys.* **1997,** *221,* 23–31. doi:10.1016/S0301-0104(97)00141-9
13. Bickmore, B. R.; Hochella, M. F., Jr.; Bosbach, D.; Charlet, L. *Clays Clay Miner.* **1999,** *47,* 573–581. doi:10.1346/CCMN.1999.0470504
14. Bosbach, D.; Charlet, L.; Bickmore, B.; Hochella, M. F., Jr. *Am. Mineral.* **2000,** *85,* 1209–1216.
15. Brandt, F.; Bosbach, D.; Krawczyk-Bärsch, E.; Arnold, T.; Bernhard, G. *Geochim. Cosmochim. Acta* **2003,** *67,* 1451–1461. doi:10.1016/S0016-7037(02)01293-0
16. Kuwahara, Y. *Am. Mineral.* **2006,** *91,* 1142–1149. doi:10.2138/am.2006.2078
17. Kuwahara, Y. *Am. Mineral.* **2008,** *93,* 1028–1033. doi:10.2138/am.2008.2688

18. Nagy, K. L.; Cygan, R. T.; Hanchar, J. M.; Sturchio, N. C. *Geochim. Cosmochim. Acta* **1999,** *63,* 2337–2351. doi:10.1016/S0016-7037(99)00118-0
19. Pachana, K.; Zuddas, P.; Censi, P. *Appl. Geochem.* **2012,** *27,* 1738–1744. doi:10.1016/j.apgeochem.2012.02.009
20. Rufe, E.; Hochella, M. F., Jr. *Science* **1999,** *285,* 874–876. doi:10.1126/science.285.5429.874
21. Sánchez-Pastor, N.; Aldushin, K.; Jordan, G.; Schmahl, W. W. *Geochim. Cosmochim. Acta* **2010,** *74,* 1954–1962. doi:10.1016/j.gca.2009.12.026
22. Kurganskaya, I.; Arvidson, R. S.; Fischer, C.; Luttge, A. *Geochim. Cosmochim. Acta* **2012,** *97,* 120–130. doi:10.1016/j.gca.2012.08.033
23. Luettge, A.; Bolton, E. W.; Lasaga, A. C. *Am. J. Sci.* **1999,** *299,* 652–678. doi:10.2475/ajs.299.7-9.652
24. Lüttge, A. *J. Electron Spectrosc. Relat. Phenom.* **2006,** *150,* 248–259. doi:10.1016/j.elspec.2005.06.007
25. Buss, H. L.; Lüttge, A.; Brantley, S. L. *Chem. Geol.* **2007,** *240,* 326–342. doi:10.1016/j.chemgeo.2007.03.003
26. King, H. E.; Satoh, H.; Tsukamoto, K.; Putnis, A. *Am. Mineral.* **2014,** *99,* 377–386. doi:10.2138/am.2014.4606
27. Sorai, M.; Ohsumi, T.; Ishikawa, M.; Tsukamoto, K. *Appl. Geochem.* **2007,** *22,* 2795–2809. doi:10.1016/j.apgeochem.2007.06.019
28. Ueta, S.; Satoh, H.; Kato, H.; Ueda, A.; Tsukamoto, K. *J. Nucl. Sci. Technol.* **2013,** *50,* 731–741. doi:10.1080/00223131.2013.799397
29. Ueta, S.; Satoh, H.; Nishimura, Y.; Ueda, A.; Tsukamoto, K. *J. Cryst. Growth* **2013,** *363,* 294–299. doi:10.1016/j.jcrysgro.2012.11.021
30. Van Driessche, A. E. S.; García-Ruíz, J. M.; Tsukamoto, K.; Patiño-Lopez, L. D.; Satoh, H. *Proc. Natl. Acad. Sci. U. S. A.* **2011,** *108,* 15721–15726. doi:10.1073/pnas.1105233108
31. Van Driessche, A. E. S.; Otálora, F.; Sazaki, G.; Sleutel, M.; Tsukamoto, K.; Gavira, J. A. *Cryst. Growth Des.* **2008,** *8,* 4316–4323. doi:10.1021/cg800782r
32. Fischer, C.; Arvidson, R. S.; Lüttge, A. *Geochim. Cosmochim. Acta* **2012,** *98,* 177–185. doi:10.1016/j.gca.2012.09.011
33. Lüttge, A.; Arvidson, R. S.; Fischer, C. *Procedia Earth Planet. Sci.* **2013,** *7,* 537–540. doi:10.1016/j.proeps.2013.03.115
34. Lasaga, A. C.; Luttge, A. *Science* **2001,** *291,* 2400–2404. doi:10.1126/science.1058173
35. Putnis, A.; Putnis, C. V. *J. Solid State Chem.* **2007,** *180,* 1783–1786. doi:10.1016/j.jssc.2007.03.023
36. Ruiz-Agudo, E.; Putnis, C. V.; Rodriguez-Navarro, C.; Putnis, A. *Geology* **2012,** *40,* 947–950. doi:10.1130/G33339.1
37. Hellmann, R.; Daval, D.; Wirth, R. *Procedia Earth Planet. Sci.* **2013,** *7,* 346–349. doi:10.1016/j.proeps.2013.03.154
38. Cappelli, C.; Van Driessche, A. E. S.; Cama, J.; Huertas, F. J. *Cryst. Growth Des.* **2013,** *13,* 2880–2886. doi:10.1021/cg400285a
39. Hellmann, R.; Penisson, J.-M.; Hervig, R. L.; Thomassin, J.-H.; Abrioux, M.-F. *Phys. Chem. Miner.* **2003,** *30,* 192–197. doi:10.1007/s00269-003-0308-4
40. Hellmann, R.; Wirth, R.; Daval, D.; Barnes, J.-P.; Penisson, J.-M.; Tisserand, D.; Epicier, T.; Florin, B.; Hervig, R. L. *Chem. Geol.* **2012,** *294–295,* 203–216. doi:10.1016/j.chemgeo.2011.12.002
41. Acker, J. G.; Bricker, O. P. *Geochim. Cosmochim. Acta* **1992,** *56,* 3073–3092. doi:10.1016/0016-7037(92)90290-Y
42. Kaviratna, H.; Pinnavaia, T. J. *Clays Clay Miner.* **1994,** *42,* 717–723. doi:10.1346/CCMN.1994.0420607
43. Turpault, M.-P.; Trotignon, L. *Geochim. Cosmochim. Acta* **1994,** *58,* 2761–2775. doi:10.1016/0016-7037(94)90112-0
44. Bisdom, E. B. A.; Stoops, G.; Delvigne, J.; Curmi, P.; Altemuller, H. J. *Pedologie* **1982,** *32,* 225–252.
45. Hu, Y.; Ray, J. R.; Jun, Y.-S. *Environ. Sci. Technol.* **2011,** *45,* 6175–6180. doi:10.1021/es200489y
46. Shao, H.; Ray, J. R.; Jun, Y.-S. *Environ. Sci. Technol.* **2010,** *44,* 5999–6005. doi:10.1021/es1010169
47. Shao, H.; Ray, J. R.; Jun, Y.-S. *Chem. Geol.* **2011,** *290,* 121–132. doi:10.1016/j.chemgeo.2011.09.006
48. Bray, A. W.; Benning, L. G.; Bonneville, S.; Oelkers, E. H. *Geochim. Cosmochim. Acta* **2014,** *128,* 58–70. doi:10.1016/j.gca.2013.12.002
49. Jozefaciuk, G. *Clays Clay Miner.* **2002,** *50,* 647–656. doi:10.1346/000986002320679378
50. Johnsson, P. A.; Hochella, M. F. J.; Parks, G. A.; Blum, A. E.; Sposito, G. Direct observation of muscovite basal-plane dissolution and secondary phase formation: An XPS, LEED, and SFM study. In *Water-Rock Interaction;* Kharaka, Y. K.; Maest, A. S., Eds.; A. A. Balkema: Rotterdam, 1992; Vol. 1, pp 159–162.
51. Van Driessche, A. E. S.; Gavira, J. A.; Patiño Lopez, L. D.; Otalora, F. *J. Cryst. Growth* **2009,** *311,* 3479–3484. doi:10.1016/j.jcrysgro.2009.04.023
52. Grasshoff, K.; Ehrhardt, M.; Kremling, K., Eds. *Methods of Seawater Analysis;* 1983. doi:10.1002/9783527613984
53. Howard, A. G.; Coxhead, A. J.; Potter, I. A.; Watt, A. P. *Analyst* **1986,** *111,* 1379–1382. doi:10.1039/an9861101379
54. Lazic, D.; Skundric, B.; Penavin-Skundric, J.; Sladojevic, S.; Vasiljevic, L.; Blagojevic, D.; Obrenovic, Z. *Chem. Ind. Chem. Eng. Q.* **2010,** *16,* 193–198.
55. Pyenson, H.; Tracy, P. H. *J. Dairy Sci.* **1945,** *28,* 401–412. doi:10.3168/jds.S0022-0302(45)95191-5
56. Ramírez-Rodríguez, G. B.; Delgado-López, J. M.; Gómez-Morales, J. *CrystEngComm* **2013,** *15,* 2206–2212. doi:10.1039/c2ce26556g
57. Parkhurst, D. L.; Appelo, C. *Description of Input and Examples for PHREEQC Version 3--a Computer Program for Speciation, Batch-reaction, One-dimensional Transport, and Inverse Geochemical Calculations*, 2013.

License and Terms

BEILSTEIN JOURNAL OF NANOTECHNOLOGY

Nanoscale rippling on polymer surfaces induced by AFM manipulation

Mario D'Acunto*[1,2], Franco Dinelli*[3] and Pasqualantonio Pingue*[4]

Review

Open Access

Address:
[1]Istituto Struttura della Materia, ISM-CNR, via Fosso del Cavaliere 100, 00133 Rome, [2]Istituto di Scienza e Tecnologie dell'Informazione, ISTI-CNR, via Moruzzi, 1, 56124, Pisa, Italy, [3]Istituto Nazionale di Ottica, INO-CNR, via Moruzzi 1, 56124, Pisa, Italy and [4]Laboratorio NEST, Scuola Normale Superiore and Istituto Nanoscienze-CNR, Piazza San Silvestro 12, 56127 Pisa, Italy

Email:
Mario D'Acunto* - mario.dacunto@isti.cnr.it; Franco Dinelli* - franco.dinelli@ino.it; Pasqualantonio Pingue* - pasqualantonio.pingue@sns.it

* Corresponding author

Keywords:
atomic force microscopy (AFM); films; nanomanipulation; nanomechanics; polymers; ripples

Beilstein J. Nanotechnol. **2015,** *6,* 2278–2289.
doi:10.3762/bjnano.6.234

Received: 01 July 2015
Accepted: 13 November 2015
Published: 02 December 2015

This article is part of the Thematic Series "Nanomanipulation and environmental nanotechnology".

Associate Editor: T. Glatzel

Abstract

Nanoscale rippling induced by an atomic force microscope (AFM) tip can be observed after performing one or many scans over the same area on a range of materials, namely ionic salts, metals, and semiconductors. However, it is for the case of polymer films that this phenomenon has been widely explored and studied. Due to the possibility of varying and controlling various parameters, this phenomenon has recently gained a great interest for some technological applications. The advent of AFM cantilevers with integrated heaters has promoted further advances in the field. An alternative method to heating up the tip is based on solvent-assisted viscoplastic deformations, where the ripples develop upon the application of a relatively low force to a solvent-rich film. An ensemble of AFM-based procedures can thus produce nanoripples on polymeric surfaces quickly, efficiently, and with an unprecedented order and control. However, even if nanorippling has been observed in various distinct modes and many theoretical models have been since proposed, a full understanding of this phenomenon is still far from being achieved. This review aims at summarizing the current state of the art in the perspective of achieving control over the rippling process on polymers at a nanoscale level.

Introduction

On deforming surfaces that are subject to external perturbations, ripple patterns commonly form over a wide range of length scales. For instance, macro ripples with a periodicity from meters to several centimeters are created by the wind blowing on sandy deserts and seashores [1]. The same behavior can be obtained by sliding loads on unpaved roads, ski slopes and rail tracks. Similarly, ion-beam sputtering on metal or semiconductor substrates can produce ripples on the microscale and

nanoscale. The first example, reported in the literature, showed that low energy ion erosion of glass surfaces could lead to the formation of self-organized periodic patterns [2]. Since then, very regular patterns have been fabricated with this technique on a variety of materials, such as metals, semiconductors, and insulators, demonstrating the universality of this process [3]. The periodicity of the patterns can be tuned by varying the energy of the ions and ranges from a few tens of nanometers up to a few micrometers, with ion beam energies ranging from 0.1 to 100 keV. In particular two types of patterns are observed: ripples oriented either parallel or perpendicular to the direction of the ion beam, depending on the angle of incidence. Ultrashort laser pulses have been also employed for micro- and nanostructuring of polymer, semiconductor and metal samples [4]. In this case the ripple periodicity is correlated to the laser wavelength, while the orientation is determined by the laser polarization direction but it is also correlated with the laser scan direction and velocity.

Finally, the advent of atomic force microscopy (AFM) has opened the possibility to study single contact asperity contacts [5]. Nanoscale ripples have been then observed after performing one or many scans over the same area on a wide range of materials, namely ionic salts, metals, and semiconductors [6-9]. Regarding some crystalline materials, D'Acunto [10,11] and Filippov et al. [12] have successfully reproduced the experimental data via computational methods. Nevertheless, it is for polymeric films that the ripple formation has been studied most extensively [13-19]. Ripple structures on polymers can be produced either by performing a single scan or many scans on the same area of the sample. One can employ a heated tip [20-22] or a standard tip, on annealed or solvent-rich polymer films [23,24]. The ripple formation has been found to depend on a variety of material properties such as the preparation method, the mean molar mass of the polymer, the degree of crystallinity, as well as on the scanning conditions, namely the applied force, the tip shape and size, and the relative velocity. A wide spectrum of polymers has been investigated including polystyrene (PS) [13,20], poly(methyl methacrylate) (PMMA) [25], poly(ethylene terephthalate) (PET) [23], poly(vinyl acetate) (PVAc) [26] and poly(ε-caprolactone) (PCL) [23].

Recently, we have reviewed wear occurring on polymeric surfaces and how it can be exploited in order to deduce the molecular properties of polymer films [27]. In this review, we wish to specifically focus on the controlled formation of 'nanoripples'. This phenomenon is related to plastic deformation, which in general does not lead to the formation of debris. In particular it can be exploited in order to pattern films for nanotechnology applications. The review is organized in three sections. The first one is dedicated to the most relevant observations reported in the literature. The second one deals with the theoretical modeling developed in order to interpret this phenomenon and predict further useful characteristics. The final section describes the strategies adopted up to now in order to achieve a good control of the phenomenon itself.

Review

Part 1: Phenomenological observations

The deformation of polymer surfaces upon contact with a sharp object is a phenomenon well known before the invention of the AFM methods. In particular, it was studied at a macroscopic level by sliding stiff objects, generally cones or spheres, over polymer samples. Plastic deformation and wear of polymer surfaces represented the subject of several experimental works carried out starting from the sixties of the last century. One of the most striking observations was the formation of macroscopic surface undulations, nowadays known as 'Schallamach waves' [28,29].

With the invention of AFM, the scientific interest moved to the investigation of plastic deformation and wear in polymer films on lower spatial scales. When one moves to smaller and smaller contact areas the wear features have dimensions well below the detection limit of optical microscopy, a typical instrument employed for the observations of Schallamach waves. Thus, grooves or ripples on the nanoscale can be imaged by means of AFM only after being formed with the same probe working in a lower load regime or in tapping mode. The first nanoripple observations have been reported when operating in the so called 'contact mode' (Figure 1), that is with the probe in contact and moved over a given area in a raster-like pattern. In this case the observed ripples were perpendicular or almost perpendicular to the fast scanning direction.

The researchers have soon realized that many parameters can affect the formation of nanoripples. These parameters depend on the characteristics of the tip–surface contact, the experimental conditions and the physico-chemical properties of the samples. Thus the dependences of nanoripple patterns on the scanning parameters have been extensively studied in the past decades. Equally, the dependences of nanoripple patterns on the properties of the samples have been qualitatively and, in some instances, quantitatively derived. The key observations and findings are reviewed in the following two sections.

Dependence on the scanning modality

Scanning parameters: Using an AFM, one can vary a range of experimental parameters such as the tip shape and surface chemistry, the applied load, the cantilever longitudinal and lateral stiffness, the scan direction and velocity, the spacing between successive lines (named 'feeding'). Depending on

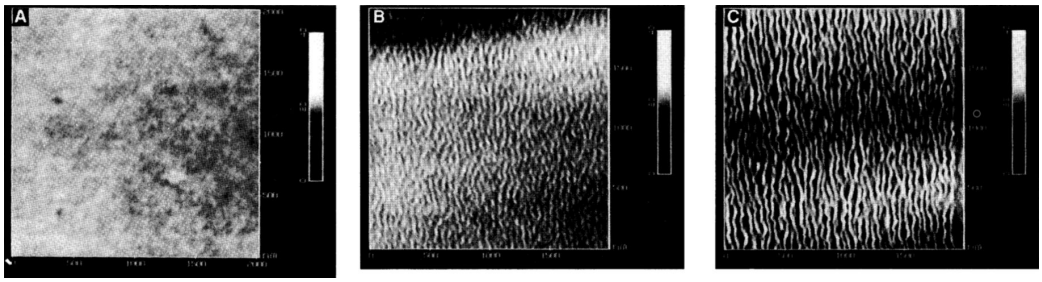

Figure 1: First experimental observations of the nanoripple formation on polymer films (2 × 2 μm^2): from a pristine surface of PS (A), through the initial stages of deformation (B), to a fully developed pattern (C). The gray scale covers a height difference of 10 nm. Reprinted with permission from [14]. Copyright 1992 AAAS.

these parameters, the nanoripple patterns form in either one or several scan frames. The most significant physical observables of the process are the lateral spacing and the vertical amplitude. In particular, they both tend to decrease with increasing the scan velocity [13]. On the contrary, both spacing and amplitude tend to increase with increasing the load applied and the number of scans [30].

Single and multiple line scratching: If one proceeds in a single line scratching mode, the nanoripple formation can be more easily controlled and determined than in a multiple line scratching mode [31,32]. In the latter case, the feeding and the number of scans over the same area are also extremely relevant. It has been reported that the patterns depend on the molecular weight (M_w), on the scan direction and on the velocity [13]. In particular, as already stated above, the periodicity and the amplitude decrease with increasing the velocity. Ripple patterns can properly form only in the multiple lines scratching mode, sometimes immediately after the first passage of the probe. They are dependent on the probe movement direction, i.e., along parallel or slightly tilted (zig-zag) lines [15,16,31,33-35]. However, an analogy between the macroscale and microscale formations of ripples can be only drawn if the feeding is small enough that the whole scan can be described as the parallel movement of a number of tips moving together along the same direction, like a blade. The final pattern could also depend on the number of scans.

Tip trajectory: Gnecco et al. have also evidenced that ripple patterns could be obtained via circular or spiral trajectories of the tip [22,36] inducing in this way the formation of a rippled structure along the circumference of a scanned circle (Figure 2). While scanning a PMMA surface with a minimum feedback, the authors have been able to record instantaneous variations in the cantilever vertical displacement. They have thus demonstrated that the ripples move after consecutive frames in a manner that can be considered similar to a wave packet travels in space. Additionally, they have managed to calculate the corresponding group velocity.

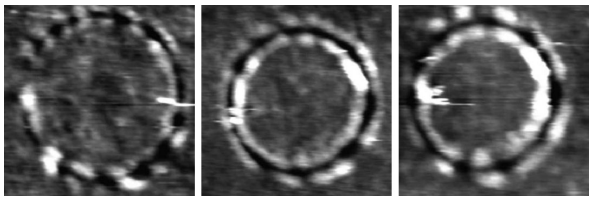

Figure 2: Topographical images in contact mode of three circular ripples created by a resistively heated AFM tip on a PPMA film. The image on the left is 410 × 410 nm^2, the image in the middle is 445 × 445 nm^2, and the image on the right is 375 × 375 nm^2. All images have been obtained after only a few circular scans with a hot tip. The gray scale covers several nanometers. Reprinted with permission from [22]. Copyright 2009 American Physical Society.

Dependence on material properties

Molecular weight (M_w): For amorphous polymers, two relevant parameters are M_w and the monodispersity index. The viscoplastic behavior of samples made with different M_w and monodispersity index values can be drastically different. In particular the propensity for the formation of nanoripples varies enormously. This is clearly visible in the case reported in Figure 3. It has been suggested that this behavior is correlated to the critical M_w (M_c) [37]. For $M_w < M_c$, the molecules are never entangled [38]. The patterns and their load dependence reveal that the ripples either do not form or they are very irregular in shape and periodicity. In addition, bunches of molecules are moved and/or disrupted in an abrasive way (Figure 3A,B). On the contrary, for $M_w > M_c$, the molecules are fully entangled, when the sample can be considered close to a thermodynamic stable state [38]. This is valid provided thermal annealing has been performed and solvent has been removed. Consequently, nanoripples form more easily, because the molecules cannot be removed from the surface but simply locally displaced (Figure 3C,D). For M_w close to M_c (approx. 30 kDa for PS)

[38], it is possible to switch from a non-wear regime to abrasive wear by increasing the applied load or the number of scans.

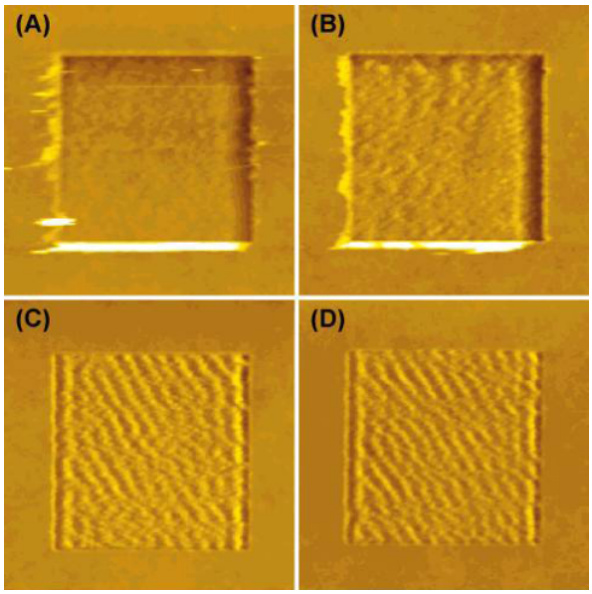

Figure 3: Topographical images (1.5 × 1.5 μm^2) of surfaces scratched in the multiple line mode. The PS films analyzed have different M_w values: (A) 8 kDa, (B) 15.8 kDa, (C) 58 kDa, and (D) 164 kDa. The applied load is constant and equal to 10 nN. Adapted with permission from [31]. Copyright 2001 American Chemical Society.

In the work of Y. Sun et al. [13] the interpretation of the ripple patterning dependence on M_w is well depicted in terms of small and large sizes of the polymer molecules. The authors found well-ordered ripple patterns forming on PS films with a M_w of 250 kDa. No ripple formation was obtained for films with M_w values of 1.3 and 13 kDa, while operating in the same load and scan velocity conditions.

Crystallinity: Compared to amorphous regions, crystalline parts are generally less prone to wear. The most extensive and comprehensive studies of this topic have been carried out by Beake et al. [39-41]. They have considered the case of PET films, as this material can crystallize and samples can be made with different ratios of crystalline to amorphous components. The films were thus produced with the goal to obtain different sizes and densities of crystalline domains, either from standard molding or by means of applying uni- or bi-axial stretch to the melt when cooled down. These results show that the periodicity of nanoripples depends on the applied load value. The authors also found that the applied load needed to form ripples is higher for densely crystalline samples than for completely amorphous ones. Specific areas that initially show different morphologies give origins to different pattern periodicity. This behaviour is interpreted with different degrees of crystallization. In general, it can be suggested that for crystalline films one needs to initially create an amorphous layer and only then the ripples can fully form. Obviously, the whole process depends on how the amorphous layer is created, as the density and molecular conformations in such a layer are quite different from amorphous films. However, the M_w value of these samples is rarely known, making the interpretation of the data more complicated.

Presence of solvents: As it is widely known, polymers dissolve in solvents with similar chemo-physical properties. This is why they can be easily molded in a variety of shapes including thin films, by means of spin coating or drop casting. The relative presence of residual solvent molecules is responsible for weakening the mechanical properties. This phenomenon is known by the name of 'plasticization' [42]. It depends on the fact that solvent molecules are intercalated into the polymer molecules and the final result is a film swelling depending on the amount of solvent. Via a thermal post treatment the solvent can be finally removed, however the process depends on several parameters such as temperature, time, and solvent employed. Therefore assessing the amount and the type of solvent present is very crucial for the rippling process [13,15,23,24,43]. In Figure 4, we report an example of PCL and PET films exposed to different environmental conditions including solvent vapours. It is found that when these films deform faster and at lower load

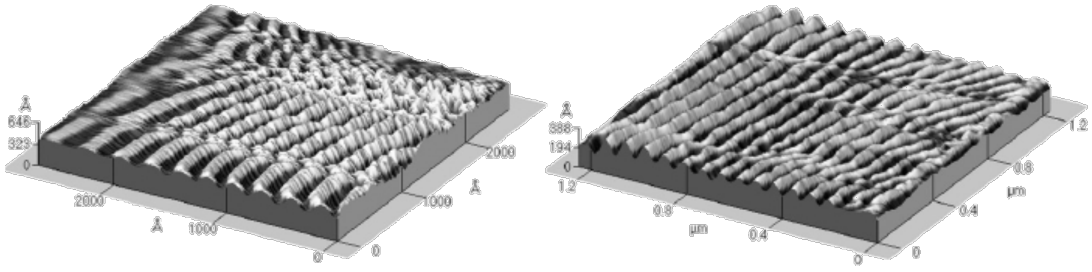

Figure 4: Solvent-enriched polymer films. Examples of 3D ripple structures on PCL (left) and PET (right). The images were obtained in air (relative humidity 40%), with a silicon conical shape tip with a nominal radius of 10 nm, a cantilever stiffness of 0.24 N/m, an applied load in the range between 2 and 10 nN, and scan velocity of 0.25 μm/s on 80 nm thick films. Reproduced with permission from [23]. Copyright 2007 Elsevier.

values compared to standard conditions. D'Acunto et al. [23] and Napolitano et al. [24] have reported that very regular ripple patterns can be created by means of a small applied load and just in a single scan on the surface of solvent-containing poly(ethylene terephthalate) (PET) films. In these works, solvent enrichment was obtained by simply avoiding the step of polymer curing and using the polymer film 'as is' after the spin coating deposition step. In this way, part of the solvent remains trapped in the polymeric thin film and the specific patterning procedure employed leads to the production of well-ordered ripple structures.

Temperature dependence: The temperature (T) dependence of nanorippling can be successfully addressed via AFM investigations. This has been done either through heating the probe [22,44] or the sample [19,20,45-47]. It is in fact commonly known that amorphous polymers have a second order thermodynamic discontinuity, named 'glass transition'. This transition can be observed to various extents in the bulk as well as in the films depending on the crystalline degree of the analyzed sample. The value, at which it typically occurs, is called glass transition temperature (T_g). In general, an AFM cannot observe the first order transition, which corresponds to crystalline melting.

Herein, we report one of the many experiments that can be found in the literature [20]. In order to create the morphology reported in Figure 5, a heated tip was scanned over a PS film (M_w = 70 kDa, bulk T_g = 100 °C) from right to left while increasing T from 30 to 410 °C. The surface starts to deform into nanoripples already at 30 °C. The lateral spacing and the vertical amplitude increase with increasing T. The transition from rippling to pileup wear occurs in a narrow window at around 237 °C. Many more studies deal with the change of the mechanical properties of polymers as a function of T. Typically the samples are heated rather than the tip, as these setups are easier to build and to control. For instance, Schmidt et al. investigated the ripple patterns, as they were concerned with the dependence of the viscoelasticity on T [45].

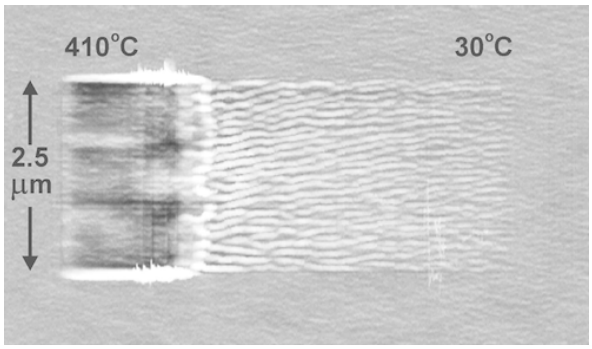

Figure 5: The worn area is the result of scanning a given surface with a variably heated tip, increasing T from 30 (right) to 410 °C (left). The PS film has a M_w of 70 kDa. The scan velocity is 50 μm/s. The gray scale covers 17 nm. Reprinted with permission from [20]. Copyright 2003 American Chemical Society.

Similarly, Rice et al. have investigated the T dependence of rippling for the thin lamellar microphases forming in polystyrene/poly(ethylene oxide) block copolymer (PS-*b*-PEO) films [48]. In particular via an analysis of the ripple patterns, they have deduced local thermochemical parameters such as the melting temperature of PEO, the T_g of PS, the specific heat of PS-*b*-PEO, the melting enthalpy of PEO, and the Helmholtz free energy for unfolding (and melting) of PEO.

Composite films: Another class of samples showing a peculiar pattern formation are polymer blends. They can be miscible or immiscible, presenting clear phase separation or a similar morphology to homopolymers. In Figure 6 we show the case of films obtained from blending two PS solutions with M_w of 8 and 164 kDa in various proportions [31]. The M_w values were chosen to be above and below M_c for molecular entanglement. For the two extreme cases, wear patterns are equal to those shown in Figure 3. Other studies carried out on heteropolymer films can be also found in the literature. Buenviaje et al. have studied blends made of two immiscible components with different T_g values [49]. In samples exhibiting phase separation, regions corresponding to different materials would present nanoripples with different periodicities depending on the T value at which the experiment is carried out and with respect to the T_g values of the two components. Maas et al. [50] have conducted an experimental work on polysterene/polyvinylpyrrolidone (PS/PVP) copolymer films where the composition ratio is varied and the wear patterns reveal the different proportions of PS and PVP within the single molecules. Finally, Aoike et al. [51] have also reported studies on random copolymers.

Part 2: Theoretical modelling

Once observed and described, like any other physical phenomenon, the formation of nanoripples should be rationalized so that it can be eventually controlled and exploited. In particular, nanorippling of polymer surfaces can be envisioned as a valid approach for lithographic purposes, particularly nowadays when nanotechnology is developing very quickly. However, achieving control of the ripple formation and therefore of polymer nanomanipulation requires a precise knowledge of all the parameters involved in the process. With the increasing number of observations, various models have been put forward to explain the occurrence of the nanopatterns. The main mechanisms proposed for nanopatterning induced by means of an AFM tip on polymer films are basically three: Schallamach

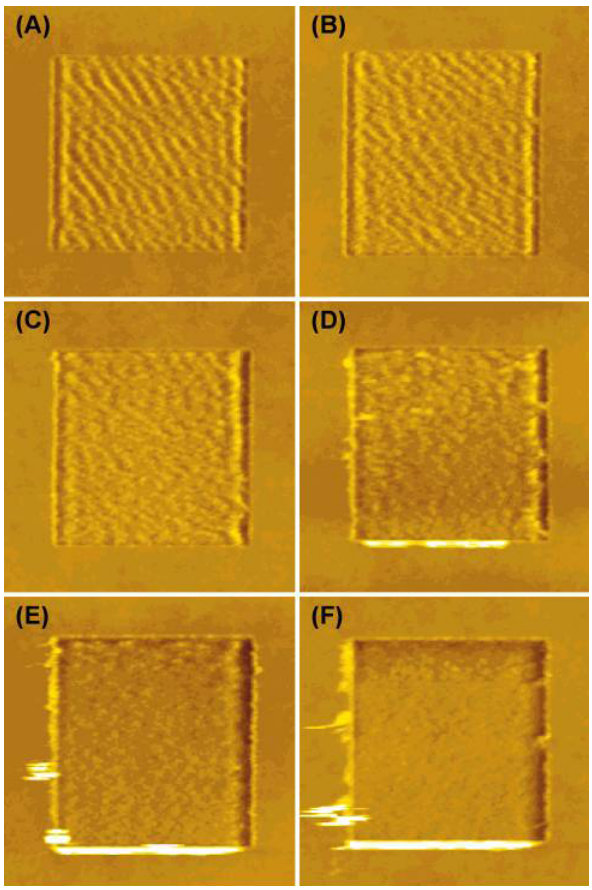

Figure 6: Topographical images (1.5 × 1.5 μm^2) of patterns induced on films obtained from blending two PS solutions with M_w of 8 and 164 kDa. The ratio of the two solutions is (8 kDa/164 kDa): (A) 0/100, (B) 10/90, (C) 30/70, (D) 50/50, (E) 70/30, (F) 90/10, and (G) 100/0. The applied load is constant and equal to 10 nN. Reproduced with permission from [31]. Copyright 2001 American Chemical Society.

waves [28], stick–slip behavior [52,53], and fracture-based descriptions [15,48].

On the macroscale, Schallamach waves are a reversible phenomenon that occurs at the surface of an elastomer when it slides past a stiff surface under compressive loads. It is attributed to buckling, i.e., waves of detachment driven by a tangential stress gradient along the contact zone of the sliding interface due to the breaking of adhesive bonds between the two surfaces [28]. On the nanoscale, however, ripples do not relax to their initial smooth shape when the tip is withdrawn and the sample is left unperturbed. Furthermore, the formation of the Schallamach waves on the macroscale was found to be dependent on a peeling phenomenon within the whole area of contact. The ripple periodicity on the nanoscale is found to be much larger than the actual contact area. Or, it is better to say that the possible formation of Schallamach waves within the contact area cannot be observed.

Therefore the formation of nanoripples is a phenomenon that occurs at the front edge of the contact. In particular, it has been suggested to be due to a stick–slip motion of the tip during the stage movement. A hole forms where the tip resides and a mound forms in front of the tip hindering the sliding motion [20]. The tip can slip over when the cantilever exerts a lateral force larger than the tip–sample adhesive interaction. Then the tip forms a new pair of hole and mound, so on and so forth. In order to form a continuous front, the positions of the mounds formed along adjacent lines need to be correlated and in phase. Notwithstanding the experimental differences, according to Aoike et al. [51], the friction coefficients measured in the macroscale and nanoscale cases are equivalent, when one normalizes the normal load values to the contact area. From this observation, they infer that the macroscale and nanoscale processes and their respective plastic deformations are determined by similar mechanisms.

Finally, Elkaakour et al. [15] have proposed another mechanism: A peeling process with the material pushed ahead of the contact via crack propagation. For an injection-molded polycarbonate surface, Iwata et al. [18] have found that the bundles are less stiff than the undamaged surface, which they have also interpreted as evidence of the presence of micro voids or cracks in the damaged region. Further experiments have been consequently stimulated pointing in this direction. It was argued that the crack formation might increase the volume of the perturbed region. This is a consequence of the mass conservation principle, assuming the incompressibility of the film. However, Rice et al. [48] did not observe the presence of peeling effects on locally heated PS-*b*-PEO copolymers. They suggested instead a vertical “crack” that may open once the tip sticks.

More recently, Gnecco et al. [54] have employed the Prandtl model [55] to describe the nanoripple evolution in single scratch tests. In this model, the atomic structure of the substrate is not considered. This makes the continuum model more suitable for polymeric materials that are amorphous and have fully entangled molecules, i.e., for $M_w >> M_c$. They have also introduced an indentation rate N, varying upon penetration of the tip. If one knows the time dependence $N(t)$ and the indenter width, the process is found to be governed only by the scan velocity v and the lateral stiffness k. Specifically, the amplitude A and ripple periodicity increase when N exceeds a critical value N_c or, vice versa, when k or v fall below the critical values of v_c and k_c, respectively (Figure 7). A transition from stick–slip to gliding can be also predicted for an indentation rate below a critical value or, alternatively, for large values of the sliding velocity, the lateral stiffness or the tip width. It is suggested also that this approach might be used to describe the evolution of similar rippling processes, by simply employing a proper inden-

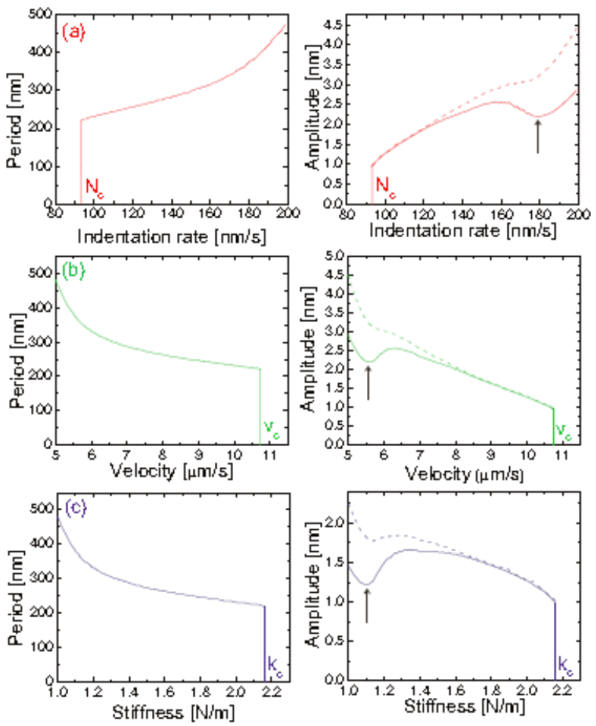

Figure 7: Ripple periodicity (left column) and ripple amplitude (right column, continuous curves) as a function of (a) the indentation rate *N*, (b) the sliding velocity *v* and (c) the lateral stiffness *k* with the other parameters kept fixed at the same values. When critical values (labelled with 'c' and corresponding to the vertical lines) are reached, the ripple pattern suddenly disappears. In the right column the maximum height (dashed curves) of the surface profiles is also shown. The corrugation can even decrease in the regions indicated by the arrows. Reproduced from [54].

tation law. This analytical model could be also useful in order to understand phenomena such as the rippling of unpaved roads, ski slopes and rail tracks. A model fully describing the nanoripple formation, independently of the material involved, is however not yet available.

Part 3: Towards achieving control

Based on the phenomenological observations and the theoretical models described in the two previous sections, some strategies have been devised and implemented in order to control the patterning, namely using cantilevers with miniaturized and integrated heaters; enriching the film with solvent; creating boundary conditions via defined tip trajectories; applying localized electrostatic fields through the tip to induce mechanical instabilities or crosslinking. Some of those efforts are summarized in this section.

Heated tip

One way to produce fast ripple patterns is to employ a heated tip (HT) as polymer properties strongly depend on *T*, especially in the glass transition regime. Vettiger et al. [56] have exploited the relative ease of patterning polymers above T_g for write/read storage operation in a thin polymer medium, obtaining bit densities similar or significantly higher than those achieved with magnetic storage systems at that time. Gotsmann and Dürig [30] have reported the creation of regular ripple structures employing HT on a 20 nm thick PS film. These patterns present a periodicity of around 100 nm and amplitude saturating at 20 nm. In addition, the authors have calculated energy activation for PS polymer pattern at *T* close to but below T_g to be on the order of about 0.4 eV.

Gnecco et al. [22] have reported that linear ripples with a period ranging from one to several hundreds of nanometers can be reproduced on the surface of polycarbonate (PC), poly(methyl methacrylate) (PMMA), and polystyrene (PS) films. Authors have clearly shown that the ripple formation varies with *T* and polymer type (Figure 8a). The dependence on *T* has been characterized and its behaviour correlated to the T_g value of the

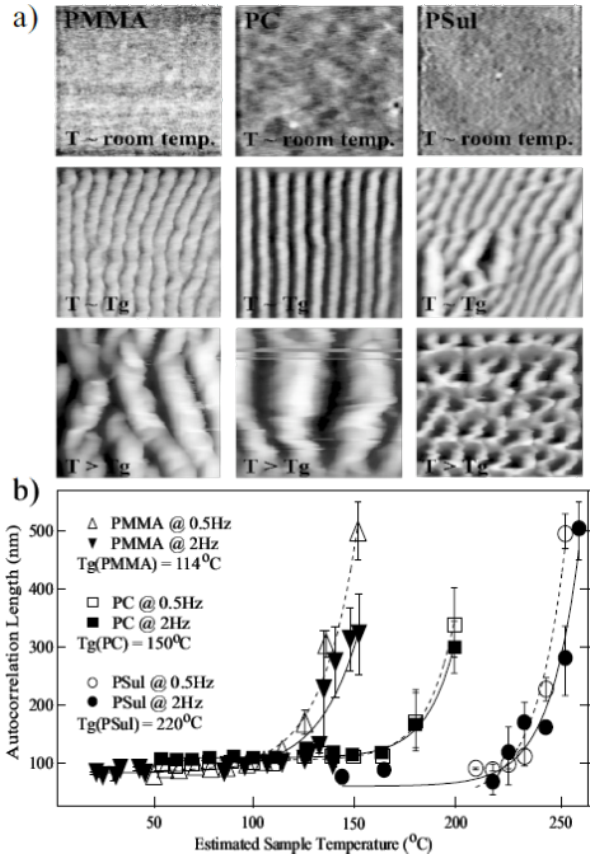

Figure 8: (a) Topographical images (1 × 1 μm^2) of nanoripples created by means of a resistively heated tip at various *T* values on PMMA, PC and PS films. (b) A plot of the autocorrelation lengths versus estimated *T*, derived from the images shown in (a). It reveals an exponential dependence with increasing *T*. The two sets of data per material have been obtained for *v* of 0.5 μm/s (dashed lines) and 2 μm/s (solid lines). Reprinted with permission from [22]. Copyright 2009 American Physical Society.

polymer investigated (Figure 8b). Such dependence can then be used to control the process. However, due to the exponential dependence on T of the ripple spacing (Figure 8), achieving a precise control over large spatial extensions is feasible but not easy.

Solvent enrichment

An alternative to fast patterning by means of HT is to scan solvent-enriched polymer films. Here, the solvent initially trapped in the vicinity of the surface has an analogous role to heating the tip. The film can be thus easily patterned under the passage of the AFM tip. Leach et al. [43] have obtained rippled PMMA surface (periodicity ≈ 100 nm) with a high normal force (180 nN) and a single scan using different solvents, such as water or alcohol–water mixtures.

Gnecco et al. [54] have shown that surface ripples on a 400 nm thick PS film diluted with toluene can be explained by the competition between the driving spring force and the plastic response of the sample (Figure 7). The authors have firstly suggested that the ripples are expected to disappear when the indentation rate is below a critical value or the scan velocity is high (Figure 9), as more recently modeled. They verified the model on PS films enriched with toluene, demonstrating a good capability in controlling the periodicity and the amplitude of the pattern (Figure 10).

Influence of boundary conditions

To further improve the control when employing solvent-rich samples, we now show in this section an experiment exploiting a key observation of the AFM-based patterning: the correlation between the nanoripple orientation and the tip movement direction. The wearing properties of polymer surfaces can be thus exploited to create ripple structures by employing scans with proper boundary conditions that allow for the fabrication of self-assembled and ordered ripples.

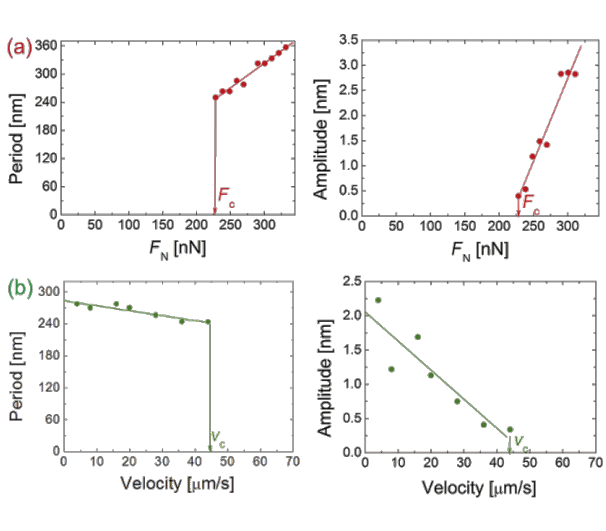

Figure 9: Theoretical variation of the ripple periodicity (left column) and ripple amplitude (right column) as a function of (a) the normal force F_N and (b) the sliding velocity v. Critical values, corresponding to the vertical lines, are labelled with 'c'. The ripples are formed only if $F_N > F_c \approx 220$ nN or if $v < v_c \approx 45$ μm·s^{-1}. Reproduced from [54].

Napolitano et al. [24] have carried out a series of experiments on PET films focusing their attention on the dependence of the ripple orientation on the boundary conditions. In particular, they have performed nanolithography by scanning the tip within circular, triangular, ellipsoidal and L-shaped areas. The results significantly show that the pattern orientation can be modified. In Figure 11, we report an example where, scanning the tip along parallel lines in a square region, the applied load is increased, compared to the rest of the area, only when moving in the central circular region.

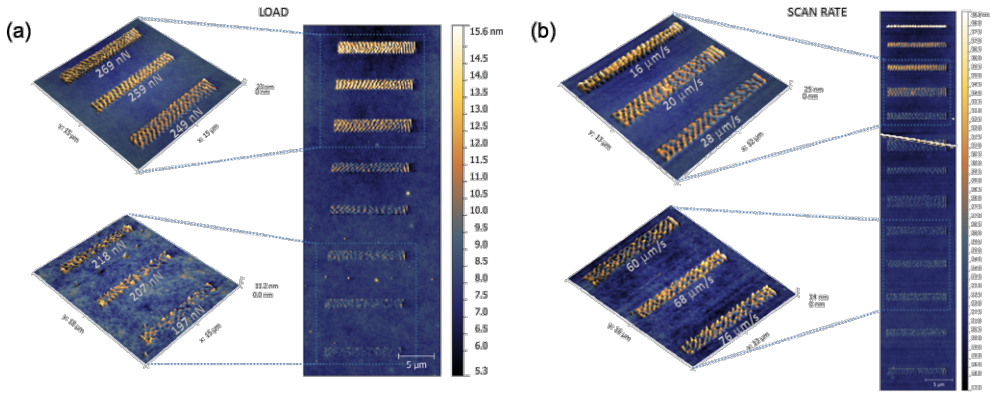

Figure 10: Topographical image of a series of scratches performed on 2 μm long lines on a PS film (M_W = 325 kDa), with increasing normal force F_N (a) and sliding velocity v (b). Unpublished data.

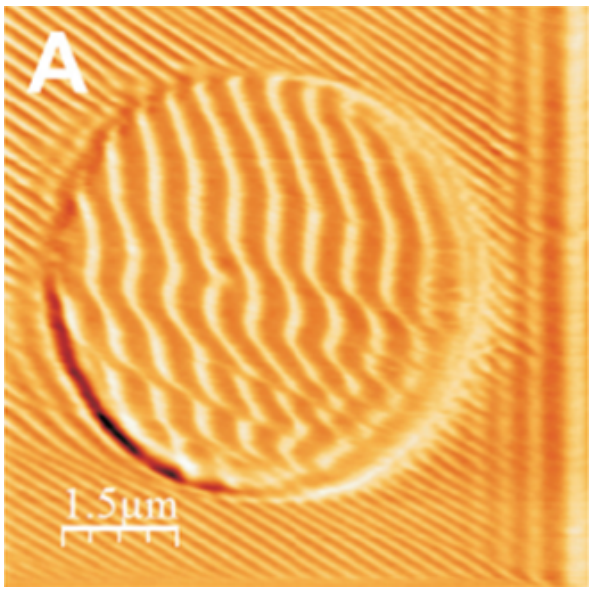

Figure 11: A topographical image of nanoripple patterns on a circular area. The color scale covers a range of 30 nm. The parallel lines on the right hand side are due to an instrumental artefact. Reproduced with permission from [24]. Copyright 2012 IOP Publishing.

High load regime: influence of scan angle, scan geometry and tip feed parameters

As reported above, most works on ripple patterning have been carried out by means of repeated scanning at small load values with a maximum of hundreds of nN. For manufacturing purposes, in order to improve the machining efficiency, it is however needed have precise periodical patterns fabricated in much shorter times. Thus some researchers have thought of increasing the load applied to the polymer films, studying the bundle formation mechanism at very high forces via a single scratch [57].

Recently, Yan et al. [35] have improved the ripple patterning regularity and efficiency by scratching at very high loads. They have studied the influence of the scratch geometry and other parameter as the tip feed during the scan. The samples are injection-molded PC films purchased from a manufacturer. PC is known to be amorphous, however the M_w value is not reported. In another paper [58] the same research group has studied the effect of the scanning angle on the ripple formation by a single scratch at very high loads on polycarbonate (PC) (Figure 12). Finally, by combining scratching angles of 90 and 0°, 90 and 45°, and 0 and 45° in two-step machining, they have been able to fabricate an array of dot and diamond-dot structures with very controlled size and orientation, demonstrating in this way the capability, from a "nanomanipulation" point of view, of the AFM ripple patterning.

Electrostatic lithography

Finally, we briefly mention another family of techniques not strictly connected with wear mechanism but capable of producing a regular pattern and not necessarily ripple-like structures. These techniques rely on mechanisms based on the application of an electrostatic field to an AFM tip not in direct contact with the sample that may induce mechanical instabilities in a polymeric surface. One of such processes has been first discussed by Lyuksyutov et al. [59] and depends on the Joule effect. The polymeric volume under the tip can be heated locally at a $T > T_g$ and attracted to the tip. Thus the film can be permanently deformed and instantly cooled once the voltage is switched off.

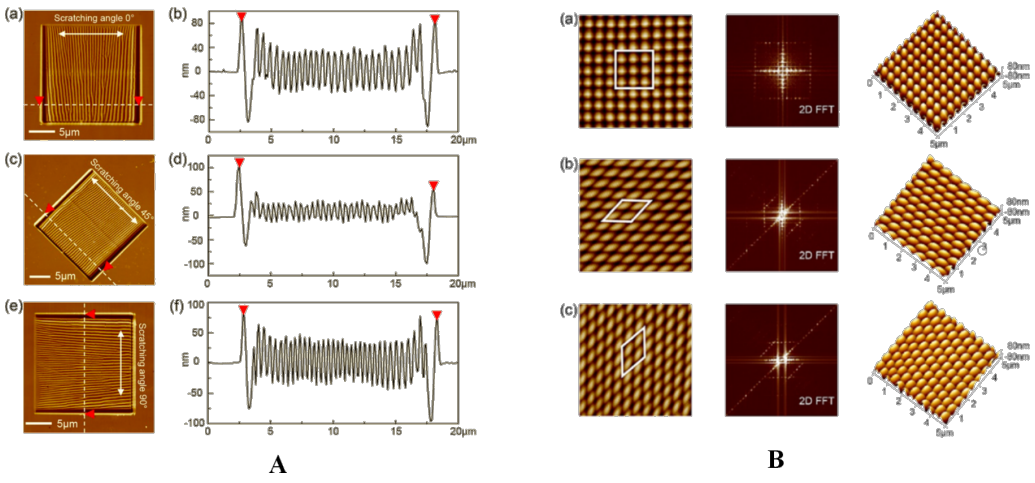

Figure 12: (A) The morphologies and cross-sections of the ripples. The corresponding scratching angles are 0° (a) and (b), 45° (c) and (d), and 90° (e) and (f). (B) Morphologies and 2D FFT images of 3D nanodot arrays. The scanning angles (a) 90° and 0°, (b) 90° and 45°, (c) and 0° and 45° of the two-step scratching method. Reproduced from [58].

J. Y. Park et al. [60] show another possible approach where lines and dot arrays having nanoscale dimensions can be formed by electrochemical patterning. In this case, a film made of the precursor of polyterthiophene/poly(methyl methacrylate) (P3T/PMMA) copolymer can be cross-linked by the application of a voltage via the AFM tip. Specifically, the patterning was performed by means of an ultrasharp conductive tip with a radius of 20 nm applying voltages up to 10 V under ambient conditions (relative humidity: 50 to 60% and T = 22–23 °C).

How to avoid ripple formation

The nanoripple formation can be either a nuisance or an opportunity. In the framework of nanolithography, one should consider the development of tools for creating but also preventing the pattern formation. Regarding this second issue in the past it has been suggested, where applicable, to apply an out-of-plane ultrasonic vibration to the sample in order to avoid the plastic deformation of polymeric surfaces [61].

The basic idea is to break the contact while scanning the tip before the mounds form and the lateral force builds up. More recently, (an example is reported in Figure 13) this principle has been successfully applied to avoid the nanoripple formation in polymeric films [62,63]. This demonstration represents an important achievement towards obtaining a AFM-based nanomanipulation tool that allows one to perform the ripple patterning only when it is desired.

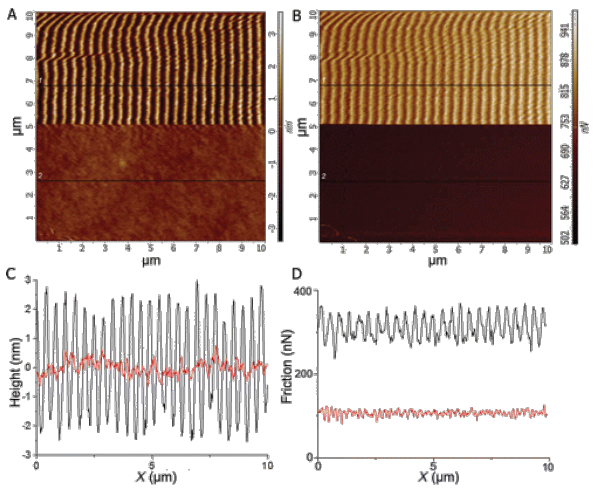

Figure 13: Topography (A) and lateral force (retrace, B) maps and profiles corresponding to the black lines (C and D) while scanning in contact mode (applied load F_N = 1378 nN) on a PS film. An AC voltage was applied to the transducer under the sample while acquiring the lower parts of the images, corresponding to a peak excitation amplitude of 0.55 nm (red profile). The drive voltage was zero while acquiring the upper parts of the image (black profile). Reprinted with permission from [63]. Copyright 2015 American Chemical Society.

Conclusive remarks and future perspectives

In conclusion, the phenomenon of nanoripple formation on polymeric films via contact with AFM probes has been extensively studied in the past decades. The key parameters ruling this physical process have been clearly pointed out and described. Many theoretical works and models have been also proposed up to now. Some of them can reasonably describe and predict the nanoripple formation for several experimental conditions and for some specific material properties. This represents an important improvement for the nanomanipulation capabilities of the AFM technique when compared with initial purely phenomenological observations. An analytical model, fully and precisely describing the phenomenon of nanoscale rippling in polymers in all its complexities, has not been yet developed. However, it is likely that such a model would be analytically too complex and not easily applicable to each particular case. We hope, however, that this review will encourage further studies and future developments in understanding and control of the nanoscale rippling process on polymers.

Acknowledgements

Authors would to acknowledge R. Szoszkiewicz for carefully reading of the manuscript and M.D. would like to thank the NanoICT laboratory for useful support.

References

1. Bagnold, R. A. *The physics of blown sand and desert dunes;* Methuen and Co.: London, United Kingdom, 1941.
2. Navez, M.; Sella, C.; Chaperot, D. *C. R. Hebd. Seances Acad. Sci.* **1962,** *254,* 240.
3. Valbusa, U.; Boragno, C.; de Mongeot, F. B. *J. Phys.: Condens. Matter* **2002,** *14,* 8153. doi:10.1088/0953-8984/14/35/301
4. Birnbaum, M. *J. Appl. Phys.* **1965,** *36,* 3688–3689. doi:10.1063/1.1703071
5. Binnig, G.; Quate, C. F.; Gerber, C. *Phys. Rev. Lett.* **1986,** *56,* 930. doi:10.1103/PhysRevLett.56.930
6. Gnecco, E.; Bennewitz, R.; Meyer, E. *Phys. Rev. Lett.* **2002,** *88,* 215501. doi:10.1103/PhysRevLett.88.215501
7. Socoliuc, A.; Bennewitz, R.; Gnecco, E.; Meyer, E. *Phys. Rev. Lett.* **2004,** *92,* 134301. doi:10.1103/PhysRevLett.92.134301
8. Teichert, C. *Phys. Rep.* **2002,** *365,* 335. doi:10.1016/S0370-1573(02)00009-1
9. Kim, Y. B.; Ban, B. S. *Liq. Cryst.* **1999,** *26,* 1579. doi:10.1080/026782999203553
10. D'Acunto, M. *Physica B* **2010,** *405,* 793. doi:10.1016/j.physb.2009.10.003
11. D'Acunto, M. *Tribol. Lett.* **2012,** *45,* 161. doi:10.1007/s11249-011-9879-2
12. Filippov, A. E.; Popov, V. L.; Urbakh, M. *Phys. Rev. Lett.* **2011,** *106,* 025502. doi:10.1103/PhysRevLett.106.025502
13. Sun, Y.; Yan, Y.; Liang, Y.; Hu, Z.; Zhao, X.; Sun, T.; Dong, S. *Scanning* **2013,** *35,* 308. doi:10.1002/sca.21069
14. Leung, O. M.; Goh, M. C. *Science* **1992,** *255,* 64–66. doi:10.1126/science.255.5040.64

15. Elkaakour, Z.; Aimé, J. P.; Bouhacina, T.; Odim, C.; Masuda, T. *Phys. Rev. Lett.* **1994,** *73,* 3231–3234. doi:10.1103/PhysRevLett.73.3231
16. Kaneko, R.; Hamada, E. *Wear* **1993,** *162–164,* 370–377. doi:10.1016/0043-1648(93)90520-V
17. Khurshudov, A.; Kato, K. *J. Vac. Sci. Technol., B* **1995,** *13,* 1938–1944. doi:10.1116/1.588112
18. Iwata, F.; Matsumoto, T.; Sasaki, A. *Nanotechnology* **2000,** *11,* 10–15. doi:10.1088/0957-4484/11/1/303
19. Wang, X. P.; Loy, M. M. T.; Xiao, X. *Nanotechnology* **2002,** *13,* 478–483. doi:10.1088/0957-4484/13/4/307
20. Schmidt, R. H.; Haugstad, G.; Gladfelter, W. L. *Langmuir* **2003,** *19,* 898–909. doi:10.1021/la015769j
21. Szoszkiewicz, R.; Okada, T.; Jones, S. J.; Li, T.-D.; King, W. P.; Mader, S. R.; Riedo, E. *Nano Lett.* **2007,** *7,* 1064–1069. doi:10.1021/nl070300f
22. Gnecco, E.; Riedo, E.; King, W. P.; Mader, S. R.; Szoszkiewicz, R. *Phys. Rev. B* **2009,** *79,* 235421. doi:10.1103/PhysRevB.79.235421
23. D'Acunto, M.; Napolitano, S.; Pingue, P.; Giusti, P.; Rolla, P. *Mater. Lett.* **2007,** *61,* 3305–3309. doi:10.1016/j.matlet.2006.11.067
24. Napolitano, S.; D'Acunto, M.; Baschieri, P.; Gnecco, E.; Pingue, P. *Nanotechnology* **2012,** *23,* 475301. doi:10.1088/0957-4484/23/47/475301
25. Prucker, O.; Christian, S.; Bok, H.; Rühe, J.; Frank, C. W.; Knoll, W. *Macromol. Chem. Phys.* **1998,** *199,* 1435. doi:10.1002/(SICI)1521-3935(19980701)199:7<1435::AID-MACP1435>3.0.CO;2-#
26. O'Connell, P. A.; Hutcheson, S. A.; McKenna, G. B. *J. Polym. Sci., Part B: Polym. Phys.* **2008,** *46,* 1952. doi:10.1002/polb.21531
27. D'Acunto, M.; Dinelli, F.; Pingue, P. Nanowear of Polymers. In *Fundamentals of Friction and Wear on the Nanoscale;* Gnecco, E.; Meyer, E., Eds.; Springer: Berlin, Germany, 2015; pp 545–587. doi:10.1007/978-3-319-10560-4_24
28. Schallamach, A. *Wear* **1971,** *17,* 301. doi:10.1016/0043-1648(71)90033-0
29. Koudine, A. A.; Barquins, M. *J. Adhes. Sci. Technol.* **1996,** *10,* 951. doi:10.1163/156856196X00030
30. Gotsmann, B.; Duerig, U. T.; Sills, S.; Frommer, J.; Hawker, C. J. *Nano Lett.* **2006,** *6,* 296–300. doi:10.1021/nl0520563
31. Aoike, T.; Yamamoto, T.; Uehara, H.; Yamanobe, T.; Komoto, T. *Langmuir* **2001,** *17,* 5688–5692. doi:10.1021/la0102962
32. Khurshudov, A.; Kato, K. *Wear* **1997,** *205,* 1–10. doi:10.1016/0043-1648(95)06893-7
33. Surtchev, M.; de Souza, N. R.; Jérôme, B. *Nanotechnology* **2005,** *16,* 1213–1220. doi:10.1088/0957-4484/16/8/040
34. Jing, J.; Henriksen, P. N.; Wang, H.; Marteny, P. *J. Mater. Sci.* **1995,** *30,* 5700–5704. doi:10.1007/BF00356708
35. Yan, Y.; Sun, Y.; Yang, Y.; Hu, Z.; Zhao, X. *Appl. Surf. Sci.* **2012,** *258,* 9656–9663. doi:10.1016/j.apsusc.2012.06.005
36. Rice, R. H.; Gnecco, E.; Wannemacher, R.; Szoszkiewicz, R. *Polymer* **2013,** *54,* 3620–3623. doi:10.1016/j.polymer.2013.05.015
37. Dinelli, F.; Leggett, G. J.; Shipway, P. H. *Nanotechnology* **2005,** *16,* 675–682. doi:10.1088/0957-4484/16/6/009
38. Fetters, L. J.; Lohse, D. J.; Colby, R. H. *Physical Properties of Polymers Handbook, Part V;* Springer: Berlin, Germany, 2007; pp 447–454.
39. Beake, D. B.; Shipway, P. H.; Leggett, G. J. *Polymer* **2001,** *42,* 7025–7031. doi:10.1016/S0032-3861(01)00186-0
40. Beake, D. B.; Leggett, G. J. *Polymer* **2002,** *43,* 319–327. doi:10.1016/S0032-3861(01)00600-0
41. Beake, D. B.; Shipway, P. H.; Leggett, G. J. *Wear* **2004,** *256,* 118–125. doi:10.1016/S0043-1648(03)00369-7
42. Sperling, L. H. *Introduction to Physical Polymer Science,* 4th ed.; John Wiley & Sons, Inc.: Hoboken, NJ, U.S.A., 2006.
43. Leach, R. N.; Stevens, F.; Seiler, C.; Langford, S. C.; Dickinson, J. T. *Langmuir* **2003,** *19,* 10225–10229. doi:10.1021/la035289n
44. Fischer, H. *Macromolecules* **2002,** *35,* 3592–3595. doi:10.1021/ma010849f
45. Schmidt, R. H.; Haugstad, G.; Gladfelter, W. L. *Langmuir* **1999,** *15,* 317–321. doi:10.1021/la980739a
46. Dinelli, F.; Buenviaje, C.; Overney, R. M. *J. Chem. Phys.* **2000,** *113,* 2043–2058. doi:10.1063/1.482012
47. Fu, J.; Li, B.; Han, Y. *J. Chem. Phys.* **2005,** *123,* 064713. doi:10.1063/1.1961228
48. Rice, R. H.; Mokarian-Tabari, P.; King, W. P.; Szoszkiewicz, R. *Langmuir* **2012,** *28,* 13503–13511. doi:10.1021/la302565s
49. Buenviaje, C.; Dinelli, F.; Overney, R. M. *Macromol. Symp.* **2001,** *167,* 201–212. doi:10.1002/1521-3900(200103)167:1<201::AID-MASY201>3.0.CO;2-P
50. Maas, J. H.; Cohen Stuart, M. A.; Fleer, G. J. *Thin Solid Films* **2000,** *358,* 234–240. doi:10.1016/S0040-6090(99)00705-1
51. Aoike, T.; Ikeda, T.; Uehara, H.; Yamanobe, T.; Komoto, T. *Langmuir* **2002,** *18,* 2949–2951. doi:10.1021/la011643a
52. Briscoe, B. J.; Pellilo, E.; Sinha, S. K. *Polym. Eng. Sci.* **1996,** *36,* 2996. doi:10.1002/pen.10702
53. Rand, C. J.; Crosby, A. J. *Appl. Phys. Lett.* **2006,** *89,* 261907. doi:10.1063/1.2408640
54. Gnecco, E.; Pedraz, P.; Nita, P.; Dinelli, F.; Napolitano, S.; Pingue, P. *New J. Phys.* **2015,** *17,* 032001. doi:10.1088/1367-2630/17/3/032001
55. Prandtl, L. *Z. Angew. Math. Mech.* **1928,** *8,* 85. doi:10.1002/zamm.19280080202
56. Vettiger, P.; Cross, G.; Despont, M.; Drechsler, U.; Durig, U.; Götsmann, B.; Haberle, W.; Lantz, M. A.; Rothuizen, H. E.; Stutz, R.; Binnig, G. K. *IEEE Trans. Nanotechnol.* **2002,** *1,* 39–55. doi:10.1109/TNANO.2002.1005425
57. Sun, Y.; Yan, Y.; Hub, Z.; Zhao, X.; Yan, I. *Tribol. Int.* **2012,** *47,* 44–49. doi:10.1016/j.triboint.2011.10.018
58. Yan, Y.; Sun, Y.; Li, J.; Hu, Z.; Zhao, X. *Nanoscale Res. Lett.* **2014,** *9,* 372. doi:10.1186/1556-276X-9-372
59. Lyuksyutov, S. F.; Paramonov, P. B.; Juhl, S.; Vaia, R. A. *Appl. Phys. Lett.* **2003,** *83,* 4405. doi:10.1063/1.1629787
60. Park, J. Y.; Taranekar, P.; Advincula, R. *Soft Matter* **2011,** *7,* 1849. doi:10.1039/C0SM00993H
61. Dinelli, F.; Assender, H. E.; Takeda, N.; Briggs, G. A. D.; Kolosov, O. V. *Surf. Interface Anal.* **1999,** *27,* 562–567. doi:10.1002/(SICI)1096-9918(199905/06)27:5/6<562::AID-SIA538>3.0.CO;2-K
62. Knoll, A.; Rothuizen, H.; Gotsmann, B.; Duerig, U. *Nanotechnology* **2010,** *21,* 185701. doi:10.1088/0957-4484/21/18/185701
63. Pedraz, P.; Wannemacher, R.; Gnecco, E. *ACS Nano* **2015,** *9,* 8859–8868. doi:10.1021/acsnano.5b02466